AN INVESTIGATION OF IMAGING APPROACHES FOR THE STUDY OF ERBB2 DISTRIBUTION AND DYNAMICS IN THE PLASMA MEMBRANE WITH RESPECT TO THE DISTRIBUTION OF THE TETRASPANIN CD82

By

EMMA LONNEN

A thesis submitted to the University of Birmingham for the degree of DOCTOR OF PHILOSOPHY

PSIBS Doctoral Training Centre
School of Chemistry
College of Engineering and Physical Sciences
University of Birmingham
25 May 2018

Abstract

Tetraspanin proteins are known to organise in the plasma membrane and form tetraspanin enriched microdomains. The tetraspanin CD82/KAI1 has been shown previously by ensemble imaging and biochemical methods to associate with ErbB2, and it has been suggested that CD82 may play a role in regulating the distribution and dynamics of ErbB2 in the plasma membrane [1], [2]. CD82 may also play a role in mediating cellular response to Herceptin. In order to investigate the effect of CD82 on ErbB2 distribution and dynamics in the plasma membrane we applied a number of imaging techniques, in particular super resolution and single molecule approaches. We found little effect of CD82 expression on either ErbB2 diffusion or confinement characteristics in MCF7 and SKBR3 cells, and little difference in either the intrinsic clustering of ErbB2 or clustering in response to treatment with a panel of ErbB targeting molecules. We did however demonstrate and quantify the importance of optimising both the imaging and analysis conditions for dual colour super-resolution imaging, and demonstrated for the first time the combination of super resolution optical fluctuation imaging and single molecule tracking.

FOR MY PARENTS

Acknowledgements

Firstly I would like to thank my lead supervisor Elena Odintsova for giving me the opportunity to work in her laboratory, and for her support and guidance in the completion of this research. I am also very grateful to my co-supervisor Rob Neely, for stepping up to the role of supervisor part-way through this project, and for insightful discussions and input to the direction of the work. I would also like to thank my co-supervisor Ela Claridge, for her continual support throughout the project.

I would like to thank the members of the Odintsova and Berditchevski groups, in particular Vera Novitskaya, whose knowledge and advice has proved invaluable on countless occasions over the last several years; and Regina Andrijes, who physically handed in this thesis when I couldn't.

Many people provided both practical and intellectual support for this project, and although I cannot list them all here, I am grateful to each and every one of them. I owe thanks to Alessandro Di Maio at the Birmingham Advanced Light Microscopy centre for training and practical support on the microscope on which the single molecule tracking data presented in this thesis was acquired, and to Eric Pitkeathly for kindly providing me with his particle tracking software. Particular thanks is also due to Steve Thomas for providing access to the NSTORM microscope, to Natalie Poulter for training and support in using it, and to both for insightful discussions on data analysis.

I would like to acknowledge the Engineering and Physical Sciences Research Council for funding my studentship through the Physical Sciences of Imaging in the Biomedical Sciences Doctoral Training Centre, and to thank those of my cohort who I now call good friends, and could not have done this without. I would also like to thank Iain Styles for his support and guidance throughout my time in PSIBS.

Lastly, I want to acknowledge my parents, Bernie and Pam. There are no words to express how grateful I am to them both, for everything.

Contents

Chapter 1 - Introduction 1
1.1 General introduction 1
1.1.1 Biological motivation 1
1.2 Structure and organisation of mammalian cell membranes 2
1.2.1 The fluid mosaic model and lipid rafts 5
1.2.2 The actin cytoskeleton and the membrane picket fence model 6
1.2.3 Dynamic protein clustering 8
1.2.4 The hierarchical three-tiered meso-scale domain architecture hypothesis 9
1.2.5 Recent concepts in plasma membrane organisation 10
1.2.6 Notes on terminology 14
1.3 Cancer 15
1.3.1 Breast cancer 15
1.4 ErbB receptors 16
1.4.1 ErbB receptors and cancer 17
1.4.2 ErbB2 18
1.5 Tetraspanins 22
1.5.1 The tetraspanin superfamily 22
1.5.2 Properties of tetraspanins 22
1.5.3 Interactions of tetraspanins 24
1.5.4 Tetraspanin enriched microdomains 25
1.5.5 Tetraspanins and cancer 26
1.6 Imaging modalities 28
1.6.1 Epifluorescence microscopy 28
1.6.2 Total internal reflection fluorescence microscopy 28
1.6.3 Confocal fluorescence microscopy 30
1.7 Imaging techniques 31
1.7.1 Fluorescence recovery after photobleaching 31
1.7.2 Single molecule tracking 32
1.7.3 Super-resolution microscopy 33
1.8 Thesis aims 36
Chapter 2 – Materials and Methods 37
2.1 Cell culture 37
2.1.1 Maintenance of mammalian cell lines 37
2.1.2 Cryopreservation and recovery of cell lines 38
2.1.3 Cell transfection 38

2.2 Antibodies 39
2.2.1 Herceptin 39
2.2.2 Fragmentation and biotinylation of antibodies 39
2.2.3 Primary antibodies 40
2.2.4 Secondary Antibodies 40
2.3 Fluorescence recovery after photobleaching of ErbB2-GFP 40
2.1 Single molecule tracking 41
2.1.1 Labelling 41
2.1.2 Imaging 42
2.1.3 Tracking and analysis 43
2.2 SOFI 44
2.3 Direct stochastic optical reconstruction (dSTORM) microscopy 44
2.3.1 Nikon nSTORM system 44
2.3.2 Preparation of dSTORM imaging buffer 44
2.3.3 Preparation of samples for imaging 44
2.3.4 Image acquisition 45
2.3.5 Reconstruction 46
Chapter 3 –Dynamic imaging studies revealing ErbB2 distribution and diffusion properties 47
3.1 FRAP 48
3.1.1 Analysis of FRAP experiments 51
3.1.2 Results 51
3.1.3 Conclusion 56
3.2 Single molecule tracking with quantum dots 57
3.2.1 Performing single molecule tracking experiments 58
3.2.2 Fluorophores 59
3.2.3 Labels 62
3.2.4 Analysing single molecule tracking experiments – from images to single molecule trajectories 64
3.2.5 Results 71
3.2.6 Conclusion 89
3.3 Super Resolution Optical Fluctuation Imaging 89
3.3.1 Mapping the distribution of CD82 on the plasma membrane with SOFI 90
3.3.2 Combination of SMT and SOFI 93
3.3.3 Conclusion 95
Chapter 4 – Imaging of static protein distribution in the plasma membrane by super-resolution fluorescence microscopy 99
4.1 Chapter overview 99

4.2 Introduction to super-resolution microscopy 99
4.2.1 The diffraction limit to resolution 100
4.2.2 Overcoming the diffraction limit 102
4.2.3 Direct Stochastic Optical Reconstruction Microscopy (dSTORM) 103
4.3 Choice of labelling strategy for dual colour data 108
4.4 Imaging procedures 112
4.4.1 Composition of the imaging buffer 113
4.5 Analysis of dSTORM data 121
4.5.1 Reconstruction 121
4.5.2 Analysis 123
4.5.3 Ripley's K-function 124
4.5.4 Density Based Spatial Clustering of Applications with Noise (DBSCAN) 125
4.6 Colocalisation analysis– molecular colocalisation and cluster colocalisation 129
4.7 Optimisation of labelling and imaging conditions 131
4.7.1 Permeabilisation of the samples improved labelling 132
4.7.2 Validating label concentration via flow cytometry 133
4.7.3 Negative controls 135
4.8 Development and optimisation of computational analysis methods 137
4.8.1 Optimisation of cluster analysis with DBSCAN 138
4.8.2 Analysis of data by ROI selection vs analysing the full field of view – investigation of whether ROI selection influences or biases the results compared to analysis of the full field of view 143
4.9 Analysis of dual colour data - combined molecular colocalisation and DBSCAN clustering 159
4.9.1 Calculating colocalisation 163
4.10 ErbB2 distribution in SKBR3 and MCF7 cell lines relative to CD82 expression 168
4.10.1 Effect of changes in CD82 expression on ErbB2 cluster properties 169
4.10.2 Effect of changes in CD82 expression on CD82 cluster properties 178
4.11 Effect of CD82 expression on ErbB2 clustering in response to treatment with the ErbB ligands EGF and heregulin, and the ErbB2 targeting drug Herceptin 185
4.11.1 Motivation 185
4.11.2 Results 188
4.11.3 Analysis of effect of stimulation on colocalisation of ErbB2 with phosphotyrosine and CD82 195
4.12 Conclusions and future work 202
4.12.1 Future work on analysis 202
1.1.1 Future experimental work 204

4.12.2 Conclusions 205
Chapter 5 – Conclusions 207
References 209

List of figures

Figure 1-1: Phospholipid bilayer structure of the plasma membrane 3
Figure 1-2. The membrane skeleton visualised by electron microscopy. 8
Figure 1-3: Schematic representation of the three tiers organising the plasma membrane. 10
Figure 1-4: A dynamic view of the tetraspanin web. 14
Figure 1-5: The ErbB family of receptor tyrosine kinases and ligands 17
Figure 1-6: Ribbon diagrams of A) sHER2 and (B) a monomer of the sEGFR/EGF complex 19
Figure 1-7: Structural features of tetraspanins 23
Figure 1-8 Comparative schematic of light path in epifluorescence and TIRF microscopy modes. 30
Figure 1-9: Schematic diagram of the principle of confocal microscopy 31
Figure 3-1: Typical plot of intensity versus time for a FRAP experiment 50
Figure 3-2: The effect of CD82 expression and Herceptin treatment on ErbB2 mobility in MCF7 cells 56
Figure 3-3: Size dependent absorption and emission spectra of semiconductor nanocrystals 62
Figure 3-4: Illustration of enzyme digestion of IgG antibody molecule to form Fab fragments 64
Figure 3-5: Mean square displacement analysis of a one-dimensional trajectory 69
Figure 3-6: Classification of experimental single molecule trajectories by calculation of the confinement index over the trajectory 73
Figure 3-7: Simulated single molecule trajectories for confinement detection validation 77
Figure 3-8: Quantification of confinement detection performance on trajectories with simulated episodes of confinement 79
Figure 3-9: Diffusion and confinement characteristics of ErbB2 in SKBR3 cell membranes 82
Figure 3-10: Diffusion and confinement of ErbB2 in MCF7 cell membranes 84
Figure 3-11: ErbB2 trajectories on MCF7 cell membrane and corresponding image of mean confinement index 85
Figure 3-12: Single molecule ErbB2 and CD82 trajectories do not show co-confinement on SKBR3 cell membranes 88
Figure 3-13: Comparison of resolution of an average intensity image of CD82, a 2nd order SOFI reconstruction of the same image, and a STORM image of Alexa-647 labelled CD82 on SKBR3 cells. 91
Figure 3-14: Multi-level Otsu thresholding segments areas of enriched CD82 signal in SOFI reconstructions 92
Figure 3-15: Single level Otsu thresholding delineates boundaries of CD82 enriched areas in SOFI reconstructions 93
Figure 3-16: ErbB2 trajectories overlaid on SOFI reconstructions of CD82 distribution in SKBR3 cells A & B – SKBR3/zeo; C & D – SKBR3/CD82. 97
Figure 4-1: Airy disk diffraction patterns 101
Figure 4-2: Pictorial representation of super-resolution microscopy by localisation 104
Figure 4-3: Comparison of labelling achieved with whole IgG and different fluorophore secondary labels and biotinylated Fab fragments with avidin conjugated secondaries on SKBR3 (ErbB2 over-expressing) and MCF7 (low ErbB2 expression) cells 111
Figure 4-4: Clusters recovered from data acquired with concentration of MEA in the imaging buffer varied from 0-100 mM 116
Figure 4-5: Localisations per μm^2 in SKBR3/zeo cells labelled imaged with different concentrations of MEA in the imaging buffer 118
Figure 4-6: Histogram of CD82 cluster area in SKBR3/zeo labelled with C33 and Alexa-647 where the concentration of MEA in the imaging buffer was varied between 0 and 100 mM. 120
Figure 4-7: Histogram of ErbB2 cluster area in SKBR3/zeo labelled with Herceptin and Alexa-488 where the concentration of MEA in the imaging buffer was varied between 0 and 100 mM. 120

Figure 4-8: Consecutive raw images from a dSTORM experiment 122
Figure 4-9: Simulated data used in calculation of optimal DBSCAN ε parameter 128
Figure 4-10: Schematic diagram illustrating steps in ClusDoc analysis 130
Figure 4-11: Effect of permeabilisation with 0.5% saponin on label distribution in dSTORM imaging samples 133
Figure 4-12: Cross-talk negative control images – MCF7 puro labelled with Herceptin and Alexa 647 136
Figure 4-13: Cross-talk negative control images – MCF7 puro labelled with C33 and Alexa 488 136
Figure 4-14: Multi-pass clustering of ErbB2 and CD82 on dual labelled SKBR3/zeo cells 140
Figure 4-15: Mean number of ErbB2 and CD82 clusters found by multi-pass DBSCAN analysis of Alexa-647 labelled ErbB2 and CD82 on SKBR3 and MCF7 cell lines 142
Figure 4-16: Mean number of molecules of ErbB2 and CD82 in clusters found by multi-pass DBSCAN analysis of Alexa-647 labelled ErbB2 and CD82 on SKBR3 and MCF7 cell lines 143
Figure 4-17: Classification of points as noise or clustered by DBSCAN 145
Figure 4-18: Example ROIs selected for cluster analysis of ErbB2 on SKBR3 cells 146
Figure 4-19: Point distribution and recovered clusters of ErbB2 in ROIs selected under the body of an SKBR3 cell (cell from Figure 4-18 A) 147
Figure 4-20: Point distribution and recovered clusters of ErbB2 in ROIs selected around the edge of an SKBR3 cell (cell from Figure 4-18 B) 147
Figure 4-21: The effect of ROI selection on the distribution of cluster parameters of ErbB2 in SKBR3/zeo cells 149
Figure 4-22: ErbB2 cluster properties in SKBR3/zeo and SKBR3/CD82 cells when determined from ROIs selected at the cell edge, or ROIs selected under the cell body. 154
Figure 4-23: CD82 cluster properties in SKBR3/zeo and SKBR3/CD82 cells when determined from ROIs selected at the cell edge, or ROIs selected under the cell body. 155
Figure 4-24: Erbb2 cluster properties in MCF7 cells 158
Figure 4-25: Distance to nearest neighbour points in data from each channel of dual labelled SKBR3/zeo 162
Figure 4-26: Number of points within ε of each point in data from each channel of dual labelled SKBR3/zeo 162
Figure 4-27: Analysis of data with Clus-Doc, combined molecular colocalisation and cluster analysis 165
Figure 4-28: Degree of colocalisation histograms for ErbB2 with CD82 in SKBR3/CD82 with corresponding DoC maps and clusters 167
Figure 4-29: Analysis of ErbB2 clusters colocalised with CD82 in SKBR3 cells – molecules per cluster 172
Figure 4-30: Density of ErbB2 clusters in SKBR3 cells in relation to colocalisation with CD82 177
Figure 4-31: Representative dSTORM localisation images of ErbB2 and CD82 distribution in SKBR3/zeo and SKBR3/CD82 cells 179
Figure 4-32: Hypothetical changes to cluster properties with increased protein expression 180
Figure 4-33: CD82 cluster properties in SKBR3 cells 182
Figure 4-34: CD82 cluster properties in MCF7 cells 183
Figure 4-35: Molecules of ErbB2 per cluster in SKBR3/zeo and SKBR3/CD82 cells after ErbB2 targeting treatments 191
Figure 4-36: ErbB2 cluster density and molecules per cluster in MCF7 cells after stimulation with 10ng/ml heregulin 194
Figure 4-37: Erbb2 molecules per cluster after stimulation with EGF or Herceptin in relation to colocalisation with phospho-tyrosine specific antibody 196

Figure 4-38: Erbb2 molecules per cluster after treatment with Herceptin or heregulin in relation to colocalisation with CD82 201

List of tables

Table 1-1: Alterations of ErbB receptors and ligands in human cancer. 18
Table 2-1: Details of cell lines used in this study 37
Table 2-2: Properties of cell lines used in this study 38
Table 2-3. Details of primary antibodies used in this study 40
Table 2-4 Details of secondary antibodies used in this study 40
Table 2-5: Details of Streptavidin conjugated quantum dots 41
Table 3-1 Diffusion and confinement of ErbB2 in SKBR3 cells 83
Table 3-2 Diffusion and confinement of ErbB2 in MCF7 cells 83
Table 3-3 Incidence of colocalisation with CD82 in ErbB2 trajectories 98
Table 3-4 Properties of ErbB2 confinement relative to colocalisation with CD82 98
Table 4-1 Validation of primary antibody concentration for dSTORM labelling by flow cytometry on SKBR3 cells 134
Table 4-2 Validation of primary antibody concentration for dSTORM labelling by flow cytometry on SKBR3 cells 134
Table 4-3 Investigating ErbB2 labelling on MCF7 cells using Herceptin, Herceptin Fab fragments and Ab-2 antibody 135
Table 4-4: ErbB2 cluster properties determined by analysis of the full field of view, ROIs selected at the cell edge or ROIs selected under the cell body in SKBR3/zeo and SKBR3/CD82 cells (N cells SKBR3/zeo = 3, SKBR3/CD82 = 3) 153
Table 4-5: CD82 cluster properties determined by analysis of the full field of view, ROIs selected at the cell edge or ROIs selected under the cell body in SKBR3/zeo and SKBR3/CD82 cells (N cells SKBR3/zeo = 4, SKBR3/CD82 = 3) 153
Table 4-6: Erbb2 cluster properties in MCF7 cells 159
Table 4-7: CD82 cluster properties in SKBR3/CD82 determined from ClusDoc analysis with DBSCAN cluster parameters MinPts and ε varied from 3-4 and 20-70 nm respectively 163
Table 4-8: ErbB2 cluster properties in SKBR3 cells relative to colocalisation with CD82 177
Table 4-9: Proportion of all molecules with degree of colocalisation greater than the threshold value of 0.4 in each cell line 177
Table 4-10: CD82 cluster properties in SKBR3 cells 184
Table 4-11: CD82 cluster properties in MCF7 184
Table 4-12: Properties of ErbB2 clusters in stimulated SKBR3 cells 193
Table 4-13: ErbB2 cluster properties in MCF7 cells after treatment with 10ng/ml heregulin 193

Abbreviations

Abbreviation	
PM	Plasma membrane
FMM	Fluid mosaic model
GPI-Aps	Glycosyl phosphatidylinositol anchored proteins
TERM	Tetraspanin enriched microdomain
TEA	Tetraspanin enriched area
IP	Immunoprecipitation
WB	Western blot
SR	Super resolution
IP	Immunoprecipitation
FC	Flow cytometry
SOFI	Super resolution optical fluctuation microscopy
FRAP	Fluorescence recovery after photobleaching
SMT	Single molecule tracking
SPT	Single particle tracking
SQT	Single quantum dot tracking
FRET	Forster Resonance Energy Transfer
FLIM	Fluorescence Lifetime Imaging
NSCLC	Non-small cell lung carcinoma
TM	Transmembrane
EC2	Extracellular loop 2
STORM	Stochastic optical reconstruction microscopy
dSTORM	Direct stochastic optical reconstruction microscopy
PSF	Point spread function
NSOM	Near-field scanning optical microscopy
MHT	Multi-hypothesis tracking
QD	Quantum dot

Chapter 1 - Introduction

1.1 General introduction

This thesis is concerned with the interaction of certain membrane proteins and the organisation of the cell membrane, and how this may mediate certain interactions and the effect this might have on the action of ErbB2 targeting drugs. In order to assess this thesis mainly focuses on the application of a variety of different imaging techniques to gain complementary information from each. The optimisation of each technique is discussed, as are the advantages and disadvantages of conducting different types of study with these methodologies and issues in analysis of the resulting data. The primary aim of this thesis is to determine the relevance of membrane microdomains for influencing protein interactions in the plasma membrane in CD82 and ErbB2 expressing breast cancer cell lines. In order to achieve this we investigated and developed methods for studying interactions and organisation in/of the plasma membrane (PM) at the single molecule level

1.1.1 Biological motivation

In this project we studied interactions of two membrane proteins – ErbB2, a receptor tyrosine kinase member of the ErbB family which is over-expressed in certain aggressive breast cancers; and CD82, a transmembrane protein of the tetraspanin family, which is also implicated in certain cancers. CD82 is involved in the formation of tetraspanin-enriched microdomains (TERMs), which have an important role in mediating protein interactions in the plasma membrane. We investigate the possibility of a role for TERMs in regulating interactions of ErbB2, possibly by physically restricting the motion of the protein on the plasma membrane. Thus tetraspanins (e.g. CD82) may impact on the efficacy of drugs targeting ErbB2 in breast cancer. If this can be conclusively demonstrated, then it may be possible to optimise the treatment of ErbB2 over-expressing cancers by identifying whether a patient is likely to respond to an ErbB2-targeting drug. In order to answer this question a variety of microscopy

techniques have been applied and combined, and computational work to extract dynamic information from the resulting images has been carried out, in an effort to determine the extent to which TERMs modulate ErbB2 behaviour in the plasma membrane.

1.2 Structure and organisation of mammalian cell membranes

The plasma membrane of mammalian cells is a dynamic environment, forming a barrier between the extracellular environment and the interior of the cell, and is responsible for a myriad of functions that regulate cell physiology. It plays a crucial role in a multitude of processes that include adhesion, migration, cell signalling and cell–cell communication. Fundamentally it is composed of a phospholipid bilayer, which forms a stable barrier between the two aqueous environments of the exterior and interior of the cell [3]. The membrane is asymmetric, with different protein composition on the inner and outer leaflets, and little 'flip-flop' of proteins between the two, maintaining differences between the inside and the outside of cells to facilitate the appropriate display of receptors, adhesion molecules, signalling systems, scaffolding structures and other molecules on opposite membrane surfaces [4]. Interactions in the plasma membrane play a crucial role in signal transduction – communication between the inside and outside of the cell. In order to interpret data regarding the respective motion and distributions of membrane proteins and their interactions, it is necessary to understand the prevailing theories used to describe the plasma membrane environment in which they reside.

The plasma membrane consists of a lipid bilayer, which behaves like a two dimensional fluid in which different molecules reside and diffuse in the membrane, shown in Figure 1-1. In the classic model proposed by Singer and Nicholson the lipid bilayer acts as a neutral solvent for membrane proteins, within which all particles diffuse freely [5]. However, significant modifications to this model have

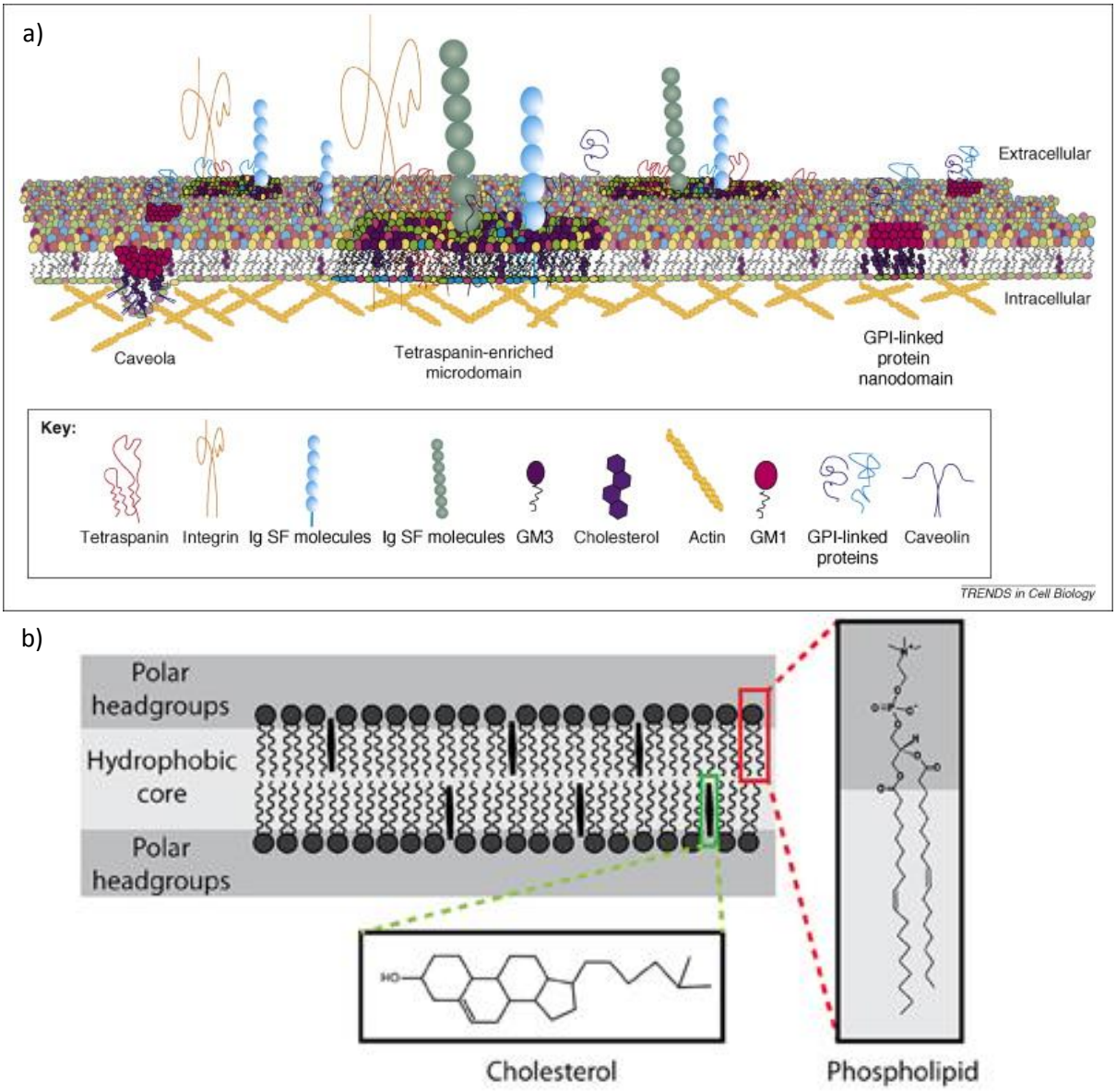

Figure 1-1: Phospholipid bilayer structure of the plasma membrane
a) Phospholipid bilayer making up the plasma membrane, containing a variety of proteins which diffuse in the membrane. Proteins may diffuse freely/singly or be involved in interactions forming higher order complexes or microdomains, such as caveola, tetraspanin-enriched microdomains and GPI-linked protein nanodomains. The membrane is underlain by the actin cytoskeleton, which plays a role in organising the constituent proteins in the membrane. Molecules and domains not drawn to scale. Modified from [6] b) Schematic representation of the phospholipid bilayer from a) shown in greater detail. Cell membranes have a hydrophobic core and a polar headgroup space. The phospholipids and cholesterol making up the membrane are shown here. Reproduced from [7].

been made in recent years, taking into account experimental results than cannot be explained by this classical model, such as the observation of 'hop diffusion', different diffusion coefficients in

artificial and blebbed membranes compared to the plasma membrane, and the observation of lateral segregation of diffusing molecules [8].

Collisions between the diffusing molecules in the plasma membrane give rise to interactions, which can initiate signalling events within the cell. It is therefore important to increase our understanding of the underlying mechanisms which mediate the dynamics and distribution of proteins in the plasma membrane, so that we can better understand how signalling processes and their consequences may be affected by changes to the plasma membrane organisation by drug treatment or genetic changes.

The importance of an underlying organisation of the plasma membrane by microdomains can be considered in terms of the impact of lateral segregation of proteins on collision rates. When two molecules become co-confined in the same domain this greatly increases the specific interprotein collision frequency of these molecules, and thus the reaction rate. Therefore mechanisms of lateral segregation of proteins may have a role in regulating the interactions of plasma membrane proteins and subsequent signalling processes, and be important for our understanding of abnormal cellular behaviour.

The plasma membrane interacts with the adjacent extracellular matrix and subjacent membrane-associated cytoskeleton, and is highly organised, with areas governed by these interactions in which specific components are enriched or to which they can be recruited, thus providing specialised cellular regions such as the basal and apical membranes in epithelial/polarised cells. While the plasma membrane was once considered a relatively unstructured sea of lipids and proteins, having the potential to form aggregates, it is now widely accepted that it is highly compartmentalized, with lipids and proteins organised in specific regions of varying size, composition and function [4], [9], [10]. The main theories of plasma membrane organisation – lipid rafts, the actin picket fence model,

and protein nanoclustering; and their recent incorporation into a three tiered hierarchical model by Kusumi [8] are summarised in the following sections.

1.2.1 The fluid mosaic model and lipid rafts

In the fluid mosaic model (FMM) presented by Singer and Nicholson in 1972 the plasma membrane could be considered as a two-dimensional fluid in which molecules were freely diffusing. Based on the experimental evidence available at the time and the thermodynamics of macromolecular systems Singer and Nicholson proposed that the plasma membrane consists of an "oriented, two-dimensional, viscous solution of amphipathic proteins (or lipoproteins) and lipids in thermodynamic equilibrium", in which the bulk of the phospholipid is organised as a discontinuous, fluid bilayer, although a small fraction of the lipid may interact specifically with membrane proteins, and in which membrane components are redistributed through translational diffusion in the viscous two-dimensional solution [5]. The FMM was highly influential, and has persisted as a mainstay of plasma membrane biology [4][8].

From this model the concept of lipid rafts – small ordered domains of lipids dispersed throughout the plasma membrane - emerged. Lipid rafts as currently understood are dynamic nanoscale domains in the membrane enriched in cholesterol, glycosphingolipids and GPI-anchored proteins that coalesce, forming platforms with functions in membrane signalling and trafficking [11].

Lipid rafts are thought to exist in both stimulated cells and cells in the resting state, although with quite different properties in the two conditions. In the resting state lipid rafts have been difficult to observe experimentally, as many preparations introduce artefactual stimulation but they are thought to exist, as highly transient domains with lifetimes from 1 ns to 1 s, or half-lives from 10-20 ms, and be between 10-200 nm in size [4], [8]. In the stimulated state protein-protein interactions result in the formation of stable larger rafts by assembling cholesterol and saturated lipids in and possibly around engaged receptor clusters. Stable domains are formed on demand by stimulation

and have lifetimes of 100-1000 s, however the constituent lipids may still be continuously exchanging with those in the membrane, making these structures dynamic also [8]. These more stable domains are readily visualised by fluorescence microscopy, in contrast to pre-stimulation domains which are extremely difficult to study due to their short lifetimes. It is thought that the numerous variety of lipids present in the membrane assemble into different microdomains to perform distinct functions based on the proteins on which they interact,

The importance of lipid rafts and domains to cells has been recently reviewed by Neumann et al.[12] – the confinement of cell membrane constituents to lipid rafts or domains can define cellular processes such as endocytosis, signal transduction and cell death. Lipid raft integrity has also been found to be important for the survival of triple negative breast cancer cells [13], giving evidence for the functional importance of these domains.

1.2.2 The actin cytoskeleton and the membrane picket fence model

Since the FMM was proposed our view of the plasma membrane has necessarily evolved to become less homogenous, incorporating other structures and domains discovered by advances in microscopy methods and other techniques, such as the role of the actin cytoskeleton in controlling and restraining membrane component distribution ([4], [8], [14]). An early model to explain protein diffusion in the plasma membrane was the hydrodynamic model of Saffman and Delbrück [15] which proposed that diffusional motion in biological membranes was Brownian in nature, and therefore diffusion coefficients would be determined by temperature and membrane viscosity. However, investigations into diffusion in the plasma membrane revealed diffusion coefficients for proteins and lipids in biological membranes an order of magnitude smaller than that which would be expected for pure Brownian motion. High-speed single molecule tracking revealed that the reason for this discrepancy is the transient confinement of membrane constituents in confinement zones known as “corrals”, with occasional hops over “walls” into neighbouring corrals [16]–[18]. The overall effect of this behaviour, termed ‘hop-diffusion’, is to cause pseudo-Brownian motion, which over longer time

scales appears Brownian and the mean-squared displacement (MSD) of diffusing molecules is proportional to time, but the diffusion coefficient is an order of magnitude smaller than that of Brownian motion [16], [19]–[21]; while the diffusion within the corrals is much faster and more similar to that seen in artificial membranes. These corrals have a “picket-fence” structure, with “fences” composed of actin filaments and “pickets” of transmembrane proteins anchored to the cytoskeleton around which steric hindrance and hydrodynamic friction like effects restrict the diffusion of surrounding lipids. These corrals restrict diffusion of cytosolic, exofacial and transmembrane proteins, until hops between neighbouring domains are enabled when the gap between the actin meshwork and the membrane becomes large enough, or by local temporary dissociation of the membrane skeleton from the membrane[8]. Further diffusional heterogeneity on longer (ms) timescales arises from interactions between diffusing molecules and dynamic domains such as lipid rafts (discussed in section 1.2.1), and protein complexes (discussed in section 1.2.3).

Kusumi presents results in his review [8] indicating that partitioning of the membrane is entirely due to the actin-based membrane skeleton and anchored transmembrane picket proteins, however confinement of proteins in relation to other structures has been shown in the literature, such as CD9 in tetraspanin enriched areas [22], which are discussed further in section 1.2.5.1.

The membrane skeleton visualised by electron tomography, as shown in Figure 1-2 implies the role of the membrane skeleton in segregating the plasma membrane, as it can be clearly seen how the actin filaments may restrict diffusion of integral proteins by interacting with the cytosolic tails [9]. Recently, Koster et al have presented further evidence of the role of actin in cell curface organisation, showing that myosin-driven actin networks affect the organization of membrane proteins [23]. Further support for this mechanism of membrane organisation is found in work presented by Kusumi et al, in which it was shown that a nonraft phospholipid and a transmembrane

protein underwent hop diffusion in the plasma membrane with equal compartment sizes in a number of different cell types [24].

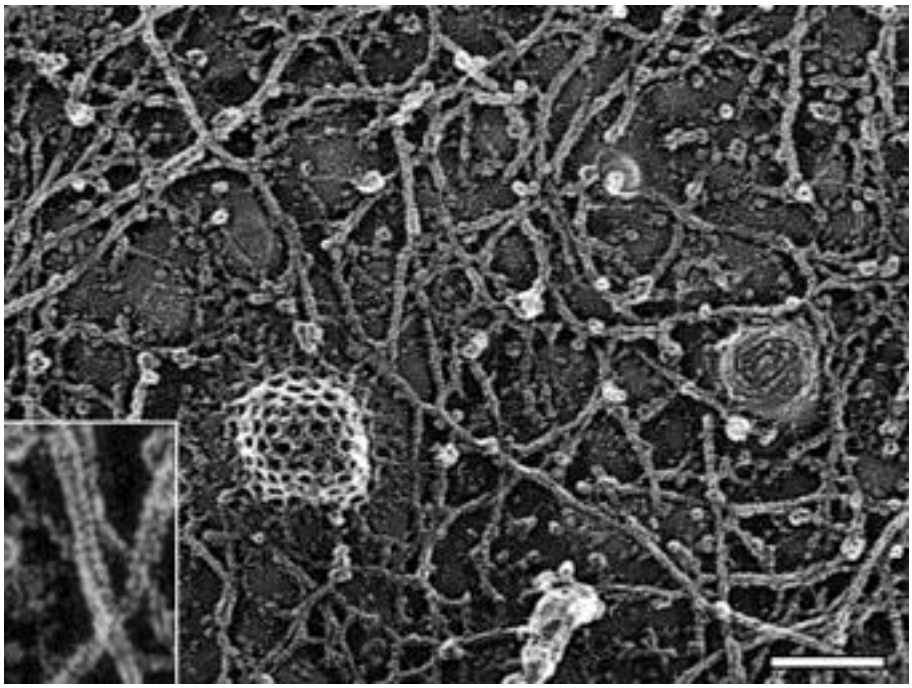

Figure 1-2. The membrane skeleton visualised by electron microscopy.

An electron microscopic image showing the membrane skeleton attached to the cytoplasmic surface of an NRK cell. The filamentous actin forms the membrane skeleton, and one can imagine how such a structure constrains the motion of proteins in the plasma membrane. Scale bar 100 nm. Figure reproduced from [25]

1.2.3 Dynamic protein clustering

Thanks to the advent of super-resolution microscopy there is an emerging picture that suggests many if not most proteins present in the plasma membrane are clustered at nanoscale lengths. The size of clusters can vary widely, from a few nanometers to several micrometers, likely due to their different molecular composition and different capacities to coalesce with or segregate from each other [26]. One suggestion regarding plasma membrane organisation is that the entire membrane may be composed of a hierarchical organization of molecules – ranging from classic protein oligomerization to nanometer-sized or micrometer-sized clusters, which may provide multi-scale regulation of membrane protein function [26]. While protein clusters are not as well characterised

as rafts with the new super-resolution techniques this is an active area of study. The reported lifespans of protein clustering interactions range from miliseconds to hours ([27]–[30]), and protein-protein interactions and the formation of nanoclusters have also been shown to have roles in restricting diffusion in the plasma membrane ([27], [31]).

Kusumi suggests there are three main types of dynamic protein cluster – oligomers of membrane anchored proteins and protein complexes based on them, with diameters 6-20nm; coat protein facilitated domains such as clathrin coated pits; and scaffolding protein induced complexes.

The interaction of multi-molecular assemblies in the plasma membrane is considered by most researchers to be crucial for signal transduction - multi-molecular assemblies enhance binding affinity and extend the duration of interactions due to avidity effects and enable assembly of molecules in different signalling pathways [8]. It is likely that proteins exist as dynamic nanoclusters, where the constituent molecules are continuously exchanging with molecules in the surrounding membrane, as proposed for Ras [32]–[34].

The actin cytoskeleton also plays a role in mediating the extent of nanoclustering, as in the case of glycosyl phosphatidylinositol anchored proteins (GPI-APs) [35].

Several studies have recently been conducted employing super-resolution microscopy to directly observe and characterise these dynamic protein clusters [26], including several examining the distribution of ErbB receptors, particularly EGFR [36], [37].

1.2.4 The hierarchical three-tiered meso-scale domain architecture hypothesis

Taking the prevailing theories of membrane organisation together, Kusumi proposes in a recent review [8] a hierarchical three-tiered meso-scale domain architecture to explain the cooperative existence of the different membrane structures, as shown in Figure 1-3. Kusumi suggests the most basic tier of organisation in the membrane is the actin membrane-skeleton-induced compartmentalisation (described in section 1.2.2), as this is the mode of organisation which

fundamentally distinguishes the plasma membrane from the Singer Nicholson type fluid mosaic model, and actin based partitioning occurs virtually everywhere in the PM [8], [9].

The second tier is then raft domains (described in section 1.2.1) which provides the second level of control via the cooperative assembly and disassembly of raft domains. The final tier of control is protein nanoclustering, which can be summarised as transient protein complex domains [8]. Kusumi supposes that the three tiers cooperatively interact to mediate signal transduction in the PM.

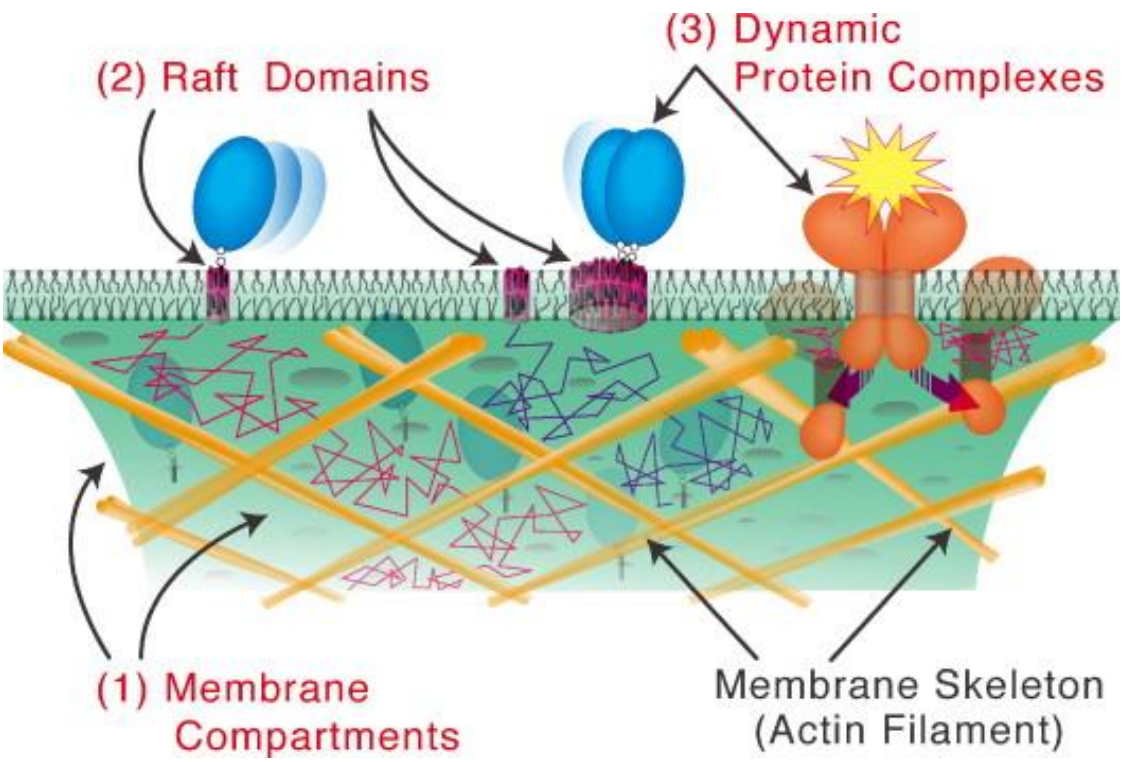

Figure 1-3: **Schematic representation of the three tiers organising the plasma membrane.**

There are three major types of dynamic meso-scale domains – actin membrane skeleton based compartments 40-300 nm in diameter (1); raft domains (2) between 2-20 nm in diameter which are accommodated within the membrane-skeleton-induced compartments; and dynamic protein complexes or clusters (3). Reproduced from [8]

1.2.5 Recent concepts in plasma membrane organisation

Aside from the main concepts of the membrane picket-fence model, lipid raft microdomains, and dynamic protein clustering, other hypotheses regarding factors that govern PM compartmentalization on different length and time-scales have been proposed. These include lipid

shells [38], tetraspanin-enriched microdomains [6], [22], flotillin microdomains [39], and galectin lattices [40]. The role of these local organisers in compartmentalising the membrane is yet to be defined; however recent evidence indicates that they work together in a cooperative manner [40], [41].

1.2.5.1 Tetraspanin enriched microdomains

The role of tetraspanin enriched microdomains (TERMs) in mediating PM organisation is of particular interest in the context of this work.

This specific type of membrane microdomain was discovered in the 1990s [42]. Results from immunoprecipitation and western blot experiments showed that all tetraspanins tested associated with one another, and that for a particular cell type and under defined lysis conditions the patterns of proteins co-immunopreciptated with different tetraspanins was identical. On the basis of this evidence the tetraspanin web – a network where tetraspanins are the organisers of molecular interactions on the cell surface – was proposed [42]–[44].

Early evidence for TERMs came from biochemical experiments, however imaging approaches have been used for some time to directly establish the existence of and begin to characterise TERMs. Colocalization of individual tetraspanins with various membrane receptors and costimulatory molecules, e.g., in adhesion complexes was demonstrated in the 1990s [45], [46]; and Forster Resonance Energy Transfer – Fluorescence Lifetime Imaging (FRET-FLIM) was used to demonstrate the interaction of CD9 and CD151 in the tetraspanin based microdomains called endothelial adhesive platforms (EAPs) in the plasma membrane [47]. Furthermore a role for CD82 in regulating the compartmentalisation and ligand-induced dimerization of EGFR was shown using a combination of biochemical and imaging approaches [48].

However, until the recent advances in resolving capability afforded by super-resolution techniques the precise properties of these complexes, such as their size and molecular occupancy, were not readily studied. The super-resolution technique of stimulated emission depletion (STED) microscopy was recently employed to shed light on nanoscale properties of TERMs in human B cells and dendritic cells. This recent study showed that clusters of CD53 and CD37 were adjacent to and displaying only minor overlap with clusters containing tetraspanins CD81 or CD82, and that tetraspanins CD53 and CD81 were found in closer proximity to their partners MHC class II and CD19 than to other tetraspanins [49], challenging the current view of the tetraspanin web which has multiple tetraspanin species organised within the same microdomain [50].

Multiple studies have provided evidence that TEMs can mediate the distribution and diffusion of proteins in the plasma membrane, although the mechanism for this control is not yet defined.

Termini et al. demonstrated using a combination of single molecule tracking and ensemble imaging that in cells expressing palmitoylation deficient CD82 an increased proportion of PKCα tracks are short-lived compared to control or CD82 over-expressing cells, suggesting that the palmitoylation of CD82 affects the length of time PKCα molecules are present in the plasma membrane [51]. In the same study in CD82 knockdown cells no change to PKCα track length was observed, suggesting that other tetraspanins may have a compensatory effect on the dynamics of PKCα membrane recruitment, and overall, that CD82 expression may have a role in mediating PKCα dynamics.

Single molecule tracking experiments indicated that CD9 restricts the diffusion of other CD9 molecules, but not CD55 (a raft resident, non-tetraspanin protein) [22]. Periods of confinement in the trajectories of CD9 molecules mainly coincided with areas enriched in CD9 (tetraspanin enriched areas (TEAs)). Additionally, the diffusion coefficient of CD9 molecules observed to cross TEAs was frequently reduced in these areas. In contrast CD55 showed little interaction with CD9 TEAs,

occasionally crossing such areas but rarely being confined in them, and in fact with the majority of confined episodes rarely co-localising with TEAs.

Barreiro et al. provide further evidence supporting the role of tetraspanins as the active organizers of TERMs that TEMs are a physical unit in plasma membranes. Specifically, it was demonstrated that the ligation of a receptor present in TERMs affects the diffusion of other components of the nanodomain, and that tetraspanins have a higher relative frequency of fast diffusion than adhesion receptors, suggesting that they are more readily exchanged between EAPs [47].

Combined, the evidence gives rise to the dynamic view of the tetraspanin web where clusters containing multiple tetraspanins and partner molecules diffuse across the membrane, exchanging constituent molecules by direct interaction of the clusters or via more stable tetraspanin enriched areas on the membrane (Figure 4) [4]. The most recent super-resolution results from Zuidscherwoude et al. [49] raise the possibility that microdomains do not contain multiple species of tetraspanin, however more live cell imaging simultaneously investigating the co-localisation and dynamics of multiple tetraspanins is required to confirm or deny this view.

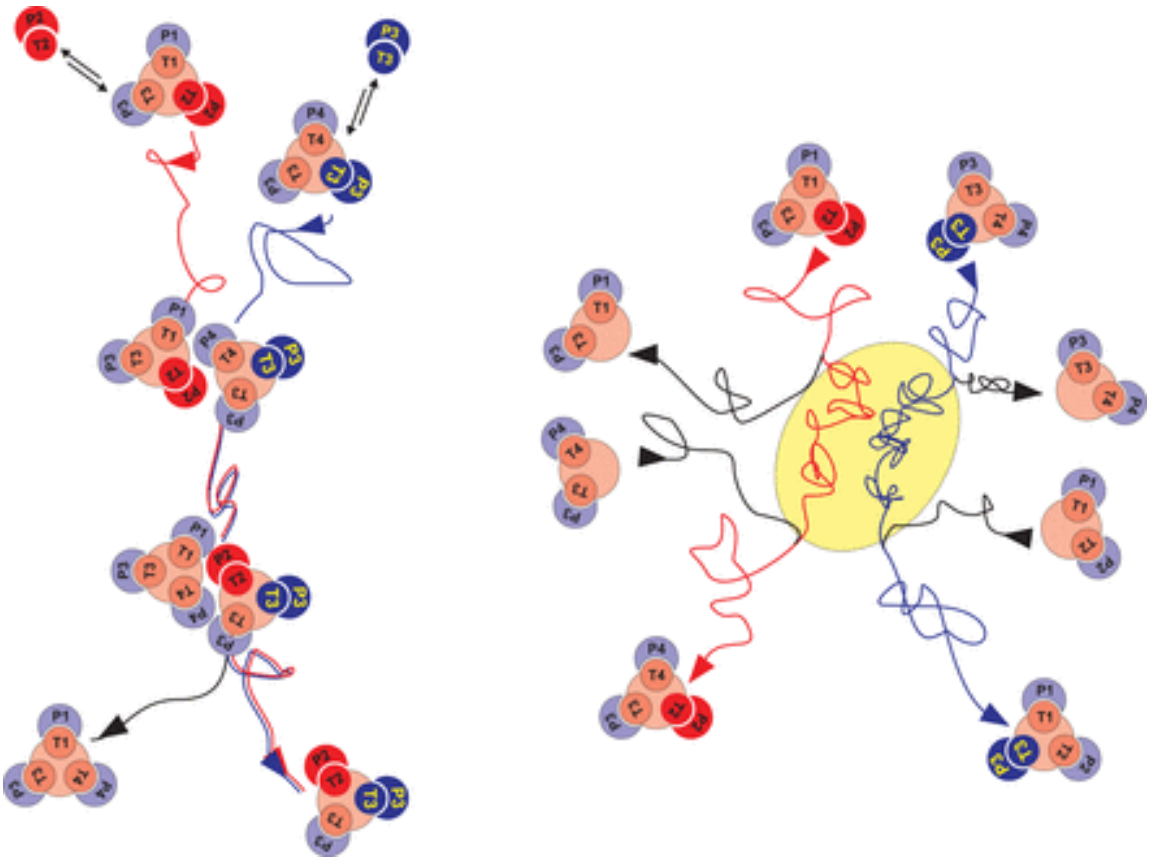

Figure 1-4: A dynamic view of the tetraspanin web.
Left: A dynamic view of the tetraspanin web, in which small clusters of tetraspanins (T1, T2 etc.), each associated with a molecular partner (P1, P2, etc.) diffuse in the plasma membrane, frequently interacting with other clusters and exchanging constituent molecules between them. Right: Representation of the situation in which upon stimulation some tetraspanins become confined within discrete areas on the plasma membrane, in which more stable interactions take place. The model shown here is based on the transfer of one tetraspanin to the tetraspanin-enriched areas, and subsequent exchange into another cluster, but other models are possible, such as the gathering of several clusters. Reproduced from [52].

1.2.6 Notes on terminology

In discussions of the distribution and dynamics of membrane proteins the terms 'microdomain/domain', 'cluster' and 'confinement zone' are often used – do these terms refer to distinct features of the plasma membrane which are structurally or functionally distinct from one another or do they represent the same underlying organisation? In this thesis we consider a cluster to be a number of the same type of molecule, while a microdomain consists of multiple types. It is possible that multiple clusters may form a microdomain, and that any given cluster may be part of a

microdomain containing other molecular types not simultaneously imaged and therefore not detected, so there is some interchangeability between these terms.

A confinement zone is commonly defined as an area in which a diffusing molecule resides for longer than a molecule undergoing Brownian diffusion would be expected to reside in the given area. Whilst it would appear that some microdomains have the ability to trap and confine diffusing proteins [22] this does not appear to be the case for all protein clusters/areas enriched in a certain protein. It may well be that only certain proteins form clusters/structures which confine other molecules, for functional reasons, or that our ability to detect microdomains at the nanoscale and track molecules as they pass by or through them is too spatially or temporally limited to determine whether co-localisation and/or interaction between the molecule and the domain is taking place.

1.3 Cancer

Cancer is the generic name given to a variety of malignant neoplastic diseases that stem from different cell types. It is characterised by six hallmarks, which combined give rise to the capacity for tumour growth and metastasis by providing a growth advantage for transformed cancerous cells over healthy ones. The six hallmarks are i) sustaining proliferative signalling in the absence of extracellular signals; ii) evading growth suppressors; iii) activating invasion and metastasis, iv) enabling replicative immortality; v) inducing angiogenesis; and vi) resisting cell death. [53], [54]

1.3.1 Breast cancer

Breast cancer originates in the breast tissue, and is the most common form of cancer in the UK (15.4% of all cases), preceding prostate (13.4%), lung (12.5%) and colorectal (11.6%) cancer [55]. Breast cancer is a heterogeneous disease which can be further classified by sub-type, each displaying distinct clinical behaviour. The subtypes of breast cancer, which are classified according to their expression profile, are luminal A; luminal B; normal breast-like; ErbB2-enriched; and basal like. Two distinct types of epithelial cells are found in the human mammary gland; basal and luminal epithelial

cells, which can be immunohistochemically distinguished from one another by staining with antibodies against the basal keratin 5/6 or the luminal keratins 8/18 [56].

1.3.1.1 The ErbB2-enriched subtype

The ErbB2-enriched subtype of breast cancer is characterised by the over-expression of the receptor tyrosine kinase ErbB2. The ErbB2 gene is amplified in approximately 15-25% of human breast cancers [57], and in many other types of cancer including ovarian [57], stomach [58], bladder [59], salivary [60] and lung carcinomas [61]. Not all ErbB2 over-expressing tumours are classified into the ErbB2-enriched subtype; ErbB2-driven breast cancers that express both the luminal and ErbB2 gene clusters are categorised into the luminal subtypes rather than in the ErbB2-enriched subtype[62]. Over-expression of ErbB2 in breast cancer is a biomarker for poor clinical outcome, with patients having substantially lower overall survival rates and shorter disease-free intervals than patients whose cancer is not characterised by overexpression of ErbB2; and is an indicator of more aggressive metastatic disease [63]–[65]. The important roles of ErbB2 in cancer progression render it an attractive target for therapeutic interventions in breast cancer.

1.4 ErbB receptors

The ErbB family of receptor tyrosine kinases (ErbB1/EGFR, ErbB2/HER2, ErbB3, ErbB4) have well established roles in normal development and in cancer [66]. As discussed in section , in particular, ErbB2 is over-expressed in around 15-25% of breast cancer cases [65], [67], [68].

Receptor tyrosine kinases are single pass transmembrane receptors, comprised of an extracellular part containing a ligand binding domain, a single transmembrane domain, and a cytoplasmic part with a tyrosine-kinase containing domain. The ErbB receptors are expressed in various tissues of epithelial, mesenchymal and neuronal origin. Under normal physiological conditions, activation of the ErbB receptors is controlled by the spatial and temporal expression of their ligands, which are

members of the EGF family of growth factors. However aberrant ErbB signalling due to gene mutation or amplification is also implicated in many cancers [65], [66].

1.4.1 ErbB receptors and cancer

ErbB family members have a prominent role in the initiation and development of several solid tumours [69]. Table 1-1 summarises known alterations to ErbB receptors and their ligands in human cancers. The ErbB family and their ligands and possible dimerisation states are shown in Figure 1-5.

In response to the identification of the role of ErbB family members in cancer specific ErbB inhibitors have been developed as cancer therapies, and are in widespread use - ErbB2 targeting cancer drugs in particular are discussed in section 1.4.2.1.

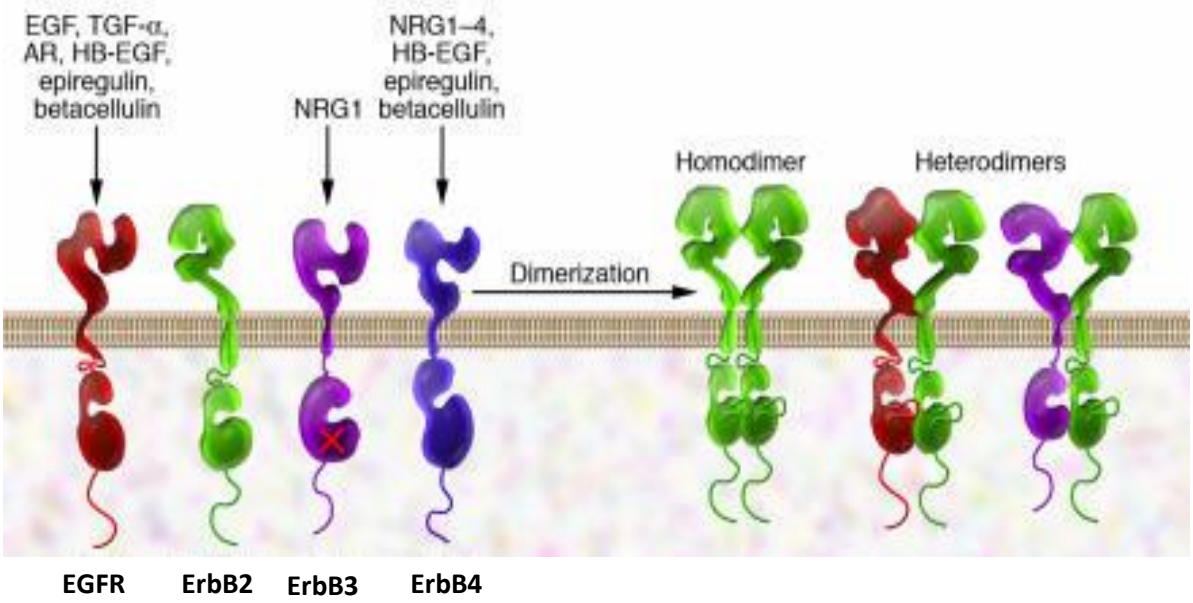

Figure 1-5: The ErbB family of receptor tyrosine kinases and ligands
The extracellular domain of all family members consists of four subdomains I-IV. Domains I and III are important for ligand binding; domain II also known as the dimerisation arm and is important for receptor-receptor interactions; and domain IV is involved in receptor auto-inhibition. In the absence of a ligand, the receptors exist in a tethered auto-inhibitory conformational state whereby subdomains II and IV interact, burying and inhibiting the dimerisation arm from interacting with neighbouring ligand-bound ErbB receptors. However, ErbB2 exists in a fixed confirmation whereby the dimerization arm is left permanently exposed – resembling the ligand bound state of the other ErbB receptors – and thus permanently poised for receptor-receptor interactions, leading to ErbB2 being the preferred dimerization partner of the other ErbB receptors, despite no ligand for ErbB2 having been identified. Abbreviations for ligands: EGF – epidermal growth factor; TGF-α –

transforming growth factor alpha; AR – amphiregulin; HB-EGF – heparin binding EGF-like growth factor; NRG1 – neuregulin 1 (also known as heregulin); NRG1-4 – neuregulin 4. Reproduced from [70]

Table 1-1: Alterations of ErbB receptors and ligands in human cancer. Table reproduced from [69]

Molecule	Alteration	Cancer types	References
EGFR	mutation	Non-small-cell lung cancer (NSCLC)	[71]–[73]
EGFR	Amplification	NSCLC (squamous), head and neck, glioma, esophageal, colorectal.	[74]
ErbB2	Amplification	Breast, gastric, esophageal	[75]
ErbB2	Mutation	Breast (lobular), lung, gastric, bladder, endometrial	[75]
Erbb3	Mutation	Breast, gastric	[76]
ErbB4	Mutation	Melanoma, NSCLC, medulloblastoma	[77], [78]
TGF-α (EGFR ligand)	Over-expression	Prostate, lung, pancreas, ovary, colon, head and neck	[79], [80]
Neuregulin-1	Overexpression	Colorectal, head and neck	[81], [82]

1.4.2 ErbB2

While Erbb1, ErbB3 and ErbB4 have identified ligands ErbB2 is an orphan receptor, having no ligand identified. Despite this ErbB2 has a central role in the family since it is the preferred dimerization partner of the other ErbBs [65]. Although lacking a ligand which directly binds it ErbB2 becomes highly phosphorylated in response to the other ErbB ligands [83], which raised the question of how the receptor becomes activated. X-ray structural studies showed that ErbB2 has a unique conformation compared to the other ErbBs, as shown in Figure 1-6, whereby ErbB2 is continually in an extended conformation with an exposed domain II, similar to that of ligand-bound EGFR. Domain

II is involved in dimerization, therefore this conformation leaves ErbB2 effectively constantly poised and ready for the formation of dimers, without the requirement of an activating ligand [84], [85].

In normal physiology, ErbB2 has a crucial role in cardiac development and function. This is particularly important since although ErbB2 is a therapeutic target in certain breast cancers, treatment with Herceptin can result in cardiomyopathy, due to the importance of ErbB2 for normal cardiac functioning [86]. Identifying the patients most likely to benefit from treatment with Herceptin and thereby mitigating the numbers exposed to this potential side effect is a key target. ErbB2 signalling also plays a role in kidney function [87].

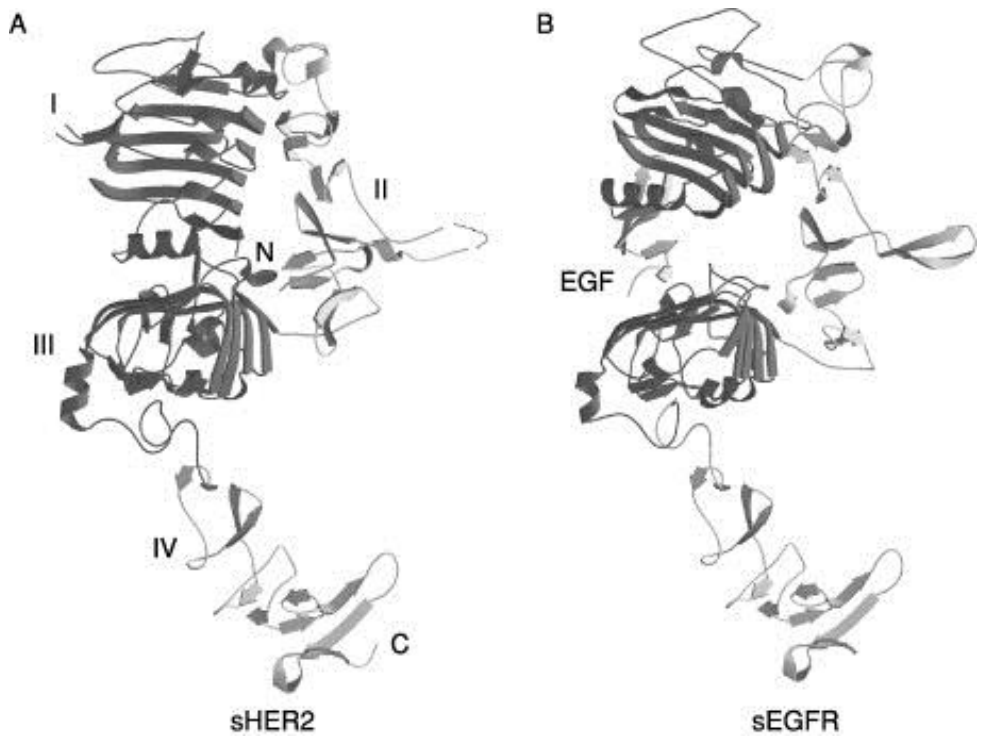

Figure 1-6: Ribbon diagrams of A) sHER2 and (B) a monomer of the sEGFR/EGF complex
sHER2 and sEGFR refer to the soluble extracellular domains of ErbB2/HER2 and ErbB1/EGFR respectively. Domains I-V and the N- and C-termini of sHER2 are labelled; domains I and III are coloured dark grey, and domains II and IV are coloured light grey. sEGF is coloured light gray. The surface buried between domains I and III of ErbB2 overlaps significantly with regions homologous to the ligand binding site of EGFR, going to some way to explain the inability of ErbB2 to bind ligand. The conformation of ErbB2 with domains I and III brought close together, and domain II exposed appears to both preclude normal ligand binding and substitute for it, as the conformation is very similar to ligand bound EGFR, and the domain II dimerization loop is exposed, with very similar

structure to the dimerization loop of ligand bound EGFR, leaving ErbB2 in a constitutively "active-like" structure. Figure reproduced from [84].

1.4.2.1 ErbB2 targeting cancer drugs

Due to the aggressive nature of ErbB2 over-expressing cancers, which comprise 15-25% of cases, the receptor is an attractive target for therapeutic intervention in cancer. Several targeted therapies are already in use, including Herceptin (HC) (or Trastuzumab), which is approved for use as mono- or combination therapy in neo-adjuvant, adjuvant, and metastatic settings [41]; with more in development, and undergoing clinical trials [88].

1.4.2.1.1 Trastuzumab

Herceptin is the brand name for trastuzumab, a humanised monoclonal antibody against ErbB2. Patients receiving treatment in combination with chemotherapy show a significantly longer time to disease progression, and improved overall survival [89]. Despite being initially effective in a number of patients, acquired drug resistance often becomes a problem.

Less than 35% of patients with ErbB2-positive breast cancer initially respond to Herceptin [90], yet there are no reliable biomarkers to predict response to Herceptin [91]. Furthermore about 70% of patients who initially responded to treatment experience progression to metastatic disease within a year, suggesting that resistance to Herceptin is developed [92], and yet the mechanism of this resistance is poorly understood.

Clinical studies have shown that the combination of trastuzumab with standard chemotherapy produces far better response rates than does chemotherapy alone [89], [93], and so combinations that include Herceptin are considered as the standard of care for ErbB2-over-expressing breast cancer patients [94]. However, there is a significant cost implication in treating patients with Herceptin, and the potential for severe side-effects, including those on the cardiovascular system, so there is considerable interest in determining possible mechanisms of resistance and biomarkers

predicting tumour response to treatment with Herceptin, in order to provide the most optimal treatment for all patients.

There are three major categories of proposed mechanisms of resistance. Firstly steric effects, such as ErbB2 acquiring a mutation which results in cleavage of its extracellular domain, thus preventing the binding of Herceptin to the receptor. In a study of tumour cells from 46 patients with metastatic breast cancer, those who acquired this mutation were less likely to respond to Herceptin than those with full-length ErbB2, however the way in which cancer cells can induce this ErbB2 proteolysis has not been studied. The second possibility is the alternative overexpression of other tyrosine kinase receptors, which may overcome Herceptin-mediated inhibition of Ebrb2 signalling. There is some evidence that cancer cells can utilize ErbB3 signalling to overcome the inhibition of ErbB2 signalling by Herceptin. Thirdly intracellular alterations to ErbB2 downstream signalling, such as the loss of PTEN and the activation of Src may confer resistance, which has been shown in 36% of ErbB2-positive primary breast tumor specimens from patients with stage IV disease, alongside the lower overall response rate to Herceptin in patients with PTEN-deficient tumours [90].

The continuing uncertainty regarding the mechanism of resistance to Herceptin makes it all the more important for us to be able to identify at the outset those patients likely to benefit from Herceptin. It may be important that the epitope for Herceptin is close to the membrane in ErbB2 so access to the epitope may be restricted, possibly by inclusion of ErbB2 in complex/microdomains, hence why we studying ErbB2 dynamics in relation to its localisation with respect to membrane microdomains.

1.5 Tetraspanins

1.5.1 The tetraspanin superfamily

Tetraspanins are a family of integral transmembrane proteins, widely expressed across a range of species. The family comprises 33 members in mammals, and in humans, tetraspanins are expressed in all cell types, each of which usually expresses multiple family members [95]. In other species there are, for instance, at least 37 in *Drosophila melanogaster* [96] and 20 in *Caenorhabditis elegans* [97].

There is increasing evidence that tetraspanins have a key role in regulating the trafficking and function of other membrane proteins, possible by regulating the membrane compartmentalization of the molecules they associate with [98]. The role of the tetraspanin web in dynamically organising proteins on the cell surface via the formation of TERMs is discussed in section 1.2.5.1; this section will focus more on specific properties of tetraspanins including their structure and interactions.

The function of tetraspanins is related to their formation of complexes with themselves and other molecules involved in the tetraspanin web via modulating, stabilizing, or preventing the activities of their associated molecules, which can vary depending on the composition of the TERM [99].

1.5.2 Properties of tetraspanins

Tetraspanins are small proteins, protruding just 4-5 nm above the plasma membrane. Members of the tetraspanin family have four transmembrane domains, and must also have several conserved amino acids, including a conserved CCG motif and two other cysteine residues that contribute to two crucial disulphide bonds in the large extracellular loop [100], as shown in Figure 1-7.

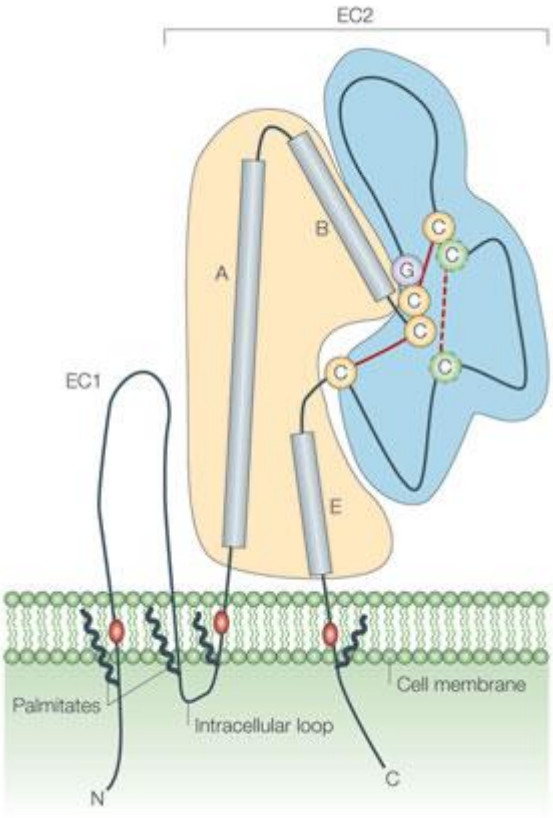

Figure 1-7: Structural features of tetraspanins
Tetraspanins are small transmembrane proteins, having four transmembrane domains, a small extracellular loop (EC1), a very short (typically 4 amino acids) intracellular loop, a large extracellular loop (EC2) and relatively short (8-21 amino acids in general) N and C terminus cytoplasmic tails. The large extracellular loop is subdivided into a constant region (yellow, containing alpha helices A - immediately following transmembrane domain 3, B and E – immediately preceeding transmembrane domain 4) and a variable (blue) region, which contains various protein-protein interaction sites. All tetraspanins contain a CCG motif after the B helix, and two other conserved cysteines (yellow) which are arranged to form two intramolecular disulphide bonds (solid red line). Many tetraspanins also contain two additional cysteines (green) which form another intramolecular bond (dotted red line). Little is known about the structure of the small extracellular loop. Nearly all tetraspanins also contain juxtamembrane cysteines that undergo palmitoylation. Figure reproduced from [100].

1.5.2.1 Structural features

The crystal structure of CD81 has recently been reported, as a representative example of a full-length tetraspanin, shedding new light on the structure of this family. The overall structure of the CD81 resembles a cone, in which the large extracellular loop EC2 covers an intramembrane cavity bounded by the four transmembrane domains, forming a cholesterol binding pocket – binding of cholesterol to which is observed in vitro. The transmembrane region consists of two largely separated pairs of antiparallel helices, one pair comprising transmembrane (TM) domains 1/2 and the other TM domains 3/4. The relative positions of the transmembrane helices are believed by to be conserved between all tetraspanins [101], [102].

In simulations with cholesterol removed, the EC2 domain adopted an "open" conformation in which it disengages from TM1 and TM2, which is consistent with the modulation of tetraspanin function by mutations that compromise cholesterol binding.

1.5.3 Interactions of tetraspanins

Tetraspanins associate with one another, and with other proteins, including integrins and other adhesion molecules; proteins with Ig domains; and signalling molecules such as growth factor and cytokine receptors and ectoenzymes [52], [98]. Mostly these interactions are indirect, and have been identified using co-immunoprecipitation with mild detergents which preserve tetraspanin–tetraspanin interactions, while the use of some detergents has enabled the identification of small tetraspanin-partner complexes. This suggests that tetraspanin-tetraspanin interactions assemble primary complexes, from which a dynamic network of secondary interactions forms – which is known as the tetraspanin web [49], [98]. The association of tetraspanins with partner molecules is referred to as primary, while interactions with other tetraspanins are known as secondary [95],[103]. An interesting feature of tetraspanin-partner interactions is that a single tetraspanin molecule can form different partnerships in different cell types. For example, CD81 associates in B cells with CD19 [104], whereas in T cells it associates with CD4 and CD8 [105]. Interactions can also form with either

the intracellular or extracellular domains of the interacting molecules, such as CD81 interacting with the extracellular domain of CD19 (5, 37) and with the transmembrane domain of another partner molecule EWI-2 (49). Tetraspanins also form indirect associations with additional proteins, which are referred to as tertiary interactions. These interactions are not disrupted in milder detergents , such as 1% CHAPS [95].

Tetraspanin-partner interactions have been shown to involve the large extracellular loop or transmembrane domains of the tetraspanin [6], [52], [106]. The functional activity of tetraspanins does not depend only on their primary interactions with partner molecules, but also on association with cholesterol and gangliosides [98], [107]. Tetraspanin-tetraspanin interactions are regulated by lipids, membrane cholesterol and gangliosides, and similarly to components of lipid raft microdomains have been shown to float in sucrose gradients after cell lysis. The palmitoylation of the intracellular, juxtamembrane cysteines is important for maintenance of tetraspanin-tetraspanin interactions.

Taken together the evidence suggests that these interactions cluster in TERMs, forming higher-order complexes, enabling lateral dynamic organization in the membrane (as discussed in section 1.2.5.1) and the cross-talk with intracellular signaling and cytoskeletal structures [95], [106], [108].

1.5.4 Tetraspanin enriched microdomains

Evidence indicates that higher-order complexes of tetraspanins and partner molecules are spatially clustered on the plasma membrane forming TERMs. TERMs may have a role in spatially modulating the distribution of certain membrane proteins, but their exact role in this sense and in modulating interactions is undefined.

A study utilising super-resolution imaging was recently conducted by Zuidscherwoude et al. [49], to interrogate the distribution and clustering of tetraspanins on the plasma membrane. The results of this work interestingly showed that tetraspanins appear to be in closer proximity to their non-

tetraspanin binding partners than to other tetraspanins in the membrane, and also that clusters of individual tetraspanins seems to be spatially separated and rarely co-localise, indicating that TERMs may be made up of a single species of tetraspanin and partner molecules, rather than multiple tetraspanin species as previously assumed.

There is also evidence among the uroplakin tetraspanins that that tetraspanin monomers do not interact with one another but rather interactions are bridged by non-tetraspanin partners, and taken together with the recent super resolution results, and the revisiting of some early experiments done with detergents which did not effectively disrupt secondary interactions, it now seems that factors other than the interaction between tetraspanins themselves are likely responsible for the formation of TERMs [102]

1.5.5 Tetraspanins and cancer

The known functions of tetraspanins in modulating cell adhesion, migration, invasion, signalling, cell-cell fusion, infection by cancer causing viruses, morphology and survival are also all relevant in cancer development [109], and certain tetraspanins have indeed been implicated in cancer.

Tetraspanins can act as both metastasis suppressors (CD82, CD9) or promoters (CD151, tspan 8) [107]. In particular loss of CD82 is associated with poor prognosis in patients with several cancers, including breast, lung, prostate, and bladder, and its expression is able to suppress metastasis formation in a mouse models [107], [110], [111]. The ability of tetraspanins to modulate metastasis may be to do with their ability to modulate growth factor signalling and integrin function, as reviewed in [52].

CD82, along with CD9 and CD151 are the most extensively studied tetraspanins in patients, and their expression is inversely correlated with metastasis formation and bad prognosis in a large number of cancers (i.e. they act as metastasis suppressors). However, expression of these proteins in certain cancers can also correlate with the reverse prognosis, such as CD9 in gastric cancer generally being

associated with a poor outcome, which is likely due to the association of tetraspanins with different proteins in different cell types [109].

1.5.5.1 Role of CD82 in cancer

CD82, also called KAI1, is a member of the tetraspanin super-family, and a metastasis suppressor. Decreased CD82 expression has been observed in a number of human cancers, including pancreatic, lung, hepatic, colorectal, breast, ovarian, esophageal, and cervical cancers, and in endometrial cancer cell lines. A number of roles for CD82 in limiting metastasis and tumour progression have been established in the literature; in endometrial cancer, loss of expression of CD82 has been observed in correlation with metastatic stage, indicating that CD82 expression may be a useful indicator of tumour progression, and may provide prognostic information on outcome of this type of disease. [112] CD82 dynamically localises to intracellular late endosomes and lysosomes [113], from where it is able to modulate endocytic trafficking of associated molecules, such as EGFR [2]. CD82 also appears to regulate the ligand-induced ubiquitylation of EGFR, likely affecting EGFR trafficking, which may contribute to the role of CD82 in metastasis suppression [2]. CD82 expression has also been shown to downregulate Frizzled proteins, inhibiting signalling through the WNT-β‑catenin pathway and decreasing tumour cell malignancy [114], and CD82 expression is associated with decreased β‑catenin degradation, leading to the accumulation of β‑catenin at the cell membrane and the stabilization of cell surface E‑cadherin–β‑catenin complexes, which promote cell–cell adhesion and limit metastasis [114], [115] .

Additionally, evidence from our group has indicated that CD82 negatively modulates the response of ErbB2-positive breast cancer cells to Herceptin by regulating the distribution of ErbB2 and its phosphorylation and downstream signalling [1]; and that overexpression of CD82 reduces proliferation of breast cancer cells in 3D cultures and alters the dynamics of ErbB2 in the plasma membrane in the presence of Herceptin (unpublished data).

1.6 Imaging modalities

Multiple modalities have been employed to study the plasma membrane, including super-resolution microscopies and high-temporal and spatial resolution techniques permitting in depth study of protein dynamics and distribution. Certain characteristics of each of the techniques outlined in this section make them particularly suitable for studies in the plasma membrane. The modalities described here form the basis of the imaging techniques utilised in this thesis.

All of the techniques described in this section have fluorescence microscopy as their basis. Fluorescence microscopy utilises the property of fluorescence to observe specific structures and proteins in cells, by labelling the molecules of interest with a fluorophore, from which fluorescence is excited (as described in section 1.6.1) and detected, allowing the observation of the distribution of the molecule of interest in real time. A number of approaches can be used to label the molecule/s of interest with a fluorophore, including immunofluorescence, transfection with fluorescent proteins, and using ligands or drugs directly conjugated to a fluorophore.

1.6.1 Epifluorescence microscopy

Epifluorescence microscopy is an optical microscopy technique which employs the phenomenon of fluorescence to image samples labelled with appropriate fluorophores. Fluorescence occurs when a fluorophore absorbs a photon, is shifted into an excited state, and then releases a photon as it becomes de-excited. The released photon is of a lower energy and therefore longer wavelength than the absorbed photon, as some energy is lost to vibrational modes, and therefore the excitation and emission light can be spectrally separated via the use of filters, enabling the production of an image showing the distribution of fluorophores in the sample. In epifluorescence microscopy, a microscope objective collects all the light from the sample.

1.6.2 Total internal reflection fluorescence microscopy

Total internal reflection fluorescence (TIRF) microscopy is a variation on epifluorescence microscopy, where by changing the angle of incidence of the laser excitation light on the sample coverslip, it is possible to set up an evanescent light field such that only parts of the sample within ~200nm of the coverslip receive sufficient excitation light as to excite the fluorophores and cause fluorescence. In this way, highly specific imaging of only the parts of the sample close to the coverslip, e.g. the plasma membrane, is possible. Background fluorescence and auto-fluorescence from the un-illuminated part of the cell is not produced, giving rise to a higher signal to noise ratio in the final image.

This optical set-up is achieved by changing the angle of incidence of the excitation light such that it enters the coverslip at the critical angle, and is coupled into the coverslip, as shown in **Figure 1-8**. Since light cannot be discontinuous at a boundary, an evanescent field is set up on the surface of the coverslip, which decays exponentially with distance from the coverslip. This evanescent field provides illumination up to a depth of 100-200 nm in the sample [116], encompassing the plasma membrane. For total internal reflection to occur the angle of incidence of the light must be greater than the critical angle, θ_c. The critical angle is dependent on the difference in refractive index at the boundary which the light encounters. The refractive behaviour of light at such an interface is governed by Snell's Law:

$$\boldsymbol{\theta_c = \sin^{-1}(n_1/n_2)} \quad (1)$$

where $n_1$is the higher refractive index and n_2 is the lower refractive index. θ_1 represents the angle of incidence of the light on the boundary with respect to the normal to the interface, and $\theta_2$is the angle of the refracted beam within the lower refractive index medium. In order for total internal reflection to be achieved, the refractive index of the sample, n_2, must be less than that of the coverslip, n_1[117]. If the angle of incidence is less than θ_c, then most of the light propagates up through the sample, as in epifluorescence microscopy.

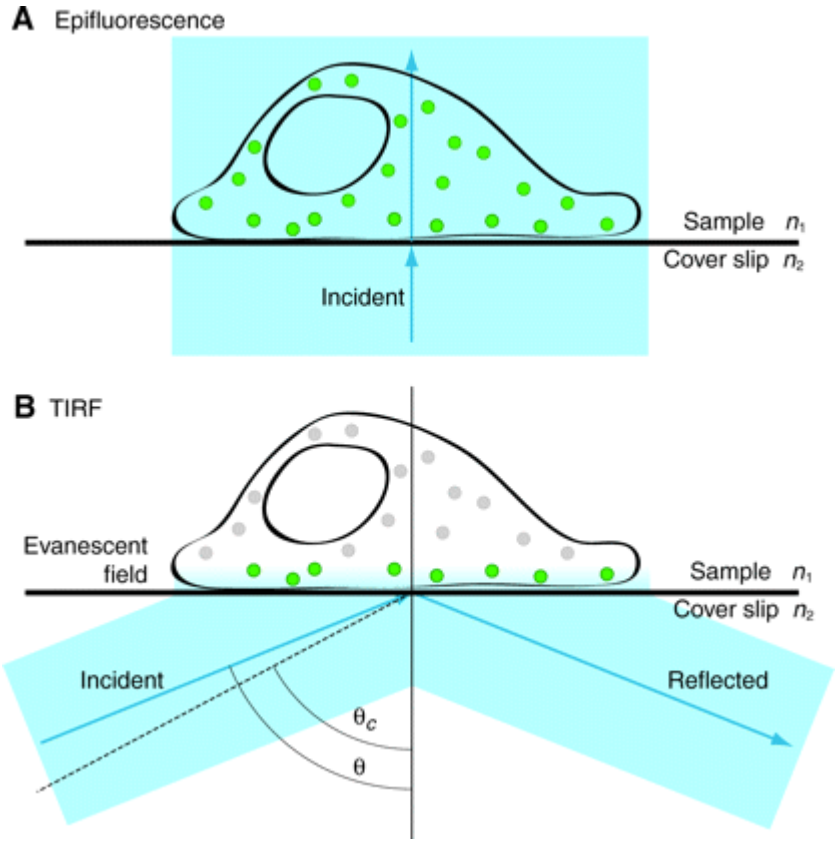

Figure 1-8 Comparative schematic of light path in epifluorescence and TIRF microscopy modes. Figure adapted from [117].

The advantages of TIRF over conventional epifluorescence microscopy for imaging events at the cell membrane are that this technique has the ability to obtain high-contrast images of fluorophores near the plasma membrane, with rapid exposure times, due to very low background fluorescence from the bulk of the cell [117]. Furthermore, cellular photodamage is reduced as the bulk of the cell is not exposed to the excitation light.

1.6.3 Confocal fluorescence microscopy

Confocal fluorescence microscopy is another technique which allows for imaging of a specific section of a specimen by illuminating a restricted area, in this case using a pinhole to focus light at a specific location and only collect the in-focus fluorescence generated at this point. In a confocal microscope an image of a focally illuminated point is projected onto a small aperture in a conjugate focal plane. Light from the illuminated point can pass through the aperture to a detector, while out of focus light

will be spread at the aperture, and mainly blocked, as shown in Figure 1-9. By scanning the illuminated point across a sample, a complete picture can be built up from the signal detected at each point. [118], [119]

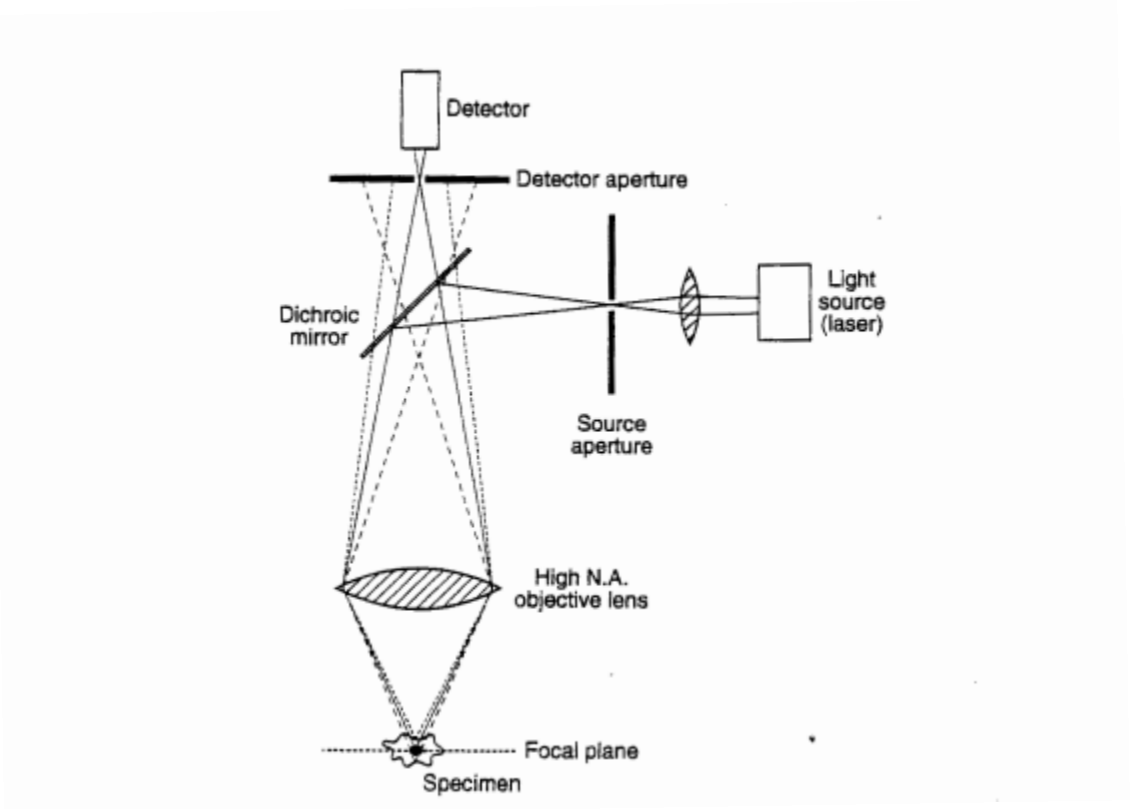

Figure 1-9: Schematic diagram of the principle of confocal microscopy
Figure adapted from [119]

1.7 Imaging techniques

This section describes briefly the imaging techniques used in this thesis to study the distribution and dynamics of proteins in the plasma membrane. More detailed explanation of each technique can be found in the chapter where it is applied.

1.7.1 Fluorescence recovery after photobleaching

Fluorescence recovery after photobleaching (FRAP) is one of the most widely used techniques to study dynamic processes in cells. Initially developed to study the mobility of lipids and proteins in

the membrane it can also be used to study the dynamics of intracellular proteins and structures. The principle of FRAP is to selectively "switch off" the fluorescence in a defined area by photobleaching the fluorophores there with high intensity laser light, and then monitor the recovery of fluorescence to the area as a function of time. The kinetics of the fluorescence recovery provide a measure of the mobility of the labelled molecules from other regions of the sample to the photobleached area, thereby providing information on the diffusion of the molecules of interest and allowing the mobile and immobile fractions of the molecule to be separated and quantified by fitting models to the fluorescence recovery curve. Whilst this technique has the temporal resolution (down to milliseconds) to quantify dynamic protein behaviour, the measurement is an ensemble one – that is an average of the contribution from many molecules, and limited in spatial resolution by the diffraction limit, and therefore does not provide access to single molecule events [120]. FRAP is typically performed on a confocal microscope, although can also be done in TIRF.

1.7.2 Single molecule tracking

Single molecule tracking (SMT) is a technique used to study the motion of single labelled proteins over time. The technique has been employed for many years utilising different imaging probes, from early implementations using gold nanoparticles and polystyrene microbeads to more recent implementations employing single fluorescent dye molecules and quantum dots. Early implementations were referred to as single particle tracking (SPT), while the newer implementations using fluorescent dyes are referred to as single molecule tracking, single dye tracking (SDT), or in the case of single molecule tracking with quantum dots, single quantum dot tracking (SQT). Whilst the early probes of gold nanoparticles and microbeads have high photostability and allow for tracking at high temporal resolution for long periods of time (up to several minutes) their large size likely introduces artefacts into the data and limits the biological processes able to be observed [120]. SMT with fluorescent dyes is not limited by probe size, although achievable resolution and imaging time are reduced due to limitations on the photostability of the dye. SMT has been widely used to study

number of different systems in living cells, including dynamic processes on the cell [121], [122], gene expression [123], [124], and 3D single dye tracking in the nucleus and cytosol of individual cells [125]–[127].

The general principle of SMT is to image over time the signal from individual nanoscopic reporter molecules (gold nanoparticles, fluorescent dyes, quantum dots etc.), then using image processing methods determine the precise, sub-resolution location of the emitter from the diffraction limited image, and reconstruct trajectories for the probes between images. The resulting trajectories can then be analysed to determine properties of the molecules motion such as velocity, diffusion coefficient, transient interactions, confinements, etc., with high spatial and temporal resolution. Single molecule tracking is typically performed on an epifluorescence microscope or in TIRF, but can also been performed using Highly Inclined and Laminated Optical sheet (HILO) illumination [128] and on confocal microscopes with certain modifications [129], [130].

1.7.3 Super-resolution microscopy

Super-resolution microscopy refers to a group of recently developed optical techniques which allow circumvention of the diffraction limit and imaging with resolution on the order of nanometres.

The diffraction limit in light microscopy was previously considered to be a fundamental limit on the resolution achievable in an optical microscope, imposed by the diffraction of light. As the light from the sample passes through the aperture in the microscope it is diffracted, and interference between diffracted rays prevents a sharp image being formed and instead a diffraction limited spot is produced. The diffraction pattern produced from the light from a point source is known as an Airy disk, and its radius, d is given by

$$d = \lambda/2NA \tag{2}$$

where λ is the wavelength of the detected light and NA is the numerical aperture of the microscope objective. This radius gives rise to the diffraction (or resolution) limit in light microscopes, as the Rayleigh criterion states that for two point-like objects the diffraction patterns must be spatially separated to such a degree as the first minimum of the diffraction pattern from one occurs at the same position as the diffraction pattern from the other has its first maximum, in order for the two points to be separately resolved [131].

There are now a number of super-resolution microscopy techniques which achieve resolution below this diffraction limit. Localisation based techniques achieve super-resolution by separating the emission from fluorophores which are spatially separated by less than the diffraction limit, either temporally or spectrally, so as to localise individual fluorophores and build up a detailed image through repeated imaging of different subsets of molecules in the sample. Other techniques use non-linear effects to sharpen the point-spread function of the microscope, such as stimulated emission depletion microscopy (STED); or use reversible saturable optically linear fluorescence transitions (RESOLFTs); or saturated structured-illumination microscopy (SSIM); or statistical evaluation of stochastic fluctuations in the diffraction limited image, stemming from single emitters, to reconstruct an image representative of their distribution, in a technique known as superresolution optical fluctuation imaging (SOFI).

In this thesis, only the localisation based technique of direct stochastic optical reconstruction microscopy (dSTORM), and SOFI have been employed.

1.7.3.1 Stochastic optical reconstruction microscopy

Stochastic optical reconstruction microscopy (STORM) is a localisation based super-resolution technique. The basic principle is to determine the localisation of individual fluorescent molecules with high precision, by utilising the properties of photobleaching and blinking of fluorophores. A sample is labelled with fluorescent molecules which can switch between the fluorescent and dark

state - in the case of STORM, fluorescent dyes, though similar techniques utilise fluorescent proteins and work by the same principle. High intensity laser light incites fluorescence from a subset of the molecules, which blink on and off, such that high speed imaging is able to capture images of resolved single molecules, even where they are more closely spaced than the diffraction limit, as the imaging process means only a subset of the fluorophores are fluorescing at any one time. As some molecules undergo photobleaching and cease to fluoresce, others begin to fluoresce and blink, and so the imaging process is iterated over many thousands of frames. Using image analysis methods, the images are analysed to determine the precise localisation of the individual fluorescent molecules in each image, which are combined into a final dataset representing of the location of each individual fluorophore in the sample.

1.7.3.2 Super resolution optical fluctuation imaging

Super resolution optical fluctuation imaging (SOFI) is a technique which provides enhanced resolution to reconstructed images based on the temporal fluorescence fluctuations of emitters, such as fluorescence intermittency (blinking) [132]. SOFI does not require controlled photoactivation, such as in STORM and other super-resolution techniques, but instead relies on the independent stochastic fluctuations of the fluorophores. Certain conditions must be met for SOFI to be achieved. Firstly the fluorophore must have two distinct emission states -typically a fluorescent and a non-fluorescent state, although any two states which are optically distinguishable, such as fluorescence at different wavelengths, may be used. Secondly, different emitters must switch between different states repeatedly and independently from each other in a stochastic way. Lastly the image should be acquired with pixels smaller than the diffraction limit of light. These conditions being met the pixel value of a SOFI image is obtained from the nth- order cumulant of the original pixel intensity time series. The nth order cumulant is a quantity related to the nth-order correlation function, and filters the signal from the original pixel in such a way that only highly correlated fluctuations are leftover. In this way, the contribution to the pixel intensity from the superposition of

fluorescence originating from nearby emitters is removed, and only the fluorescence originating from emitters spatially located within that pixel is retained. The fluorescence signal contribution of these emitters to neighbouring pixels will nonlinearly yield lower correlation values, leading to increased resolution.

SOFI can be applied, in principle, to any type of fluorescence imaging method, including widefield microscopy, spinning disk or scanning confocal, TIRF etc., making it a versatile imaging technique with potential for combining with other approaches in order to obtain complementary information.

1.8 Thesis aims

The overall aim of this project was to investigate the role of tetraspanins, specifically organisation of the plasma membrane by TERMs, in the distribution and diffusion of ErbB2 in breast cancer cell lines.

Specific aims of the study were:

- Investigate different imaging techniques for studying dynamic changes in distribution of membrane proteins, and identifying clusters and microdomains, and interactions of individual proteins with these.
- Determine optimal imaging and analysis methods for the above.
- Study the distribution of CD82 both dynamically and in super-resolution.
- Study dynamic interactions of ErbB2 with CD82 enriched areas and identify changes to the motion of ErbB2 in relation to CD82 distribution.

Chapter 2 – Materials and Methods

2.1 Cell culture

2.1.1 Maintenance of mammalian cell lines

All cell lines used in this study and their corresponding features are summarised in Table 2-1. MCF7 and SKBR3 cells engineered to express high levels of CD82 were used along with control cell lines. These cell lines were established and characterised in a previous project in the group [1].

All cells were cultured in sterile culture dishes or flasks (Corning) under complete growth medium at 37°C, in a 5% CO_2 humidified incubator. Culture medium consisted of DMEM supplemented with 10% heat inactivated foetal bovine serum (HI-FBS), and 50 units Penicillin/ 50µg/ml Streptomycin for both MCF7 and SKBR3. For sub-culturing, the culture medium was aspirated and the cell monolayer rinsed twice with phosphate buffered saline (PBS). To detach cells, 0.05% EDTA was added to the monolayer, followed by incubation at 37°C for 5 minutes. Detached cells were resuspended in complete growth medium and pelleted by centrifugation at 400g for 3 minutes. Supernatant was removed from the pellet and the remaining cells resuspended in growth medium. Aliquots of the cell suspension were divided between fresh culture vessels and incubated as above for further propagation.

Table 2-1: Details of cell lines used in this study

Cell line	Tissue	Cell type	Tumour
MCF7	Human breast	Epithelial	Invasive ductal carcinoma
SKBR3	Human breast	Epithelial	Invasive ductal carcinoma

Table 2-2: Relative properties of cell lines used in this study

Cell line	CD82 expression	ErbB2 expression
MCF7/puro	Low	Low
MCF7/CD82	High	Low
MCF7/CD82cys5	High expression of CD82 cys5 palmitoylation deficient mutant	Low
SKBR3/zeo	Low	High
SKBR3/CD82	High	High

2.1.2 Cryopreservation and recovery of cell lines

Cells were detached, collected and pelleted as described in section 2.1.1. The supernatant was removed and cells were resuspended in 1ml of a freezing solution comprising 10% dimethyl sulfoxide (DMSO) and 90% HI-FBS. The suspension was transferred to a CryoTube™ vial, which was then wrapped in paper towels and stored in a -80°C freezer, before eventually being transferred to liquid nitrogen for long-term storage.

To recover cells, the CryoTube™ was gradually warmed to room temperature, and the thawed cells transferred into 9ml of pre-warmed culture medium before centrifugation at 400g for 3 minutes. The pellet was then resuspended in fresh complete growth medium, and seeded on a culture vessel for incubation at 37°C in a 5% CO_2 humidified incubator and maintenance as described above.

2.1.3 Cell transfection

Cells were transfected for fluorescence recovery after photobleaching (FRAP) experiments using polyethylenimine (PEI). Cells were transfected at 70% confluence. A DNA:PEI ratio of 1:1.5 was used, and the quantities were scaled according to the area of the culture dish. For transfection of cells cultured in an 8 well Lab-Tek 0.1 µg of DNA was used with 0.1 µl PEI for each well. The DNA was added to serum-free medium (Opti-MEM) followed by the addition of PEI. The DNA-PEI solution was incubated for 10 minutes at room temperature to allow DNA-PEI complex formation. The plates to be transfected were washed twice with PBS and replaced with fresh media. The DNA-PEI complex was added drop-wise to the cells, which were used 48h later for imaging.

2.2 Antibodies

2.2.1 Herceptin

Herceptin (Trastuzumab) from Roche was reconstituted from 150mg powder for infusion, resulting in a 21 mg/ml stock solution, stored at 5°C, from which aliquots were drawn and fresh dilutions made for each experiment.

2.2.2 Fragmentation and biotinylation of antibodies

Fab fragments of Herceptin and C33 were prepared for single molecule tracking experiments using the Pierce™ Fab Preparation Kit from ThermoFisher, which was used according to the protocol supplied with the kit. Briefly, 0.25mL of a slurry containing 50% papain immobilised on agarose resin and 50% glycerol was added to a microcentrifuge tube and rinsed twice before use with a digestion buffer solution containing 35 mg cysteine HCl/10ml digestion buffer. 125 µl of 2mg/ml Herceptin was prepared from a starting solution of 21 mg/ml solution prepared as described in section 2.2.1. The IgG solution was desalted by centrifugation in a Zeba Spin Desalting column and diluted to a final volume of 0.5 mL in digestion buffer. The diluted sample was incubated with the activated papain resin on a mixer at 37°C for 6 hours. The digest was separated from the column by centrifugation, and then purified by passing through a Protein A Plus Spin Column, which binds the Fc portion in the digest. Digestion was confirmed by detection of Fc portions using SDS-PAGE analysis. The concentration of Fab fragments in the purified digest was then determined by UV-Vis spectrometry using a BioSpec-nano device.

Biotinylation was then performed using the FluoReporter Mini-Biotin-XX Protein Labelling Kit from ThermoFisher, according to the protocol supplied.

2.2.3 Primary antibodies

Table 2-3. Details of primary antibodies used in this study

Antibody	Host species	Target	Supplier	Catalogue number	Dilution
c-erb B-2 Ab-2 (Clone 9G6.10)	Mouse	ErbB	Thermo Scientific	MS-229-P1	1:1000
Anti-hu CD82 (clone C33)	Mouse	CD82	EXBIO	11-559-C025	1:1000

2.2.4 Secondary Antibodies

Table 2-4 Details of secondary antibodies used in this study

Antibody against	Conjugated fluorophore	Host species	Supplier	Catalogue number	Lot number	Degree of labelling	Dilution
Human IgG (H+L)	Alexa fluor 488	Goat	ThermoFisher	A11013	1668688	5	SR: 1:300
Human IgG (H+L)	Alexa fluor 647	Goat	ThermoFisher	A21445	1748339	4	SR 1:300
Mouse IgG (H+L)	Alexa fluor 488	Goat	ThermoFisher	A11017	1557766	4	SR 1:300
Mouse IgG (H+L)	Alexa fluor 647	Goat	ThermoFisher	A21235	1704598	4	SR 1:300

2.3 Fluorescence recovery after photobleaching of ErbB2-GFP

Live-cell confocal imaging was performed using the Zeiss LSM510 META confocal microscope with a 63x/1.4NA planapochromat oil objective at 37°C using a temperature-controlled microscope chamber. Four images of the selected cell were taken before GFP in a rectangular region selected on the cell was continuously bleached using the 488 nm laser line at 60% laser power to cause at least a 50% reduction in the fluorescence intensity in the bleached region. Image acquisition was performed at low laser power. Fluorescence recovery in the bleached region was recorded for 30 to 40 frames at 10 second intervals, so as to allow recovery of the fluorescence to a stable level. Cells expressing moderate levels or ErbB2-GFP were selected for imaging. At least 12 individual cells were bleached and imaged under the same conditions for each experiment, and experiments were repeated three times.

A custom script was written in MATLAB to process the data. For each experiment the intensity of fluorescence in the bleached region and over the whole image, was extracted and used for background correction. The fluorescence intensity values in the bleached region were then normalised to the values prior to bleaching. These values were imported into MATLAB for curve fitting. For each cells sampled, an exponential fit to the normalised recovery curve was calculated. From this, the point at which the curve plateaued (the recovered value of the fluorescence intensity) was determined, from which the half-time to recovery and mobile fraction were determined using the equation $M_f = ((F_\infty - F_0))/((F_i - F_0))$ as described in section 3.1.

2.1 Single molecule tracking

Single molecule tracking was performed in 8-well Lab-Tek Chambered Coverglass with a no 1.5 borosilicate glass bottom. $1x10^4$ cells were seeded into each well 2 days in advance of imaging and cultured under standard culture conditions.

2.1.1 Labelling

Strepatividin conjugated quantum dots from Invitrogen, the details of which are set out in Table 2-5 were used for tracking in conjunction with the biotinylated Fab fragments prepared as described in section 2.2.2

Table 2-5: Details of Streptavidin conjugated quantum dots

Name	Supplier	Catalogue number	Emission peak (nm)
Qdot™ 525 Streptavidin Conjugate	Invitrogen	Q10141MP	525
Qdot™ 525 Streptavidin Conjugate	Invitrogen	A10196	625

For imaging, labelling of the protein to be tracked was performed in a two-step process where single colour imaging was performed, and a single-step process using pre-mixed complexes of QDs and antibodies.

A quantum dot binding buffer (QD binding buffer) containing borate was prepared to minimise nonspecific binding [133].

The two-step labelling process was as follows: culture medium was carefully removed from the wells and cells were rinsed twice with PBS; 200µl of 6nM biotinylated Herceptin Fab diluted in 2% BSA was added to the cells and incubated at 37°C for 15 minutes. Cells were carefully rinsed again with PBS to remove unbound antibody, before 200 µl 1 nM Streptavidin conjugated QD diluted in QD binding buffer was added for 15 minutes and the cells incubated again; the QD solution was removed and cells rinsed thoroughly with PBS to remove unbound QDs; warmed live-cell imaging medium was added to the cells and imaging performed immediately.

For single-step labelling, which was used where dual colour labelling was required pre-mixed antibody-QD complexes were prepared by mixing the streptavidin conjugated QDs and biotinylated Fab fragments to a final concentration of 1 nM complexes in QD binding buffer on a rotary mixer at 4°C for 1h prior to use. To label cells, culture medium was removed and cells rinsed with PBS as for two-step labelling, and the pre-mixed complexes added to the cells and incubated at 37°C for 15 minutes. The pre-mixed complexes were then removed from the cells, and rinsing and imaging was carried out as for the two-step labelling process described above.

2.1.2 Imaging

Imaging was performed on an Olympus IX81 inverted microscope in TIRF mode, under a temperature and and CO_2 controlled incubation chamber, with a 150x objective, Hamamatsu ImageEM camera, using the 491 and 640nm solid state lasers for excitation of the fluorophores. Imaging was performed for 2 minutes, at a frame rate of 100 ms. For dual colour imaging, a red/green beam splitter was used to split the field of view.

Where dual colour imaging was performed, a transform to register the channels was calculated using the positions of TetraSpeck beads, which fluoresce at 360/430 nm (blue), 505/515 nm (green),

560/580 nm (orange) and 660/680 nm (dark red), and are therefore visible in both the green and red channels. These beads were prepared for imaging by spreading 1 µl of the TetraSpeck solution as supplied on a microscope slide, and sealing with coverglass.

2.1.3 Tracking and analysis

Some QDs appeared to bind non-selectively to the coverglass outside the area of the cell and were therefore visible in the final images, in order to ensure these did not contribute to the track analysis, a brightfield image acquired immediately before tracking in TIRF was used to create a mask in ImageJ, which was applied to all frames of the movie to zero the contribution to the intensity from outside the cell area, and therefore ensure no signal detected here was used in tracking.

De-noising, spot detection and tracking were performed using a plug-in for ImageJ developed by W Pitkeathly [134].

2.1.3.1 Track analysis

For track analysis, only those tracks consisting of at least 50 points (corresponding to 5s tracked time) were kept and progressed for further analysis. Prior to mean square displacement and confinement analysis drift correction was applied to the tracks. The correction was applied by calculating the mean displacement of all tracked molecules in between frames, and subtracting this from the position of each molecule in the subsequent frame. Following drift correction, tracks were analysed as described in detail in 3.2.4.

For dual colour imaging registration of trajectories performed by applying 2^{nd} degree polynomial transform calculated from tetraspeck images. Two images were created from the full field representing the green and red channel. Noise removal and spot detection performed. Manually identified beads visible in both images and recorded the index of each detection. List of paired points used to calculate the polynomial transform using polynomial mode of MATLAB cp2tform function.

2.2 SOFI

For SOFI imaging an APEX labelling kit from ThermoFisher was used to conjugate Alexa488 to the C33 anti-hu CD82 antibody. For imaging, the conjugated Alexa488/C33 was diluted to 2µg/ml in 0.5% BSA and added to the cells at the same time as the QDs according to the single step labelling procedure outline in section 2.1.1. Images were acquired using the 491 nm laser for excitation under the same conditions as for single molecule tracking.

2^{nd} order SOFI reconstructions were calculated using the Localizer plugin for IgorPro [135]

2.3 Direct stochastic optical reconstruction (dSTORM) microscopy

2.3.1 Nikon nSTORM system

dSTORM imaging was conducted on the Nikon nSTORM system with a 100x TIRF oil lens with 1.49 NA. The nSTORM system is equipped with 405, 488, 561 and 640 nm laser lines, of which the 405, 488 and 640 were used for dual colour imaging. Images were capture with an iXon Ultra EMCCD camera.

2.3.2 Preparation of dSTORM imaging buffer

Oxygen scavenging solution was prepared by dissolving 10mg glucose oxidase and 18 µl catalase (from 45mg/ml stock solution) to make a 100x solution. To prepare imaging buffer 5 ml of T50 buffer was combined with 50 µl of oxygen scavenging system stock solution, and 50 µl 1M MEA-HCl.

2.3.3 Preparation of samples for imaging

Cells were plated at a density of $3x10^4$ cells per 35 mm dish 3 days in advance of imaging to allow sufficient spreading. 35 mm MatTek dishes with 10mm no. 1.5 coverslips embedded in the dish were used for culture and imaging. For imaging culture medium was removed and cells were rinsed and fixed with freshly prepared 4% PFA for 10 minutes. The PFA was removed and cells were permeabilised with 0.5% saponin for 5 minutes.

Where cells were treated prior to fixation, cells were serum starved for 1 hour prior to treatment, before incubation with the appropriate treatment in serum-free media for 1 hour, followed by rinsing and fixation as detailed above.

After rinsing, the fixed cells were treated under blocking buffer (4ml HINGS (goat serum) in 16 ml PBS, plus 40 µl 10% sodium azide (NaN_3)) for 1 hour. Cells were then incubated with primary antibody at 2µg/ml at 4°C overnight, before rinsing 3x with PBS on a rocker for 15 minutes, followed by incubation with secondary antibodies diluted in blocking buffer according to Table 2-5 for 1 hour immediately prior to imaging. Cells were then rinsed 3x in PBS as above for 15 minutes, before imaging buffer prepared as above was applied to the cells. Imaging was carried out immediately.

2.3.4 Image acquisition

Data for dSTORM imaging was always acquired in sets of 20000 frames. Acquisition was synchronised with the laser switching for dual colour imaging where 40000 frames were acquired (20000 for each channel). Alexa 488 was excited with a 491 nm laser line, supplemented with a 405 nm laser incremented manually in steps of 2.5% every 30s during the duration of imaging, up to a maximum value of 15% of maximum intensity. Alexa 647 was excited with a 647 nm laser line supplemented with the 405 nm laser in the same way. Both lasers were used at 100% initially, and image acquisition was started at the point at which it was judged by eye that bleaching of the fluorophores had occurred to the extent that individual blinking events were visible (typically for around 30s, although less densely labelled samples such as ErbB2 on MCF7 required less time to bleach). During dual colour imaging the 405 nm laser line was not used, as the system does not allow simultaneous use of 3 laser lines. Acquisition in dual colour imaging mode was always simultaneous (switching between 488 and 647 laser lines with continuous acquisition, laser activation coupled to each imaging channel such that frames of the 488 and 647 channels were acquired alternately). Sequential acquisition – imaging first the 647 label and then the 488 - was investigated to enable simultaneous use of the 405 nm laser to increase signal, but the change in recovered data, either

due to the sample having drifted during the first acquisition, or apparent bleaching of the second label during the first was deemed unacceptable so continuous simultaneous acquisition without the 405 nm laser was the method used for the acquisition of all dual colour data presented here.

2.3.5 Reconstruction

Image reconstruction was performed in the Nikon NIS analysis software. A minimum photon count of 500 was used to select localisations to carry forward for analysis. Analysis of the localisations by clustering is detailed in Chapter 4.

2.4 Statistics

Data in tables is presented as mean ± standard deviation, unless otherwise indicated. Number of cells imaged in each condition is indicated in the figure legend for each data set presented and the number of single molecule tracks or clusters identified in each condition is indicated where relevant.

Unless otherwise stated, distributions (e.g. of cluster area, diffusion coefficient, confinement time etc.) were compared using the non-parametric Kolmogorov-Smirnov test, with significance set at $p < 0.05$. Mean values were compared using the Wilcoxon rank sum test with significance set at $p < 0.05$. Where no statistical significance is indicated, the test did not indicate a statistically significant difference between the conditions.

Chapter 3 –Dynamic imaging studies revealing ErbB2 distribution and diffusion properties

This chapter describes the work conducted in dynamic protein imaging; investigating the distribution and motion of ErbB2 in the plasma membrane, in particular with respect to the expression and localisation of CD82. Section 3.1 describes the how fluorescence recovery after photobleaching (FRAP) experiments were used to examine the dynamics of the bulk ErbB2 population in MCF7 cells. Section 3.2 describes how single molecule tracking with quantum dots was utilised to study the motion of ErbB2 at the single molecule level, and in particular episodes of temporary lateral confinement. Section 3.2 introduces the work performed in dual colour to look directly at the localisation and diffusion of ErbB2 with respect to CD82, and describes the need for the work performed in the following section. Section 3.3 describes how super resolution optical fluctuation imaging was used to study the distribution of CD82 in living cells at super resolution, and the combination of super resolution optical fluctuation imaging CD82 distribution with single molecule tracking of ErbB2 to examine the effect of colocalisation with CD82 on ErbB2 diffusion and confinement.

As the plasma membrane environment is so complex, and occupied by a diverse range of proteins, there is significant interest in trying to understand the organisation of the interactions which take place here, by directly observing them via imaging methods. The advancements of recent years in microscopy instrumentation, fluorophores and image and data analysis mean that it is now possible to observe, at high spatial and temporal resolution, behaviour at the single molecule level. Of particular interest for this project are methods which allow the specificity of single molecule imaging to be combined with techniques allowing mapping of the distribution of membrane proteins, such that the impact of membrane structure/organisation on single molecule dynamics may be discerned. In particular, live cell imaging reveals a different picture of the plasma membrane and interactions

taking place therein, which is complementary to the static information provided by super-resolution techniques such as dSTORM, as discussed in the previous chapter.

The following sections detail the approaches which we employed to reveal the distribution and motion of CD82 and ErbB2 on the plasma membrane.

3.1 FRAP

Fluorescence recovery after photobleaching (FRAP) is a technique used to study the lateral mobility of proteins in both the plasma membrane and interior parts of the cell. By labelling a protein of interest with a fluorophore and bleaching a defined region of the cell it is possible to use the rate of recovery of fluorescence in the bleached area to deduce information about the mobility of the labelled protein, as the diffusion and transport of labelled protein from outside the bleached area gives rise to the recovery of fluorescence. Originally lipophilic or hydrophilic fluorophores, like fluorescein, coupled to proteins and lipids were used, but the cloning of green fluorescent protein (GFP) from the jellyfish *Aequorea Victoria* in 1992 and subsequent work by Osamu Chiamora, Roger Tsien and Martin Chalfie (Nobel prize recipients 2008), introduced a new reporter protein, which could be used to directly visualise the localisation of proteins in cells, allowing FRAP on living cells expressing GFP to be performed. Now there are many types of fluorescent proteins, and labelling with fluorescent proteins is widely used to perform FRAP experiments thanks to the specificity of the label and the lack any need to disrupt the behaviour of the cellular/membranous environment by labelling procedures. Typically cells are transfected with a fluorescent protein construct tagged to the protein of interest in the days before the experiment is to be performed, such that on the day of imaging cells visibly expressing the fluorescent protein may be selected and imaged without the need for further labelling.

A FRAP experiment consists of three phases:

1) Pre-bleach acquisition – images acquired of the sample area at low laser power to determine the baseline fluorescence signal
2) Bleaching – high power laser exposure of the sample area to bleach the fluorophores in the area
3) Post-bleach recovery – acquisition of images over an extended period of time (seconds-minutes) to monitor the recovery of fluorescence in the sample area, giving a measure of the mobility of the protein to which the fluorescent reporter is attached.

FRAP can be used to determine the mobile fraction of a protein in a defined area M_f, and the rate of mobility of the mobile fraction, expressed as the "half-time to recovery" t_{half}, determined from the typical fluorescence recovery curve (post bleach portion Figure 3-1). The mobile fraction M_f is defined as:

$$M_f = \frac{(F_\infty - F_0)}{(F_i - F_0)}$$

Where F_∞ is the fluorescence in the bleached region after recovery, F_i is the initial fluorescence before photobleaching, and F_0 is the fluorescence immediately after bleaching [136]. The mobile fraction is affected by factors including local membrane environment such as barriers (e.g. actin picket-fence) and membrane microdomains restricting protein diffusion, as well as interaction with other molecules, therefore the mobile fraction can be a useful parameter for determining the overall mobility of a population of proteins under certain conditions.

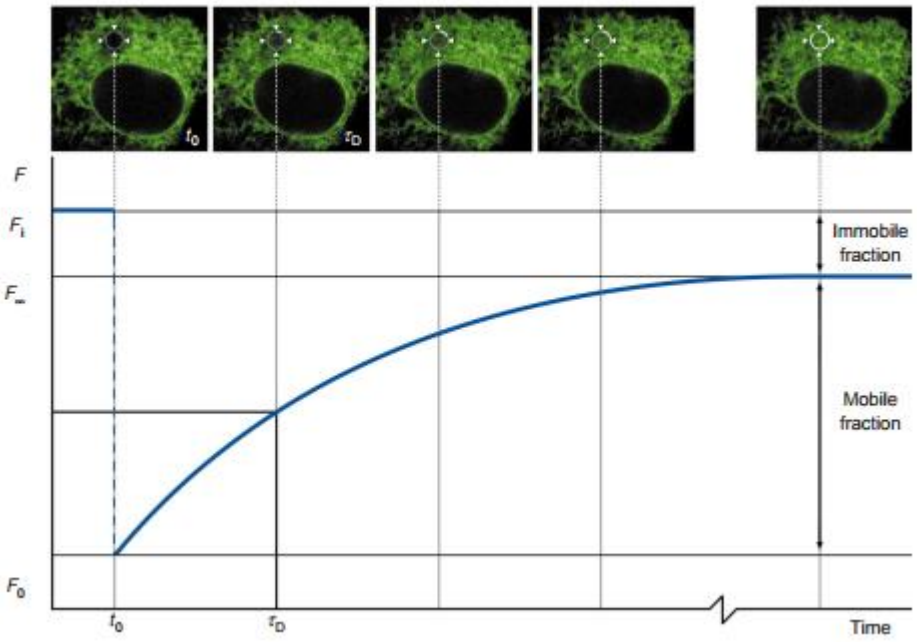

Figure 3-1: Typical plot of intensity versus time for a FRAP experiment
A region in the cell is bleached at time t_0 and the fluorescence decreases from the initial intensity F_i to F_0. The fluorescence recovers over time until it reaches a plateau F_∞. The portion of the curve in between bleaching and recovery is known as the recovery curve, and is fit to determine the mobile and immobile fraction and used to determine the characteristic time τ_D (also called $\tau_{1/2}$) at which the fluorescence has half recovered. Reproduced from [137].

The effect of temperature on diffusion of both soluble and transmembrane proteins has been shown in multiple studies – with 1.4 fold faster recovery rate for soluble GFP transfected to the endoplasmic reticulum shown at 37°C compared to 23°C, due to differences in viscosity. This highlights the importance of performing all dynamic experiments where diffusion of membrane proteins is key at consistent, physiological, temperatures [138].

FRAP experiments may be performed using confocal microscopy to investigate a protein mobility in a particular slice through the cell, or in TIRF mode to look specifically at protein mobility in the plasma membrane.

3.1.1 Analysis of FRAP experiments

FRAP data consists of a series of images containing the pre-bleach and post-bleach images as described above, from which the intensity of the bleached region (defined by known coordinates) before and after bleaching is extracted. Pre-bleach intensity is used to determine the level to which fluorescence recovers post-bleaching, while the intensity values extracted from post bleach frames each represent a time point on the fluorescence recovery curve. The intensity immediately after bleaching is extracted from the first post-bleach image, and the recovered fluorescence value can be extracted from the asymptote of an exponential fit to the recovery curve. The half-time to recovery is easily extracted from the exponential fit given the initial post-bleach value and the recovered intensity.

3.1.2 Results

FRAP experiments were performed on live cells expressing GFP-tagged ErbB2, to monitor the mobility of ErbB2 in a non-ErbB2 overexpressing breast cancer cell line, MCF7.

MCF7 cells stably expressing high levels of CD82 or CD82 cys5 were transiently transfected to express ErbB2-GFP. Experiments were performed on non-treated and Herceptin treated cells, which where indicated was added to the cells for at least 1 hour prior to imaging.

For consistency with the dSTORM and SPT data which were acquired in TIRF, the FRAP data was acquired using confocal microscopy by selecting the slice as close to the basal membrane as possible. Precise details of the image acquisition parameters are provided in Chapter 2. Analysis of the acquired images was carried out as detailed in Chapter 2 to determine the mobile fraction and half-time to recovery of – parameters representing the mobility of ErbB2. The aim of these experiments was to determine whether CD82 expression in cells expressing low levels of ErbB2 affected ErbB2 mobility, and examine the effect of Herceptin on ErbB2 mobility.

Representative images from a FRAP experiment are shown in Figure 3-2 A. In each experiment, at least 12 such cells, selected on the basis of having a moderate level of ErbB2-GFP expression, were imaged in the presence and absence of Herceptin. The images in Figure 3-2 A show the cell before the bleaching step was carried out (leftmost images), demonstrating that these cells expressed the GFP-tagged ErbB2 across the membrane before bleaching. The images acquired immediately post-bleach (middle images) demonstrate that a significant reduction in fluorescence intensity was achieved, and the images showing fluorescence recovery demonstrate that ErbB2 is highly mobile, and diffuses into the bleached area causing fluorescence recovery over the timescale of the experiment. Additionally these images also demonstrate that the bleaching is confined to a defined region, and does not affect the fluorescence in the rest of the cell.

Figure 3-2 B-D show the pooled recovery curves from four independent experiments in each cell line respectively. The recovery curves reveal that ErbB2 is mobile in the membrane of MF7 cells, recovering to at least 60% of the initial fluorescence value in most cases. In every cell line the addition of Herceptin reduces the fluorescence recovery relative to the untreated condition, however we also see that the standard deviation on these curves is very large. This demonstrates the high level of heterogeneity in ErbB2 expression in the cell population, despite only selecting cells expressing moderate amounts of ErbB2-GFP.

Analysis of the recovery curves was performed for each experiment separately, by pooling the results from that experiment only, before average values for the mobile fraction and half-time to recovery were calculated by taking together the four sets of results, whereas the pooled recovery curves shown here are an average of every acquired recovery curve from all four experiments.

The mobile fraction found for untreated MCF7 cells, summarised in Figure 3-2 E shows no significant effect of CD82 expression on ErbB2 mobility, as can be seen from the large standard deviation on the bar chart in Figure 3-2 D. However, it is interesting to compare these results to those for SKBR3 cells,

which over-express ErbB2, as previously shown by this group [1]. In this previous work SKBR3 cells exhibited a higher mobile fraction of Erbb2, which seems counter-intuitive as the higher expression level of ErbB2 in SKBR3 cells would be likely to result in a larger number of interactions occurring (assuming interactions are governed by a simple mass action law), thereby reducing the mobility of ErbB2 - assuming that interactions result in the formation of larger molecular complexes which would diffuse more slowly. By this argument, a longer half-time to recovery would be expected in ErbB2 over-expressing cells, which was in fact observed, although the higher mobile fraction is not explained. The mobile fraction in SKBR3 was similarly reduced in response to Herceptin treatment.

The $t_{1/2}$ value was increased with Herceptin treatment in all cell lines, but no significant difference in this or the mobile fraction was observed in any cell line between the untreated and treated conditions.

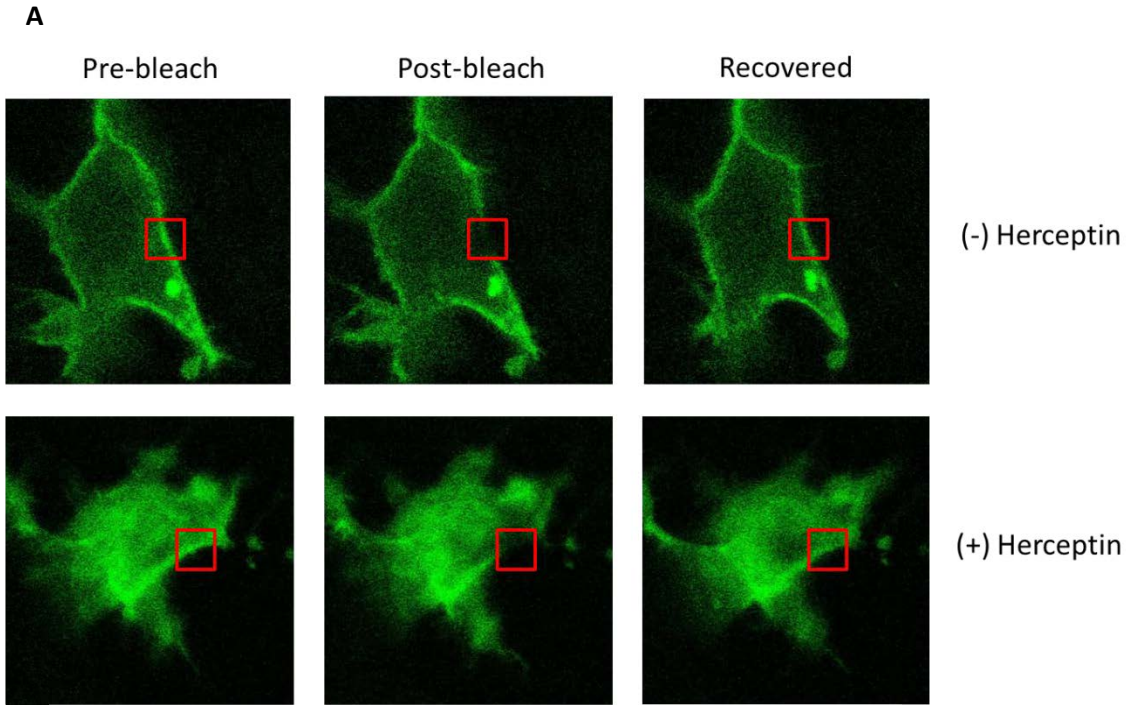
A
Pre-bleach
Post-bleach
Recovered
(-) Herceptin
(+) Herceptin

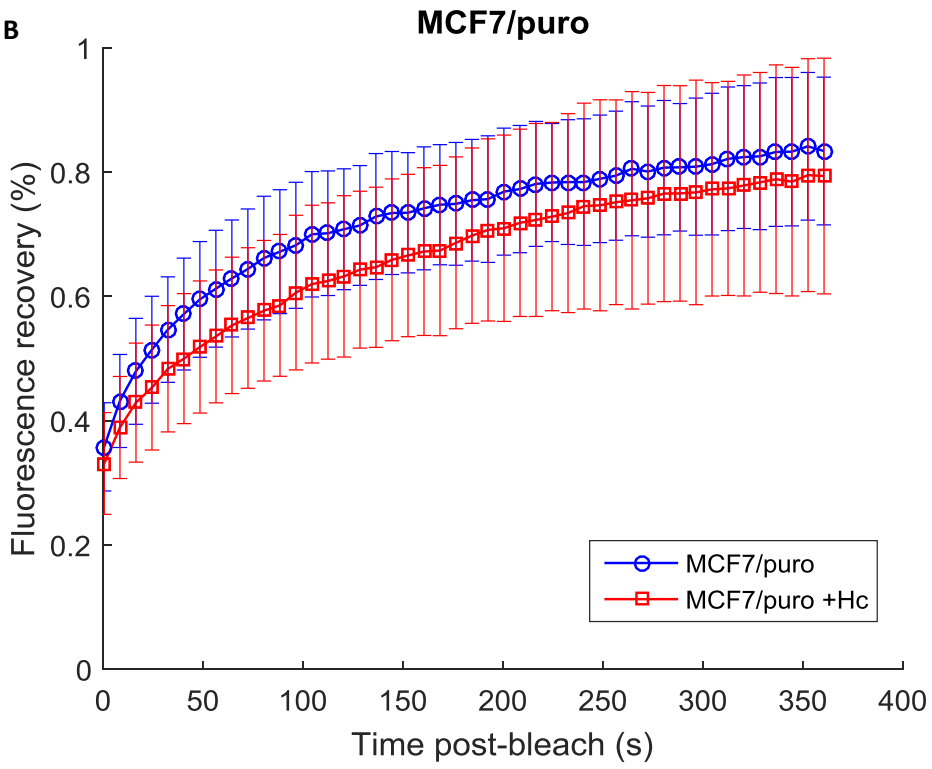
B
MCF7/puro
Fluorescence recovery (%)
Time post-bleach (s)
MCF7/puro
MCF7/puro +Hc
0
0.2
0.4
0.6
0.8
1
0
50
100
150
200
250
300
350
400

C

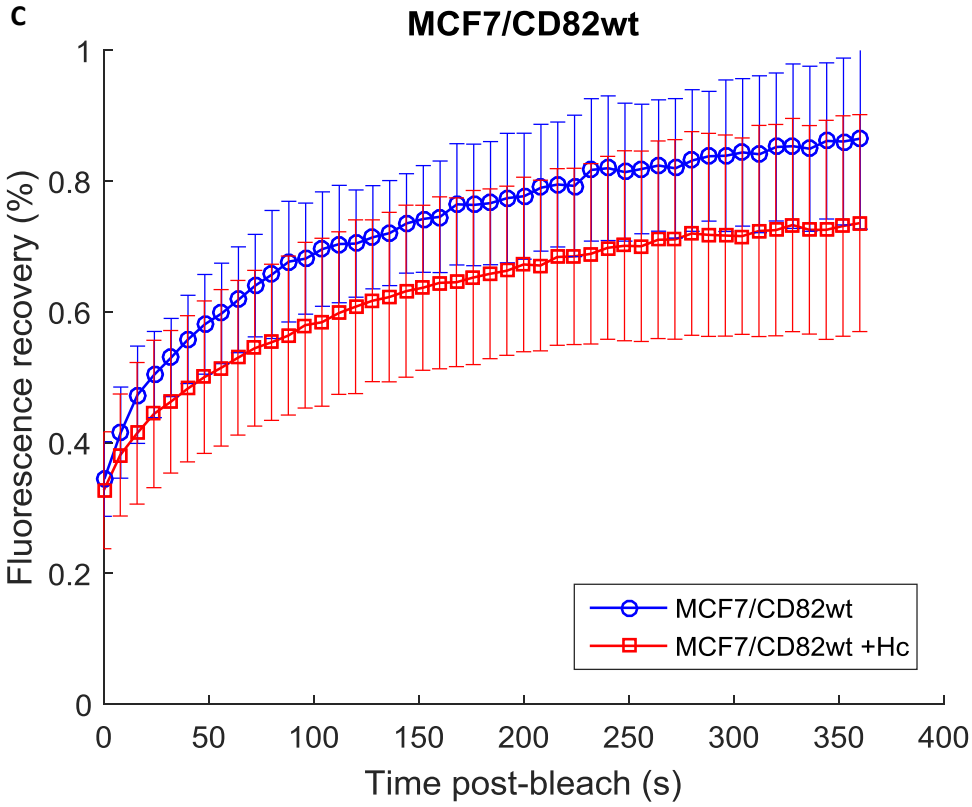
MCF7/CD82wt
Fluorescence recovery (%)
Time post-bleach (s)
MCF7/CD82wt
MCF7/CD82wt +Hc

D

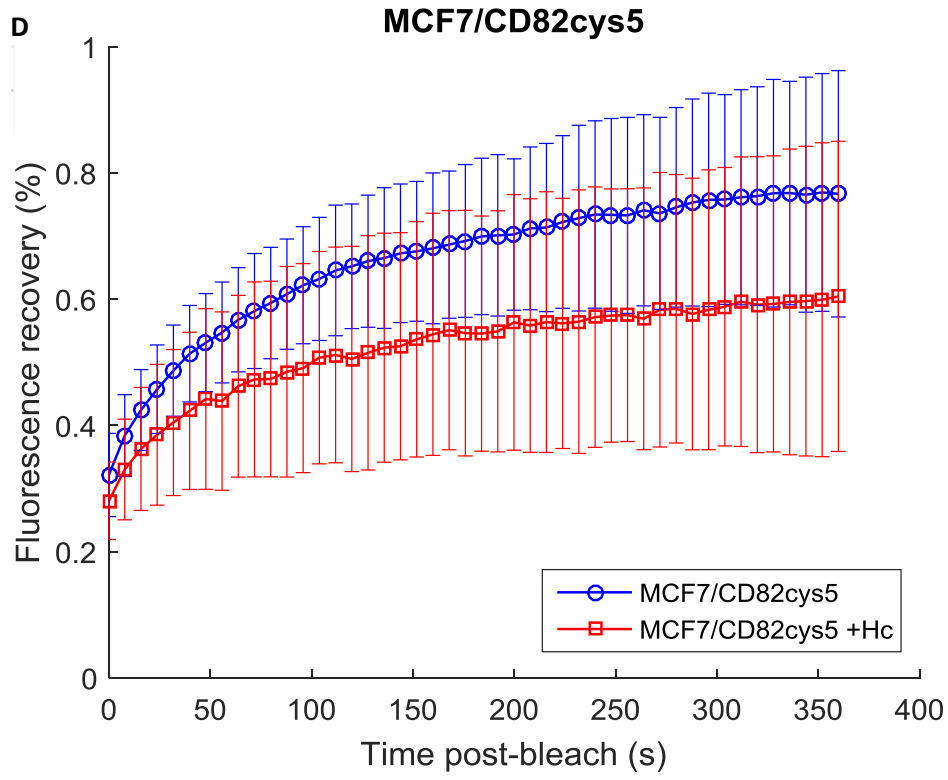
MCF7/CD82cys5
Fluorescence recovery (%)
Time post-bleach (s)
MCF7/CD82cys5
MCF7/CD82cys5 +Hc

E

	MCF7/puro (-Hc)	MCF7/puro (+Hc)	MCF7/CD82wt (-Hc)	MCF7/CD82wt (+Hc)	MCF7/CD82cys5 (-Hc)	MCF7/CD82cys5 (+Hc)
M_f (%)	0.71±0.03	0.63±0.06	0.66±0.20	0.60±0.10	0.61±0.16	0.53±0.07
$t_{1/2}$ (s)	54.67±10.00	69±14.86	54.74±9.67	75.5±11.90	54.25±11.18	76.75±23.06

F

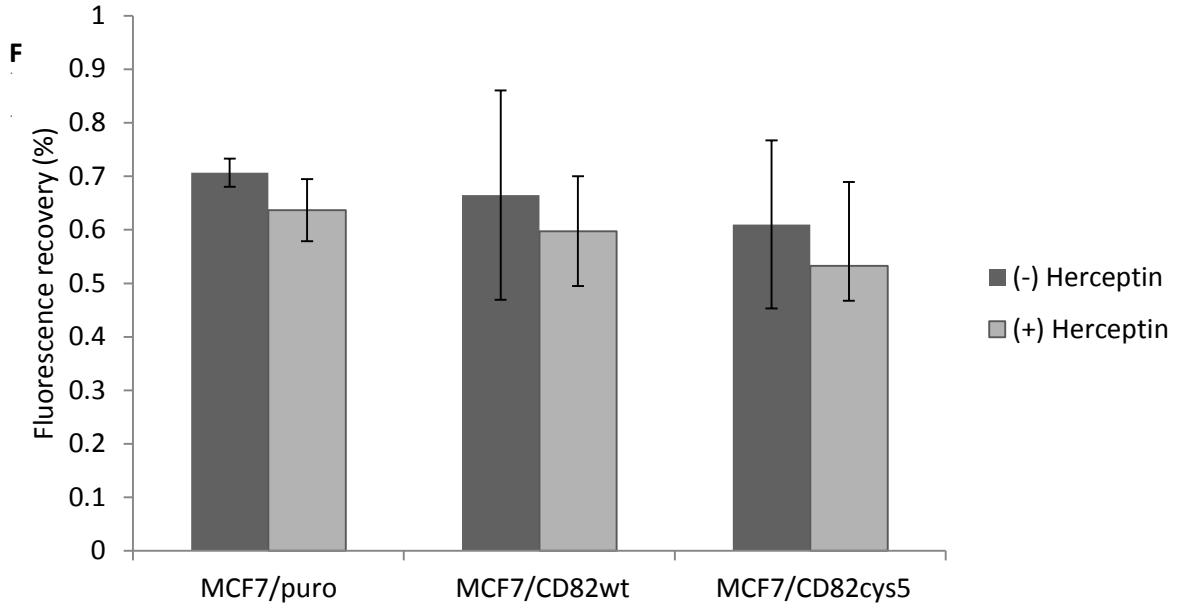

Figure 3-2: The effect of CD82 expression and Herceptin treatment on ErbB2 mobility in MCF7 cells
A) Example FRAP images showing the pre-bleach acquisition, immediately post-bleaching, and the recovered fluorescence. Illustrated are MCF7/CD82wt cells, without Herceptin and after incubation with Herceptin for 1 hour. B-D) Pooled fluorescence recovery curves from 4 independent experiments in MCF7/puro, MCF7/CD82wt and MCF7/CD82cys5. 10-12 cells were analysed in each condition E) Summary results ± standard deviation (M_f, mobile fraction, $t_{1/2}$, half-time to recovery). F) Graphical summary of effect of Herceptin incubation and CD82 expression on ErbB2 mobility.

3.1.3 Conclusion

The results of FRAP in both MCF7 and SKBR3 cells (taking together the work presented in this thesis and the cited prior work in the group) the expression of CD82 does not itself seem to effect the mobility of ErbB2 overall. However, given the evidence that CD82 expression correlates with a poor response to Herceptin, and regulates the phosphorylation and downstream signalling of the receptor, we chose to employ a more specific technique to look at the dynamic behaviour of individual ErbB2 receptors, and ultimately correlate this with CD82 localisation, in order to understand if CD82 microdomains play a role in this regulation.

3.2 Single molecule tracking with quantum dots

Classical techniques, both imaging and biochemical, have offered insight into the molecular underpinnings of biological systems, however are typically based on ensemble measurements of many thousands of molecules or entire cell populations, and are unable to provide information about the behaviour of sub-populations due to the averaging of signals. FRAP is an example of such a technique. Microscopy studies have revealed that cellular components distribute in a non-homogenous fashion, and therefore techniques which are able to probe this distribution are necessary in order to understand the complex workings of the cellular environment.

Single molecule tracking (SMT) is a technique allowing the direct interrogation of molecular movements in living cells, by attaching an imaging probe to a single molecule and observing its motion over time. Provided the spatial and temporal resolution of the imaging is high enough, trajectories can be extracted which reveal the mechanism involved in the motion of the particle [139] such as whether the motion is directed or diffusional, random or confined. Typically SMT experiments are conducted at a frame rate of upwards of 10 frames per second, with a spatial precision of around 20 nm, allowing the tracked molecules to be observed at sufficient spatial and temporal resolution to discern the nature of their motion and interactions.

There are several aspects to single molecule tracking experiments, including selecting the imaging probe, attaching it to the target molecule, performing the imaging, and a significant amount of data processing to extract particle positions from the images, construct trajectories and analyse the motion described by those trajectories. These aspects will be discussed in the following sections.

In methods such as FRAP, and fluorescence correlation spectroscopy (FCS), which are also widely used to study protein dynamics, signal from many molecules is averaged – these techniques take

'ensemble measurements', where single molecule events such as confinement or binding can be very difficult to detect, as they are obscured by the averaging of many signals [139]. Averaging can be a problem in the context of cellular dynamics, as the imaged particles can interact with multiple targets, resulting in populations with different mobility properties. Furthermore, the dynamics of the particles may change over time or space, making averaging of the signals a problem as these multiple populations/changes in dynamics are hidden in the averaging process. Imaging the motion of single molecules allows these processes to be revealed, and even for trajectories to be sub-classified according to parameters such as their motional mode, diffusion coefficient, or location on the cell for further in depth analysis.

SPT had been widely used to study the motion of molecules in the plasma membrane, including ErbB2 on breast cancer [140]–[142] and normal [143] cell lines; and tetraspanins including CD9 [22], and CD81 [144], [145]; as well as G Protein-coupled receptors [146], [147], and GPI-anchored proteins [18], [148], [149] amongst many others.

3.2.1 Performing single molecule tracking experiments

SMT experiments may be performed with a number of different imaging modalities depending on the localisation of the protein of interest. TIRF is most commonly used for the selective imaging of proteins localised on the basal membrane, thanks to the specificity of the technique, and the lack of background autofluorescence from the cell body, which is especially beneficial in SMT as it results in higher signal-to-noise ratio, which in turn allows for more precise localisation of the single fluorophores. Other imaging modalities are used, including but not limited to wide-field fluorescence microscopy for 2D tracking, highly inclined and laminated optical sheet (HILO) or selective plane illumination microscopy (SPIM) for imaging at depth in samples; and spinning disk confocal and multifocal plane microscopy for 3D tracking. The use of these techniques to extend the capabilities of SMT will not be discussed further in this thesis but many thorough reviews are available [120], [122].

3.2.2 Fluorophores

Single particle tracking was first demonstrated in the mid-1980s, when Bradabander and colleagues showed that gold nanoparticles down to 40nm in size could be visualised on the surface of living cells, in a technique originally coined 'nanovid microscopy' [150], [151]. This method relied on the sparse use of colloidal gold nanoparticles rigidly attached to the biomolecule of interest, which thanks to their large Rayleigh scattering intensity could be localised with nanometre precision in successive frames recorded using differential interference contrast (DIC) microscopy [151]. Subsequently SPT was performed using large latex, polystyrene or silica particles, with sizes ranging from 200 nm to 1μm diameter, imaged using standard optical microscopy [120], [152]. These probes were widely used and contributed to the understanding of heterogeneity of diffusion of plasma membrane proteins, as techniques were developed along with molecular targeting strategies, to reconstruct trajectories and analyse the diffusion and dynamics of the labelled particles. An advantage of these early probes was that they did not exhibit photobleaching, and therefore were highly stable and able to be imaged for long periods of time (up to minutes), however their bulk could constrain biological processes and introduce artefacts into the data. After the breakthrough in 1993 by Betzig, showing that single molecules could be detected at room temperature by means of fluorescence [153], SPT with fluorescent molecules as the reporter was soon implemented [154]–[156]. SPT by means of fluorescence was called single molecule tracking, or single dye tracking (SDT). Since then advances in molecular targeting strategies and fluorophore development has led to a plethora of suitable probes for SMT, including fluorescent proteins, organic fluorophores, nanocrystals, gold nanorods and quantum dots [127]. The trajectory length and spatial precision of SMT using fluorescent proteins or dyes is typically limited to a few seconds and 20-50 nm [14], [121], which is lower than the performance using the older, non-fluorescent reporters, but with the advantage of the smaller size of modern probes. This lower performance compared to non-fluorescent reporters is due to the limited number of photons a fluorescent molecule can emit

before photobleaching (typically 10^5-10^6) limiting the time over which it can be tracked, autofluorescence from the cell at the same wavelength reducing the signal to noise ratio (SNR) and the lower brightness of fluorescent probes compared to the contrast achieved with non-fluorescent reporters limiting localisation precision. Localisation precision is determined by the number of photons emitted. Quantum dots are able to overcome the problems associated with rapid photobleaching, as they are resistant to photobleaching and therefore can be followed for long periods of time, making them highly suitable probes for SMT, as first demonstrated in 2003 by Dahan and coworkers [157].

3.2.2.1 Quantum dots

Since first demonstrated in 2003 [157] quantum dots have found enormous use in SMT (also called SQT, when referring to tracking with quantum dots specifically, but referred to as SMT throughout this thesis)[121], [127], [133], [158]–[161].

Quantum dots are inorganic semiconductor nanocrystals, typically composed of a CdSe core surrounded by a ZnS shell, which is exhibit fluorescence at a wavelength proportional to their physical size. The interesting properties of these materials bridge the gap between bulk semiconductors and single molecules. Bulk semiconductors are characterised by a specific band gap energy E_g, which is the minimum energy required to excite an electron from the ground state valence band to a vacant position in the conduction band. This process results in an electron-hole pair, known as an exciton, which on relaxation of the electron back to the valence band can cause emission of a photon in a process known as radiative recombination. The exciton has a finite size in the crystal given by the Bohr exciton diameter $a_{B,}$ which varies from 1-100 nm depending on the material. If the size of a_B is larger than the size of the semiconductor nanocrystal then the charge carriers in the exciton become spatially confined, raising their energy. The exciton size therefore defines the transition between the regime of bulk crystal properties and the quantum confinement

regime, in which the optical and electronic properties are dependent on the nanocrystal size. Quantum dots with a semiconductor nanocrystal size smaller than a_B exhibit size dependent absorption and fluorescence spectra, which can be tuned from the ultraviolet through visible spectrum depending on the nanocrystal core size, as shown in Figure 3-3. The discrete emission profiles, and broad excitation profiles, coupled with the high quantum yield, are properties highly desirable for biological imaging purposes [162]. In order to exploit the desirable optical properties of quantum dots for biological imaging a passivation layer such as a ZnS shell must be applied around the nanocrystal core. A ZnS shell also serves the purpose of increasing the efficiency and brightness of the quantum dot, as the inorganic coating limits the non-radiative de-excitation channels which would be supported by an organic coating. Quantum dots with layers of another higher band gap semiconducting material around them form a class known as core-shell quantum dots, and exhibit excellent fluorescence yield. This type of quantum dot was employed in this study, yielding high SNR and allowing for precise localisation against the background of the cell.

Surface modifications must also be made to the quantum dot to biofunctionalise it, by the addition of protein or small molecules. For imaging, quantum dots are typically conjugated either directly to antibodies, or to streptavidin, to employ the biotin-streptavidin interaction for targeting.

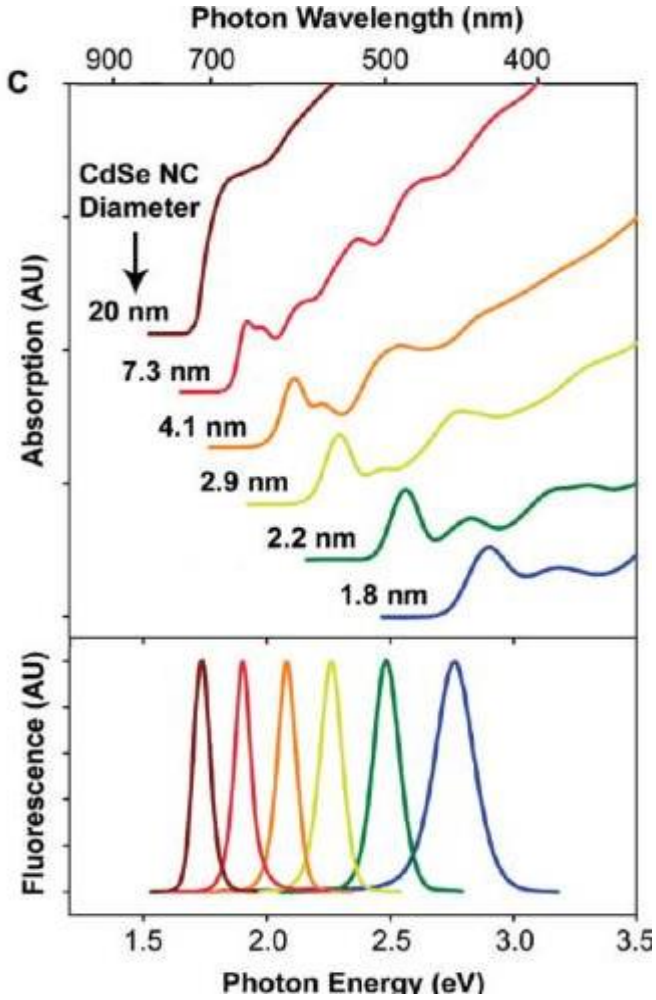

Figure 3-3: Size dependent absorption and emission spectra of semiconductor nanocrystals
Figure reproduced from [162]

3.2.3 Labels

Fluorophores for SMT may be targeted to the protein of interest via a number of different strategies, including antibodies, Fab fragments of antibodies, nanobodies, ligands and small molecules. For single molecule tracking, it is generally desirable to reduce the size of the label-probe complex as much as possible to avoid introducing artefacts caused by large labelling complexes into the processes under observation. Therefore, the smaller options such as Fab fragments and nanobodies are quite desirable. Ligands such as EGF are also small in size, however whether it is desirable to label with a ligand depends on the specific process under study, and the desired condition of the

protein under observation. For studying the behaviour of molecules without greatly altering the underlying processes, antibody fragments can be a good choice.

This study employed Fab fragments for single molecule tracking, so as to reduce the size of the label-probe complex as much as possible, and ensuring a 1:1 label-probe ratio to achieve the most accurate tracking. Fab fragments are generated by digestion of whole antibodies, to separate the Fc and Fab fragments. Digestion with papain results in the generation of two Fab fragments, each containing an antigen binding site, and an Fc portion containing only the lower portions of the two heavy chains, which can be separated by Protein A purification. Digestion with pepsin results in the formation of one F(ab')2 fragment and numerous small peptides of the Fc portion, as illustrated in Figure 3-4. F(ab')2 portions can be further digested into Fab' fragments, however this additional step is often unnecessary and Fab fragments may be generated directly from IgG molecules by papain digestion.

Enzymatic digestion with papain produces two Fab fragments of the IgG molecule, each containing an antigen binding site, and one larger Fc (fragment crystallizable) fragment containing only the lower portions of the two heavy chains [164]. Otherwise, pepsin cleavage produces one large F(ab) 2 fragment containing two antigen binding sites and many smaller peptide fragments from extensive degradation of the Fc region [164]. Specific reduction of the disulphide bonds which hold the F(ab) 2 fragment together using 2-mercaptoethylamine-HCl (MEA-HCl) produces two Fab fragments, each of which has one antigen binding site.

The combination of a small and specific label such as a biotinylated Fab fragment, with a bright and photostable probe such as a streptavidin functionalised quantum dot results an excellent combination for labelling single molecules for tracking with minimal disturbance to the cellular environment and maximal fluorescence signal.

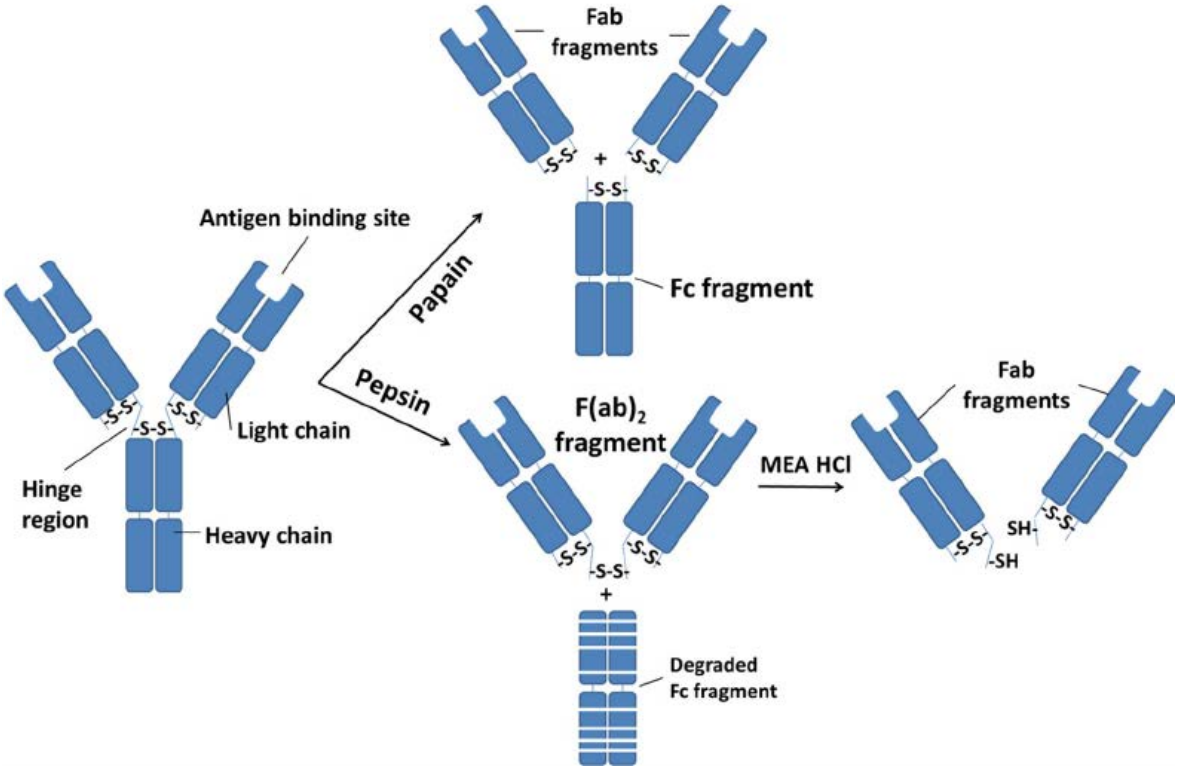

Figure 3-4: Illustration of enzyme digestion of IgG antibody molecule to form Fab fragments
IgG antibodies (shown left) can be digested by papain or pepsin to form Fab (upper middle) or $F(ab)_2$ (lower middle) fragments respectively. $F(ab)_2$ fragments can be further reduced to form Fab fragments. Reproduced from [163]

3.2.4 Analysing single molecule tracking experiments – from images to single molecule trajectories

Experimental data from an SMT experiment consists of a stack of images, comprising the distribution single molecule diffraction limited spots in the biological sample, from which the position of the single fluorescent emitters can be precisely determined. Each image represents a particular temporal point, so as well as image analysis to remove noise, and detect the spatial locations of the fluorophores, further analysis must be performed to derive the temporal connections between the spatial locations in different frames, and thus build up trajectories representing the molecular motion over the imaging time. This section describes the basis of image analysis and tracking, and subsequent analysis of the generated trajectories. Extensive reviews on each of these topics is available [120], [164], [165], so this section will focus primarily on the methods applied in this thesis.

3.2.4.1 Image analysis – noise removal and spot detection

It is necessary to remove the noise in SMT images, which can occur as a result of photon noise, related to the fact that measurements of stochastic quantum events such as numbers of photons are fundamentally limited by Poisson statistics [166]; dark noise, which is noise related to the thermal excitation of electrons causing currents which build up over time, or external sources such as cosmic rays; and readout noise, which occurs as a result of the imperfect function of electronic components used to amplify the signal from each pixel in the CCD [167]. Background from autofluorescence and out of focus fluorophores will also contribute non-specific signal, reducing the signal to noise ratio of the single molecules. Noise in the images makes fluorescent spot detection more challenging by reducing the contrast between the spots and the background. The noise present in microscopy images is typically characterised by a mixed Poisson-Gaussian distribution [168].

De-noising and background subtraction are the first steps in processing SMT images, to maximise the contrast between the signal from the single fluorescent molecules and the rest of the image and enable more precise detection and localisation. Typically, it is possible that signal from background features can be even higher than the peak intensity of the signal from the single fluorescent molecules in some areas, precluding the use of simplistic segmentation methods based purely on pixel intensity.

A method of spot detection employing variance stabilisation, optimal Gaussian filtering, and wavelet de-noising, developed by W. Pitkeathly [134] was used to perform the spot detection in this study. By employing the generalised Anscombe transform the mixed Poisson-Gaussian noise distribution present in microscopy images can be transformed to have a Gaussian distribution with a variance approximately equal to one. Once this has been performed the data can then be denoised using a Gaussian denoising scheme. After denoising, the fluorescent spots need to be separated from the background regions in the image – the method developed by W. Pitkeathly employs wavelet analysis

using the undecimated wavelet transform to decompose the Gaussian transformed image into wavelet planes. The noise in each wavelet plane is also Gaussian, and has a spatially constant variance, so a global threshold can be defined for the noise in each wavelet lane, based on the standard deviation of the noise in that plane. It is possible to determine whether the signal in each wavelet plane originated from noise or a true signal, and thus modify or set to zero the value of wavelet planes containing noise. Identifying spot like features in the image can then be achieved by reconstructing the wavelet transform with the de-noised planes. In this method an additional precaution is taken in the image processing to ensure that low intensity true signal is not lost, however since we have employed quantum dots for imaging, which have very high brightness and therefore provide high contrast against the background, this feature was not of vital importance for the present study. It would however be of use if alternative, less bright fluorophores were used in future work.

After wavelet analysis, detected spot-like features appear as diffuse clusters of pixels on a zero-valued background. Where spots are well separated each cluster of pixels likely corresponds to one fluorescent molecule, while in situations where fluorophores are more closely spaced a cluster may correspond to more than one particle. Both the morphology of the cluster and the intensity of the pixels can therefore be used to segment and precisely localise the particles.

3.2.4.2 Building trajectories - tracking

The use of quantum dots as a probe removes some of the typical challenges associated with spot detection in live cell fluorescence microscopy images, as the signal is typically much brighter than the background, and imaging in TIRF mode reduces the background further, making detection of single QDs relatively straightforward. However, the fluorescence intermittency of QDs (blinking) for which they are well known, provides a challenge in tracking, as the signal from a single QD can be lost for one or several frames before appearing again.

A number of methods for linking the spots detected in different frames into trajectories representing the motion of the underlying molecule. The approach employed in this study for trajectory construction was developed, with vesicle tracking in mind, by W Pitkeathly [134]. In order to cope with the different dynamics of vesicles in an efficient way – i.e. vesicles may undergo directed or diffusional motion – state estimation is performed via the interacting multiple model filter based on two motion models. In addition, trajectory initiation is treated more cautiously than in some other tracking frameworks and separated from the main data association. By doing this, fewer tracks are entered into the data association stage where trajectory fragments are linked, which allows better calculation of measurement to track probabilities [134].

The method developed for trajectory construction is a probabilistic approach which approximates the generally more accurate but more computationally intensive deterministic approaches such as multi-hypothesis tracking (MHT). In this method, both single- and multi-frame deterministic particle and track segment linking stages are replaced by data association using probabilistic reasoning. The first wave of data association is provided by the nearest neighbour probabilistic data association (NNPDA) algorithm, which considers the set of most likely track assignments. It yields a single optimal solution and a probability of each individual assignment. Before updating each track with the measurement (molecule position) assigned from the optimal solution, the probability of each individual assignment is reviewed, with the idea that forming linking with very low probability as defined by the global solution can be avoided, since these may be due to noise; and additionally not to force assignments where two or more tracks have very similar assignment probabilities for the same measurement. Assignment decisions for ambiguous situations such as these are delayed until the multi-frame analysis is performed, where information from other time frames can be used to inform the decision. To cope with the different dynamics of vesicles, which can undergo different types of motion (i.e. directed or diffusional), the interacting multiple model filter based on two motion models is used to efficiently estimate perform state estimation. The combination of these

approaches yields a tracking algorithm which is able to efficiently and accurately form links even in the presence of blinking QDs undergoing different motional modes.

3.2.4.3 Analysing trajectories

3.2.4.3.1 Mean square displacement

Mean square displacement (MSD) analysis is a mainstay of single molecule trajectory analysis. There are a number of different methods available to determine diffusion coefficient, with MSD analysis being one of the fundamental tools. Approaches which can determine the diffusion coefficient in different regimes are powerful and important, since in performing MSD analysis over a whole trajectory, the measured diffusion coefficient would reveal nothing about the underlying different diffusion coefficients, and would be biased towards the larger value. However, although several approaches have been proposed for analysing trajectories which exhibit different diffusion regimes over the time course of the trajectory, many of these still rely at some stage on evaluating the diffusion coefficient of a single regime, therefore MSD analysis is key even in these more powerful approaches.

MSD is commonly defined as:

$$\boldsymbol{MSD(n)} = \frac{\mathbf{1}}{\boldsymbol{N-n}} \sum_{\boldsymbol{i=1}}^{\boldsymbol{N-n}} (\boldsymbol{r_{i+n}} - \boldsymbol{r_i})^{\mathbf{2}}, \quad \boldsymbol{n} = \mathbf{1}, \dots, \boldsymbol{N} \tag{3}$$

which uses all available displacements of a given duration $n\Delta t$, where $\boldsymbol{r}$ is the position of the molecule, and N is the length of the trajectory. A visual representation of the contribution of different points in a trajectory to the MSD curve can be seen Figure 3-5, which illustrates how for small values of time lag τ $(= n\Delta t)$ many points contribute to the MSD curve, while for higher time lags far fewer points contribute. This is the reason that a common criterion when calculating MSD is to restrict the analysis to τ values lower than 1/4 of the total time of the trajectory [144].

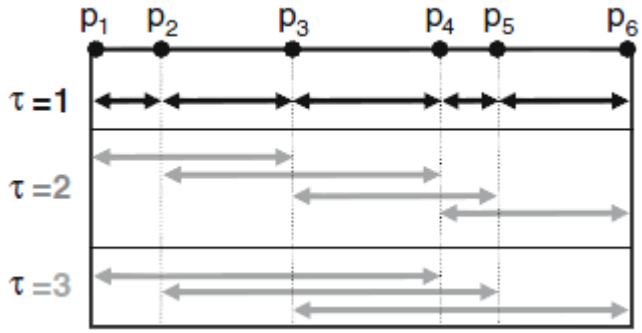

Figure 3-5: Mean square displacement analysis of a one-dimensional trajectory.
Smaller lag times are calculated with more data, as can be seen comparing the calculations for τ_1 with τ_2. Reproduced from [139]

Although MSD, and other whole trajectory analysis methods such as cumulative probability analysis are powerful methods and provide the possibility for making ensemble measurements, they do not reveal information about the underlying diffusional states in single trajectories. Ensemble analysis does not take full advantage of the specificity of SMT for probing behaviour at single molecule level, so a method which makes it possible to determine the motional mode of a specific molecule at a specific location and time was required to fully utilise SMT to answer the questions posed in this project.

3.2.4.3.2 Detection of temporary lateral confinement

For analysing single molecule tracks on the whole-trajectory level, several methods exist, including Mean Square Displacement (MSD) analysis [169], Moment Scaling Spectrum (MSS) analysis. [170], [171] Approaches based on machine learning techniques such as neural networks [172], self-organizing maps [173], and hidden Markov models [174] have also been used with success. [175] However, analysis of dynamics based on entire trajectories can be misleading when the motion of the molecule contains multiple different modes - such as directed motion, for molecules undergoing trafficking; Brownian motion, of molecules freely diffusing in the membrane; and confined motion, of molecules restricted in clusters or microdomains. These episodes can be missed due to the

averaging nature of most whole trajectory analysis methods. For more detailed analysis of single molecule trajectories which is able to reveal these underlying motion modes, other methods have been proposed, such as applying a moving window to global analysis methods[169], support vector machines [175], and thresholding based on probability that the observed motion is not due to random diffusive behaviour [176]. We elected to use the approach based on thresholding a probability that the observed behaviour in a trajectory has a non-random origin, as first described by Saxton [177] and further developed by Simson and colleagues [176].

Despite the fact that the magnitude and direction of every step in a random walk is unpredictable, it is possible to determine the probability that a molecule, with diffusion coefficient D will stay in a region of radius R for a period of time t. By solving the diffusion equation for a point source at the origin and rigid absorbing walls at R, Saxton [177] determined this probability to be

$$\log \Psi = 0.2048 - 2.5117 Dt/R^2 \quad (1)$$

For fixed $R$and$D$, ψ will decrease with increasing t because the likelihood of the particle reaching the wall and disappearing increases with the time. For a defined $D$and t, ψ increases with the size of the region R. For analysis the trajectory is broken into segments containing successive points of the trajectory, with length varying from 4 to S_m points. The point within a segment with the largest displacement from the starting point of the segment defines the value of R for that segment. Equation 1 is evaluated for every segment, with D calculated for every trajectory from the highest instantaneous diffusion coefficient. The value of ψ is then converted into a probability level according to

$$L = \begin{cases} -\log(\psi) - 1 \\ 0 \end{cases} \quad (2)$$

If a segment has a probability <10% of arising due to non-random behaviour, the value of the confinement index L is set to zero for that point, as only behaviour of non-random origin is of

interest. The value of L is then averaged at every time point, as each point will be a member of multiple segments. Regions of the trajectory are classified as confined if L rises above a threshold level L_c for a period longer than the threshold time t_c, where L_c is given by:

$$\boldsymbol{L_c = \alpha\langle L\rangle} \quad (4)$$

A number of parameters must be set to perform the calculations according to this method, and these are detailed further in section 3.2.5.1.

3.2.5 Results

In order to determine whether CD82 expression directly affected the mobility of individual ErbB2 molecules in the cell membrane we initially employed single molecule tracking with quantum dots on cells expressing CD82 and ErbB2 at high and low levels – SKBR3 and MCF7. We analysed the images produced using the algorithm to detect temporary confinement of the molecules described in section 3.2.4.3.2, after validating the approach for our conditions using simulated single molecule trajectories as described in section 3.2.5.1.

We performed single molecule tracking in two colours, as described in section 3.2.5.3, however we found that there was minimal colocalisation between individual CD82 and ErbB2 molecules, and this approach would not provide dense enough molecular trajectories to map out the localisation of CD82 enriched areas on the membrane.

To overcome this we then developed a method combining super resolution optical fluctuation imaging (SOFI) with single molecule tracking, allowing us to simultaneously detect tetraspanin enriched areas with improved resolution and to track and analyse the movement of ErbB2 molecules with respect to their localisation, which is described in sections 3.3. This method allowed us to determine whether CD82 enriched areas have a direct influence on the motion of ErbB2 molecules.

3.2.5.1 Validating the method for detecting temporary lateral confinement in single molecule trajectories

In order to examine the dynamics of single molecules of ErbB2, a method to determine the motional modes contained within an individual trajectory was required. We elected to use the method first proposed by Saxton [177], which was implemented in an algorithm reported by Simson and co-workers [176], and developed further by Meilhac *et al.*[178], as described in section 3.2.4.3.2.

This algorithm was chosen as the results reveal the motional mode of the tracked molecule at every point in the trajectory, allowing the motional mode to be directly correlated to the spatial location of the molecule on the cell, which was of particular interest as in conjunction with dual colour imaging the motional mode of ErbB2 with direct correlation to its localisation with CD82 was able to be determined. The additional merits of this approach are its relative simplicity and the availability of open source code [179]. The algorithm is a well-established method to determine confinement in single molecule trajectories, and its use has been reported in recent publications [180]–[183].

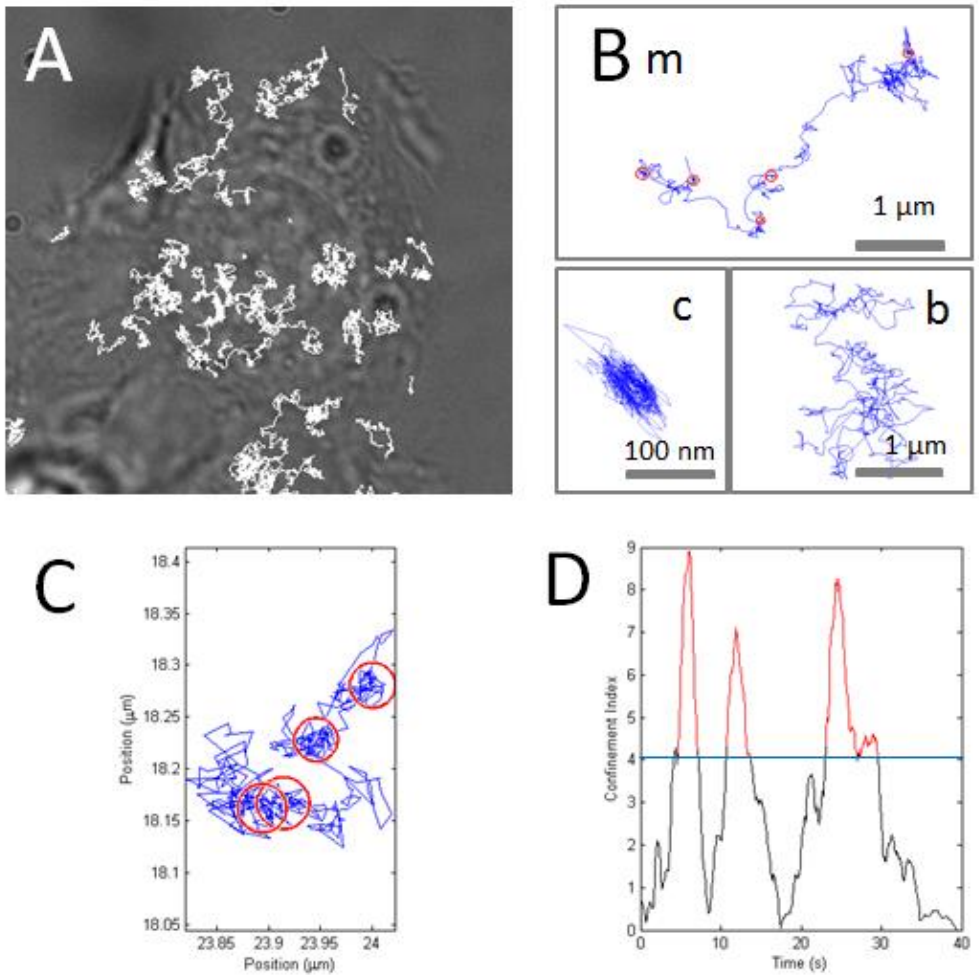

Figure 3-6: Classification of experimental single molecule trajectories by calculation of the confinement index over the trajectory.
A) Example Section of a bright field image, with single molecule trajectories overlaid. B) Example (real) trajectories exhibiting different motional modes– Mixed (m), Confined (c) and Brownian (b) - red circles around sections of the mixed trajectory indicate detection of confinement. C) Example of mixed trajectory classification for the confinement index shown in D). Red circles around areas of the trajectory indicate areas of confinement. Blue line across D indicates the threshold L_c for confinement index.

Figure 3-6 illustrates the detection of temporary lateral confinement episodes in trajectories from an exemplary SMT experiment. The trajectories illustrated in Figure 3-6 are taken from the set shown overlaid on the brightfield image of the cell in Figure 3-6 A, and represent the three different types of motion we expect to see – Brownian, completely confined, and mixed. Some directed motion may occur, however we can see from inspection of the set of trajectories in Figure 3-6 A that the majority of trajectories exhibit diffusional rather than directional motion. The confinement index shown in

Figure 3-6 D corresponds to the trajectory shown in Figure 3-6 D – the areas of the profile highlighted in red are those where the value of the confinement index is above the threshold value for confinement for a period longer than the threshold time, and therefore is classified as a confinement episode.

The calculations require a number of parameters to be set - the maximum segment length over which the confinement index is calculated, S_m; the parameter α which relates the threshold for the confinement index L_c to the average value over the trajectory by $L_c = \alpha\langle L\rangle$, the minimum value that L_c can take; and the threshold for confinement time, t_c. These parameters determine the performance of the algorithm, so we used simulations to characterise the performance of the algorithm with the certain parameters.

Trajectories were simulated with a 10Hz frame rate for consistency with the experimental data. Purely Brownian trajectories were stimulated and used to determine the false positive rate, and trajectories with an episode of confinement were generated as follows. Each simulated track was initialised with a particle at position (10,10). To determine the step size a vector of displacements was generated, by randomly selecting two numbers from a normal distribution between -1 and 1 to give the direction of the step as a magnitude of the displacement in x and y, and multiplying these values by a scaling factor $k = \sqrt{4D\tau}$ where D is the diffusion coefficient of the molecule, and τ is the sampling rate [176]. For each step in the trajectory the new position of the molecule was determined according to whether the molecule was in a confined portion of the trajectory or a Brownian part. In the Brownian segments the new position of the molecule after each step was determined by adding the displacement calculated for that step to the previous position of the molecule. In the confined segments of the trajectory the displacement was added to the previous position, and then a test was performed to see if the newly generated position would place the molecule outside the simulated confinement zone (the confinement zone was determined by

simulating a rigid walled circle with the given confinement radius, centred at the point where the confinement episode begins). If the molecule would fall outside the simulated confinement zone then a new position was calculated by reflecting the vector defined by the difference between the old and new positions of the molecule from the inside edge of the rigid walled circle, until the new position was inside the confinement zone.

The position of the confinement episode was randomly chosen to be either at the very beginning or the trajectory; at the 150th frame of the trajectory; or at the very end of the trajectory, as in experimental data it is possible that a molecule trajectory could be in any of these conditions. The diffusion coefficient was varied from 0.01-0.1 $\mu m^2/s$, which is comparable with the range observed in experimental data, while the radius and duration of the simulated confinement were varied from 50-400 nm and from 1-5 s. Each combination of confinement radius, duration and diffusion coefficient was simulated 10 times, giving 7200 trajectories overall.

First we determined the false positive rate on purely Brownian trajectories. Five hundred purely Brownian trajectories with diffusion coefficients between 0.01-0.10.1 $\mu m^2/s$ were generated, and analysed to detect apparent confinement. The false positive rate on purely Brownian trajectories was very low, with only 0.17% of the total simulated time classified as confined, using the parameters $S_m = 25$, $L_c = 4$, $t_c = 15$. This result correlates with the literature, with the developers of the open-source APM_GUI code which was utilised in this work citing a false positive rate of less than 1% in all cases tested [179].

Having determined these parameters resulted in very low false positive confinement detection in Brownian trajectories the performance of the analysis on mixed trajectories was tested. For each combination of confinement radius and duration trajectories with diffusion coefficient varied from 0.01-0.1 $\mu m^2/s$ were generated, with the position of the confinement episode at either the

beginning, middle or end of the track randomly selected, in order to validate detection performance on a similar mix of behaviours as can be observed in real experimental data.

Trajectories were created in general by sampling displacements in x and y from a random distribution and scaling by $\sqrt{4Ddt}$ to mimic Brownian motion. In each trajectory an episode of confinement was simulated, assuming confinement within a rigid walled domain of radius r for a time M led to inelastic scattering of the molecule from the domain wall. The trajectories were simulated with diffusion coefficients ranging from 0.01 to 0.1 μm2/s, with the confinement radius and time varied from 50-400 nm and 10-50 frames (1-5 s) respectively. The location of the confinement episode at either the very beginning of the trajectory, the end of the trajectory or at the 150th frame was randomly selected for each simulation. Every combination of diffusion coefficient, radius and confinement time was sampled 10 times, resulting in the generation of 7200 trajectories with confinement. A selection of these simulated trajectories are shown in Figure 3-7. These were analysed using the Saxton method with the parameters Sm = 25, Lc = 4, tc = 15. For every trajectory, the detected confinement episodes were compared to the simulated ones, to determine both the percentage of the simulated confinement episode which was correctly detected, and the percentage of the Brownian portion of the trajectory which was erroneously classified as confined.

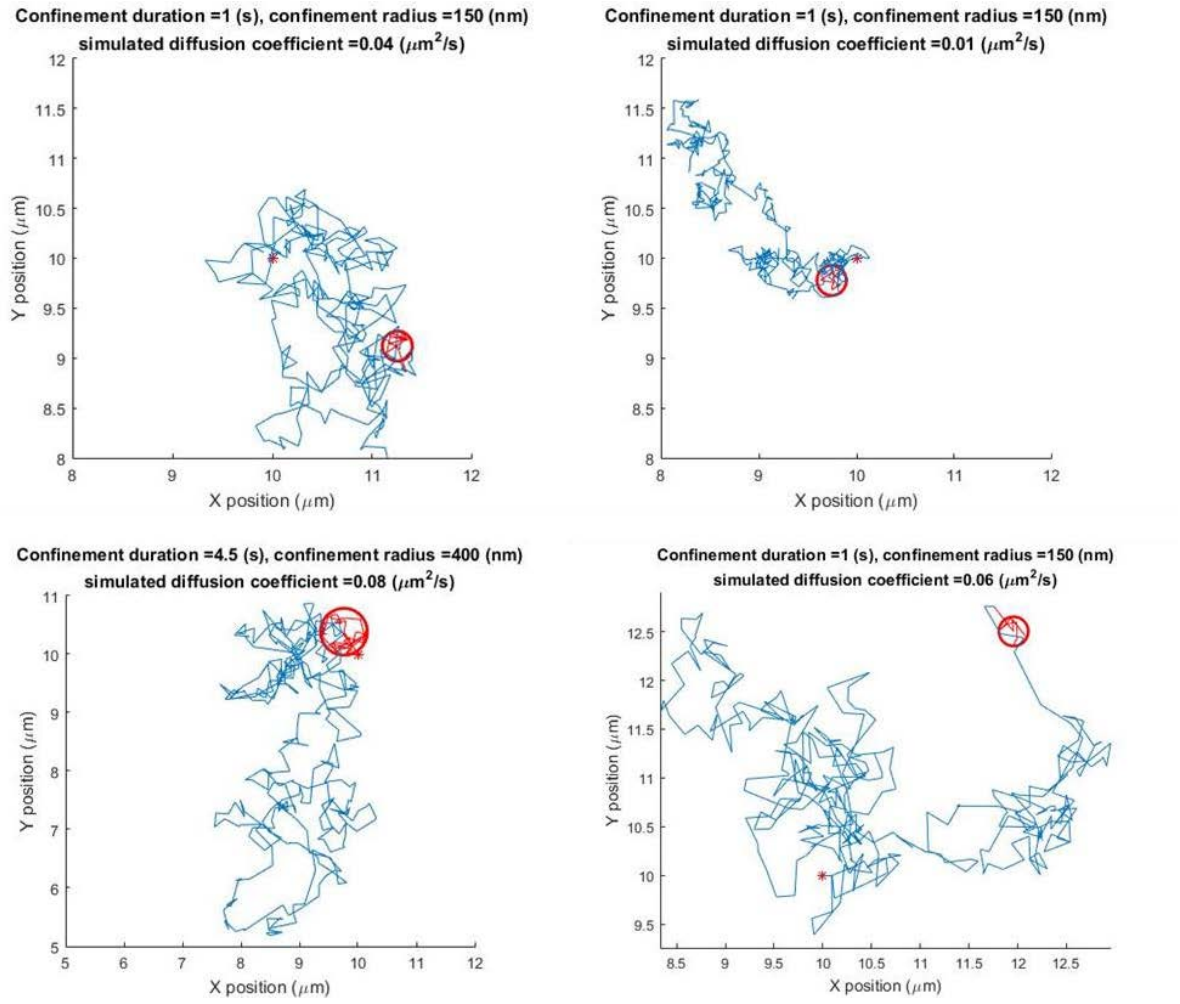

Figure 3-7: Simulated single molecule trajectories for confinement detection validation
Simulated single molecule trajectories were generated with a sampling rate of 100 ms, diffusion coefficients varied from 0.01-0.1 $\mu m^2/s$, and confinement episodes of varying duration (10-50 frames) and radius (50-400 nm) randomly simulated at either the beginning, middle or end of the trajectory. The four trajectories above are example trajectories selected from the set of 7200 trajectories simulated as described above.

Figure 3-8 shows how the algorithm performed for different combination of confinement radius and duration. It can be seen that the performance on confinement times 25 frames (2.5 s) or greater in duration is nearing 100%, so high confidence can be had in the detection of longer confinements. For shorter confinements, especially 15 to 20 frames (1.5 to 2 s) the detection power is around three quarters and a half respectively of that for longer confinement episodes, indicating that a large proportion of these shorter episodes are still detected. The detection power on shorter confinement episodes is lower because these shorter confinements results in there being generally fewer

interactions with the confining boundary, leading to less clear definition of its presence, and is seen in other implementations of the algorithm. It can also be seen that the detection power decreases for all confinement lengths with increasing confinement radius, for the same reason, with the larger radius of confinement making it less likely that collisions will occur to reveal the presence of a boundary. The conclusion of this segment of work is that there can be fairly good confidence in the detection of confinement where the radius is around 250 nm or less, and the duration of confinement is 25 frames (2.5 s) or more. Confinement zones with parameters outside of these ranges are less well detected, but still likely to be detected at least in part.

A last step in characterising the performance of the algorithm was to check the average proportion of mixed trajectories incorrectly classified as confined where the simulated motion was Brownian. In the dataset used to generate the results in Figure 3-8 only 1.6% of the trajectory on average was incorrectly classified. Given the low false positive rate in purely Brownian trajectories it is likely that this slight increase in false positives relative to the result for the purely Brownian trajectories can be explained by the incorrect classification of frames either side of the simulated confinement zone.

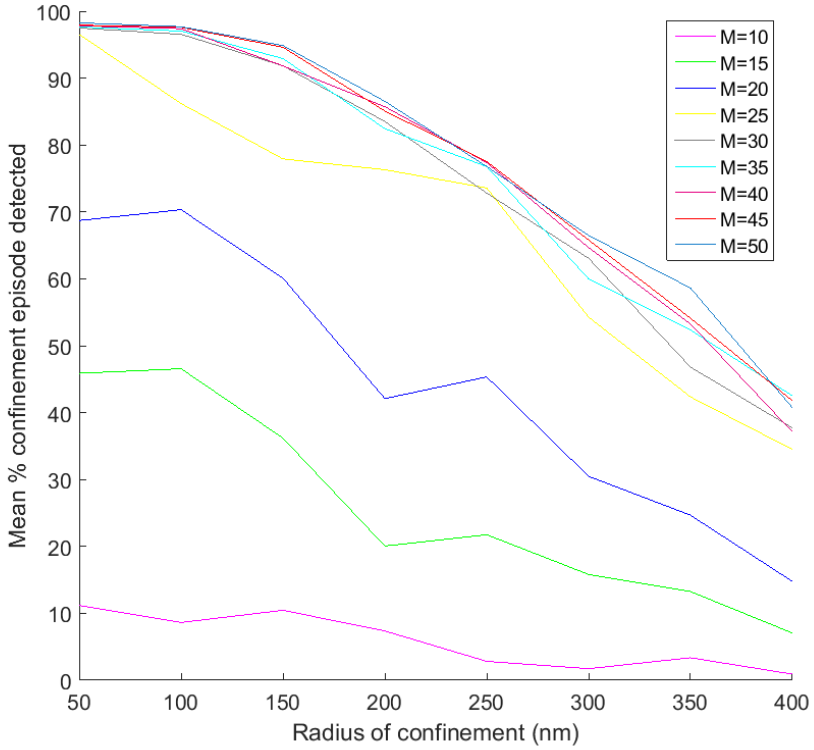

Figure 3-8: Quantification of confinement detection performance on trajectories with simulated episodes of confinement

Simulated trajectories were used to validate the performance of the confinement detection algorithm. Simulated single molecule trajectories were generated with a sampling rate of 100 ms, diffusion coefficients varied from 0.01-0.1 $\mu m^2/s$, and confinement episodes of varying duration (M = 10-50 frames) and radius (50-400 nm) randomly simulated at either the beginning, middle or end of the trajectory. Episodes of confinement detected using the Saxton method with the parameters Sm = 25, Lc = 4, tc = 15 were compared with the simulated confinement episode, and the proportion of the confinement episode correctly detected was calculated. For each combination of confinement duration and radius, the mean percentage of a confinement episode with those parameters correctly detected by this method was calculated, and is shown here. 10 trajectories were simulated for each combination of confinement radius, duration and diffusion coefficient and pooled for analysis. Each point of the series therefore represents the mean % confinement detected over 100 simulated trajectories.

3.2.5.2 Diffusion and confinement of ErbB2 in SKBR3 and MCF7 cell membranes

We used the validated Saxton method to analyse the motion of ErbB2 in both SKBR3 and MCF7 cell membranes, which express high and low levels of ErbB2 respectively. In each cell line we examined the effect of CD82 over-expression on overall ErbB2 mobility and confinement.

We elected to use biotinylated Fab fragments for labelling ErbB2 in order to minimise the size of the fluorophore-label complex and minimally disrupt the native conditions. The precise concentration of antibody to use was validated by imaging in order to have a sparsity of signal that would allow tracking to be carried out. In contrast to the approach for dSTORM where saturating the binding sites is desirable, in order to produce the most detailed picture of protein distribution possible, for SMT a much lower density of labelling is required, so that individual molecular trajectories can be observed.

Figure 3-9 shows the distribution of diffusion coefficients and the characteristic confinement episodes identified in trajectories of ErbB2 molecules in SKBR3 cells. These results and other quantification are also presented in Table 3-1. The corresponding data for MCF7 cells is presented in Figure 3-10 and Table 3-2.

We can see from Figure 3-9 A that over-expression of CD82 does not have a significant effect on the distribution of ErbB2 diffusion coefficients in SKBR3 cells, or on the characteristics of ErbB2 confinement episodes, which are of similar duration and size in both the control and CD82 over-expressing condition. Comparing this data to that in Figure 3-10 it is interesting to note that the distribution of diffusion coefficients in MCF7 cells, which express low levels of ErbB2, appears to be wider, and shifted towards higher values relative to the diffusion coefficients observed in SKBR3. It is possible that this the lower levels of ErbB2 expression in MCF7 cells lead to a lower frequency of ErbB2 complex formation, through either homo or heterodimerisation, and therefore a higher diffusion coefficient for the ErbB2 molecules not involved in interactions, resulting in the shift towards higher diffusion coefficients seen in the distribution.

It is also interesting that in MCF7 cells, although over-expression of CD82 or CD82cys5 does not significantly affect the mean diffusion coefficient when all trajectories are averaged, when only those trajectories displaying purely Brownian motion are averaged, over-expression of CD82 causes

a statistically significant increase in the diffusion coefficient of these ErbB2 trajectories. The reason for this difference is unclear.

Overall, over-expression of CD82 does not seem to have a significant effect on the diffusion coefficient or confinement characteristics of ErbB2, in either SKBR3 or MCF7 cells. When those trajectories only exhibiting Brownian motion are compared between the CD82 overexpressing and control condition, there is a slight but not significant increase in diffusion coefficient in SKBR3 cells, and a statistically significant increase in diffusion coefficient in MCF7 cells. This difference will require further investigation to explain, but one possible explanation could be that CD82 over-expression negatively mediates some interactions with ErbB2, such that smaller complexes of ErbB2 are, in general, found in cells over-expressing CD82, and therefore diffuse faster.

We examined the properties of ErbB2 trajectories visually, and inspected the corresponding values of confinement index for the same dataset, mapped over the spatial extent of the image, as shown in Figure 3-11. From the top plot of Figure 3-11 we can see that the majority the tracked motion is Brownian (black and blue segments), with occasional entry into transient confinement zones (red). We chose to inspect the average level of the confinement index over the whole cell, to see whether any interesting features emerged in areas with high or low average confinement index, as shown in the bottom image of Figure 3-11. From this image we can see that across most of the cell the confinement index is low, with small areas where the mean confinement index peaks. There are no obvious features evident in the distribution of these areas, however in future work it could be interesting to label other proteins of interest on the membrane to produce images which could be analysed for colocalisation with maps of confinement index.

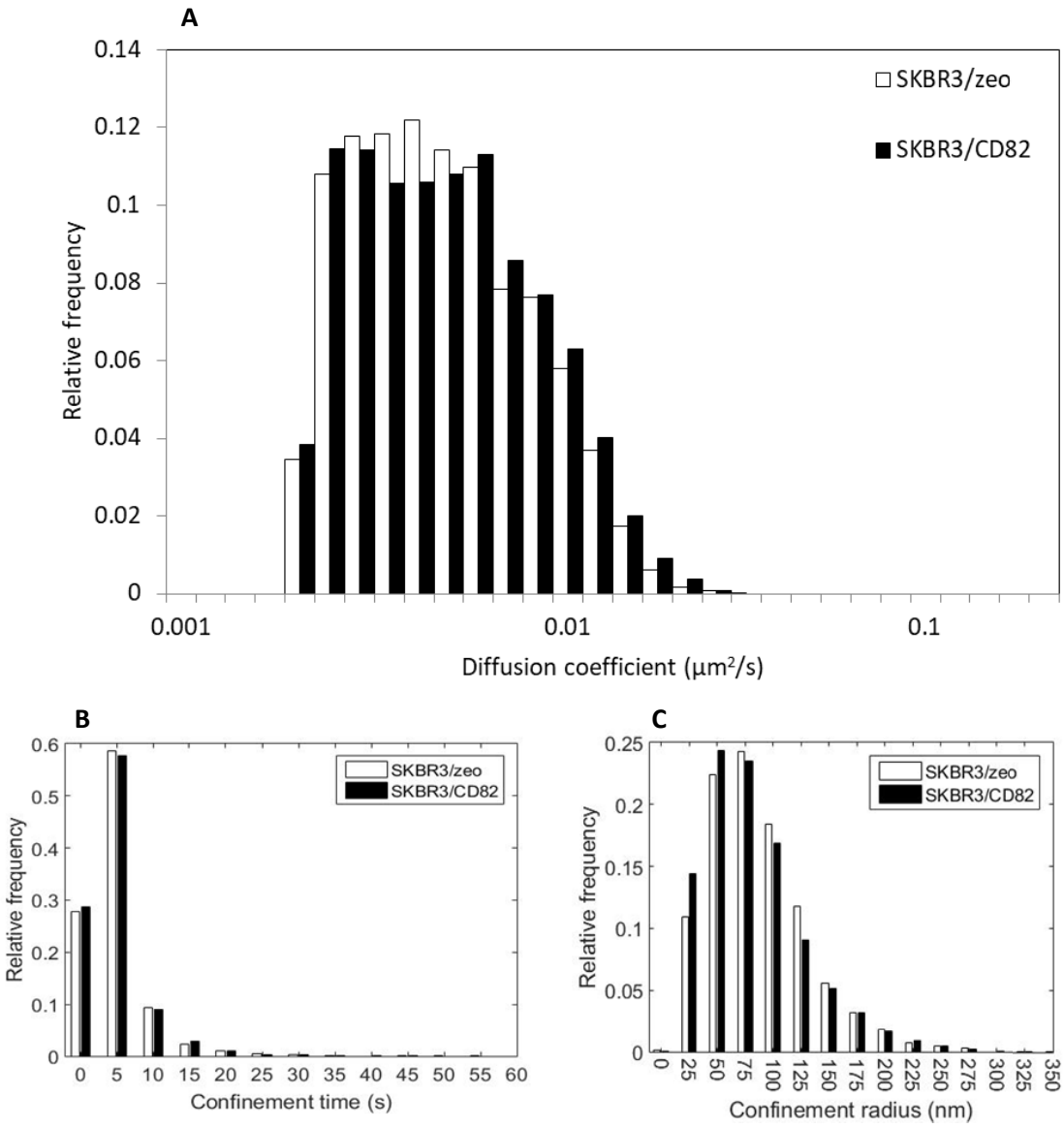

Figure 3-9: Diffusion and confinement characteristics of ErbB2 in SKBR3 cell membranes
ErbB2 labelled with 6 nM biotinylated Herceptin-Fab fragment and 1nM streptavidin-conjugated QD-625 was imaged using TIRF microscopy on the basal membrane of SKBR3 cells. Single molecule trajectories were constructed for individual ErbB2 molecules and analysed to determine the diffusion coefficient of each tracked molecule and identify episodes of confinement. Confinement was detected and parameterised using the Saxton method detailed elsewhere in this chapter A) Distribution of diffusion coefficients, calculated from a linear fit to the 2^{nd}-4^{th} points of the mean square displacement versus time curve, in the tracked ErbB2 population; B) Distribution of radius of confinement zones detected in the trajectories of the tracked ErbB2 molecules; C) Distribution of duration of confinement episodes (confinement time) detected in the ErbB2 trajectories. Number of tracks analysed: SKBR2/zeo = 3959, SKBR3/CD82 = 3274.

Table 3-1 Diffusion and confinement of ErbB2 in SKBR3 cells

Cell line	Mean diffusion coefficient ± s.d. (All tracks)	Mean diffusion coefficient ± s.d. (Brownian tracks)	Proportion of tracks with purely Brownian motion (%)	Proportion of tracks with mixed motion (%)	Proportion of totally tracks confined (%)	Mean confinement time (s)	Mean confinement radius (nm)
SKBR3/zeo	0.0104± 0.0083	0.0131 ± 0.0118	19.80	78.48	1.72	4.75± 4.02	86.7± 45
SKBR3/CD82	0.0109± 0.0089	0.0141 ± 0.0121	20.73	77.15	2.11	4.72± 3.84	82.6± 46

Table 3-2 Diffusion and confinement of ErbB2 in MCF7 cells

Cell line	Mean diffusion coefficient ± s.d. (All tracks)	Mean diffusion coefficient ± s.d. (Brownian tracks)	Proportion of tracks with purely Brownian motion (%)	Proportion of tracks with mixed motion (%)	Proportion totally confined (%)	Mean confinement time (s)	Mean confinement radius (nm)
MCF7/puro	0.029 ± 0.023	0.038 ± 0.025	49.79	49.96	0.25	4.08 ± 3.87	117 ± 61.7
MCF7/CD82wt	0.034 ± 0.031	0.051 ± 0.034*	43.43	55.41	1.16	4.54 ± 4.60	104 ± 79.6
MCF7/CD82cys5	0.027 ± 0.024*	0.037 ± 0.027	47.91	50.87	1.21	4.38 ± 4.06	103 ± 64.4

(*$p < 0.05$ determined by Wilcoxon rank sum test)

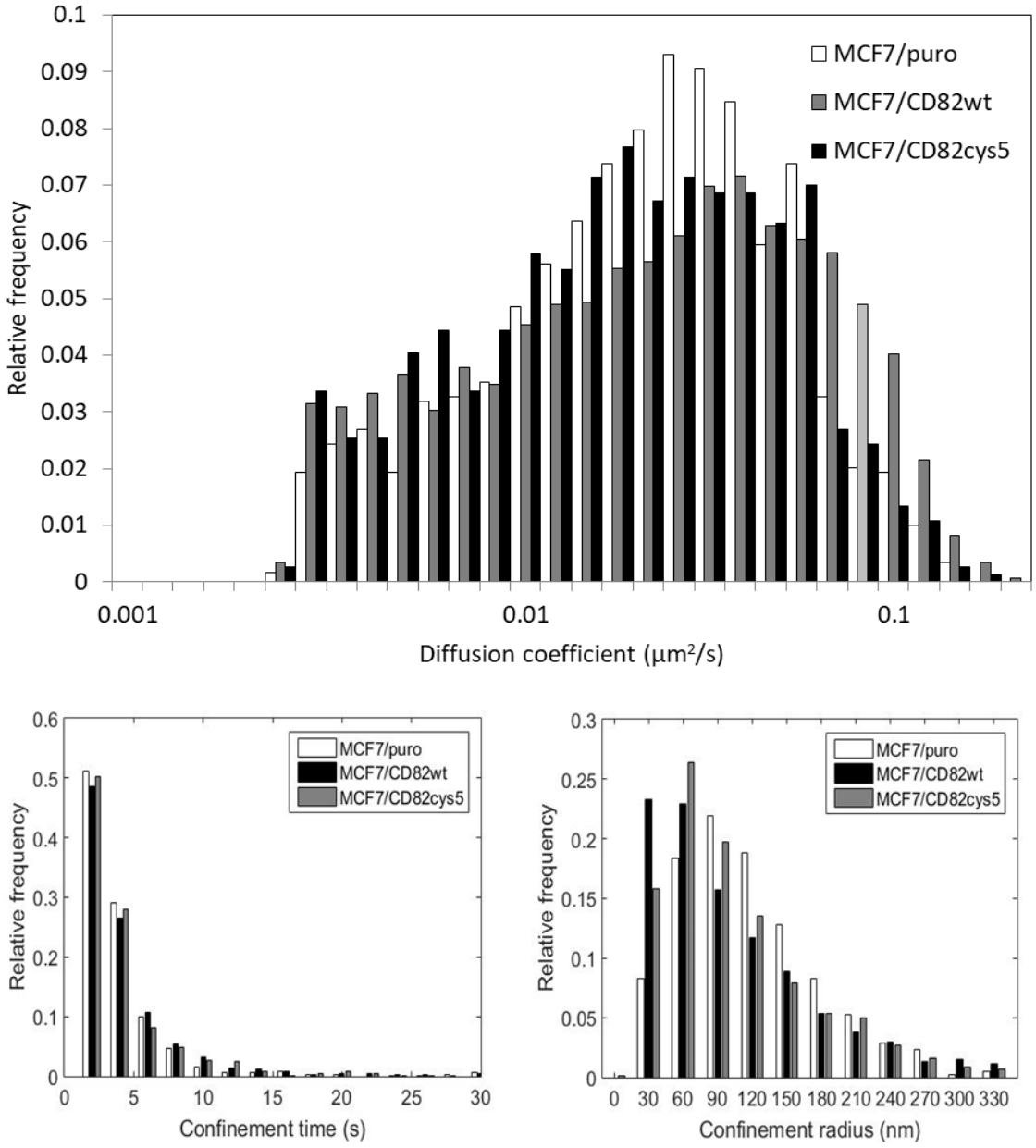

Figure 3-10: Diffusion and confinement of ErbB2 in MCF7 cell membranes
ErbB2 labelled with 6 nM biotinylated Herceptin-Fab fragment and 1nM streptavidin-conjugated QD-625 was imaged using TIRF microscopy on the basal membrane of MCF7 cells. Single molecule trajectories were constructed for individual ErbB2 molecules and analysed to determine the diffusion coefficient of each tracked molecule and identify episodes of confinement. Confinement was detected and parameterised using the Saxton method detailed elsewhere in this chapter A) Distribution of diffusion coefficients, calculated from a linear fit to the 2nd-4th points of the mean square displacement versus time curve, in the tracked ErbB2 population; B) Distribution of radius of confinement zones detected in the trajectories of the tracked ErbB2 molecules; C) Distribution of duration of confinement episodes (confinement time) detected in the ErbB2 trajectories. Number of tracks analysed: MCF7/puro = 1193, MCF7/CD82wt = 1720, MCF7/CD82cys5 = 743.

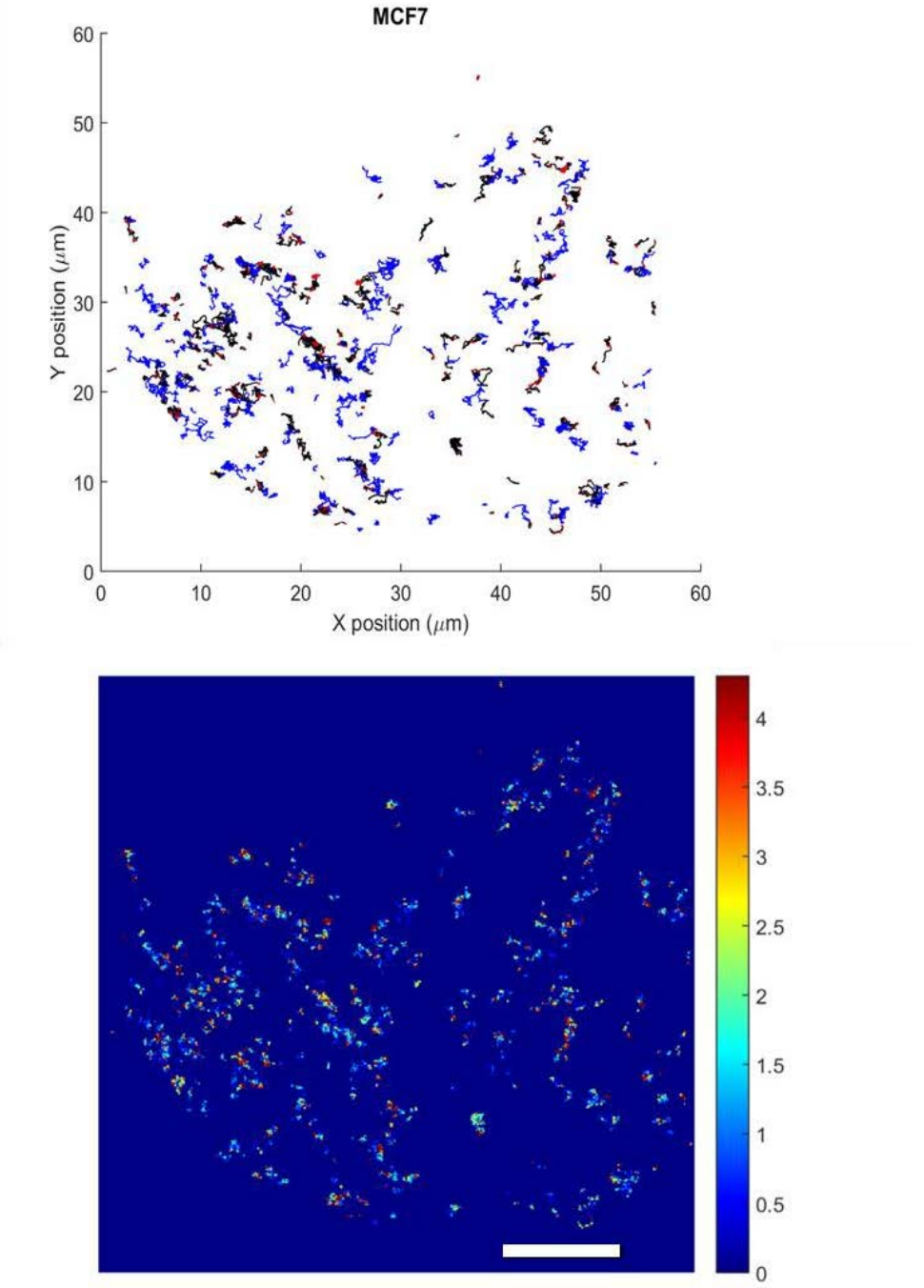

Figure 3-11: ErbB2 trajectories on MCF7 cell membrane and corresponding image of mean confinement index

ErbB2 molecules were tracked on the surface of MCF7/puro cells as described above, and analysed to detect confinement episodes in the trajectories. Top) All trajectories which met the threshold for mobility (minimum diffusion coefficient of 0.0027 $\mu m^2/s$ across the trajectory) were plotted – trajectories exhibiting purely Brownian motion are plotted in blue, Brownian portions of the trajectories exhibiting confinement in black, and confined portions in red. Bottom) An image representing the mean confinement index of all trajectories crossing each pixel was calculated, by dividing the sum of the confinement index of each trajectory in each frame in which the trajectory

was in a particular pixel for all trajectories, by the number of frames in which a trajectory was in a the pixel. Colormap set to scale between 0 and 4.3 (the minimum threshold for the confinement index for confinement detection). Scale bar 10 µm.

In order to see whether these areas of high confinement index could be correlated with the localisation of CD82 at all, we next investigated approaches which allowed us to directly study the effect of the localisation of ErbB2 with respect to CD82 on its diffusion, by imaging in dual colour.

3.2.5.3 Dual colour single molecule tracking of ErbB2 and CD82

We performed single molecule tracking in dual colour on the membrane of SKBR3 and MCF7 cells in order to look for colocalisation and co-confinement in ErbB2 and CD82 trajectories. The trajectories from the two channels were registered using a 2nd degree polynomial transformation calculated from an image of Tetraspeck beads, which appear brightly in both the red and green channel. The mean error in registration achieved with this transformation was 10.6 ± 19 nm.

We considered that areas in which CD82 exhibited confinement could represent CD82 enriched areas or TERMs, and so decided to attempt to identify areas of ErbB2 and CD82 co-confinement in the data to determine if ErbB2 undergoes interactions in CD82 enriched areas.

Images of the mean confinement index across each channel were calculated as for the single colour data presented in the previous section, as shown in the top row of Figure 3-12, and merged to produce the lower left image. In the merged image any pixels in which signal is contributed from both channels will appear yellow – as we can see from the figure there is no such colocalisation apparent. In order to highlight any spatial relationship between CD82 and ErbB2 confinement we produced a binary image in which pixels in which ErbB2 trajectories exhibited confinement are plotted in green, and the pixels in which CD82 trajectories exhibited confinement are plotted in red, with the same intensity irrespective of the number of trajectories/frames in which confinement occurred. From this lower right image of Figure 3-12 we can see that in this cell there was no colocalisation between confinement episodes of ErbB2 and CD82. Since the mean error in the

colocalisation is significantly less than the pixel size, detection of colocalisation in the merged image should not be significantly affected by errors in localisation.

The data set shown in Figure 3-12 was representative of the results observed on other cells, and evidences why we decided to develop an alternative approach for dual colour studies. It was not clear from the dual colour single molecule tracking whether the lack of colocalisation was due to the density of trajectories not being high enough to map out a significant area of the cell membrane, or whether ErbB2 and CD82 trajectories do not occupy or pass through the same areas of the cell membrane. It was not possible to simply increase the concentration of the label in order to obtain a more dense picture of the motion of the proteins, since too high a density of quantum dots complicates the tracking procedure, and is particularly likely to introduce errors and result in spurious links between particles due to the blinking of QDs.

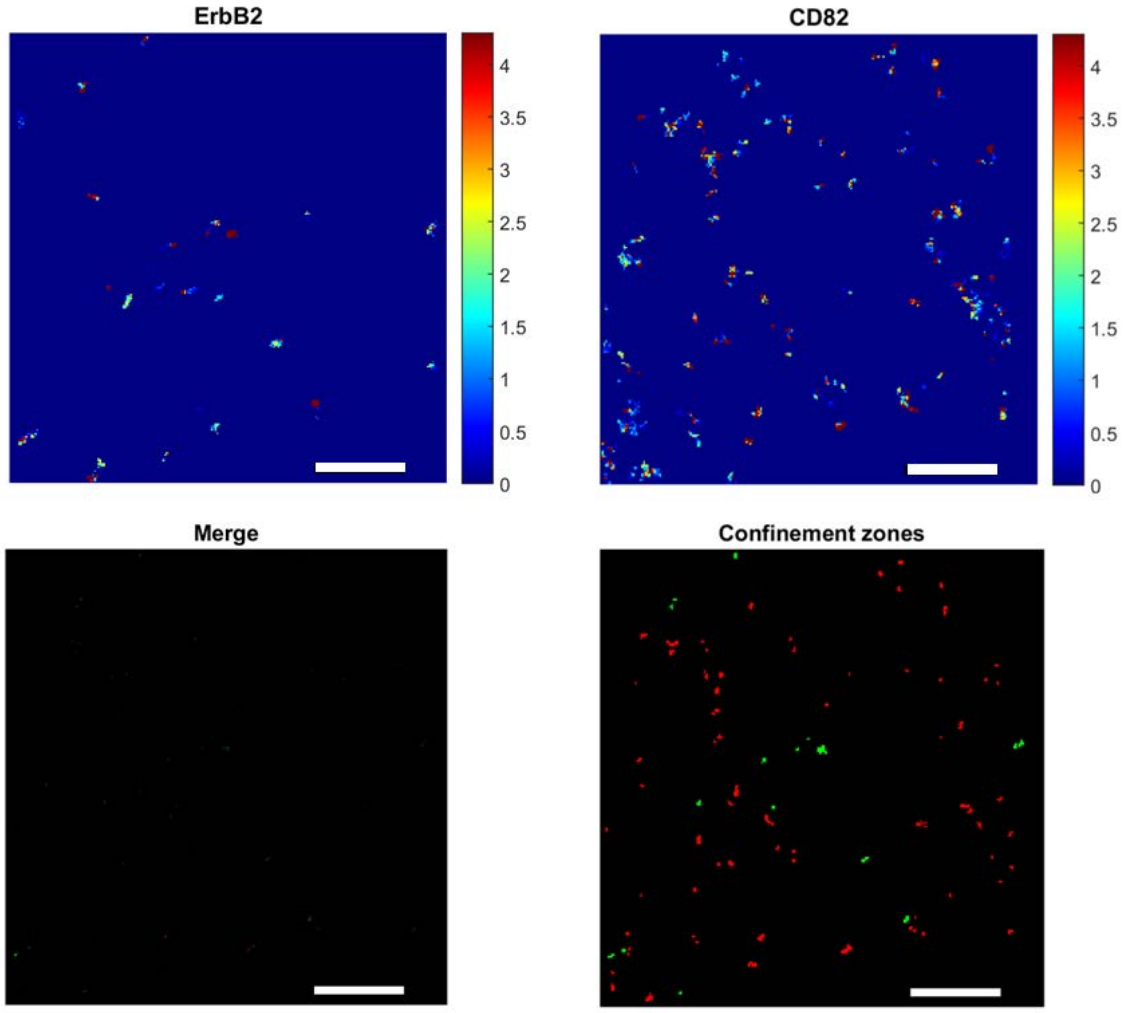

Figure 3-12: Single molecule ErbB2 and CD82 trajectories do not show co-confinement on SKBR3 cell membranes

ErbB2 and CD82 were labelled on SKBR3 cell membranes using (pre-mixed or two step labelling) concentration and imaged using TIRF.

Top row) An image representing the mean confinement index of all trajectories crossing each pixel was calculated for each imaging channel, representing ErbB2 and CD82 trajectories.

Bottom right) A merged image of the mean confinement index images for ErbB2 and CD82 was produced, in which areas where the signal contributed from each channel is different appear in green for ErbB2 contributed signal and magenta for CD82 contributed signal, and would appear yellow in areas of overlapping singal. Bottom left) Since there was no colocalisation of high confinement index areas visible in the merged image a binary plot was produced to better illustrate the relative localisation of the confinement zones detected in the ErbB2 and CD82 trajectories. In this image, pixels in which ErbB2 exhibited confinement, as determined by a confinement level above the threshold for at least the threshold time, are plotted in green and those in which CD82 exhibited confinement are plotted in red. Scale bar 5 µm.

3.2.6 Conclusion

SPT in single colour did not reveal significant differences in ErbB2 diffusion or confinement between control and CD82 over-expressing conditions in the bulk ErbB2 population. Attempts to perform dual colour single molecule tracking to look specifically for interactions between ErbB2 and CD82 were not successful since it was not possible to obtain dense enough trajectories to observe colocalisation. As a result, we identified that a different imaging approach was required to answer the question of what effect CD82 expression has on ErbB2 diffusion – one which would provide a picture of CD82 distribution and allow us to identify enriched areas/TERMs, and correlate the motion of single ErbB2 molecules with this information.

3.3 Super Resolution Optical Fluctuation Imaging

Following on from the dual colour single molecule tracking which did not reveal any colocalisation of ErbB2 confinement we elected to use a technique which would reveal the distribution of CD82 across the membrane, and allow us to study the colocalisation of ErbB2 trajectories with any enriched areas.

In order to achieve greater resolution than is possible using standard ensemble labelling and microscopy, we elected to combine the super-resolution technique super-resolution optical fluctuation imaging (SOFI).

SOFI makes use of the random temporal signal fluctuations of single emitters, and uses the spatio-temporal information contained in movies of a sample where many emitters are exhibiting this intermittent fluorescent signal to produce reconstructed images with higher resolution than the original movie [184]. In contrast to the requirements of dSTORM and other photoswitching methods, many emitters can be ‘on’ in a diffraction limited volume, at the same time, in a movie for SOFI and still contribute to enhanced resolution. Also, SOFI makes use of the inherent fluorescent

intermittency of the emitters, and does not require special imaging buffers, making it more suitable for live-cell imaging than some of the other super-resolution techniques.

The SOFI procedure consists of taking a movie of the fluctuating signal, and then calculating the n^{th} order cumulant for each pixel. By plotting the value of the n^{th} order cumulant, an image with a resolution enhancement of $\sqrt{n}$ over the original image can be produced. A more detailed explanation of the maths underlying the resolution improvement can be found in [185]. SOFI has been demonstrated with blinking quantum dots, organic dyes, and fluorescent proteins [184]–[186]

SOFi has the advantages of being a super-resolution technique, whilst also being simple to implement on a standard microscope with conventional fluorophores.

3.3.1 Mapping the distribution of CD82 on the plasma membrane with SOFI

To examine the colocalisation of ErbB2 confinement with areas of CD82 we utilised super-resolution optical fluctuation imaging (SOFI) to produce super-resolved images of CD82 distribution obtained simultaneously with ErbB2 tracking.

An example of a representative SOFI image of CD82 distribution, in comparison with a dSTORM reconstruction of CD82 on the same cell type is shown in Figure 3-13, along with an average image produced from the same set of images as the SOFI reconstruction, to show the improvement in resolution compared to the original diffraction limited image.

The SOFI image in Figure 3-13 clearly shows greater contrast between the CD82 enriched areas and the rest of the cell, and finer detail is resolvable. The STORM image has the highest resolution, with the SOFI image clearly not approaching the same level of detail; however we can see that the scale of the CD82 enriched spots in the SOFI image of around 1μm corresponds with the size of groups of CD82 clusters in the STORM image.

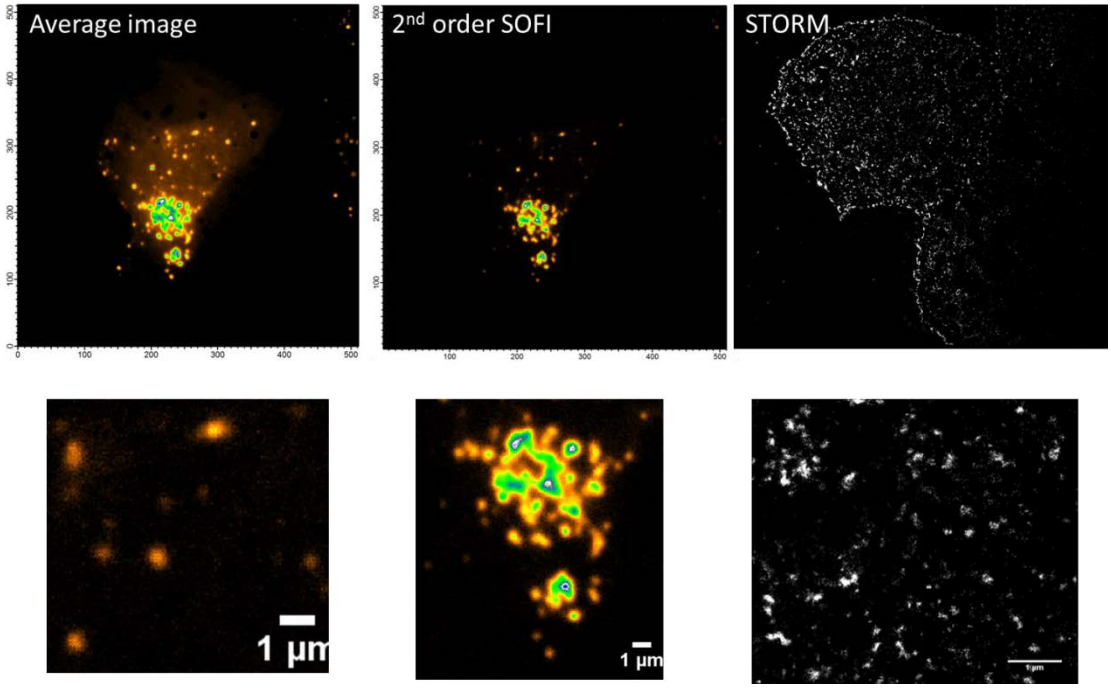

Figure 3-13: Comparison of resolution of an average intensity image of CD82, a 2nd order SOFI reconstruction of the same image, and a STORM image of Alexa-647 labelled CD82 on SKBR3 cells. MCF7 cells labelled with anti-CD82 antibody and Alexa-488 and imaged using TIRF microscopy. The Localizer package in IGOR Pro was used to produce an average intensity image (top leftmost image), and a 2nd order SOFI reconstruction (bottom leftmost, and middle images), for comparison with the reconstructed STORM image (rightmost images). The SOFI image does not have the pointillistic nature of the STORM image due to the different methods by which the images are formed, but does show detail of CD82 distribution on a larger scale. Scale bars 1µm.

In order to segment the areas of the SOFI image showing high signal from CD82 for colocalisation analysis with single molecule ErbB2 trajectories we needed a method which would allow us to delineate these high signal areas and create a binary map for use in colocalisation analysis. We elected to use Otsu's method to perform the segmentation.

Otsu's method is a method of automatic threshold selection for image segmentation, based on minimising the intra-class variance of the segmented pixels [187]. It should therefore enable us to detect and segment areas of high and low-no CD82 signal respectively.

To implement segmentation of the SOFI image we used the MATLAB graythresh function, which uses of Otsu's method, to calculate the threshold for segmentation, followed by the imbinarize function

using the threshold value produced by graythresh to produce the maps as shown below in Figure 3-14.

Figure 3-14 shows an example of a reconstructed SOFI image of CD82 distribution, and the segmentation achieved using single level, two-level and three-level thresholding with Otsu's method. We examined the level of detail and structures visible at each level of segmentation and determined that binarisation with just the single-level Otsu thresholding resulted in a binary map which most closely resembled that which the skilled person would manually produce from the same image. Figure 3-15 shows in greater detail the edges of the areas which are detected by the Otsu thresholding process described above.

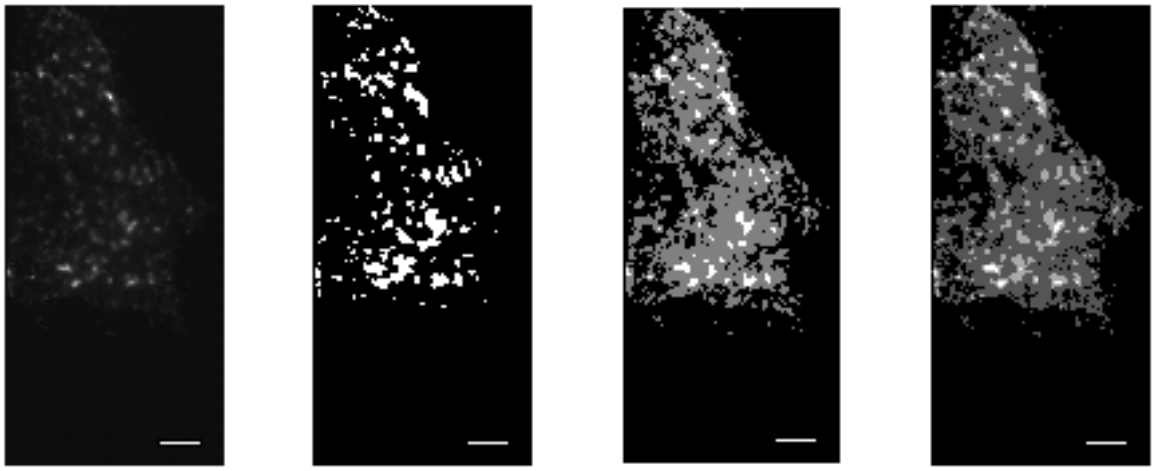

Figure 3-14: Multi-level Otsu thresholding segments areas of enriched CD82 signal in SOFI reconstructions
The distribution of Alexa-488 labelled CD82 on SKBR3/CD82 cells was imaged in TIRF microscopy and processed to produce SOFI reconstructions. Otsu's method was tested as an approach to segment CD82 enriched areas. L-R: Raw SOFI image, thresholding using Otsu's method, 2-level thresholding with Otsu's method, 3-level thresholding with Otsu's method. Different shades of grey indicate segmentation. Scale bar 5 μm

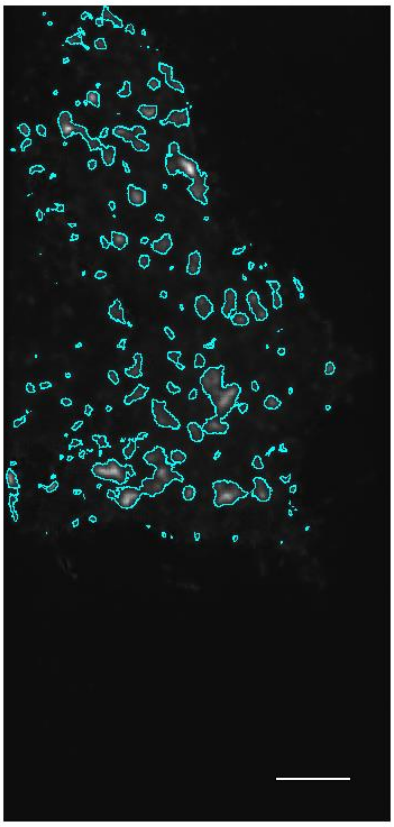

Figure 3-15: Single level Otsu thresholding delineates boundaries of CD82 enriched areas in SOFI reconstructions
A SOFI reconstruction of Alexa-488 labelled CD82 in SKBR3 CD82 cells was processed by single level Otsu thresholding. Scale bar 5 µm. Boundaries determined by finding the edges from the binarised SOFI image after single level Otsu thresholding plotted (cyan lines) over the SOFI image. These boundaries define the areas in which an ErbB2 trajectory would be considered colocalised with CD82.

3.3.2 Combination of SMT and SOFI

In order to determine if colocalisation of ErbB2 with the CD82 enriched areas visible in the SOFI reconstruction affected the motion of ErbB2, for example mediating confinement of the receptor, we used channel registration to overlay the ErbB2 trajectories determined from quantum dot tracking with the SOFI reconstruction.

Using the combination of SOFI to produce super-resolution images of CD82 distribution and segment CD82 enriched areas in combination with single molecule tracking of ErbB2 we were able to compare the properties of ErbB2 trajectories during periods of colocalisation with CD82 with non-colocalised periods. Figure 3-16 shows several cells imaged and analysed using this combination of

techniques. It is possible to see from the data presented here how trajectories classified as colocalised or not colocalised can be examined in more detail and reveal possible interactions or exclusion of ErbB2 with/from CD82 enriched areas. Table 3-4 summarises the results of confinement and colocalisation analysis on the data collected. In SKBR3/CD82 cells we detected that the diffusion coefficient of ErbB2 is significantly higher when colocalised with CD82, and the radius of colocalised confinement episodes is also larger than non-colocalised episodes. Interestingly this seems to imply that ErbB2 colocalised with CD82 has a slightly higher mobility than non-colocalised ErbB2. One possible explanation for this could be that CD82 plays a role in negatively mediating ErbB2 interactions, and therefore colocalised molecules are less likely to be involved in large complex forming interactions which would cause them to diffuse more slowly. This would also be consistent with the results found from single colour ErbB2 tracking.

The numbers of trajectories it is possible to obtain from a single image is smaller using this technique than in the conventional single molecule tracking described above, since the dual view results in the field of view being halved, and imaging must be performed over a relatively short space of time to minimise the potential for drift-related artefacts in the SOFI reconstruction. This is a slight drawback to the technique since more imaging will be required to have comparably large datasets to those achievable with conventional single molecule tracking, however is offset by the increase in information it is possible to gain, and may even be removed in future by performing the imaging on a microscope which is highly temperature stable or equipped with a stage position correction/PFS system.

The number of cells we were able to image at the end of this study was limited by the lack of a functioning perfect focus system (PFS) on the Olympus microscope, meaning that small temperature shifts caused by the functioning of the incubator caused movement in the images over the 1-2 minute time-scale of acquisition. It was not possible to use the Nikon A1R which had a PFS as this

microscope lacked the capability for simultaneous or rapidly switching dual colour imaging. Future work would need to be performed on equipment with both PFS and the capability to perform simultaneous dual colour acquisition. This was not so critical for pure tracking experiments since drift correction could be applied to the trajectories by subtracting the mean displacement between frames of immobile quantum dots (some of which adhere to the glass coverslip) from the trajectory coordinates.

3.3.1 Conclusion

The combination of SOFI and SMT represents a possible new imaging approach for studying the interaction of single molecule trajectories with areas enriched in certain proteins, such as TERMs. In microscopes equipped for multi-colour imaging (i.e. having an appropriate beam splitter or rapid channel switching capability) it may be possible to use this new combination of techniques to examine the colocalisation/distribution of two or more species in combination with the single molecule dynamics of one or two other proteins/molecules. Such a combination would make possible direct observation of the effect of coconfinement or coclocalisation with TERMs and other membrane microdomains or protein enriched areas on the molecular dynamics of proteins in the cell membrane. Particularly in studies such as this one where it is not possible to obtain sufficient single molecule trajectories at a sufficient density or over a long enough time to employ cartographic approach to visualise protein distribution, SOFI offers improved resolution over conventional microscopy approaches for visualising protein distribution along with the specificity of single molecule tracking.

In future, more work could be done to examine the characteristics of the segmented areas of the SOFI picture of protein distribution, to check that the size and morphology of the enriched areas identified with this technique tally with those identified by other super-resolution microscopy approaches.

Work is also being done on quantifying protein densities on cell membranes using SOFI [188], and on the effect of probe diffusion on SOFI imaging accuracy [189]. There are thus many potential avenues down which this combination of techniques could be pursued and developed in future studies.

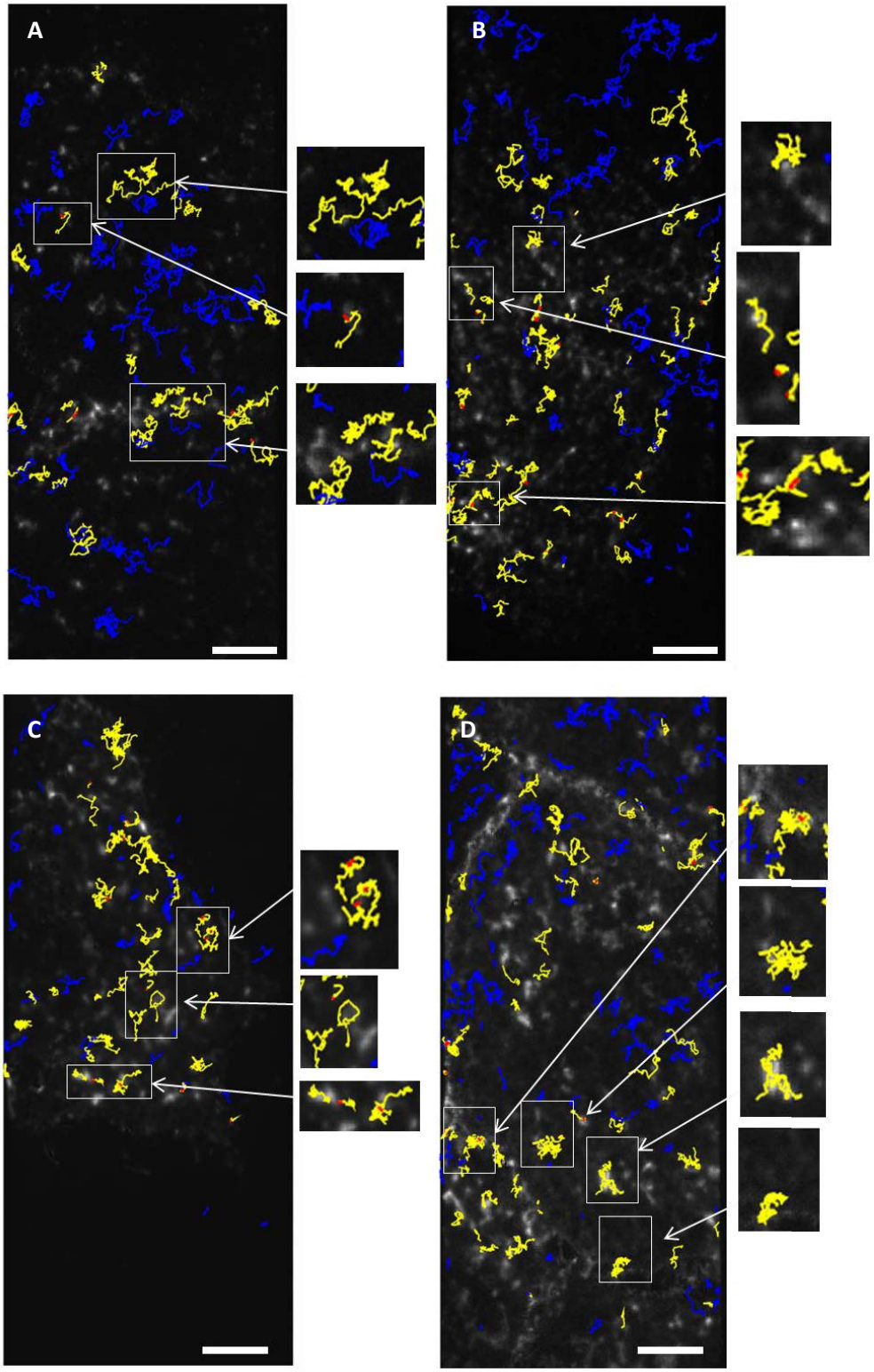

Figure 3-16: ErbB2 trajectories overlaid on SOFI reconstructions of CD82 distribution in SKBR3 cells A & B – SKBR3/zeo; C & D – SKBR3/CD82.
Trajectories colour-coded according to motional mode and colocalisation. Blue trajectories represent Brownian motion, yellow trajectories cross CD82 enriched areas, and red segments indicate confinement episodes. Scale bar 5 µm.

Table 3-3 Incidence of colocalisation with CD82 in ErbB2 trajectories

	% of ErbB2 trajectories colocalised with CD82	Mean % of ErbB2 trajectory colocalised with CD82 *for trajectories with colocalisation
SKBR3/zeo	46.05	58.95±58.85
SKBR3/CD82	39.23	52.92±42.33

Table 3-4 Properties of ErbB2 confinement relative to colocalisation with CD82

	% of confinement episodes colocalised with CD82	Mean % of confinement episode colocalised[+] ±s.d	Mean radius of colocalised confinements ±s.d. (nm)	Mean radius non-colocalised confinements ±s.d. (nm)	Mean duration of colocalised confinement episodes ±s.d. (s)	Mean duration of non colocalised confinement episodes ±s.d. (s)	Mean diffusion coefficient while colocalised ±s.d. ($\mu m^2/s$)	Mean diffusion coefficient while not colocalised ±s.d. ($\mu m^2/s$)
SKBR3/zeo	21.49	22.24±59.83	142±73	145±95	4.67±5.14	3.67±2.43	0.0038±0.031	0.0411±0.027
SKBR3/CD82	13.54	12.60±46.34	148±46	106±72*	3.77±2.86	4.10±3.33	0.0458±0.0360	0.0362±0.0262*

[+]of those confinement episodes which colocalise

*$p<0.05$ determined by Wilcoxon rank sum test

Number of confinement episodes analysed in SKBR3/zeo = 288, SKBR3/CD82 = 192. Number of trajectories analysed in SKBR3/zeo = 430, SKBR3/CD82 = 339.

Chapter 4 – Imaging of static protein distribution in the plasma membrane by super-resolution fluorescence microscopy

4.1 Chapter overview

The aim of the work presented in this chapter was to determine the effect of CD82 expression on the distribution and cluster properties of ErbB2 in the plasma membrane. To achieve this, a secondary aim of determining the optimum methods to perform imaging and analysis in order to extract quantitative cluster properties from single molecule localisation microscopy (SMLM) images, in particular dual colour images, was required. To further characterise the effect of CD82 expression on ErbB2 distribution the final aim was to employ the chosen SMLM analysis techniques to investigate the effect of pre-incubation with a panel of molecules targeting ErbB family members (EGF, Herceptin and heregulin) on ErbB2 cluster properties, and determine whether CD82 expression alters clustering of ErbB2 in response to these treatments.

SMLM was chosen as the technique to study ErbB2 distribution at the molecular level over alternatives such as electron microscopy (EM), since the resolution which can be achieved with SMLM approaches that of EM, but with more flexibility in the labelling approach that can be applied; and as SMLM is still a relatively new technique, there is a need to conduct studies into the optimal ways in which to process and analyse the images and data to provide an answer to the biological problem at hand.

4.2 Introduction to super-resolution microscopy

The development of super-resolution microscopy techniques has brought in a new era of capabilities in biological imaging, at resolutions previously thought unachievable. Imaging below the diffraction

limit of light is now possible via a multitude of techniques, and has already yielded new information on the nanoscale organisation of cells. More recent developments are beginning to yield the ability to image in super-resolution at higher speed and in live cells, allowing the observation of fast biological processes and dynamic reorganisation. These advances are providing the capability to analyse the organisation and structure of cells at the molecular level, however there remain significant challenges to be overcome in the optimisation of both imaging procedures and analysis, which will be discussed later in this chapter.

As briefly discussed in Chapter 1 and in further detail in the following sections, super-resolution microscopy refers to a number of techniques which achieve resolution below the diffraction limit in various ways. The diffraction limit, previously thought to impose a fundamental limit to the resolution achievable with light microscopy, arises from the diffraction of light waves passing through an aperture and the interaction of the diffraction patterns produced, as detailed in the following section.

4.2.1 The diffraction limit to resolution

When a wavefront is partially blocked by an obstacle, the unblocked part of the wave bends around the obstacle, in the process known as diffraction [190]. The interference of diffracted wavefronts originating from either side of an aperture causes the characteristic interference pattern known as the Airy disk, or diffraction limited spot, shown in Figure 4-1. This limits resolution, as the two diffraction patterns cannot be individually resolved if they are not sufficiently spaced apart. The limit at which spaced apart diffraction patterns can be separately resolved is known as the Rayleigh criterion.

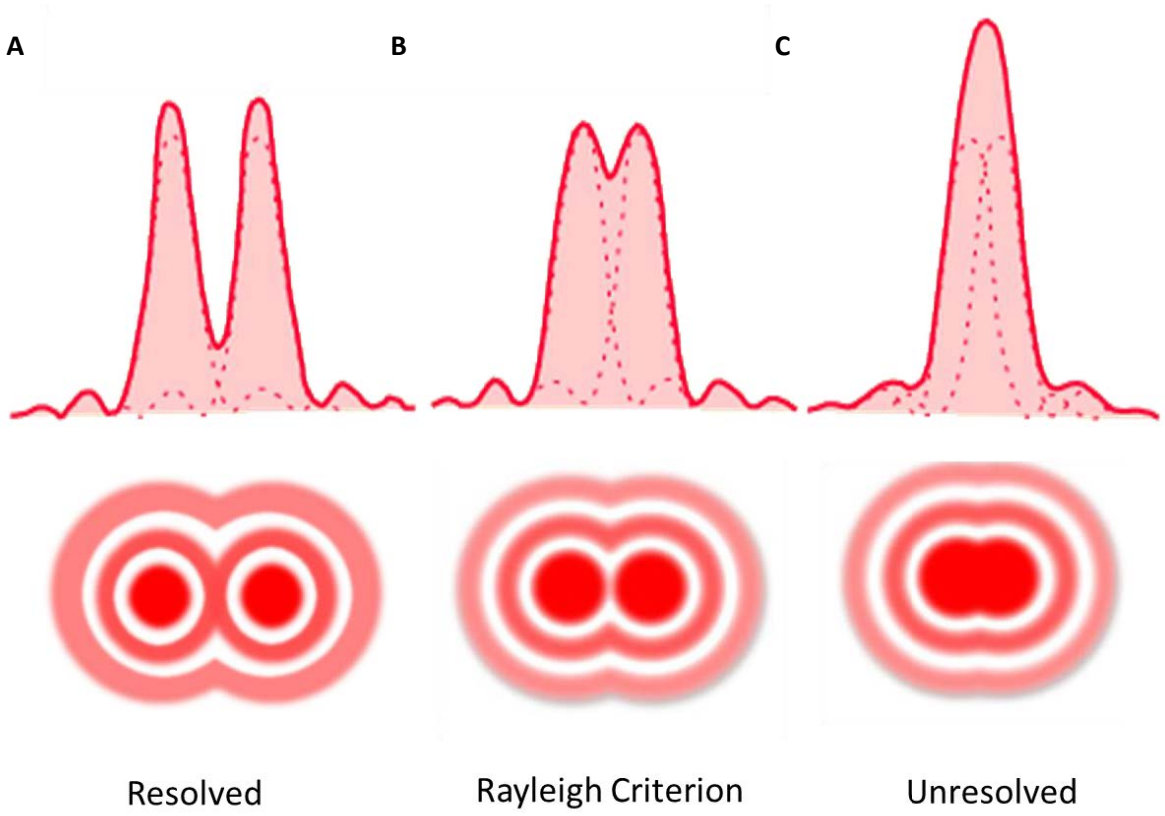

Figure 4-1: Airy disk diffraction patterns
The diffraction pattern shown in A) is the image of a two single molecules which are separated by a distance greater than the Rayleigh criterion. The two overlapping patterns are Airy disks, which will be returned by an imaging system due to the diffraction and interference of light leading to light and dark concentric bands around the central maximum. B) shows two diffraction patterns, spaced such that these two molecules would be separately resolvable, as the diffraction minima overlap and the central peaks may be separately identified, at a distance given by the Rayleigh criterion. C) shows two Airy disk patterns more closely spaced than the Rayleigh criterion, which is the case observed where imaging probes are be more densely spaced on the sample than the Rayleigh criterion, and thus an image composed of many of these overlapping diffraction patterns which cannot be separately resolved is returned. Figure adapted from [191]

The Rayleigh criterion is given by

$$d = 0.61\lambda/\mathrm{NA} \tag{5}$$

where d is the Rayleigh criterion, λ is the wavelength of the emitted light, and NA is the numerical aperture of the objective through which the light is collected. For high NA optical microscopes this leads to a typical resolution limit of around 200 nm [192].

4.2.2 Overcoming the diffraction limit

A number of techniques have been developed to achieve sub-diffraction-limit resolution. The forerunning techniques of stochastic optical reconstruction microscopy (STORM), photoactivation localisation microscopy (PALM) and stimulated emission depletion microscopy (STED) were developed concurrently in three separate labs, and jointly earned their creators W.E. Moerner, Eric Betzig, and Stefan Hell, the Nobel prize in Chemistry in 2014. Other techniques include ground state depletion (GSD), reversible saturated optical fluorescence transitions (RESOLFT), structured illumination microscopy (SIM) and saturated structured illumination microscopy (SSIM) [193].

There are broadly two main classes of super-resolution techniques – localisation based, and the patterned excitation approach [194]. Localisation based techniques make use of spectral or temporal fluctuations in the emission of the molecules being imaged, and use this information to determine the location of the molecules with high precision. By making use of the information contained in these fluctuations it is possible to localise molecules with a precision higher than the diffraction limit, and therefore reconstruct super-resolved images. Techniques in this class include STORM/dSTORM and PALM. This class of techniques is discussed further in section 4.2.3.

The patterned excitation class of techniques uses a different approach, utilising sub-diffraction limit features in the excitation pattern to read out small-scale information from the sample. Techniques in this class include STED, RESOLFT and SSIM [194].

This thesis employs a variation on STORM microscopy - direct stochastic optical reconstruction microscopy (dSTORM), which is part of the localisation based class of techniques. The rest of this introduction will therefore focus only on the theory and implementation of single molecule localisation microscopy (SMLM).

The nature of localisation based techniques for super resolution microscopy means these techniques are suited to the niche area of cell imaging that is the study of spatial heterogeneity in protein

organisation [195]. SMLM has been applied widely in the study of membrane proteins, including for examination of ultrastructure and clustering, stoichiometry of protein complexes [196] and investigation of TERMs [49].

4.2.3 Direct Stochastic Optical Reconstruction Microscopy (dSTORM)

4.2.3.1 Principle of dSTORM

Direct STORM (dSTORM) is a variation on STORM microscopy, although both rely on the same fundamental principle of single molecule localisation. STORM microscopy utilises photo-switchable fluorophores which are induced to switch on and off using light of different colours, over a series of imaging cycles. In each cycle only a fraction of the fluorophores are switched on, such that the fluorescence signal from individual molecules is spatially resolvable (fluorescing molecules are separated by more than the Rayleigh criterion). This allows the position of individual fluorophores to be determined with high accuracy by fitting the diffraction limited image of the molecule with a function describing the "spreading" induced by diffraction, to recover the true location of the emitter. Repeating this process over several cycles, each causing a stochastically different subset of fluorophores to be turned on, allows a highly detailed image containing the localised positions of molecules separated by less than the diffraction limit to be reconstructed, resulting in a super-resolved image. This concept is demonstrated pictorially in Figure 4-2.

.

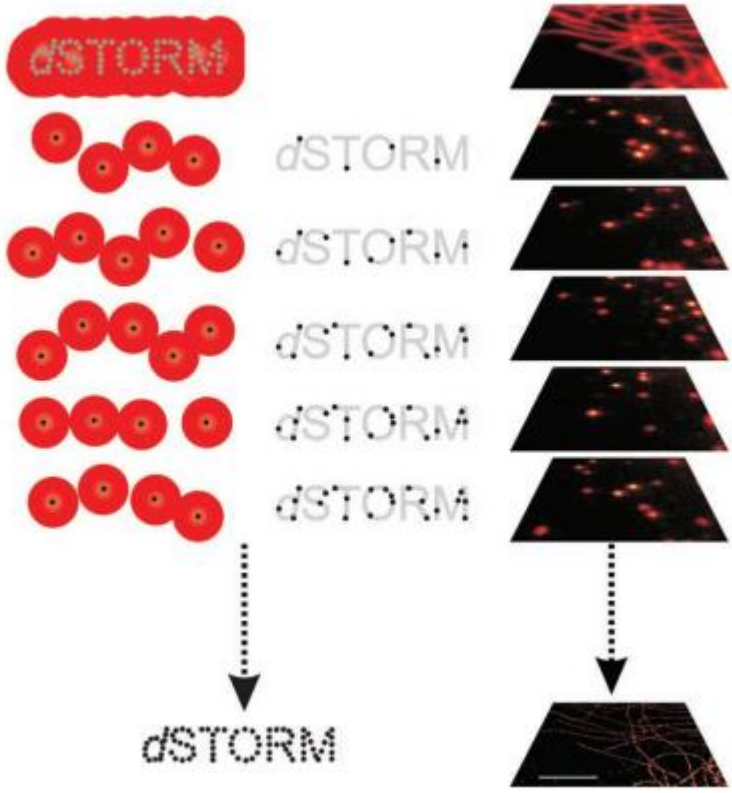

Figure 4-2: Pictorial representation of super-resolution microscopy by localisation
Left - In this diagram, the word 'dSTORM' represents the underlying structure to be resolved. The distorted shape around the word represents the overlapping point spread functions of the fluorophores on the underlying structure, which are more closely space than can be separately resolved. The individual point spread functions are imaged sequentially by stochastic switching of the fluorophores between the bright and dark state such that their positions may be precisely determined. Over the course of several imaging cycles molecules which are more closely spaced than the resolution limit may be localised, and this information builds up a picture of the underlying structure as shown in the centre. The positional information from the sequential localisations can then be combined as shown on the final line, where the underlying structure is resolved. Right – The principle of localisation microscopy as described for the dSTORM example on the left, applied to a real biological structure such as microtubules. Scale bar 2 μm. Reproduced from [197]

The position of fluorophores can be determined with nanometre accuracy by fitting a two-dimensional Gaussian profile to the individual point-spread functions (PSF) of the fluorescent molecules. In the ideal situation the localisation precision depends only on the number of photons collected, n, and the standard deviation of the PSF σ and can be approximated by $\sigma/\sqrt{n}$ [198] –

illustrating the need for bright and photostable fluorophores and optimised imaging conditions, and high numerical aperture objectives.

STORM uses a pair of dyes, typically Cy3-Cy5. Cy5 is switched between a fluorescent and dark state in a controlled, reversible manner, by illumination with light of different wavelengths – green laser light converts Cy5 back to the fluorescent state but the recovery rate depends on the proximity of Cy5 to a donor molecule Cy3. Together Cy3-Cy5 are referred to as a switch, and it was originally shown that such a switch could cycle on and off hundreds of times before photobleaching, allowing for the detailed dataset to be built up [199]. STORM using the dye-pair approach was first presented by Rust et al. in 2006 [199], then in 2008 Heilemann et al. demonstrated a varation to the technique called direct STORM (dSTORM) [200]. dSTORM requires only a single fluorescent emitter, using a conventional carbocyanine dye such as Cy5 or Alexa Fluor 647, which is induced to reversibly switch between fluorescent and dark states by excitation with a high power laser and the use of an imaging buffer containing a mixture of chemicals which support blinking and prolong fluorescence by reducing photobleaching. The most commonly used buffer system for STORM/dSTORM consists of glucose, and the enzymes glucose oxidase and catalase, which oxidise glucose to remove molecular oxygen from solution, and a thiol, commonly cysteamine (MEA). The use of a single fluorophore enables a simpler implementation of the technique, yet still achieves the same order of magnitude improvement in resolution over diffraction limited techniques as conventional STORM [200].

4.2.3.2 Labelling samples for dSTORM

A key parameter limiting the resolution of a dSTORM image is the brightness and photostability of the fluorescent probe. The number of photons collected from a fluorescent molecule being directly related to the precision with which it can be localised by:

$$\Delta \boldsymbol{x} = \frac{\boldsymbol{k_1}}{\boldsymbol{N^{1/2}}} + \frac{\boldsymbol{k_2 b}}{\boldsymbol{N}} \qquad (6)$$

where Δx is the error in localisation, k_1 and k_2 are determined from the excitation wavelength, numerical aperture of the objective and pixel size, N is the number of photons collected and b is the background noise per pixel [201], [202]. Since k_1 and k_2 can be constants for a given system, N is the driver of localisation precision. dSTORM and other SMLM techniques can be performed with a variety of fluorescent labels, including small molecule synthetic dyes such as the Alexa probes; quantum dots; and genetically encoded fluorescent protein fusions. The most important property of a fluorescent label is that is it capable of being either photoactivated, photoswitched or photoconverted by light of a specific wavelength, in order to enable the detection of distinct subpopulations [203], but brightness and stability are of high importance also to maximise the number of photons that can be detected before the probe photobleaches or switches to the dark state. Brightness is given by the product of the molar extinction coefficient (ε_{abs}) and the fluorescence quantum yield (φ) [204], meaning the best probes are those with high extinction coefficients and quantum yields, providing high contrast against the background [202], [205].

The attachment of the fluorescent label to the target protein is also important, and impacts on the effective resolution of the resultant image. It is important to minimise the distance between the target and the fluorescent label (label-target distance) in order to have the final image accurately reflect the location of the target, and to minimise localisation error due to movement of the label about the target.

In the case of fluorescent proteins a genetic tag can be used to directly attach the fluorescent protein to the protein of interest, while for small molecule dyes and quantum dots an intermediary molecule with specificity to the target protein, such as an antibody, drug, or ligand, and means of attaching the fluorescent protein is required. The immunofluorescence technique which is widely used to label samples for conventional (diffraction limited) fluorescence microscopy involves labelling the target with a primary antibody, before the fluorescent probe is attached by means of a

fluorophore conjugated secondary antibody. Advantages of this technique are its relative simplicity, compared to preparing a genetically encoded fluorescent protein construct for example, and the availability of a large number of commercial primary and secondary antibodies against many targets and conjugated with a huge number of different fluorophores, which tend to show increased brightness and photostability compared with fluorescent proteins. A significant disadvantage however, is that the size of the primary antibody, secondary antibody, and linker molecules attaching the fluorophore lead to an effective distance of 10-20 nm between the target and the fluorescent label [202], limiting the resolution achievable.

Direct conjugation of fluorophores to primary antibodies is also possible using a number of kits or NHS ester conjugated labels, however while this does reduce the label-target distance it also removes some of the flexibility of immunolabelling as the concentration of secondary antibody and consequently fluorophore cannot be changed if more or less signal is desired, and alternative fluorophores cannot be used without the expense and delay of conjugating a new batch of antibody. Another alternative approach involves fusing the target protein to a peptide or protein recognition sequence which then recruits the small-molecule fluorophore/dye [202], which does reduce the label-target distance but also adds another layer of complication to the labelling process.

One way to reduce the label-target distance is to use fragments of whole antibodies called Fab fragments, which are smaller antibody fragments produced via cleavage from the whole antibody using papain or pepsin digestion. Fab fragments contain only the light chain and upper part of the heavy chain of whole antibodies, and have a molecular weight of about 50 kDA. They still bind antigens, but are monovalent and smaller compared to whole IgG molecules. Fab fragments can be used with in combination with fluorophore conjugated secondary antibodies which recognise the Fab fragment (which may also be Fab fragments), or biotinylated and used with avidin-conjugated fluorophores. Using Fab fragments in combination with avidin conjugated fluorophores would likely

result in a 1:1 fluorophore to target ratio which is useful for determination of the molecular composition of imaged structures, but does make detection more challenging due to the lower signal from a single target. Using Fab fragments in conjunction with secondary antibodies would not result in a 1:1 fluorophore:protein ratio as the degree of labelling of secondary antibodies is typically from 5-8 fluorophores per antibody. Although the target-label distance would be reduced compared to whole IgG antibodies, the trade off in terms of reduced antibody concentration and the time taken to generate the Fab fragments may not make this scenario worth pursuing.

Removal of the Fc domain and generation of Fab fragments may also be useful in other single molecule studies as the Fc domain can mediate unwanted binding events, which is a factor considered in work presented in chapter 5 of this thesis.

Other approaches to labelling involve single domain antibodies or nanobodies for reducing target-label distance, or fluorescent proteins, which are particularly well suited for live cell imaging, and have been successfully used by this group in the study of both CD82 and ErbB2, however tend to be significantly less bright than synthetic fluorophores.

4.3 Choice of labelling strategy for dual colour data

One of the initial considerations in this super-resolution imaging study was the labelling approach. This section details the initial investigations carried out to determine the method which would produce the best results for this study.

As discussed in the previous section, a number of different approaches to labelling exist. A primary consideration was the size of the label, and the number of dye molecules carried. Reducing the size of the label is desirable, to minimise the distance between the fluorescent label and the target protein, as is maximising the signal detected from a single protein.

We considered the antibodies available against the main protein of interest ErbB2 – commercial antibodies, Herceptin, and a biotinylated Fab fragment of Herceptin, and trialled each of them. Fab fragments are a desirable label for super-resolution imaging as they reduce the distance between the fluorophore and the target protein, thereby decreasing the possible range of locations of a fluorophore attached to a single protein relative to labelling with an intact IgG, or larger molecule, and thus in theory increase the effective resolution [206]. However, Fab fragments will generally only bind one fluorophore, making detection of proteins expressed at a low level more difficult than if the protein is bound with multiple fluorophores. There is also the issue of the precise labelling strategy chosen – ideally Fab fragments would be directly conjugated to a fluorophore, as this minimises the distance between the fluorophore and the protein the most. However, the production of Fab fragments can be challenging and result in low yield/concentration, which can then be further diluted in the process of conjugating the fluorophore and purifying the labelled Fab fragment of free dye, making this an inefficient method. Alternatively Fab fragments may be biotinylated and bound with a streptavidin conjugated fluorophore. Fab fragments are highly suitable for reducing the target-label distance, however used in conjunction with biotinylation and avidin conjugated fluorophores the number of dye molecules per target (DOL of avidin conjugated complex x 1 due to single biotin per Fab) is less than in the case of a whole IgG which is can be bound by >1 secondary antibody labelled with multiple (typically 5-8) fluorophore molecules.

To fully investigate the options and their impact on the recovered data we investigated three labelling strategies – whole Herceptin IgG and anti-human Alexa 647, whole Herceptin IgG and anti-human Alexa 488, and a biotinylated Fab fragment of Herceptin and avidin conjugated Alexa 488. It was clear that Alexa 647 would outperform the other strategies in terms of brightness, however, Fab fragments were investigated in the interest of minimising the target-label distance, and since only 488 conjugated avidin secondary was available in the lab.

The possibility of using of a GFP tagged protein in combination with an Alexa 647 conjugated secondary was also investigated, to remove the need for double immunolabelling and the potential for non-specific binding and cross-talk, however the GFP did not seem to provide adequate signal for dSTORM reconstruction under the optimal imaging conditions for Alexa 647, and it was decided that double immunolabelling was the most appropriate method at this stage of the investigation.

As can be seen from Figure 4-3, both the choice of antibody and fluorophore affect the quality of the recovered data. The antibody is important since high labelling efficiency ensures the maximum number of binding sites are available for the secondary antibody. The performance of the fluorophore clearly also has a significant effect on the data, as can be seen from Figure 4-3 C, which shows that on the same cell type with the same antibody (as compared to Figure 4-3 A), significantly more points are recovered with Alexa 647 as the fluorophore compare to Alexa 488.

Since the performance of Herceptin Fab fragments and whole IgG Herceptin seemed similar in the density of recovered points, and utilising whole Herceptin removed the additional steps of Fab fragmentation and biotinylation, neither of which was highly efficient and resulted in significant loss of antibody, we elected to use whole Herceptin. In future studies where even greater resolution is required, or more accurate representation of molecule numbers desired, directly labelled Fab fragments could be employed.

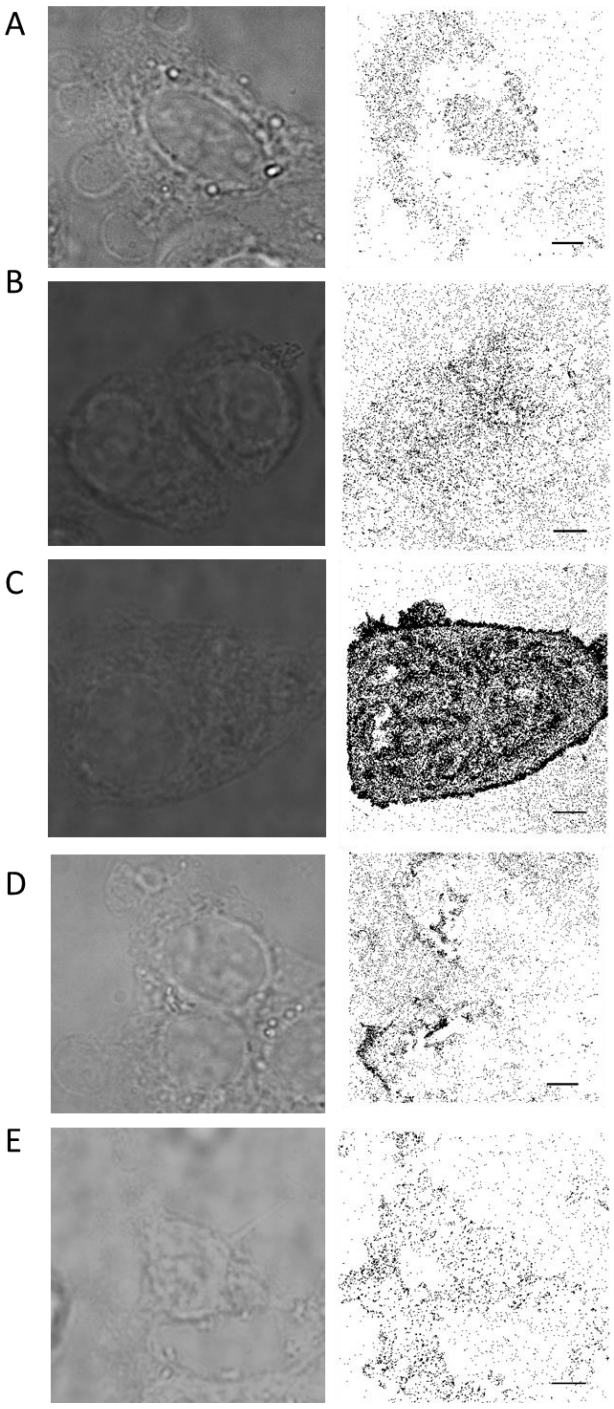

Figure 4-3: Comparison of labelling achieved with whole IgG and different fluorophore secondary labels and biotinylated Fab fragments with avidin conjugated secondaries on SKBR3 (ErbB2 over-expressing) and MCF7 (low ErbB2 expression) cells

The left-hand column shows brightfield images to show the extent of the cell, while the right-hand column shows the points recovered after dSTORM imaging and reconstruction with standard parameters. Points are all plotted in black to show the distribution and density and labelling. A) SKBR3/zeo cells, 2 µg/ml biotinylated Herceptin Fab and 0.66 µg/ml avidin-conjugated Alexa 488; b) SKBR3/zeo cells, 2 µg/ml Herceptin and 0.66 2µg/ml anti-human Alexa 488; C) SKBR3/zeo cells, 2 µg/ml Herceptin and 0.66 µg/ml anti-human Alexa 647; D) MCF7/puro cells, 4 µg/ml biotinylated

Herceptin Fab and 0.66 µg/ml avidin-conjugated Alexa 555; E) MCF7/puro cells, 2 µg/ml Herceptin and 0.66 µg/ml anti-human Alexa 647. Scale bar 5 µm.

4.4 Imaging procedures

There are several key elements in the STORM/dSTORM imaging procedure – choice of a suitable fluorescent probe; selection of imaging buffer conditions to facilitate photoswitching; intensity of laser excitation, and use of a supplementary laser to induce photoswitching. Whilst all of these parameters are important for generating the best quality images, the following section focuses particularly on the importance of the buffer in which the sample is immersed for imaging.

The dSTORM imaging procedure, assuming a sample has already been prepared and labelled with appropriate fluorescent dyes is as follows:

1) immersion of the sample in an appropriate imaging buffer (typically containing thiol and an oxygen scavenging system) supporting transition of fluorophores into the bright 'ON' state buffer;
2) illumination with laser light of an appropriate wavelength for the fluorophores, driving the majority into a reversible dark state [197];
3) sequential imaging over several thousand frames with laser illumination;
4) post-processing/reconstruction of the super-resolution image.

The sample is irradiated with laser light of the appropriate wavelength for the fluorophore, and can be imaged in either wide-field or TIRF mode. The initial laser intensity is high, to drive the majority of fluorophores into the dark state, so that in subsequent imaging cycles subsets can be recovered to the fluorescent state for sequential imaging. Supplementing the excitation laser with 405 nm laser light also allows for further control of the fluorophore switching by facilitating recovery of the fluorescent form [197].

4.4.1 Composition of the imaging buffer

The composition of the imaging buffer is important, and should be optimised for the specific fluorophore in use [207]. The optimisation of the buffer conditions is especially challenging in the case of multicolour imaging, as some of the best probes for super-resolution are cyanine derivatives (Cy3, Cy5, Alexa Fluor 647) or rhodamines (Alexa Fluor 488, Atoo 488, Alexa Fluor 568), which have widely different requirements for buffer composition. Where cyanines work best in oxygen-free buffers, rhodamines don't blink properly in the absence of oxygen [207], [208].

The choice of buffer composition can affect the robustness of the on-off switching process, and the survival time of the fluorophore before bleaching. In general dyes have been found to perform best in the presence of both a reducing agent (usually a primary thiol) and an oxygen scavenging system, although the specific type and concentration of these components resulting in best performance does vary [207], [209]. The oxygen scavenging system is important, as molecular oxygen in solution is primarily responsible for photobleaching, and its removal prolongs the time during which signal can be acquired from a given fluorophore. In the on-state fluorophores are rapidly and repeatedly excited to the excited singlet state, and return to the ground state by the emission of red shifted photons which are detected by the camera. A small number of molecules however enter the fluorescence triplet-state, which is dark, and relatively long-lived (µs-ms). Molecules in the triplet state can interact with molecular oxygen, either by the transfer of energy from the fluorophore to molecular oxygen leading to the formation of energetically excited singlet oxygen; or by electron transfer from the excited fluorophore to molecular oxygen leading to the formation of a superoxide radical. Singlet oxygen and superoxide radicals, along with subsequently formed oxidising species are collectively termed reactive oxygen species (ROS) and can degrade fluorophores and damage biomolecules [210]. The specific role of ROS in photobleaching is not well understood, but the importance of oxygen scavenging systems for increasing dye performance in STORM imaging has been verified experimentally numerous times [211]. While removing molecular oxygen from solution

tends to increase the time to photobleaching, on the other hand O_2 is a triplet state quencher, meaning that the large fraction of fluorophores which end up in the triplet state under intense illumination are effectively quenched (brought back to the fluorescent state) by atmospheric O_2 levels within seconds [208], and in its absence the triplet state may exist for many seconds, strongly reducing the photon flux and increasing the probability of other follow-up reactions occurring from the triplet state [212]. Therefore, reducing agents such as MEA are added at millimolar concentration to mitigate this effect by replacing O_2 as triplet state quenchers, restoring the high count rate and blinking behaviour of the fluorophores. The thiols most commonly used in the buffer are Mercaptoethilamine (MEA) [200], Mercaptoethanol (BME), or recently TCEP [213], although recent work by Olivier et al. also demonstrated a doubling of resolution in 3D-STORM imaging of microtubules by adding the polyunsaturated hydrocarbon cyclooctatetraene (COT) to the imaging buffer, resulting in significantly higher photon yields from Alexa 647 [209].

The optimisation of the buffer system for fluorophore performance is an active area of research, and new systems, such as a reducing and oxidising system (ROXS)[212], and a new oxygen scavenging system (OxEA) [208] have recently been proposed to overcome some of the limitations of current systems, such as the acidification of the buffer and occurrence of photobleaching dependent on the dye used.

4.4.1.1 Dependence of clustering results on buffer conditions

As can be observed in Figure 4-3 the choice of labelling strategy – particularly the fluorophore choice, strongly affects the density of localisations and the quality of the reconstructed image. It is necessary to consider how the choice of imaging probe, and the imaging conditions, which is different for different fluorophores [207], affect the cluster parameters recovered and the subsequent quantification of the experimental results. In particular, for multi-colour imaging studies this is an important consideration, as in comparing results obtained from the imaging of different

fluorophores, where one may have been imaged in conditions closer to its optimum than the other the effect on the localisations recovered for that label may lead to erroneous conclusions regarding the distribution relative to the other label.

To investigate the effect that different compositions of imaging buffer can have on the imaging/blinking performance of the label and the subsequent effect on the clusters recovered after analysis the imaging buffer described in 2.3.3 was supplemented with different amounts of the thiol MEA, to a final concentration ranging from 0-100 mM.

Buffer containing 100 mM MEA was recommended as the starting concentration, so early dSTORM experiments in this study were performed under these buffer conditions, however moving towards dual colour imaging the optimisation of the buffer conditions became more important. We noted that the performance of Alexa 488 was significantly worse than Alexa 647 under these initial conditions and so we sought to understand the impact this could have on the results obtained and if it was possible to optimise the imaging conditions for future dual colour imaging. The dual colour images presented in this thesis were obtained with 100 mM MEA in the imaging buffer, however work in this section identified better overall performance of this particular combination of dyes at 20 mM MEA concentration, which will be useful for future studies.

SKBR3 zeo (control cells) and SKBR3 CD82 over-expressing cells were labelled with 2 μg/ml Herceptin and Alexa 488 or 647 conjugated anti-human secondary antibody; and 2 mg/ml C33 (CD82 antibody) and Alexa 488 or 647 conjugated anti-mouse secondary antibody. The samples were then imaged under the same conditions (laser power, number of images acquired, reconstruction settings constant etc.) with varying concentrations of MEA in the imaging buffer (a fresh sample was used for each MEA concentration condition). Results presented in figures Figure 4-6 to Figure 4-4 are averaged from 2 images in each condition, with 5 5000nm^2 regions of interest selected in each image. The total number of cells sampled in each condition was equal to or greater than 3.

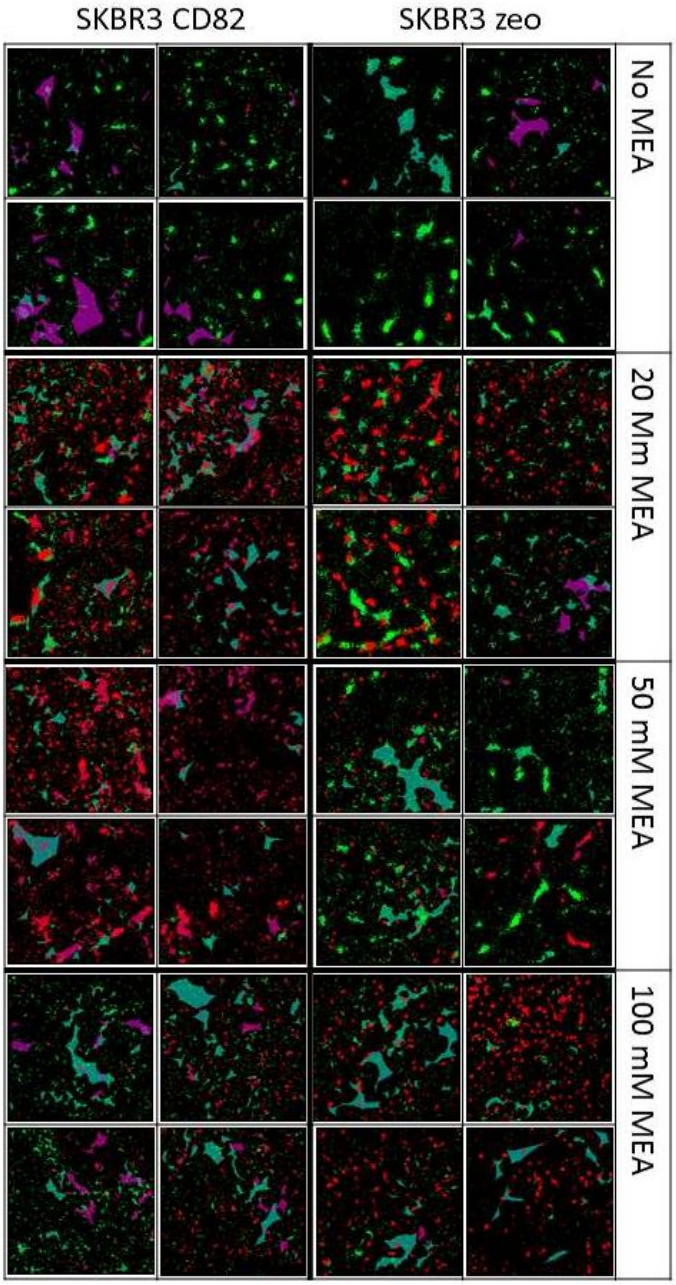

Figure 4-4: Clusters recovered from data acquired with concentration of MEA in the imaging buffer varied from 0-100 mM

Varying the concentration of MEA in the imaging buffer effects the amount of signal returned for each fluorophore, which in turn has an effect on the performance of the clustering algorithm. Each square represents a 5000 nm^2 region of interest representative of the clustering observed in cells in that condition. Cells are non-stimulated SKBR3 zeo/SKBR3 CD82, labelled with 2ug/ml Herceptin/488 and 2ug/ml C33/647 after fixation. Images shown are 2 of the 5 analysed ROIs from 2 images in each condition. Green points represent localisations of Alexa-488 (ErbB2) and red of Alexa 647 (CD82). The teal areas represent the clusters returned by the DBSCAN algorithm for points in the green channel, and the purple areas the clusters returned in the red. These images show how in the case of more sparse localisations (such as where the dye is under suboptimal buffer conditions) larger clusters are returned.

Figure 4-4 shows the localisations of ErbB2 and CD82 labelled with Alexa-488 and Alexa-647 respectively, in ROIs selected from images of SKBR3/zeo (control) and SKBR3/CD82 (CD82 over-expressing) cells with the concentration of MEA in the imaging buffer varied from 0-100 mM, and he clusters recovered by DBSCAN analysis (using the multi-pass implementation and parameters described in 4.5.4.1).

Where no MEA is present in the media Alexa-647 performs poorly, as the fluorescence recovery/switching performance of the dye is not good. This results in apparently large clusters being found in the data (purple areas, uppermost images), while on visual inspection of the localisations included in these clusters they appear to be made up of several smaller clusters, which are classed as one cluster as the difference in density between the apparent cluster and the inter-cluster spacing is not high enough for the two to be separated by the clustering algorithm. With the addition of 20 mM MEA to the imaging buffer the performance of Alexa-647 improves, as can be seen from in the significant increase in number of localisations/μm^2 and in the shift in cluster size towards smaller clusters in Figure 4-5 and Figure 4-6 respectively.

Further increasing the concentration of MEA seems to support the blinking of Alexa-647, based on the images in Figure 4-4 although this does not appear to be reflected in the number of localisations, while for Alexa-488 it results in reduced performance, reflected in the visibly larger clusters in the 50 and 100 mM MEA conditions in Figure 4-4, which when assessed visually appear not to be consistent with the type of cluster observed in the 20 mM MEA condition.

The quantification in Figure 4-5 seems not to support the data shown in Figure 4-4, however the sample size here is small, and it may be that localisations per μm^2 is highly variable depending on the precise area selected on the cell, and therefore is not a reliable measure of dye performance without

a much larger sample size. Despite this, the images in Figure 4-4, combined with the data in Figure 4-5 and other experimental observations support the authors' conclusion that Alexa 647 performs well at high (20 mM+) concentrations of MEA.

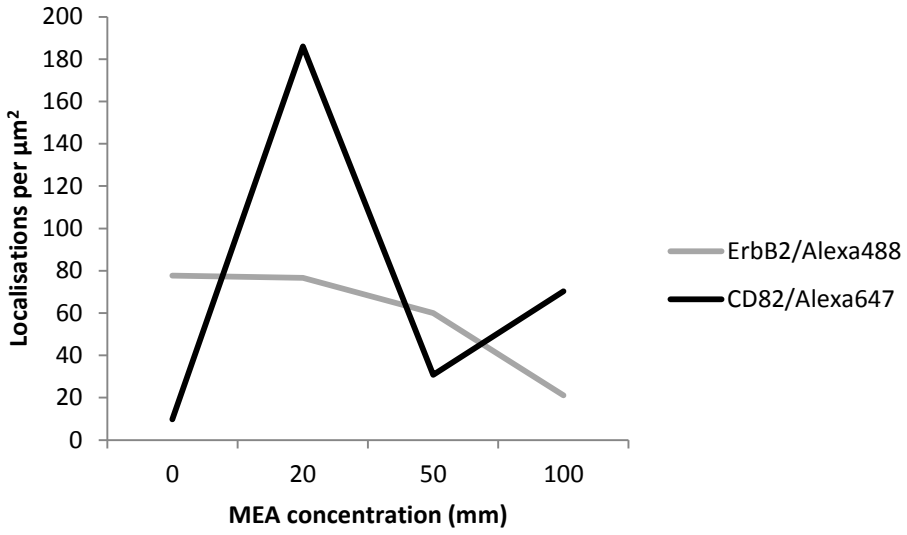

Figure 4-5: Localisations per µm² in SKBR3/zeo cells labelled imaged with different concentrations of MEA in the imaging buffer
SKBR3/zeo cells were double labelled for ErbB2 and CD82 with Herceptin and anti-human Alexa-488, and C33 and anti-mouse Alexa-647 respectively and imaged under buffer containing different concentrations of MEA. A fresh dish was used for imaging at each concentration rather than repeat imaging the same sample with changing MEA concentration, to avoid any effects due to bleaching of the fluorophore. At 0 mM MEA the number of localisations for Alexa 647 is low. Localisations in the 647 channel increase significantly with the addition of 20 mM MEA to the buffer, but seem to decrease again at higher concentrations. Alexa-488 seems to perform equally well at 0 and 20 mM MEA, with reduced performance at higher concentrations. This data is from analysis of 5 ROIs on 2 images in each condition.

With no MEA present in the imaging buffer Alexa 647 performs poorly, resulting in sparse signal in the images. We see that for Alexa 647 (Figure 4-6) the smallest proportion of clusters fall into the smallest size bracket in the no MEA condition, and as the MEA concentration increases the proportion of clusters in the smallest size bracket also increases. Comparing this result with the images in Figure 4-4, it seems that the reduction in cluster size is due to the increased signal density from the Alexa 647 resulting in better performance of the clustering algorithm, and in turn a truer representation of the actual distribution of the protein. Conversely for Alexa-488 the largest

proportion of clusters falls into the smallest size bracket in the no MEA condition, and this proportion decreases with increasing MEA concentration.

Taken together, these figures demonstrate the effect of a sub-optimal MEA concentration in the buffer during dual colour imaging, and the subsequent effect on the recovered clusters in terms of their size. This may then effect the apparent colocalisation of clusters of the two proteins. This highlights the importance of optimising labelling conditions and being aware of the potential effect on recovered cluster properties if conditions are sub-optimal for one of the dyes. In order to determine if the resultant image is representative of the sample, it may be good practise in future dual colour studies to repeat the experiment in various buffer conditions, to determine the extent to which, with all other parameters kept constant, the apparent protein distribution and resultant cluster properties are affected.

As well as influencing the apparent interaction between clusters labelled with different fluorophores due to poor performance of the clustering algorithm on sparse data sets, the number of photons detected from each fluorophore is also a fundamental limit to the localisation precision in STORM [198], and therefore seeking to optimise and/or develop a buffer system resulting in maximised photon detection is important.

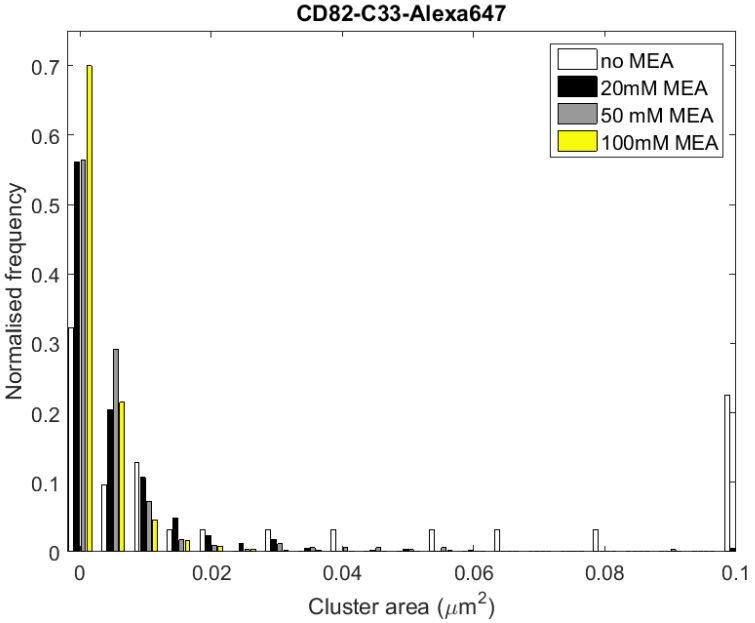

Figure 4-6: Histogram of CD82 cluster area in SKBR3/zeo labelled with C33 and Alexa-647 where the concentration of MEA in the imaging buffer was varied between 0 and 100 mM.
When no MEA is present in the imaging buffer a large proportion of the recovered clusters are in the largest size bracket, and the smallest proportion of any condition are in the smallest size bracket. As the concentration of MEA in the media increases the proportion of clusters in the smallest size bracket increases concurrently. Results are from analysis of 5 ROIs in at least 2 images in each condition, number of clusters analysed in conditions 0-100mM MEA respectively: 31, 757, 346, 2170.

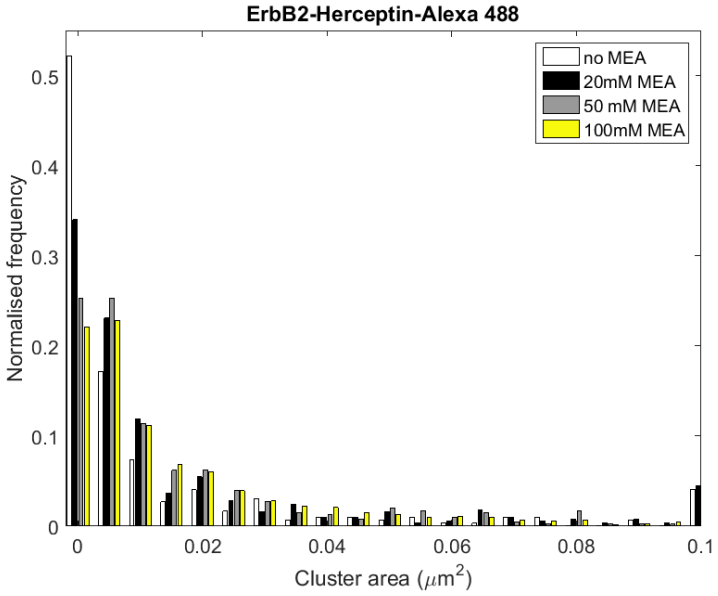

Figure 4-7: Histogram of ErbB2 cluster area in SKBR3/zeo labelled with Herceptin and Alexa-488 where the concentration of MEA in the imaging buffer was varied between 0 and 100 mM.
The largest proportion of clusters in the smallest size bracket comes from the no MEA condition, however this condition also results in a large proportion in the largest size bracket. As the concentration of MEA in the imaging buffer increases, so the proportion of clusters in the smallest

size bracket decreases. A concurrent shift in the distribution of cluster sizes towards the larger areas is also observed with increasing MEA concentration. Results from analysis of 5 ROIs in at least 2 images in each condition, number of clusters analysed in conditions 0-100mM MEA respectively: 297 494, 403, 714.

The work presented in this section led to the conclusion that for dual colour imaging, a 20 mM concentration of MEA in the imaging buffer would lead to the best overall results, with the specific dye pairing of Alexa 488 and Alexa 647, when the performance of both dyes was taken into account. Further work to improve dual colour imaging would need to identify different combinations of fluorophores where the imaging conditions could be optimised for both simultaneously, or look to employ other techniques for dual colour imaging not requiring simultaneous imaging of the two colours, such as DNA-PAINT [214]. We chose to use Alexa 488 and Alexa 647 as these are two of the most commonly used dyes for dSTORM, however based on the literature and these experimental results, Alexa 647 and Alexa 488, although being leading probes for single colour dSTORM, are not the most optimal combination for dual colour imaging. In future, dyes from the same class (e.g. carbocynanine or rhodamine) should be paired together for dual colour imaging in more optimal buffer conditions [207]. Ideally, where it is not possible to optimise the buffer conditions for both dyes simultaneously, imaging should be performed with the dyes reversed, to ascertain what effect sub-optimal dye performance may be having on the recovered cluster properties and/or apparent level of colocalisation. In this study, due to time constraints, it was not possible to repeat the experiments in this way.

4.5 Analysis of dSTORM data

4.5.1 Reconstruction

The raw data produced in a dSTORM experiment consists of a stack of images (typically 20,000 [197]) such as those shown in Figure 4-8. From these raw images the precise position of each fluorophore is determined by selecting out the individual PSFs and fitting a two-dimensional Gaussian to the image to determine the centre. The coordinates of these fitted points are returned

in a list, representing the position of the fluorescent molecules in the imaged sample, which can be plotted as a 2-dimensional graph, or convolved with a Gaussian on the order of the resolution of the system to render an image.

Although the precise algorithm implemented in the Nikon N-STORM system used for this study is proprietary and not disclosed, we can consider the processes described for open-access software such as rapi*d*STORM [215] to be representative of the general approach.

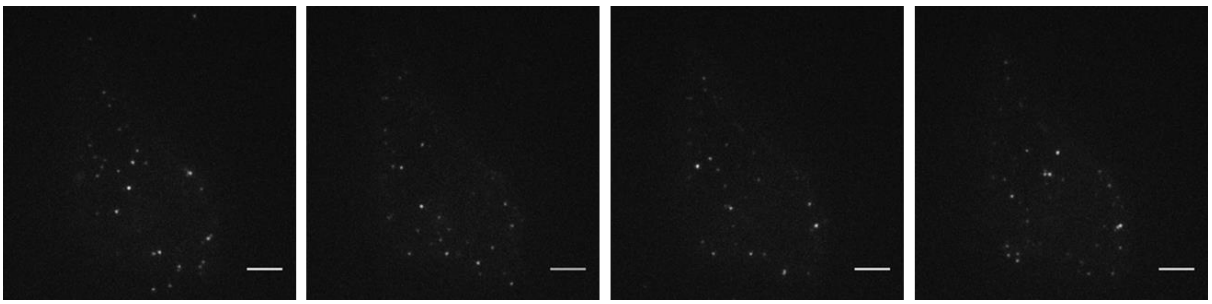

Figure 4-8: Consecutive raw images from a dSTORM experiment
In a dSTORM experiment, typically around 20000 images are taken, from which the positions of blinking fluorophores are extracted to reconstruct the super-resolution image. The images shown here are consecutive frames from a sequence of images of SKBR3/zeo cells labelled with Alexa-647. These consecutive images illustrate the blinking process, with a different subset of emitters visible in each frame. Scale bar 5μm.

Nikon state that the reconstruction algorithm used by the N-STORM system to fit overlapping peaks, allowing densely labelled samples to be successfully imaged, is based on that published by Babcock et al. [216], called 3D-DAOSTORM. 3D-DAOSTORM is an extension of the DAOPHOT analysis method published by Stetson et al. [217] for applications in astronomy; and developed by Holden et al. [218] for super-resolution microscopy, where it was termed DAOSTORM.

The basic idea of the DAOPHOT algorithm, on which the DAOSTORM algorithm is based, is to fit the detected emitters in an image, then subtract the fit and examine the residual image for evidence of any undetected emitters. The undetected emitters in the residual image are then simultaneously fit with the emitters identified in the previous cycle, and the process repeated until no further

undetected emitters are indicated in the residual image. This allows reconstruction of super-resolution images from samples/images with a higher density of active fluorophores than previous sparse reconstruction algorithms [218]. The coordinates of detected points are typically returned in list, along with other properties such as brightness, full-width half maximum of the fitted Gaussian, certainty of localisation, number of photons detected, etc.

4.5.2 Analysis

The nature of dSTORM means that the data returned after reconstruction is pointillistic, and in order to extract meaningful and quantifiable information the relationship between the points needs to be determined. The major way in which such analysis is performed is to make use of clustering algorithms, and apply them to extract data regarding the distribution of points in the super-resolution image. A mounting number of studies have indicated that the majority of membrane proteins appear clustered when observed by super-resolution techniques and that this clustering may be important to understand the role of spatial organization of the plasma membrane in mediating and regulating cellular processes [193], [219], [220].

The approaches used for cluster analysis of single molecule localisation based super-resolution techniques such as dSTORM can be divided into two broad categories:

1. Analysis tools using spatial statistics that have been developed and used for similar problems in electron microscopy such as the pair-correlation function[221], Ripley's K-function [222], or the nearest neighbour distance distribution [223];
2. Spatial clustering analysis, using algorithms such as the density-based DBSCAN [224], or Voronoï tessellation [225]–[227]; followed by analysis of the properties of the obtained clusters to determine cluster parameters. [195]

Multiple implementations and variations on the above methods have been published, and the field of data analysis for single molecule super-resolution imaging is rapidly advancing with many new

approaches published in recent years [225], [226], [228], [229]. There has been in particular a move towards publication of accessible and user-friendly packages which do not require the user to code, in order to increase the usability of these techniques by biologists. Only the techniques which have been applied in this thesis are discussed in detail here however, with the following sections detailing Ripley functions, analysis based on density based spatial clustering of applications with noise (DBSCAN) and molecular co-localisation analysis.

Other types of analysis include approaches for molecular counting and correlation based analyses but these will not be discussed here.

4.5.3 Ripley's K-function

Ripley's K-function, and related functions the L and H functions, are increasingly used to identify clustering of proteins in cell membranes in super resolution imaging data, having previously been applied to study the organisation of immunolabelled proteins in membrane sheets imaged via electron microscopy [230]. These spatial statistics identify clusters based on deviation from a random distribution with a cluster identified if the average number of proteins within a distance r of another protein is statistically greater than that expected for a random distribution [222].

The function uses the concept of statistical moments, where the first moment of a pattern of molecular localisations is the number of points per area and the second moment is the expected number of points N within a distance r of another point. Ripley's K-function is the second moment normalized by the number of points per area λ [231]:

$$K(r) = \frac{1}{n}\sum_{i=1}^{n} N_{p_i}(r)/\lambda \quad (7)$$

where p_i is the i^{th} point and the sum is taken over n points. The expected value of $K(r)$ for a random Poisson distribution is πr^2, therefore deviations from this expectation can provide information on scales of clustering and dispersion. Ripley's K-function can further be normalised so

that its expected value is r, giving the L-function, or zero, giving the H-function. Typically a point distribution under investigation is tested against the null hypothesis that points are randomly distributed. The value of the H-function can be used to indicate if this is the case, where a positive value would indicate clustering over that scale, and a negative one dispersion [222].

A linearised version of Ripley's K-function, Ripley's L-function, which is defined as $L(r) - r = \sqrt{K(r)/\pi} - r$, where $K(r)$ is Ripley's K-function at radius r, can be used to reduce the size of datasets to speed up clustering analysis. Points whose $L(r) - r$ value at a given radius is less than that expected for a spatially random distribution at that density of points can be classified as noise and removed from a dataset before clustering, reducing the computational load for large or dense datasets [232]. Ripley's K-function analysis was employed in this study in this way, being used in the ClusDoc package described in section 4.6 to remove noise points from a dataset prior to cluster analysis with DBSCAN.

4.5.4 Density Based Spatial Clustering of Applications with Noise (DBSCAN)

The DBSCAN algorithm was initially developed to overcome the problem of identifying features in spatial information with minimal requirements for domain knowledge to determine appropriate input parameters, and the ability to discover clusters with arbitrary shape and good efficiency [224]. These properties make it also suitable for use in the analysis of the coordinate lists produced by SMLM, and as such it has gained prevalence as one of the forerunning algorithms for analysis. A particular strength of DBSCAN is the ability to detect clusters of arbitrary shape rather than being biased towards circular clusters, as in Ripley's K-function cluster analysis. DBSCAN is now the most widely employed method for clustering of SMLM data, and significant analysis can follow cluster identification to determine parameters such as the cluster area, circularity, number of proteins within a cluster, etc.

DBSCAN relies on a density based notion of clustering; intuitively we can see clusters when faced with a spatial distribution of points where the point density varies, and DBSCAN uses this density information to identify clusters. Although DBSCAN can be applied in 3D or higher dimensional feature space in this thesis it is only applied in 2D and therefore this explanation will only consider the 2D case with Euclidean distance.

Two key parameters determine the clusters that are found in a dataset: ε and MinPts. ε defines a neighbourhood (distance) around a point in which the search for other points in the cluster will be carried out, and MinPts defines the minimum number of points required in a cluster. DBSCAN classifies all points in a dataset as either a noise point, an edge point, or a core point depending on whether it is 'density connectable' to another point satisfying certain conditions.

DBSCAN analysis starts with an arbitrarily selected point in the data set. If this point has more than MinPts neighbours within the ε neighbourhood then a cluster is started, containing this point and its neighbours. The neighbours are then examined, and if they too have MinPts neighbours within the distance given by ε then the cluster is propagated and these points are included, and if not they are classified as boundary points. If a point does not have MinPts neighbours within the ε neighbourhood, then the point is classified as a non-clustered point. The clustering progresses by selecting a new point which has not yet been visited, until all of the points in the data set have been classified either as clustered or outliers.

Challenges in using DBSCAN for analysis include identifying appropriate input parameters; often this is solved empirically [223], [233], although some have used the heuristic suggestions of the original DBSCAN paper on how to set the parameters, including the one of the implementations used in this thesis [234]. Recent publications have proposed extensions to DBSCAN, such as ordering points to determine the clustering structure (OPTICS) [235], which may be useful for ensuring optimal parameter selection.

4.5.4.1 Selection of DBSCAN parameters

The clusters detected by DBSCAN are heavily affected by the choice of parameters used in the analysis, so it is of vital importance that appropriate parameters are chosen. There are two broad approaches to selecting appropriate parameters – using the distribution of the data itself to determine the appropriate spatial scale and density; or using prior knowledge regarding the expected distribution of the data or of some underlying spatial or biological feature to select appropriate parameters. In practise, a combination of these two approaches yields the best results, ensuring that the parameters chosen are appropriate for the spatial scales present in the data and justifiable from an experimental or biological perspective.

For the DBSCAN analysis of membrane protein clustering presented in this chapter, two implementations of the algorithm were employed. The multi-scale DBSCAN analysis, results of which are discussed in sections 4.4.1.1-4.8.1 and 4.8.1 uses the method proposed by Daszykowski et al. [236] to determine the optimal neighbourhood radius. This method for determining ε does not use the distribution of distances for objects in the dataset, but estimates ε for a data set with the same dimensionality as the data studied, but uniformly distributed, an example of which is shown in Figure 4-9 b. The distance from each object in the uniformly distributed dataset to its k^{th} nearest neighbour is calculated, where k is equal to MinPts. The calculated distances are sorted, and ε is calculated as the distance equal to the 95% quantile. In this method, ε is dependent on the value of MinPts, with higher values of MinPts resulting in higher values for ε.

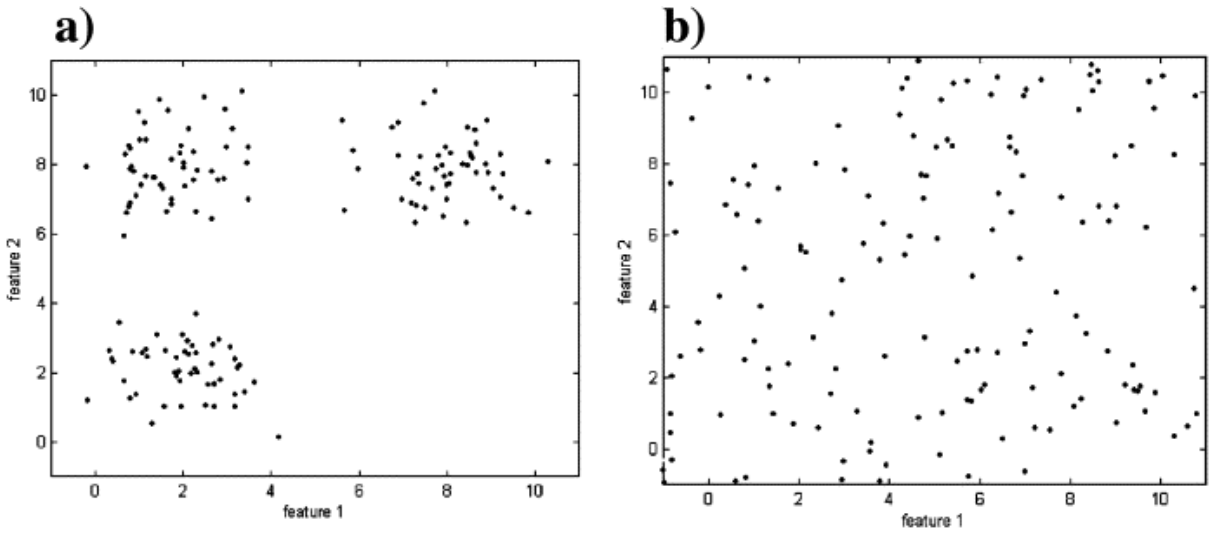

Figure 4-9: Simulated data used in calculation of optimal DBSCAN ε parameter
a) An experimental data set containing 150 objects; b) 150 objects uniformly distributed within the same range as the data in a. Reproduced from [237].

Approaches to selecting ε and MinPts based on the distribution of the data itself, often in combination with some prior knowledge are widely used. It has been suggested that for SMLM approaches a good starting point for choosing ε can be the median localisation precision [232]. Median localisation precision is a measure of the precision with which the position of a single fluorescent emitter can be estimated, and is often reported as an estimate for the achieved resolution [238]. ε should also be chosen to be higher than the localisation precision, to increase the likelihood that the localisations found in the cluster are representative of more than one molecule (assuming that a single molecule is represented by several localisations due to multiple blinking events) [234]. An extension of this argument says that the number of points required to form a cluster should also be sufficiently high that the localisations grouped together are likely to represent more than one molecule, however, without performing experiments to determine the number of localisations typically resulting from a single molecule, this should be treated with caution as setting the value too high would risk not discovering clusters containing a small number of molecules, where each molecule may only have been localised once or twice.

Looking at the distribution of distances between points in the data set can also help in selecting an ε value at the appropriate spatial scale [224]. For example, looking at the histogram of distances to nearest neighbours in the dataset can give an idea of the scale at which the data is organised, and assist with selecting a highest sensible value for ε, if the localisation precision is the minimum value. Having selected ε it is then possible to look at the number of neighbours each member of the data set has within the ε-radius, and combine this with any knowledge of the data from a biological persepective or based on other experimental results, such as electron microscopy (e.g. protein A is found in dimers so MinPts should be an even number, or protein B is known to form clusters of 10 molecules) to determine sensible values for the parameters ε and MinPts.

The method described in the original DBSCAN paper to determine ε can also be used, and is based on the turning point in the graph of the distance from each point to its k^{th} nearest neighbour [224], [234].

4.6 Colocalisation analysis– molecular colocalisation and cluster colocalisation

Co-localisation analysis of SMLM poses an extra challenge over the colocalisation analysis routinely performed for diffraction limited images, which actually only measures the colocalisation of the diffraction patterns, and so does not tell us about molecular colocalisation, but really only proximity. Determining colocalization in SMLM data is more complicated, because whilst we have coordinates for the fluorophores, there is still a limit to the localisation precision of 10-20 nm, and uncertainty in position due to the attachment of the fluorophore to the molecule of interest. A recently published approach for analysis of multi-colour SMLM data – ClusDoc, combines molecular colocalisation analysis and DBSCAN clustering [232]. The approach taken by ClusDoc results in a measure of colocalisation of the molecules in the two imaging channels (e.g. protein A and protein B) for every

molecule in the data set, where colocalisation of protein A with protein B is calculated, and vice versa. A schematic diagram illustrating the steps in ClusDoc analysis is shown in

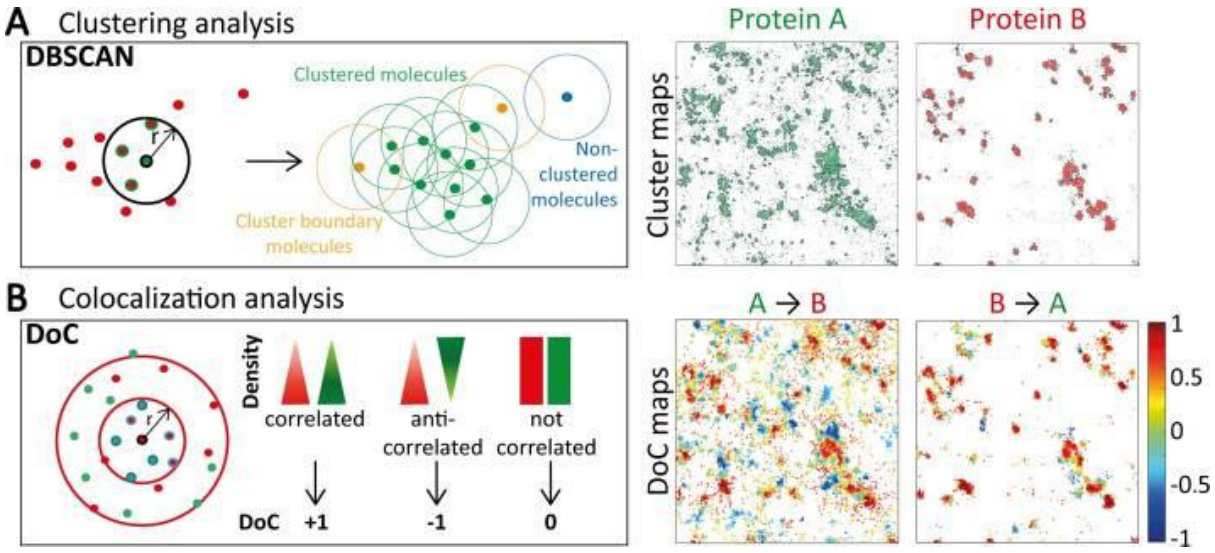

Figure 4-10: Schematic diagram illustrating steps in ClusDoc analysis
A) Illustration of DBSCAN clustering - DBSCAN detects and propagates a cluster if the number of points within a given radius r (ε elsewhere in this thesis) is at least a certain number, in this case 3. On the left-hand side of the left image are the points input for cluster analysis, and on the right-side is the classification of points which would be output from the analysis. The right-most images are maps of clusters detected in an exemplary set of points. Molecules in clusters are coloured green or red and molecules outside clusters are in grey. Cluster contours are highlighted with black lines. B) Illustration of colocalisation analysis – from the coordinates in both channels, the local density in each channel is calculated at increasing radii around each molecule, providing a density gradient for each point in each channel. The two gradients of density are tested for correlation, resulting in a degree of colocalisation (DoC) score for each molecule. DoC scores range from −1 to +1, with −1 indicating segregation, 0 indicating random distribution, and +1 indicating colocalization. This analysis yields colocalization maps for both proteins in which each molecule is color coded according to its DoC score. The cluster and colocalisation maps in this figure are 4 x 4 µm. Reproduced from [232]

The colocalisation analysis is a coordinate based method based on that proposed by Malkusch et al. [239]. Using a coordinate based method rather than an intensity based approach retains information at the single molecule level, where intensity based approaches would lose this by requiring histogramming or blurring of localisations, thereby losing the single molecule resolution. The ClusDoc approach relies on the comparison of the spatial distribution of surrounding localisations from both channels around each individual point. For each molecule of protein A the number of

molecules of protein A and protein B within circles of increasing radius is calculated, respectively, giving a density gradient for both protein A and protein B around the molecule. These density gradients are then corrected by the density at the maximum radius respectively for A and B. The two distributions are then compared by calculating a rank correlation coefficient using Spearman correlation, in which the correlation coefficient is weighted by a value proportional to the nearest neighbour, to avoid long distance effects [232], [239]. This process is repeated for every molecule of protein B, allowing the colocalisation of protein A with protein B and protein B with protein A to be analysed separately. Each molecule is assigned a degree of colocalisation (DoC) score, ranging from -1 to 1, where -1 indicates anti-colocalisation or segregation of the proteins, and 1 indicates perfect colocalisation. This method enables the visualisation of the distribution of colocalisation on a per-molecule basis, separately for each channel, and for the segmentation of clusters into colocalised and non-colocalised populations for further analysis. This is achieved by the use of a threshold for DoC, above which a molecule is considered colocalised, which can then be applied to molecules in the clusters determined by DBSCAN. The DoC threshold is based on the distribution of DoC scores determined in a study performed by Malkusch *et al* [239], where a SMLM dataset was duplicated, and the duplicate set shifted by 10 nm. The majority of localisations in this dataset (>90%) exhibited a DoC score >0.4, and as 10 nm is around the minimum localisation precision which is achieved by SMLM in practise it is reasonable to assume that a 10 nm shift replicates experimental conditions, and therefore 0.4 can be considered a threshold for molecular colocalisation [232], [239]. Applying this to the data generated in this study allowed us to analyse the properties of ErbB2 clusters separately, depending on whether any ErbB2 molecules in the cluster were colocalised with CD82.

4.7 Optimisation of labelling and imaging conditions

Whilst the order of magnitude improvement in resolution offered by super-resolution techniques over diffraction limited imaging does allow unprecedented detail in biological samples to be

resolved, the nature of the techniques also means that optimisation of imaging procedures is arguably more critical than for diffraction limited techniques. Whilst the higher resolution achievable means more detail can be resolved, it also means that changes to the distribution and ultrastructure of proteins and cellular components caused by the many steps involved in fixation, permeabilisation and labelling may be observed, and as such must be taken into account [240], as they can give rise to artefacts in the resulting images. Hence, we undertook several experiments to validate the labelling, imaging and analysis (described in section 4.8) to ensure that artefacts were minimised where possible and at least characterised where not.

In this section steps taken to ensure labelling procedures were appropriate for the samples under investigation, and to assess possible sources of artefacts resulting from the labelling and imaging conditions are detailed.

4.7.1 Permeabilisation of the samples improved labelling

In order to accurately recover information on the distribution of molecules across the surface of the cell, it is important that the fluorescent label is able to access the whole cell membrane so as to be evenly distributed and not introduce artefacts related to the labelling, such as a falsely high density at the cell edge compared to the cell body due to the dye not penetrating under the cell as efficiently. As such, permeabilisation of the samples with 0.5% saponin was trialled to increase penetration of the label under the cell. As shown in Figure 4-11 permeabilisation increased the penetration of the label resulting in more even labelling, but did not seem to introduce artefacts or re-organisation of the membrane. While further work would be required to definitively establish whether there is any effect on the distribution and clustering of proteins under investigation, no obvious disruption is evident from the images presented in Figure 4-11. In addition, previous work from this group and others has shown that permeabilisation with 0.5% saponin does not disturb the distribution of tetraspanins.

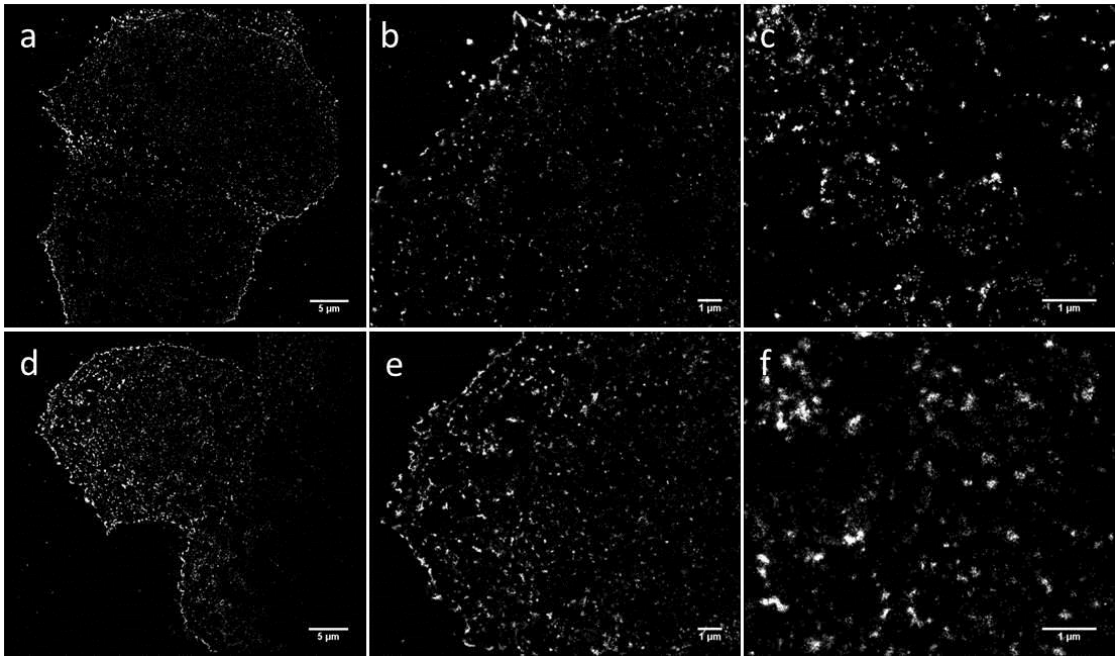

Figure 4-11: Effect of permeabilisation with 0.5% saponin on label distribution in dSTORM imaging samples
dSTORM images of SKBR3 cells over-expressing CD82, labelled with an anti-CD82 antibody (C33) and an Alexa fluor 647 labelled secondary antibody. (a-c) Cells labelled directly after fixations and rinsing, (d-f) cells labelled after permeabilisation with 0.5% saponin for 5 minutes after fixation. (d-f) compared to (a-c) show increased penetration of the label under the cell, whilst not displaying any obvious artefacts introduced by permeabilisation. (a & d scale bars 5 µm, all other scale bars 1 µm)

4.7.2 Validating label concentration via flow cytometry

For optimal labelling of samples for dSTORM, use a concentration of primary antibody that saturates all the available binding sites should be used, so that all the proteins of interest are tagged with an antibody. In this way the resulting super-resolution image will accurately reflect the distribution of protein in the sample, whilst not being over-labelled, so as to minimise the probability of non-specific binding. In order to validate the concentration of antibody used in the experiments presented in this thesis, we performed flow cytometry on samples labelled with varying concentrations of primary antibody.

We performed flow cytometry assays on SKBR3/CD82 (control) cells using concentrations of ErbB2 mAb-2 between 0.4 and 0.13µg/ml and 0.013 mg/ml Mouse IgG FITC-conjugated (Sigma), and the

anti-CD82 mAb C33 at concentrations ranging from 0.67-2 μg/ml and 0.013 mg/ml Mouse IgG FITC-conjugated (Sigma).

Table 4-1 Validation of primary antibody concentration for dSTORM labelling by flow cytometry on SKBR3 cells

Antibody/concentration (μg/ml)	0.4	0.2	0.13
Ab-2 (ErbB2)	100	100	99.5

Table 4-2 Validation of primary antibody concentration for dSTORM labelling by flow cytometry on SKBR3 cells

Antibody/concentration (μg/ml)	2	1	0.67
C33 (CD82)	100	100	100

The data indicated that cells were being efficiently detected even at the lowest concentrations, of 0.13 μg/ml for Ab-2 and 0.67 μg/ml for C33. Although according to this data the concentration of antibody could be reduced further, as the dilutions were in line with manufacturer recommended amounts and other lab protocols we chose to use 0.5 μg/ml C33 and 0.2 μg/ml Ab-2 for most experiments.

To determine whether it was possible label MCF7 cells, which express low levels of ErbB2, effectively enough to return sufficient signal for imaging we trialled labelling with Herceptin, Herceptin Fab fragments, and Ab-2 at concentrations from 1-4 μg/ml. Herceptin was chosen as the whole IgG is known to specifically bind ErbB2, and being a humanised antibody would allow dual colour labelling in conjunction with a second mouse antibody. Herceptin-Fab was investigated as the use of Fab fragments over whole IgG antibodies reduces label-target distance and can therefore result in higher effective resolution for SMLM. Ab-2 was chosen as a control, as this commercial antibody has previously been used successfully by this group to label ErbB2 for immunofluorescence.

We elected to use higher concentrations than for SKBR3 cells to ensure the binding sites were saturated, as at lower concentrations visual assessment of samples appeared to show poor labelling.

As the signal we expect to see from ErbB2 is much lower on MCF7 cells than on SKBR3, the optimisation of this concentration was especially important.

Table 4-3 Investigating ErbB2 labelling on MCF7 cells using Herceptin, Herceptin Fab fragments and Ab-2 antibody

Antibody/concentration (μg/ml)	1	2	3	4
Herceptin	94.16	97.95	93.09	88.09
Herceptin-Fab	91.85	93.87	91.17	91.62
Ab-2	92.97	93.8	91.88	92.4

Detection percentages were similar for both Herceptin and Herceptin Fab fragments, as well as the control Ab-2 antibody, so we trialled whole Herceptin with anti-human secondary antibodies, and Herceptin Fabs with avidin conjugated secondary antibodies to determine which gave the best labelling for imaging. These results are presented in section 4.3.

4.7.3 Negative controls

We performed negative controls to ensure the secondary antibodies were binding only the target labelled with the appropriate primary antibody, and not binding to other sites or antibody of a different species. Samples labelled with either human or mouse primary antibody were incubated with a mouse or human fluorophore tagged secondary antibody respectively, to demonstrate that in dual colour experiments cross-talk between the probes did not occur.

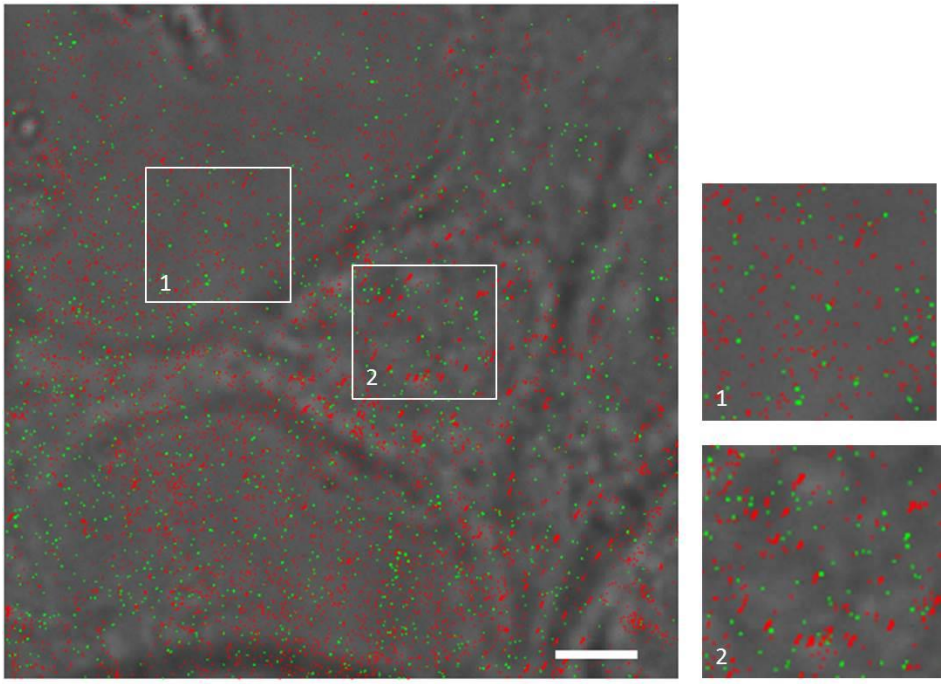

Figure 4-12: Cross-talk negative control images – MCF7 puro labelled with Herceptin and Alexa 647
MCF7 puro cells labelled with Herceptin and anti-human Alexa 647, and anti-mouse Alexa 488. Plotted points represent a localised molecule position after reconstruction, green points representing Alexa 488 molecules and red Alexa 647. Scale bar 5 μm.

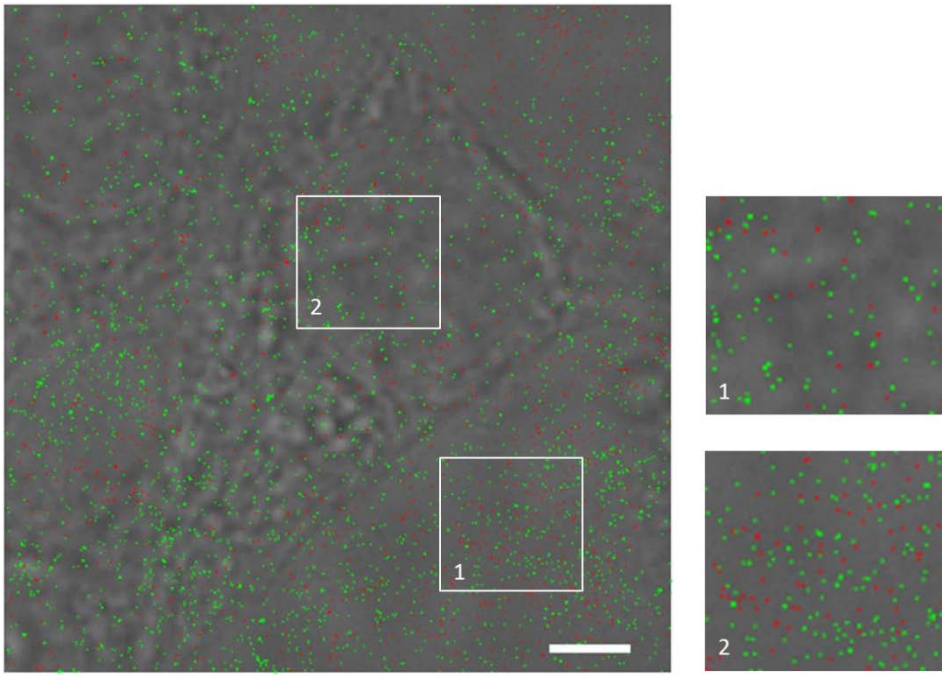

Figure 4-13: Cross-talk negative control images – MCF7 puro labelled with C33 and Alexa 488
MCF7 puro cells labelled with C33 and anti-mouse Alexa 488 and anti-human 647. Plotted points represent a localised molecule position after reconstruction, green points representing Alexa 488 molecules and red Alexa 647. Scale bar 5 μm.

Low level background signal across the whole cell is evident in Figure 4-12, however where there is no cell (region 1), the label appears more randomly distributed, while in region 2 underneath the cell the distribution is evidently different, and appears to contain clusters, indicating that recovered clusters are likely to be representative of the true distribution of the protein and not non-specific binding. We can also see 488 signal across the image, which appears randomly distributed in both regions 1 and 2, and is not colocalised with 647 signal indicating that cross-talk between the antibodies is absent.

Similarly, in Figure 4-13 background signal from both labels is evident across the whole image, however the signal from the 647 label is much lower in this image, where there was no primary antibody to bind the anti-human 647 label applied, indicating that a possible cause of the background signal is primary antibody sticking to the glass, rather than probe cross-talk. We can see little to no colocalization of the labels indicating the absence of crosstalk between the antibodies, however the distribution of the 488 label on the cell is not as markedly different as for the 647 label in Figure 4-12, and in fact the level of signal appears lower here. Despite permeabilisation of the cells improving dye penetration the dye may not access the underneath of the cell as easily as the coverslip so this may be one reason why signal appears lower underneath the cell. As MCF7 cells express a low level of the target protein, this may also explain the lower density of signal, as there is little protein available for the antibody to bind.

4.8 Development and optimisation of computational analysis methods

In order to fulfil the aims of classifying ErbB2 cluster properties in different cell lines, under different conditions and coincidentally with differing levels of CD82 expression quantitative analysis methods were required. Previous work has shown that ErbB2 is clustered on the surface of the cell lines used in this study [37], [241]–[243], but the precise size and shape of clusters expected - particularly with respect to the distribution of CD82 - was not known. Hence, we elected to use DBSCAN to perform

clustering on the data as this method can extract arbitrary cluster shapes rather than looking for circles (as Ripley's K does). We then performed further investigations to determine how to optimise the analysis to maximise the information recovered from the data. Initially we used a multi-pass implementation of DBSCAN, which allowed us to determine the detailed sub-structure of cluster distribution. This implementation of DBSCAN used the Daszykowski method described in section 4.5.2 for selecting the ε radius parameter for DBSCAN using the distance to the k^{th} nearest neighbour. We initially chose to use this method to estimate a value for ε, since doing so results in a selection unbiased by any expectations regarding the spatial distribution of the data. After developing an analysis procedure using this method, we moved on to performing dual colour imaging, and discovered a solution for combining molecular colocalisation with DBSCAN analysis – ClusDoc [232]. ClusDoc uses a different implementation of DBSCAN, and requires the clustering parameters to be input manually rather than determined by the data. At this point we conducted a further investigation of the importance of the DBSCAN parameters, and methods for selecting appropriate values. Subsequently, we determined that the values returned by the Daszykowski method for ε were higher than those being suggested in the literature for analysis of SMLM data, and changing with each iteration as the filtered set of points from the last pass was treated as a new point distribution and the optimal ε calculation repeated. The values of ε returned were also higher than those that would be suggested by the experimental data and biological justifications. We selected the parameters to use for the ClusDoc analysis based on a combination of the spatial distribution of the data and biological justifications. We were subsequently able to detect colocalisation of the molecules in each channel, and examine the effect of different cellular conditions on the cluster properties and colocalisation.

4.8.1 Optimisation of cluster analysis with DBSCAN

The implementation of DBSCAN which was used to analyse the results presented in this section has the capability of performing multiple passes over the data set. In each pass the data is clustered, and

then the clusters found in that pass are carried forward, while the points deemed to be background/non-clustered are not, and the clustering is iterated again. Effectively, each pass over the data finds clusters within clusters. It was necessary to determine which pass of clustering the clustering algorithm would reveal the most information.

Figure 4-14 shows the clusters detected by each iteration of DBSCAN, demonstrating how the clusters from earlier iterations are “re-clustered” and broken down further, revealing finer structure. However, two problems with the clustering approach are also evident. Firstly in Figure 4-14 A in particular it can be seen that some clusters from later iterations of DBSCAN appear larger (yellow clusters from the third pass, and red from the sixth) than those from earlier iterations, where the expectation is that the clusters should be smaller. This is due to the density of points being low, as the number of points passed to the clustering algorithm decreases with each iteration as the noise points from previous iterations are discarded, and therefore the automatically determined value for ε being high, resulting in artefactually large clusters being detected. This is also evident in Figure 4-14 A where the fluorophore used was Alexa-488 compared to Figure 4-14 B where it was Alexa-647, resulting in a lower signal density, and therefore much larger clusters being detected, including those outside the cell area, which seems to happen where the signal density is not high enough for noise points outside the cell (randomly distributed) and true signal underneath the cell (expected to be clustered) to be distinguished.

In future work, this investigation would be repeated with the ε value kept constant between iterations. In the analysis presented here, ε was recalculated for each pass of the algorithm, based on the spatial distribution of the points carried over from the previous iteration.

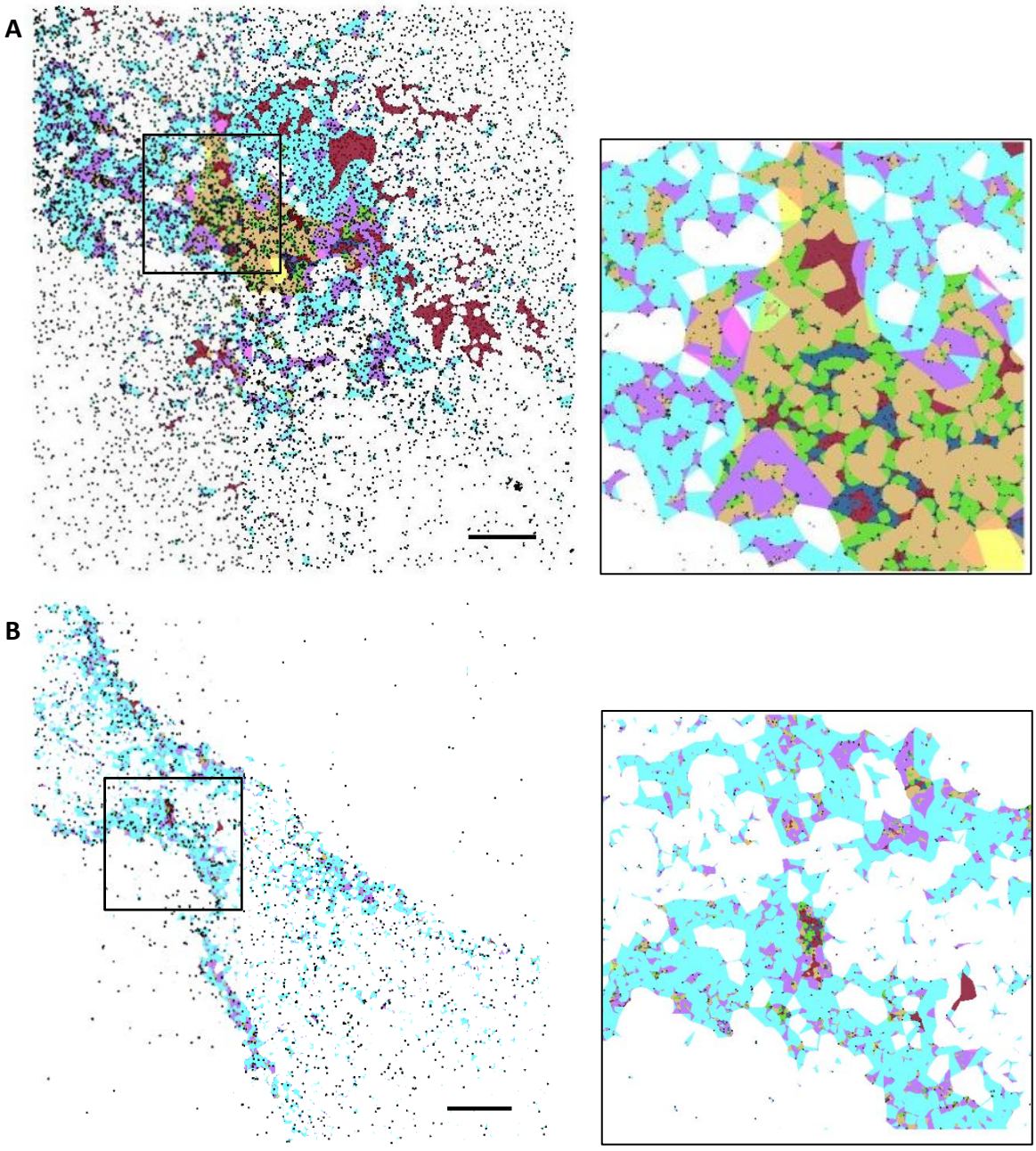

Figure 4-14: Multi-pass clustering of ErbB2 and CD82 on dual labelled SKBR3/zeo cells
A)All clusters recovered by DBSCAN analysis of the full field of view of Alexa-488 labelled ErbB2 on SKBR3/zeo cell, overlaid with molecule localisations. B) All clusters recovered by DBSCAN analysis of the full field of view of Alexa-647 labelled CD82 on SKBR3/zeo cell, overlaid with molecule localisations. Not all localisations from the 647 channel are plotted in B - although all were used to calculate the clusters - as due to the high density of localisations the coloured clusters cannot easily be distinguished from the black points representing the molecular localisations when all are plotted and overlaid. In both A and B the colours of the clusters correspond to the iteration of DBSCAN from which they were returned as follows: cyan – 1; magenta – 2; yellow – 3; green – 4; blue – 5; red – 6. Insets – 10x10 μm zoomed in view to better show subclusters. Scale bar 5μm.

In order to determine which level of clustering revealed the most information, we examined the number of clusters detected in each pass. Figure 4-15 shows how the number of clusters recovered varies according to the number of iterations of the multi-pass DBSCAN algorithm, while Figure 4-16 shows how the number of molecules per cluster varies.

The shape of the curve of the number of clusters versus pass number shows that as the multi-pass clustering iterates those clusters carried forward from the first pass, from analysis of ErbB2 localisations, and the first and second pass when analysing CD82 localisations, are broken down into finer structures in the subsequent pass, revealing more detail regarding the distribution of the protein. Beyond this, the number of clusters returned in a pass begins to decrease, indicating that information is being discarded. That the cluster number peaks for CD82 in the third pass and for ErbB2 in the second pass indicates that the spatial organisation of CD82 has structure on a smaller scale than ErbB2.

The fact that the number of molecules per cluster increases in the later iterations of the clustering is due to the fact that as the density of points in the data-set reduces (due to noise points from the previous iteration not being carried forward for further analysis) the value calculated for the neighbourhood radius ε increases, and therefore larger clusters are found (as also observed in the dual colour data acquired with varying MEA concentration shown in Figure 4-4). For this section of work data returned from the second pass of the algorithm was used to maximise the information recovered from both proteins. If this algorithm is applied in future work it may be necessary to consider optimising the pass number separately for each protein under investigation, to maximise the information returned from both channels simultaneously.

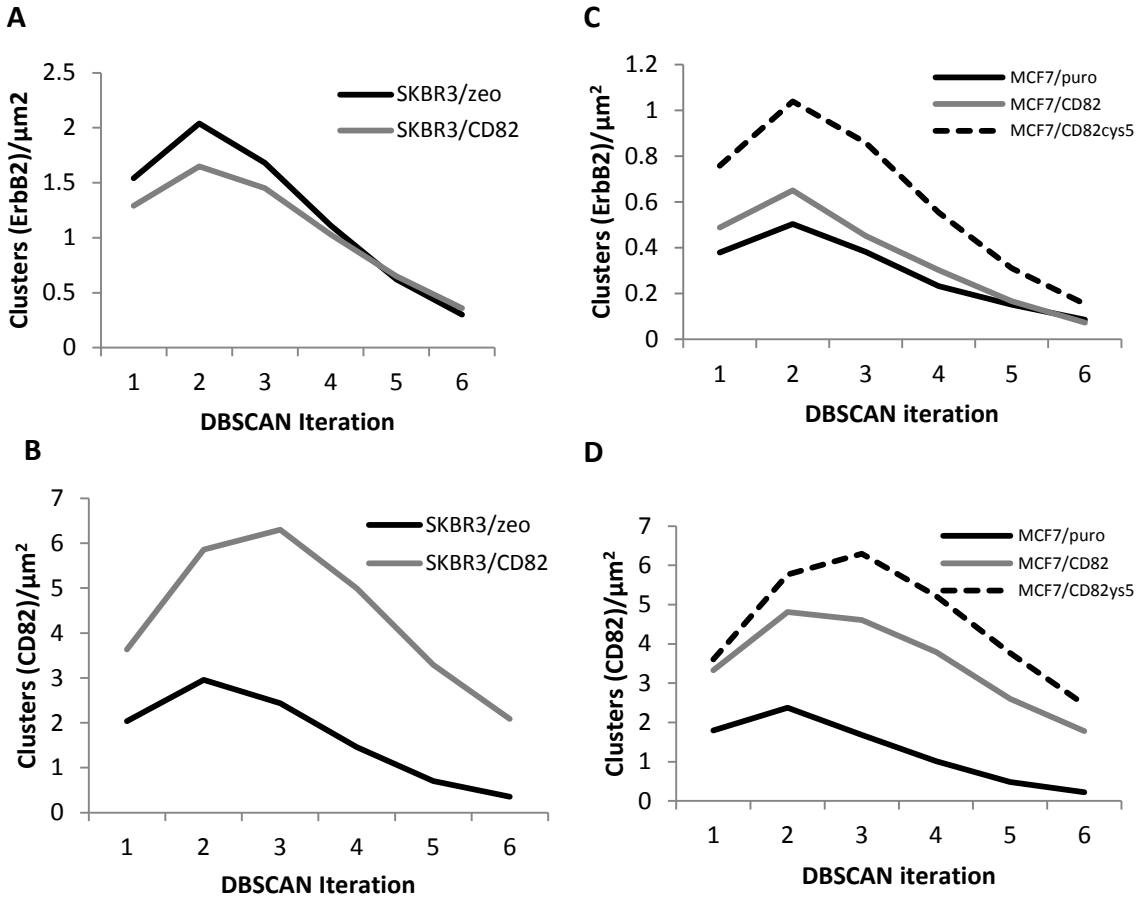

Figure 4-15: Mean number of ErbB2 and CD82 clusters found by multi-pass DBSCAN analysis of Alexa-647 labelled ErbB2 and CD82 on SKBR3 and MCF7 cell lines

5 ROIs, selected from areas entirely within the boundary of the cell, in at least 3 images for each condition were analysed using multi-pass DBSCAN. The number of clusters per μm^2 was calculated by pooling the results of all ROIs analysed in each condition, and dividing the total number of clusters detected after each iteration by the total area analysed. The number of clusters returned is highest after the second iteration of the clustering, for ErbB2 in both cell lines, and CD82 in SKBR3/zeo cells. The maximum number of CD82 clusters in SKBR3/CD82 cells in found after the third iteration of clustering, but the trend of number of clusters increasing between the first and second iteration is observed for both proteins in both cell lines. The images analysed here were acquired in single colour.

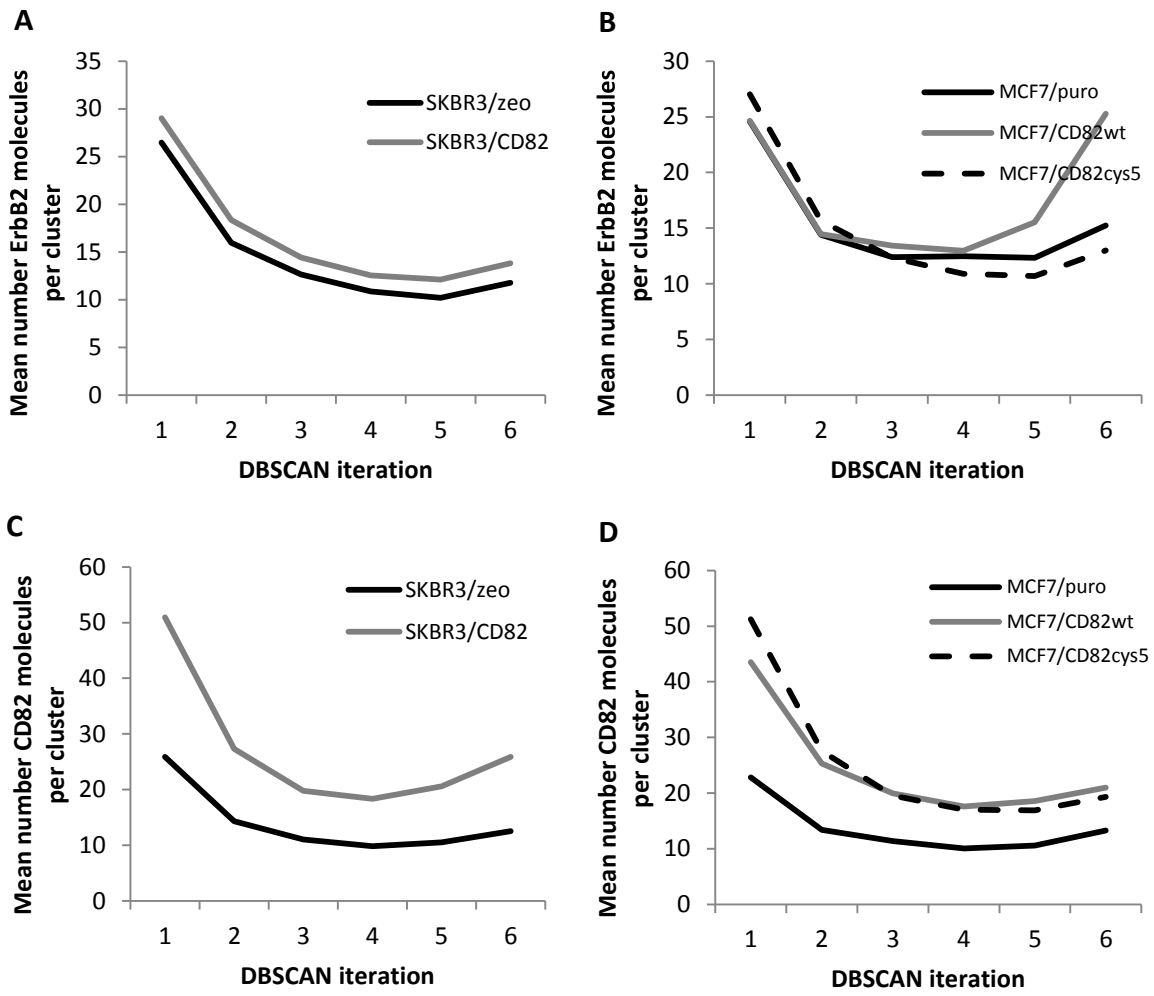

Figure 4-16: Mean number of molecules of ErbB2 and CD82 in clusters found by multi-pass DBSCAN analysis of Alexa-647 labelled ErbB2 and CD82 on SKBR3 and MCF7 cell lines
5 ROIs in at least 3 images for each condition were analysed using multi-pass DBSCAN, and the mean number of molecules per cluster was calculated for all clusters of ErbB2 or CD82 found in each iteration of the clustering. In all cases the mean number of molecules per cluster (data pooled as described above) reduces between the first and third iteration of the clustering algorithm. Beyond the third iteration the mean number of molecules begins to increase as the clusters detected begin to encompass more of the molecules in the ROI.

4.8.2 Analysis of data by ROI selection vs analysing the full field of view – investigation of whether ROI selection influences or biases the results compared to analysis of the full field of view

Deschout et al. suggest that selection of regions of interest (ROIs) to conduct cluster analysis can result in a significantly biased estimation of the protein distribution [195], and it seems especially likely for this to be true if care is not taken to choose ROIs in a consistent manner across different images/datasets, as by visual inspection of dSTORM images it can be seen that protein distribution

appears to be different across the body of the cell compared to at the cell edge. In this work, analysis was performed using ROIs selected under the body of the cell so that sampling was consistent. However, to determine whether ROI selection was introducing bias to the results, or resulting in the exclusion of clusters which could contain interesting information, a study examining the results of clustering with DBSCAN on images of ErbB2 labelled with Ab-2 and Alexa 647 on SKBR3 cells was carried out, where clustering was performed on either the full field of view of the image, ROIs selected under the body of the cell, or ROIs selected around the edge of the cell.

This allowed determination of whether analysis of cell-edge points or cell-body points was more appropriate, and whether different results are seen when the cell-edge points are included or excluded from the analysis.

The first consideration was how well DBSCAN performs in terms of classifying noise points outside of the cell, which are expected to be randomly distributed due to non-specific binding of the fluorophore to the glass coverslip, as noise.

Figure 4-17 shows a plot of the localisations in an exemplary dSTORM image from this study, and how these points were classified by DBSCAN analysis as either noise (black points) or clustered (red points); illustrating that in general DBSCAN performs well in terms of classifying these points as noise, and that within the cell both clusters and randomly distributed noise points are found. Few clusters are found in the points which are outside the cell, in comparison to the number which can be observed within the cell where they are expected to be found. This indicates that it may be possible to use the full field of view for cluster analysis, without results being significantly influenced by signal resulting from the non-specific binding of the probe to the glass coverslip. However, in this case it would not be possible to compare parameters such as molecules or clusters per unit area without applying some kind of segmentation to separate the cell from the background and

accurately calculate the area covered, which would be difficult to implement due to the lack of a clear boundary in the image between the cell and the coverslip.

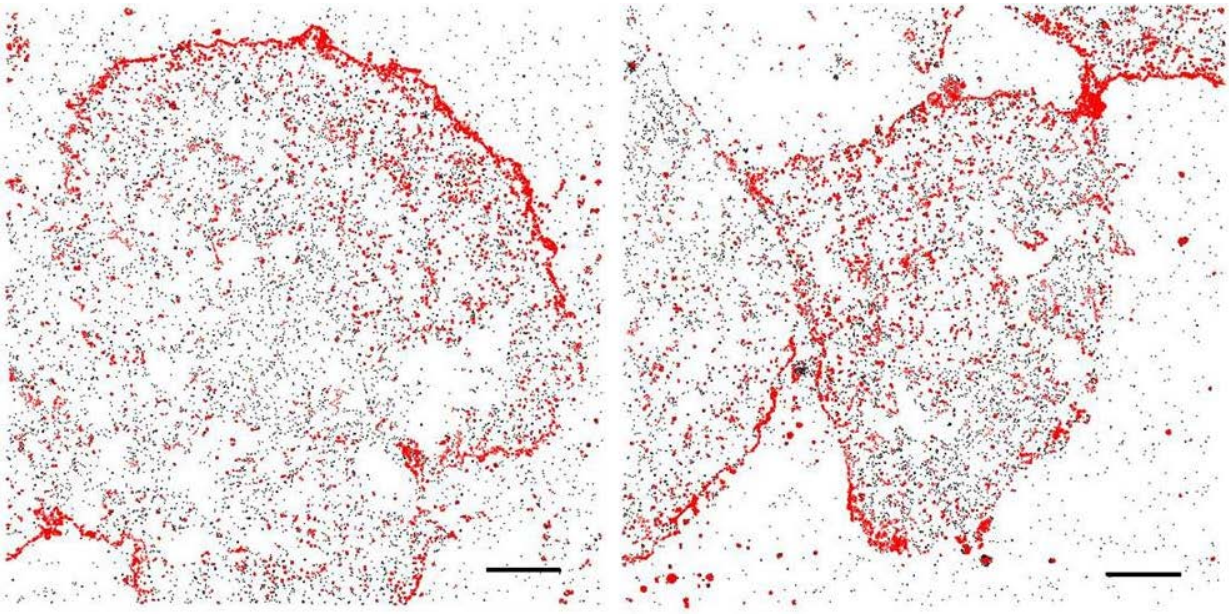

Figure 4-17: Classification of points as noise or clustered by DBSCAN
Using the entire field of view of the reconstructed super-resolution data clustering was carried out using the multi-pass DBSCAN algorithm. All points classified as noise by the analysis are plotted in black, with points classified as within a cluster plotted in red. The images shown here are exemplary dSTORM reconstructions of ErbB2 on SKBR3/zeo, labelled with anti-ErbB2 mAb-2 and goat anti-mouse conjugated Alexa 647. Scale bar 5 μm.

Figure 4-17 highlights the difference in protein distribution at the edge of the cell vs under the cell body, with proteins seeming more densely localised at the cell edge. To consider the effect that this local distribution has on the overall cluster analysis, and to determine if cluster properties are significantly different at the cell edge, or showing changes in cluster properties different to those clusters in the cell body, cluster analysis was carried out under three conditions – using the whole field of view, using ROIs selected at the cell edge, and using ROIs selected under the cell body. An example of the latter two of these conditions is shown in Figure 4-18.

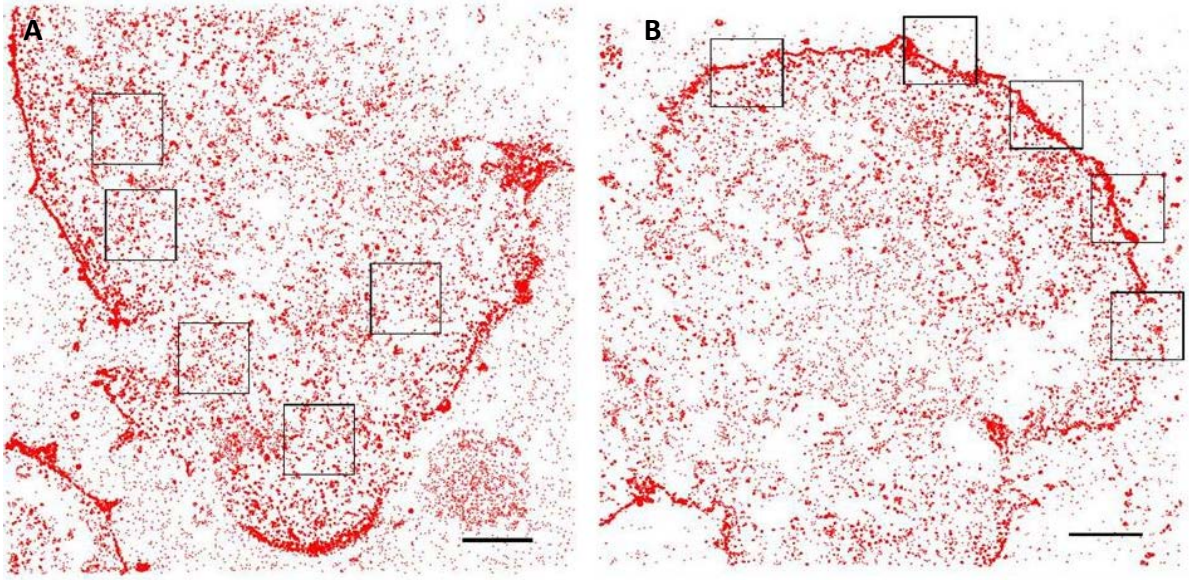

Figure 4-18: Example ROIs selected for cluster analysis of ErbB2 on SKBR3 cells
Figure shows two examples of ErbB2 on SKBR3/zeo cells, labelled with anti-ErbB2 mAb-2 and goat anti-mouse conjugated Alexa 647 with the ROIs used for DBSCAN analysis. ROIs were selected either under the main cell body (A) or around the periphery of the cell (B) to compare clustering results.

Using ROIs selected as shown above cluster analysis was performed on 3 localisation images of ErbB2 distribution on SKBR3/zeo and SKBR3/CD82 over-expressing cells, and the results obtained from the different analysis conditions compared. Figure 4-19 and Figure 4-20 show the ROIs selected from the cells shown in Figure 4-18, along with the recovered clusters.

To verify whether a difference in the respective distribution of either protein would be observed in the different analysis conditions, analysis was repeated using the full-field of the image, or ROIs selected from the cell-body or cell-edge), on each cell line (SKBR3/zeo and SKBR3/CD82) for both ErbB2 and CD82. The data from all ROIs in all images was pooled for each condition, and the distribution of cluster parameters compared, shown in Figure 4-21 and quantified in Table 4-4 and Table 4-5.

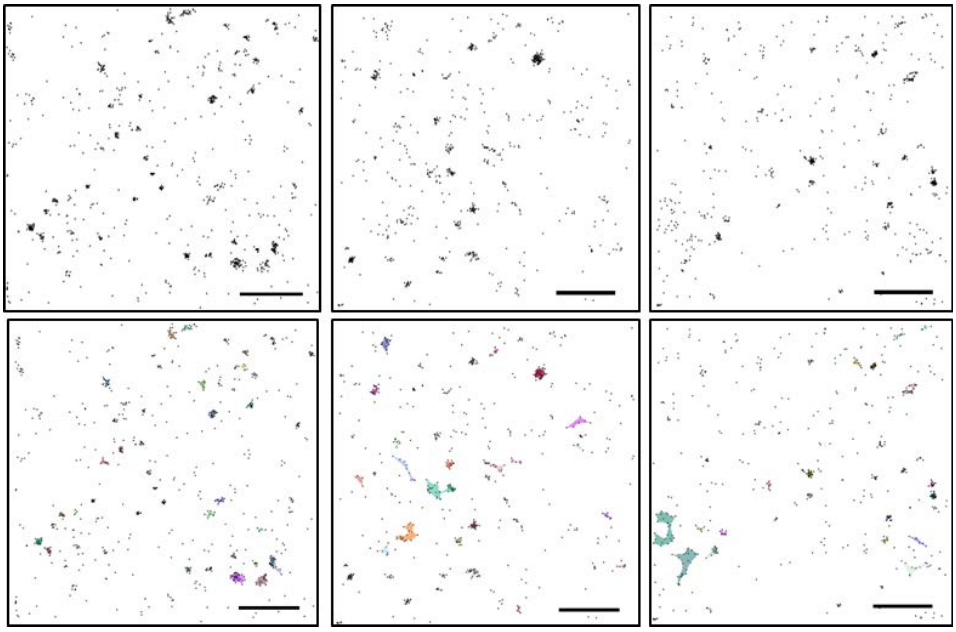

Figure 4-19: Point distribution and recovered clusters of ErbB2 in ROIs selected under the body of an SKBR3 cell (cell from Figure 4-18 A)
Molecule coordinates contained within three ROIs selected under the body of an SKBR3/zeo cell are shown here. Top row – Molecule coordinates recovered after dSTORM reconstruction are plotted in black (point size arbitrary) to demonstrate the distribution of the protein in cell-body ROIs. Bottom row – Clusters detected by DBSCAN are plotted in randomly generated colours over the top of the molecule coordinates. Scale bar 1 μm.

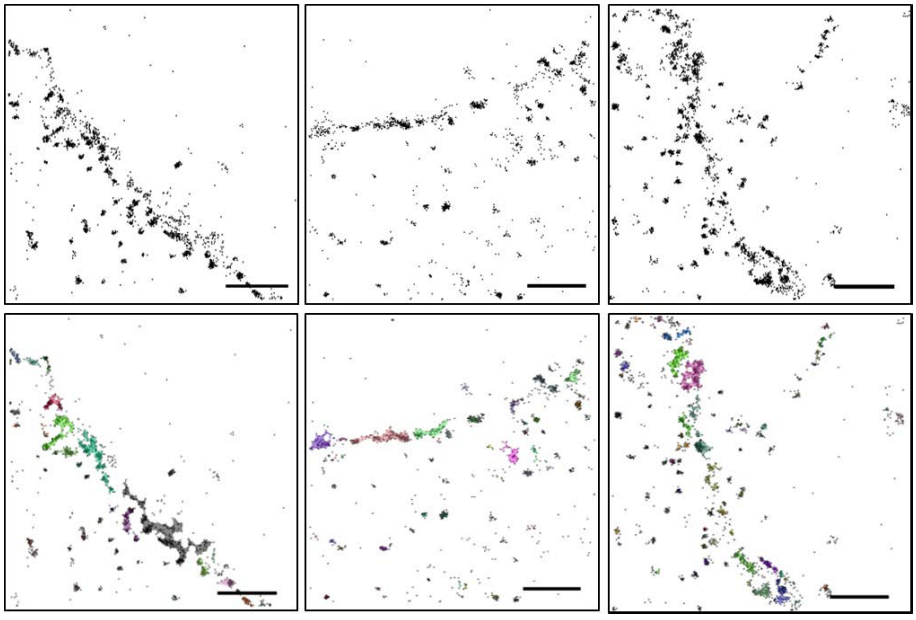

Figure 4-20: Point distribution and recovered clusters of ErbB2 in ROIs selected around the edge of an SKBR3 cell (cell from Figure 4-18 B)
Molecule coordinates contained within three ROIs selected at the edge of an SKBR3/zeo cell are shown here. Top row – Molecule coordinates recovered after dSTORM reconstruction are plotted in black (point size arbitrary) to demonstrate the distribution of the protein in cell-edge ROIs. Bottom

row – Clusters detected by DBSCAN are plotted in randomly generated colours over the top of the molecule coordinates. Scale bar 1 μm.

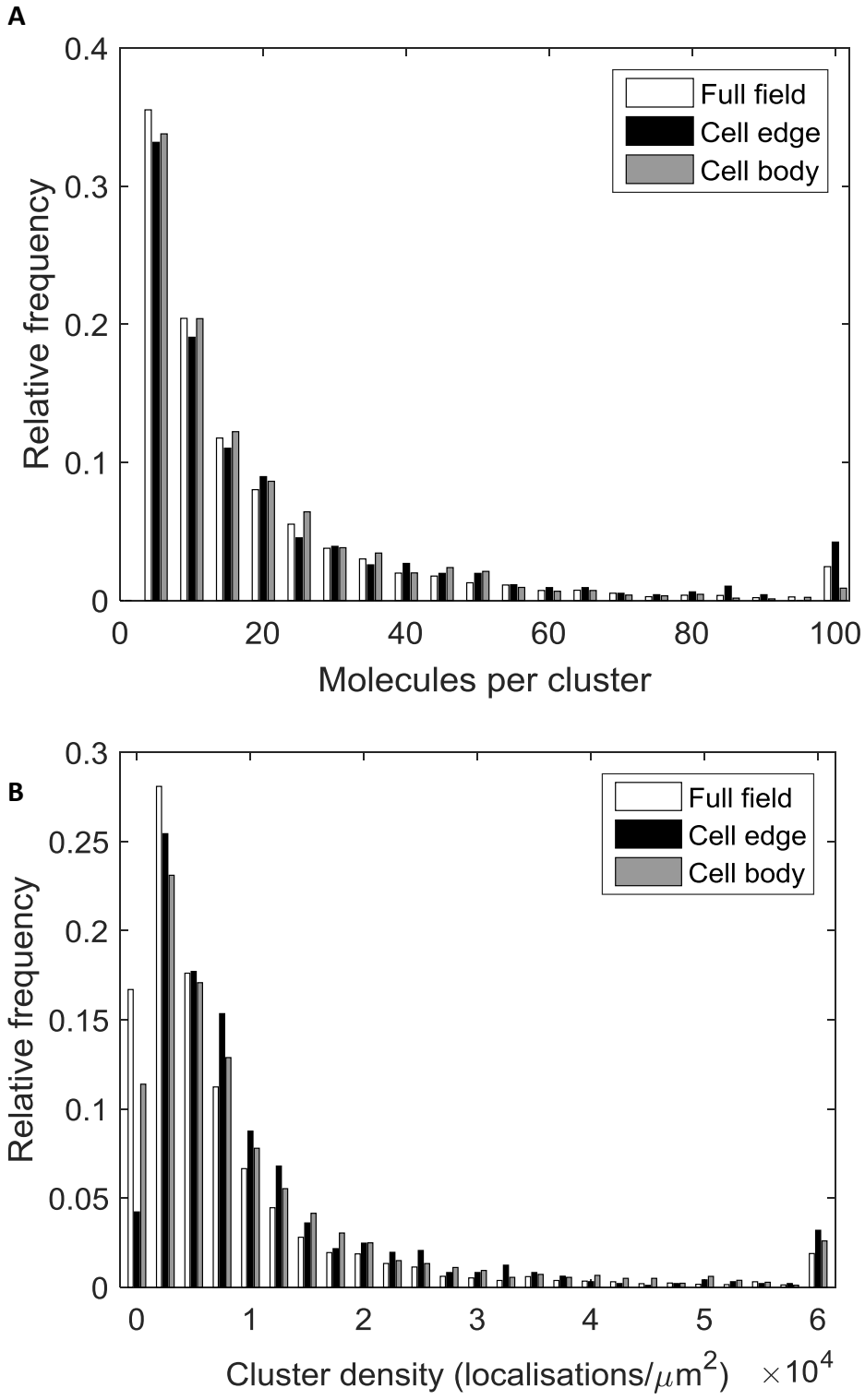

Figure 4-21: The effect of ROI selection on the distribution of cluster parameters of ErbB2 in SKBR3/zeo cells

A) Histogram of number of molecules per cluster against the frequency normalised to the total number of clusters analysed. In the three conditions of full field, cell-edge ROI and cell-body ROI analysis the shape of the distribution is similar, with the majority of clusters being composed of a small (<10) number of molecules. B) Histogram of molecular density inside the cluster calculated

from within the bounds of the alpha shape defined by the cluster. 4 cells were analysed in each condition.

From the data presented in Figure 4-21 A showing the cluster sizes determined in each set of ROIs, it appears that selecting ROIs at the cell edge or under the cell body does not change the distribution of the number of molecules per ErbB2 cluster sizes relative to analysis of the full field of view. From Figure 4-21 B it appears that the distribution of the density in ErbB2 clusters at the cell edge is shifted slightly towards higher densities compared to those under the cell body, with the cell edge having the lowest proportion of clusters in the least dense bin of the histogram. Since the number of molecules per cluster is similar in all conditions, it may be that at the cell edge clusters typically have a smaller area. However, imaging effects must also be considered when analysing these results, as at the cell edge where the membrane curves up around the cell, a larger area of membrane will be within the ~200nm depth of the TIRF field, and fluorescent molecules bound here will therefore contribute signal, which may imply a higher density of localisations, leading to a higher apparent density of molecules, as the z-positions of the molecules are not resolved and therefore are assumed to be present on the same plane as the rest of the membrane.

Table 4-4 shows the mean properties of ErbB2 clusters obtained in all the analysis conditions. Of particular interest is the number of clusters found per μm^2, which is different between the conditions. For the full field analysis this result is not meaningful, as varying but significant amounts of each image analysed were taken up by glass coverslip, where clusters of protein would not be present. Between the cell-edge and cell-body analysis conditions there is a slight difference, with more clusters of ErbB2 being found at the cell edge, as would be expected based on the type of molecule distribution observed in the representative images shown in Figure 4-19 and Figure 4-20. The data also seems to indicate that under the cell body the molecular density within the clusters is decreased in SKBR3/CD82 cells relative to SKBR3/zeo, while remaining relatively unchanged in ROIs selected at the cell edge.

Similar cluster properties for CD82 are recovered from cell-body and cell-edge ROIs, as shown in Table 4-5. The number of clusters per μm^2, the proportion of molecules clustered, and the number of molecules of CD82 per cluster is higher in SKBR3/CD82 than in SKBR3/zeo, although the density of molecules inside the clusters is similar. This indicates that the effect of CD82 overexpression on CD82 clustering in SKBR3 cells is to increase the number and size of CD82 clusters, but not the density within them. There is a slightly higher change in the number of CD82 molecules per cluster between SKBR3/zeo and SKBR3/CD82 in the cell-edge ROIs (1.4x vs 1.02x) however the standard deviation on these numbers is so high this change could be attributable to cell-cell heterogeneity as much as ROI selection.

Taking the results presented in Table 4-4 and Table 4-5, and Figure 4-21 together we observe that at the cell edge more clusters of ErbB2 are found per unit area, but the properties of the clusters are broadly similar between the body and the edge of the cell. Obviously, for ROIs selected at the cell edge not all of the ROI is actually taken up by the cell, so the real number of clusters per unit area is even higher than that calculated, however there is also the possibility that the membrane curvature at the cell edge contributing to a seemingly higher number of localisations and clusters in this area. Therefore, analysis of dSTORM data by selection of cell-body ROIs, which readily allows for standardisation of the area calculated, is an appropriate method which does not result in missing information despite the exclusion of cell-edge features. If there is a particular biological justification for conducting analysis at the cell edge then this can be done also, but for analysis of protein distribution across the membrane, analysis of areas under the cell body is appropriate.

Analysis of the full field of view has the advantage of removing any possibility of user bias in selecting ROIs and would return the most information per image; however other considerations must also be made. From data in Table 4-4 and Table 4-5 we can see that the mean cluster density for both CD82 and ErbB2 is lowest in the full-field analysis, and that although the full-field contains a

significant area which is not covered by the cell and where therefore we would not expect to detect clusters, as any localisations here are most likely due to adherence of the probe to the glass coverslip, we do not see a significant drop in the proportion of molecules which are clustered. Taking into account the fact that the full-field contains all the cell edges, and the proportion of molecules clustered in this area is higher than under the cell body, so this might push up the proportion of molecules clustered, we would still expect to see a drop overall due to the large area not covered by the cell. The fact that this is not observed coupled with the reduced mean density of the clusters found from full-field analysis of both CD82 and Erbb2, indicates that some noise points outside the cell are erroneously clustered. Such clusters add noise into the dataset and should preferably be excluded from the analysis. Simply selecting ROIs around the cell is the best approach for avoiding this. Secondly, as previously described, parameters such as clusters or molecules per μm^2 cannot be compared between conditions without a further step in analysis to accurately calculate the area of the image taken up by the cell, which would increase the complexity and time required for the analysis, and any clusters detected outside the cell area would add noise to the final results.

Finally, the computational requirements for analysing the entire field of view are much higher both in terms of the memory required and the time for the calculations to be made, as the full-field of view contains upwards of 100000 localisations per channel (for 20000 frames of imaging) – analysis of ROIs takes less than 1 minute per image, after ROI selection, while analysis of the full field of view takes 10+ minutes on a PC with 32GB RAM, and is not possible on a laptop with 4GB due to insufficient memory. Thus analysis of the full field of view is limiting in terms of both time and portability of approach. Analysis by ROI selections gives similar results without the added computational requirements.

Choosing ROIs allows analysis to be standardised, and requires considerably less time and computational power. Analysis of ROIs under the cell body is an appropriate method, but

consideration should also be given to the possibility that interesting effects may be seen at the cell edge, and this analysis may be interesting to perform for certain applications. In future work a technique using the bright field or wide-field fluorescence image to produce a mask that could be applied to select only localisations under the cell for cluster analysis could be developed, which would keep the advantages of analysing the whole cell, whilst ensuring noise points outside the cell do not contribute to the total clusters detected.

Table 4-4: ErbB2 cluster properties determined by analysis of the full field of view, ROIs selected at the cell edge or ROIs selected under the cell body in SKBR3/zeo and SKBR3/CD82 cells (N cells SKBR3/zeo = 3, SKBR3/CD82 = 3)

ErbB2 cluster properties	Full-field		Cell-body ROIs		Cell-edge ROIs	
	SKBR3/zeo	SKBR3/CD82	SKBR3/zeo	SKBR3/CD82	SKBR3/zeo	SKBR3/CD82
Molecules per cluster ± s.d.	24.97 ±156.94	32.96 ± 202.23	17.93 ±18.39	18.35 ±21.69	25.44 ±43.66	36.77 ±84.36
Cluster density ± s.d. (molecules/µm^2)	9.84x10^3 ±2.81x10^4	9.78x10^3 ± 4.85x10^4	1.31x10^4 ±4.31x10^4	0.768x10^4 ±2.08x10^4	1.42x10^4 ±4.86x10^4	1.51x10^4 ±4.66x10^4
Clusters/µm^2	1.13	1.20	2.07	1.65	2.59	2.06
Proportion molecules clustered	80.26%	80.88%	73.16%	71.72%	83.22%	84.31%
Total clusters analysed	5564	5909	1809	1028	971	772

Table 4-5: CD82 cluster properties determined by analysis of the full field of view, ROIs selected at the cell edge or ROIs selected under the cell body in SKBR3/zeo and SKBR3/CD82 cells (N cells SKBR3/zeo = 4, SKBR3/CD82 = 3)

CD82 cluster properties	Full-field		Cell-body ROIs		Cell-edge ROIs	
	SKBR3/zeo	SKBR3/CD82	SKBR3/zeo	SKBR3/CD82	SKBR3/zeo	SKBR3/CD82
Molecules per cluster ±s.d.	16.73 ±21.87	31.93 ±75.34	14.31 ±13.26	27.32 ±46.05	16.93 ±21.68	38.28 ±83.89
Cluster density ±s.d. (molecules/µm^2)	8.82x10^3 ±1.79x10^4	9.66x10^3 ±2.21x10^4	1.00x10^4 ±2.09x10^4	1.08x10^4 ±1.89x10^4	0.937x10^4 ±1.42x10^4	1.46x10^4 ±2.76x10^4
Clusters/µm^2	2.36	3.45	2.95	5.86	2.23	5.43
Proportion molecules clustered	77.32%	85.59%	73.50%	81.31%	75.15%	87%
Total clusters analysed	15475	16935	1477	2197	1113	2036

To confirm that choosing to perform analysis on ROIs under the cell body and not including cell edge data would not exclude any changes in cluster properties evident at the cell edge but not under the body, we compared the histograms for cluster density and number of molecules per cluster at the cell edge and under the cell body for in SKBR3/zeo and SKBR3/CD82, as shown in Figure 4-22 and Figure 4-23. We see that in both areas (cell-edge and cell body ROIs), the distributions of cluster properties look similar in both SKBR3/zeo and SKBR3/CD82 cells, and that no significant change is observed in one condition and not the other. Based on these results we can conclude that for ErbB2 and CD82, it is appropriate to carry out analysis using ROIs selected exclusively under the cell body.

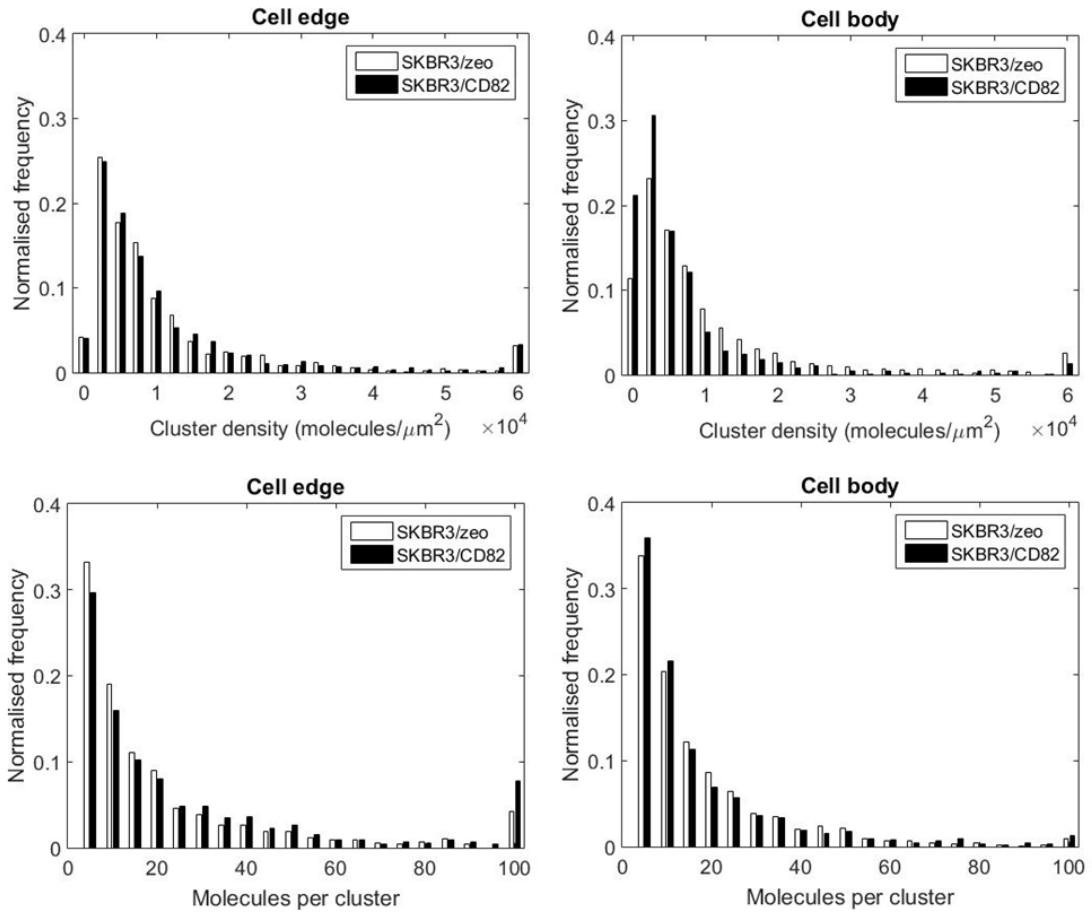

Figure 4-22: ErbB2 cluster properties in SKBR3/zeo and SKBR3/CD82 cells when determined from ROIs selected at the cell edge, or ROIs selected under the cell body.
Top row – cluster density distributions for clusters detected in ROIs at the cell edge (left) or under the cell body (right); bottom row – molecules per cluster distributions for clusters detected at the

cell edge or under the cell body as above. Images were acquired with Alexa-647/Ab-2 labelled ErbB2 in buffer containing 100 mM MEA, and analysed using multi-pass DBSCAN. Cluster properties were calculated from the second iteration of DBSCAN. Frequency was normalised relative to the maximum value of any bin in each condition. Number of cells analysed SKBR3/zeo = 3, SKBR3/CD82 = 3.

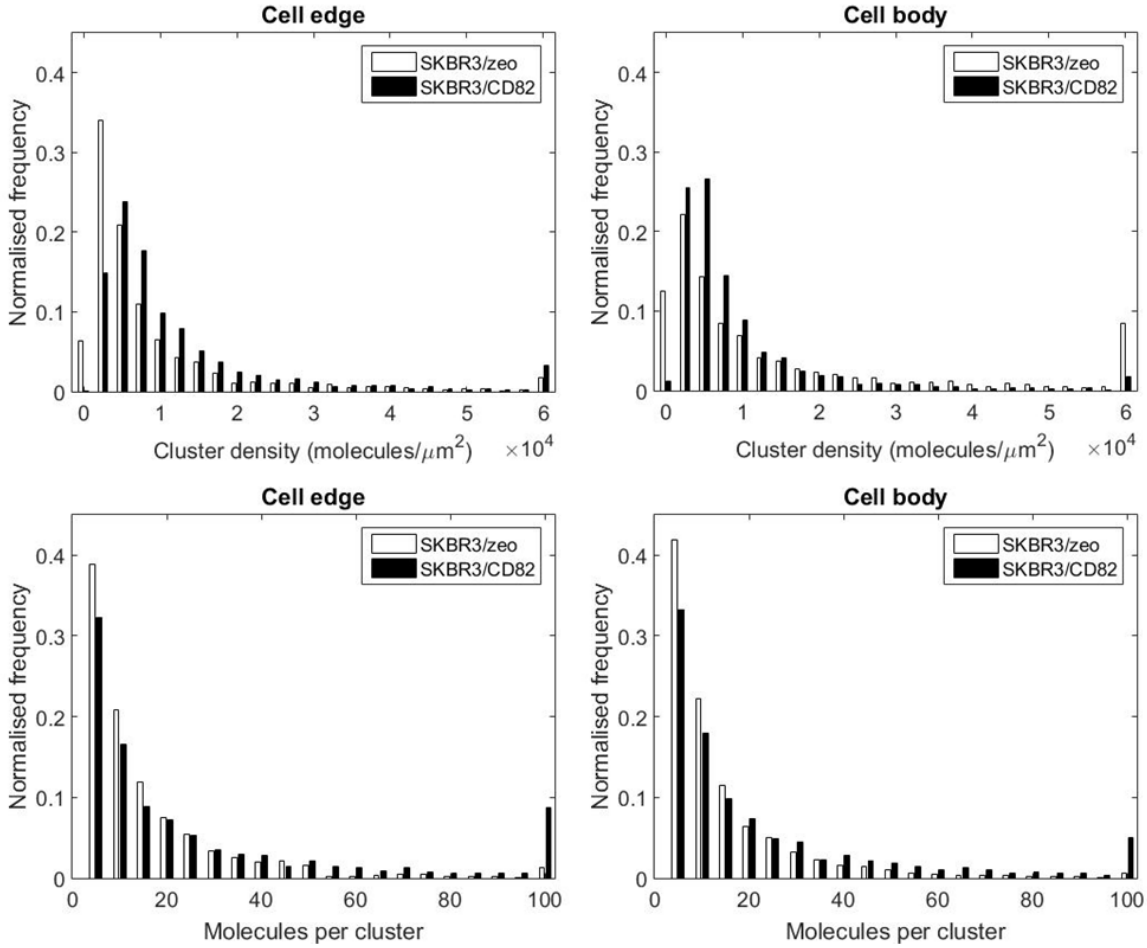

Figure 4-23: CD82 cluster properties in SKBR3/zeo and SKBR3/CD82 cells when determined from ROIs selected at the cell edge, or ROIs selected under the cell body.
Top row – cluster density distributions for clusters detected in ROIs at the cell edge (left) or under the cell body (right); bottom row – molecules per cluster distributions for clusters detected at the cell edge or under the cell body as above. Images were acquired with Alexa-647/C33 labelled CD82 in buffer containing 100 mM MEA, and analysed using multi-pass DBSCAN. Cluster properties were calculated from the second iteration of DBSCAN. Frequency was normalised relative to the maximum value of any bin in each condition. Number of cells analysed SKBR3/zeo = 3, SKBR3/CD82 = 3.

We used the approach to ROI selection validated in the previous section to examine the effect of CD82 expression on ErbB2 clustering in MCF7 cells, which express much lower levels of ErbB2 compared to SKBR3 cells. MCF7 control cells (MCF7/puro), and cells expressing high levels of CD82 (MCF7/CD82wt) were studied, along with cells expressing palmitoylation deficient CD82 (MCF7/CD82cys5). The juxtamembrane cysteines in tetraspanins are potential sites for

palmitoylation, and CD82cys5 is a CD82 mutant where all 5 potential palmitoylation sites were mutated (C>A) to prevent acetylation. Palmitoylation plays an important role in the organisation of tetraspanins into tetraspanin-enriched microdomains [52], [95], [100], as discussed in the thesis introduction. By removing the possibility for CD82 palmitoylation we expect it to be excluded from TERMs, but not prevented from forming clusters and possibly to see this reflected in the CD82 cluster properties. We may also observe an effect on ErbB2 cluster properties if CD82 TERMs are important for mediating Erbb2 clustering. The effect of removing CD82 palmitoylation has been studied by several groups, and has been shown to reduce the membrane recruitment of PKCα to CD82-enriched microdomains, decrease PKCα cluster diameter and possibly increase the cluster density in acute myeloid leukemia cell lines [51]; and, in the acute myelogenous leukemia progenitor-like cells KG1a, to regulate α4 integrin clustering and cluster density, increasing the number of molecules per cluster relative to the control KG1a cell line and reducing cluster density relative to wild-type CD82 over-expressing KG1a [244]. The palmitoylation of CD82 has also been shown to have an inhibitory effect on migration and invasion of PC3 cells, which was reversed on expression of the palmitoylation deficient mutant, and to effect motility-related subcellular events such as lamellipodia formation and actin cytoskeleton organization, indicating that palmitoylation of CD82 is crucial for the functional integrity of CD82 in the suppression of cancer cell migration and invasion [245].

We did not look at the colocalisation of ErbB2 with CD82 in these cells due to constraints on imaging and analysis posed by the challenges of imaging these cells which express ErbB2 at low levels. However we were able to examine the effect of CD82 expression on the ErbB2 population overall, as shown in Figure 4-24, and quantified in Table 4-6.

The size of ErbB2 clusters both in terms of molecules per cluster and cluster area is increased in MCF7 compared to SKBR3. This may be because ErbB2 is less densely packed on the surface of the

non-overexpressing MCF7 cells, and therefore less likely to be present in homodimers than in the over-expressing SKBR3 - additional quantitative imaging would be required to test this hypothesis. Based on the results presented in Figure 4-24, and Table 4-6 we see that in both MCF7/CD82wt and MCF7/CD82cys5 the size and density of Erbb2 clusters is increased relative to in MCF7/puro, and from Table 4-6 we also see that there are more clusters per μm^2.

There is an increase in the mean number of ErbB2 molecules per cluster in the CD82 over-expressing cells, which is not consistent with the results from CD82 over-expressing SKBR3 cells, and, surprisingly, when the palmitoylation deficient CD82 is expressed, the number of ErbB2 molecules per cluster rises again relative to the wild-type CD82 over-expressing condition. This may indicate that CD82 TERMs play a role in limiting the size of ErbB2 clusters and thus the removal of CD82 palmitoylation results in increased sizes of ErbB2 clusters. However, this would be inconsistent with the rise in ErbB2 cluster size seen between the control and wild-type CD82 over-expressing condition. Further work will be required to investigate the reason for the presence of larger ErbB2 clusters in this cell line.

There is significant variation in ErbB2 level and distribution between cells, and even between ROIs on the same cell. The number of cells imaged in this study was low, but with the acquisition of more data from further studies the effect of inter and intra-cell variation should decrease, and cells could be categorised at the analysis stage as high or low expressors, such as in [243] and [230], and considered as separate populations in subsequent analyses. Such pre-analysis classification may reduce the large variance in the results and yield a more accurate characterisation of cluster properties.

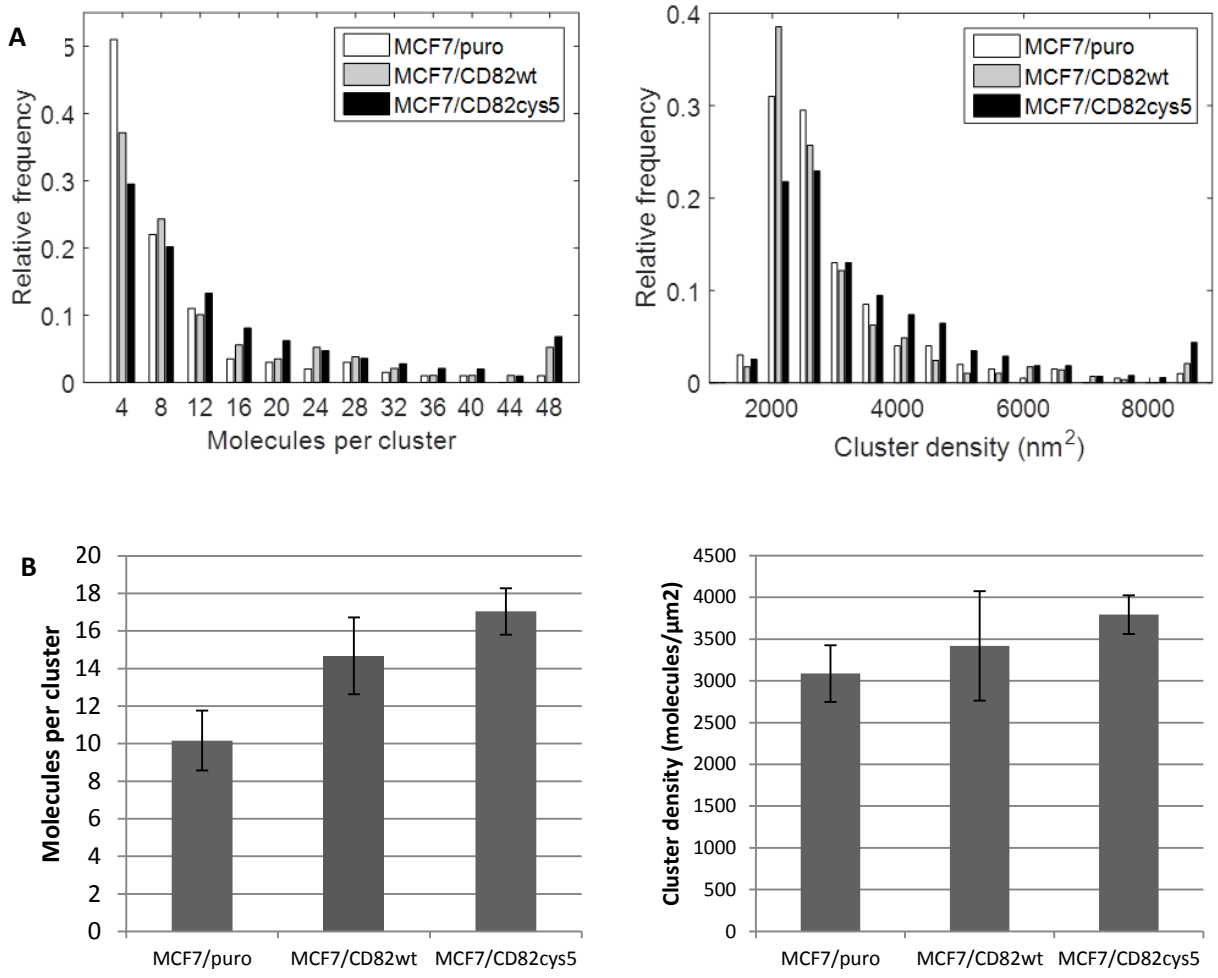

Figure 4-24: Erbb2 cluster properties in MCF7 cells
The properties of ErbB2 clusters detected by DBSCAN analysis of dSTORM data from MCF7 cells labelled with Herceptin and Alexa-647 were determined. Cluster analysis was performed using the ClusDoc implementation of DBSCAN A) Cluster properties in MCF7 cells over-expressing CD82 or a palmitoylation deficient CD82 (CD82 cys5) were compared with those in control cells. Two sample Kolmogorov-Smirnov tests were performed and no statistically significant difference was detected between the distributions of cluster properties (molecules per cluster, cluster area, or cluster density) in cells overexpressing CD82 or expressing the palmitoylation deficient version, and the control cells. B) Mean molecules per cluster and cluster density of ErbB2 in MCF7 cells. Error bars represent twice the standard error on the mean. Number of cells analysed MCF7/puro = 4, MCF7/CD82wt = 4, MCF7/CD82cys5 = 8.

Table 4-6: Erbb2 cluster properties in MCF7 cells

	MCF7/puro	MCF7/CD82wt	MCF7/CD82cys5
Molecules per cluster	10.16±11.25	14.68±17.37	17.04±18.21
Cluster area (nm^2)± s.d.	4027±4562	5478±5890	5302±5526
Cluster density (molecules/ μm^2) ± s.d.	3087±2394	3418±5572	3792±3427
Clusters/μm^2	0.4	0.58	0.87
Total number of clusters	200	288	868

4.9 Analysis of dual colour data - combined molecular colocalisation and DBSCAN clustering

Having shown in section 4.8.2 that CD82 expression does not have a large effect on the cluster properties of ErbB2 in SKBR3 we decided to look more specifically at the spatial interactions between CD82 and ErbB2, and the properties of clusters which colocalised with CD82 to see if any relation between colocalisation with CD82 and ErbB2 cluster properties could be found.

Moving on to consider the analysis of dual colour imaging data with ClusDoc, a MATLAB based GUI for combined molecular colocalisation and cluster analysis [232], the primary consideration for optimising the analysis was the selection of appropriate parameters. As discussed in 4.5.4 the parameters required for DBSCAN are ε and MinPts, and in addition, for the colocalisation analysis, a degree of colocalisation (DoC) threshold is required.

As a starting point, we extracted the values of ε returned by the calculation made in the multi-pass DBSCAN implementation. In one image, the value of ε for the first pass of DBSCAN on the 488 channel (ErbB2 in this experiment) ranged from 174-315 nm, and from 92-112 nm on the 647 channel (CD82); the second pass yielded values ranging from 26-140 nm and 29-75 nm respectively, for 3 ROIs analysed on this image. Given that much published work using DBSCAN for SMLM analysis reports values of around 20-30 nm these values, even for the second pass, seemed high. The value

was calculated separately for every ROI analysed, so may also have been subject to local variations in the protein distribution/label density. In particular, an electron microscopy study of ErbB2 organisation on SKBR3 cells has revealed that the local distribution of ErbB2 can vary significantly across the cell depending on the membrane topography [243]. Although from an optimisation point of view it seems sensible to choose the ε value for each data set, in this case for each ROI, to be optimal for that particular point density, from a biological perspective it is more appropriate to keep the value consistent unless there is reason to suspect that the cluster properties would be distinctly different between different ROIs.

Having made these determinations we decided to use a fixed value of ε and MinPts for all analyses, rather than apply the Daszykowski method to the data from each ROI. To select appropriate parameters we examined the distribution of the data, and combined this with biological justifications.

Firstly, to determine the minimum number of points of ErbB2 and CD82 we would count as a cluster we considered the biology- ErbB2 is found in heterodimers and homodimers (ErbB2 preferentially forms heterodimers with ErbB1/3/4 when it is overexpressed [79]) so we elected to set MinPts for ErbB2 to 4, as this would likely represent the presence of either 2 homodimers or multiple heterodimers in close proximity. For CD82 we elected to set MinPts to 3, since we hypothesise that a minimum of 3 tetraspanins clustered together may be part of a TERM. These parameters assume that one molecule is represented by just one localisation, which in practise may not be the case, however by setting the parameters higher to account for this, smaller clusters, or those where molecules have only been localised once would be missed.

To select a value for ε we then looked at the distribution of the data for ErbB2 and CD82 localisations. These are shown in Figure 4-25 A, from which we can see that a large number of ErbB2 molecules labelled with Alexa 488 are within 40-50 nm of their nearest neighbour, while for CD82

the distribution is shifted more towards smaller distances of 10-20 nm, likely due to the much higher point density in the 647 data.

The intermolecular distance between ErbB2 molecules with Cy3- and Cy5-labeled Herceptin Fab has been determined experimentally by fluorescence resonance energy transfer as 7.1 ± 0.2 nm in N87 cells [246]. In this study whole Herceptin was used as the label for dSTORM, which is larger and therefore introduces an extra distance, such that the total distance between ErbB2 and the label may be 10-20 nm [202]. The mean localisation precision in the 488 channel is 17 nm, so with the label-protein distance of 10-20 nm, plus localisation precision, plus the intermolecular distance, a distance of 50 nm between two localisations could represent two interacting ErbB2 molecules, and therefore this value was chosen as ε for ErbB2 cluster analysis. For CD82 which seemed to more densely localise a lower value for ε of 30 nm was selected. In addition, CD82 is both a smaller molecule than ErbB2, having a molecular weight of around 50k Da, and was labelled with Alexa 647, which has a higher brightness than Alexa 488 and therefore results in a higher mean localisation precision of 13 nm. These factors combined mean that CD82 localisations may have a lower separation than ErbB2 and still be representative of interacting molecules.

Having chosen ε we determined the number of nearest neighbours around each point in each channel, shown in Figure 4-26, to check whether the MinPts values previously selected would result in clusters being propagated. For ErbB2 (Figure 4-26 A) only 12% of points have >3 points within ε, so only these points will be able to form core cluster points, however larger clusters may still be formed from additional boundary points with fewer neighbours. For CD82 (Figure 4-26 B) a larger proportion of points have >2 points within ε, so more points are available as cluster core points. In both cases we can see that the chosen parameters will result in clusters being detected, and furthermore the parameters are justifiable from a physical perspective.

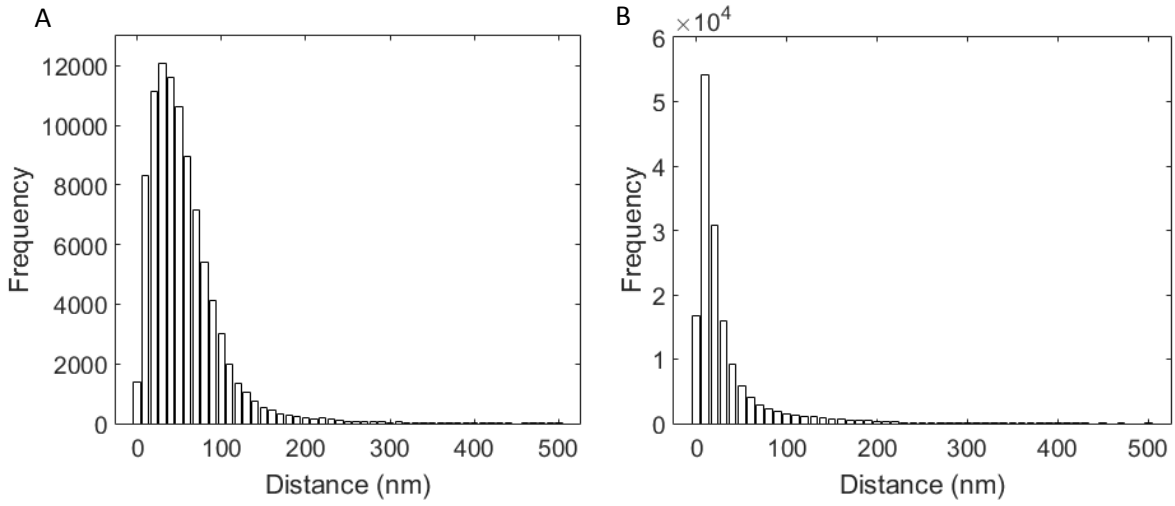

Figure 4-25: Distance to nearest neighbour points in data from each channel of dual labelled SKBR3/zeo

Histogram of distance from each point to its nearest neighbour in the 488 channel (A, ErbB2) and 647 channel (B, CD82) Cells were SKBR3/zeo dual labelled with Hercepting and goat anti-human conjugated Alexa 488, and anti-CD82 mAb-C33 and goat anti-mouse Alexa 647.

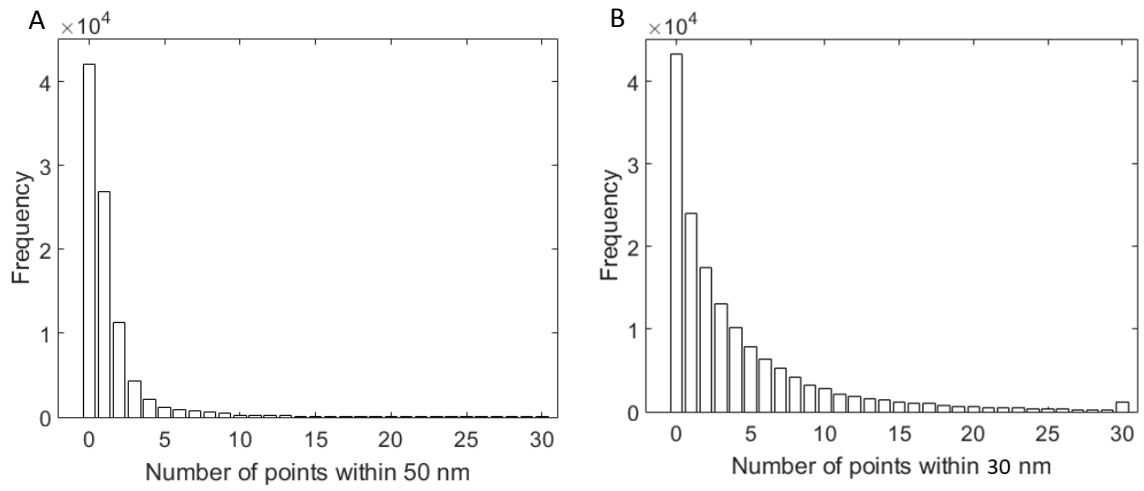

Figure 4-26: Number of points within ε of each point in data from each channel of dual labelled SKBR3/zeo

A) The data in the 488 channel represents ErbB2 localisations. An ε value of 50 nm was chosen for analysis of ErbB2 data, and the histogram above shows the number of points within ε of each point in the channel. The majority of points have < 4 neighbours within the selected ε value of 50 nm. B) The data in the 647 channel represents CD82 localisations, for which a lower ε value of 30 nm was chosen. The histogram represents the number of points within ε of each point in the channel. A higher proportion of molecules in this have >3 neighbours within the selected ε value of 30 nm.

We also investigated the effect that the choice of DBSCAN parameters has on the data recovered, by analysing one image with 6 different parameter combinations, ranging from those suggested by the literature to those determined by the Daszykowski method . The results obtained, shown in Table 4-7 demonstrate that changing the clustering parameters can significantly alter the resultant cluster properties, and that therefore when comparing results between studies the specific clustering method and parameters used should be borne in mind if seeking to make quantitative comparisons.

Table 4-7: CD82 cluster properties in SKBR3/CD82 determined from ClusDoc analysis with DBSCAN cluster parameters MinPts and ε varied from 3-4 and 20-70 nm respectively

	MinPts= 3 ε = 20	MinPts= 3 ε = 50	MinPts=3 ε =70	MinPts= 4 ε = 20	MinPts = 4 ε = 50	MinPts = 4 ε = 70
Clusters per um^2	10.07	5.95	5.21	5.77	4.92	4.43
Cluster area (nm^2)	5237	8108	8115	4791	8443	8354
Molecules per cluster	44.89	29.39	32.50	20.87	29.34	32.41
Density in cluster (mols/um^2)	3986	3040	2881	4247	3041	2881

The other parameter to be selected in ClusDoc analysis is the threshold degree of colocalisation (DoC) above which two localisations are considered to be colocalised. As described in section 4.6 >90% of localisations in a SMLM dataset duplicated and shifted by 10 nm were found to have a DoC >0.4. The mean experimental localisation precision in this work (taking an average from the data in both channels) is comparable at 13 nm, so a DoC threshold of 0.4 is an appropriate selection.

4.9.1 Calculating colocalisation

Using the parameters selected above, analysis using ClusDoc was performed on all dual labelled data. The output of the colocalisation analysis is a list containing a value for the point density around each point, a DoC value, the value of Ripley's L-function at the user input radius, and a binary indicator of whether the value of Ripley's L-function is above the value that would be expected for

randomly distributed points at the same density. These results can be used to produce maps of point density for each molecular species across the ROI; maps of DoC; and pooled to produce histograms of the DoC values for all molecules in an experiment, which can be further sub-classified using the DBSCAN results into DoC distributions for clustered and non-clustered points. Figure **4-27** shows - on an exemplary set of data containing localisations of ErbB2 and CD82 in SKBR3/zeo cells - the stages in ClusDoc analysis, taking the raw data and removing the noise points, calculating density of localisations around points in either channel and the degree of colocalisation at each point.

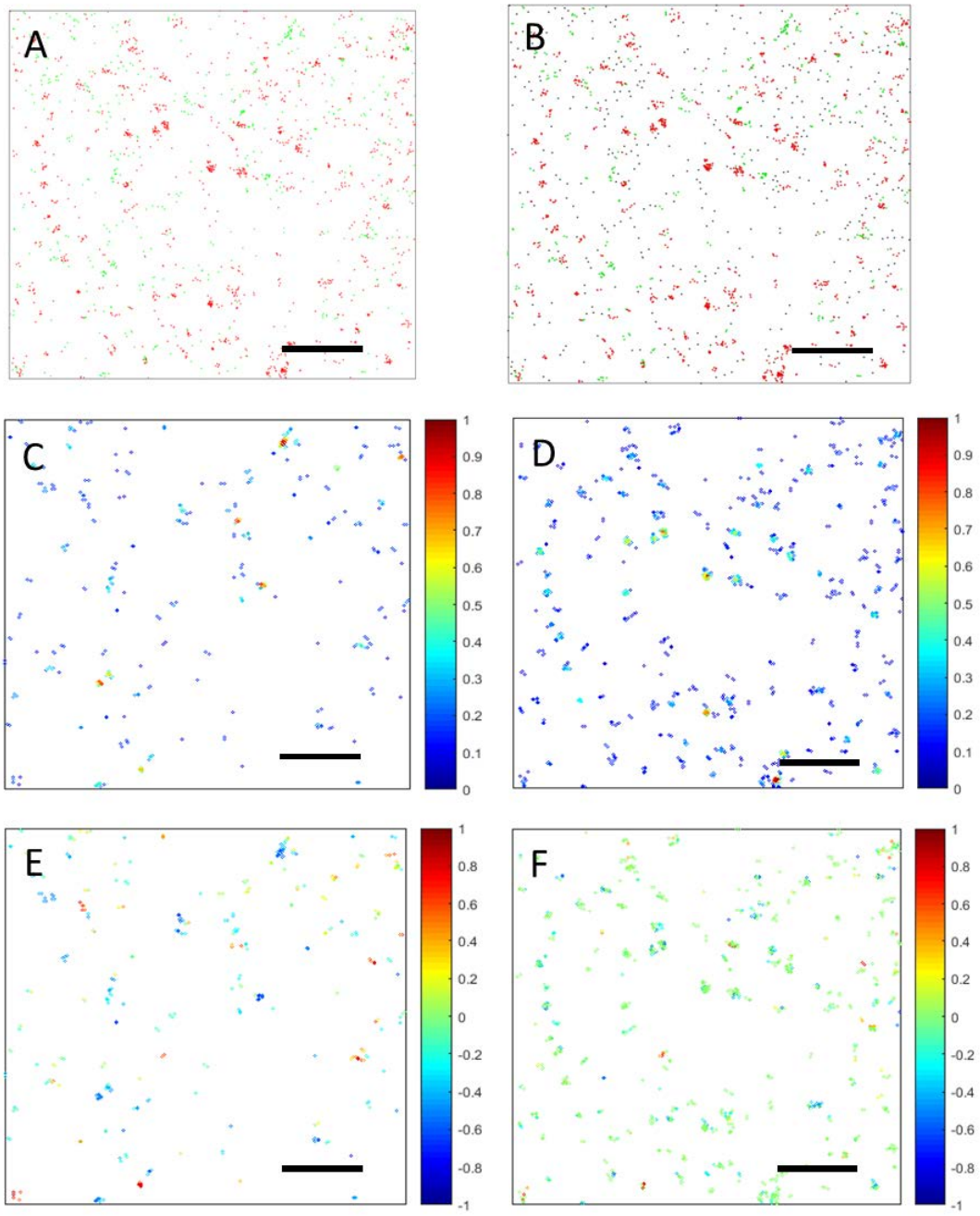

Figure 4-27: Analysis of data with Clus-Doc, combined molecular colocalisation and cluster analysis
A) Exemplary raw data from a single 5000 nm^2 ROI. Green points - localisations in 488 channel; red points - localisations in 647 channel. B) Raw data from A with outliers as detected by Ripley's L(r)-r analysis in black - these points are removed before clustering, but included in DoC calculations. C) Normalised relative density map of points in 488 channel. D) Normalised relative density map of points in 647 channel. Colour bar in C&D shows relative density between least (0) and most dense areas (1) of the ROI. E) Degree of colocalisation score with localisations in the 647 channel for noise filtered points from the 488 channel. -1 indicates negative correlation, or segregation of points from those in the other channel, 1 indicates perfect colocalisation, 0 indicates no correlation between localisations. F) Degree of colocalisation score with localisations in the 488 channel for noise filtered points from the 647 channel. Scale bars 1 µm

Clusters can be sub-classified as colocalised or non-colocalised using the DoC values of the cluster points– a threshold of 2 or more points per cluster with a DoC value > 0.4 was chosen as the threshold for classifying a cluster as colocalised. This threshold was selected as using a proportional threshold (e.g. 50% of cluster points having DoC >0.4) would bias the colocalisation results towards smaller clusters, as it is unlikely that larger clusters would display such a large amount of overlap, when it may only be a few molecules in the cluster which participate in an interaction with the species in the other channel or with intermediary molecules. Requiring two points to be colocalised seems likely to reduce the probability that the colocalisation is due to a noise point in either channel and rather is representative of a real interaction between the two molecular species.

Figure 4-28 illustrates the combination of colocalisation and cluster analysis. Inspecting the DoC histograms for clustered molecules versus the entire population gives the first indication whether there is any spatial relationship between the arrangement of the two molecular species – if there is a relationship, either colocalisation or separation of clusters, then the histogram of clustered molecules will be shifted compared to that of the entire population, which we do indeed observe in these results (Figure 4-28 B). The shift in the DoC histogram for clustered molecules towards more negative values indicates that clustered molecules of ErbB2 are less colocalised with CD82 than non-clustered molecules, showing that there is a relationship between the distributions of the two proteins. Taken together Figure 4-28 D and E show that even within a cluster the DoC scores of molecules can be very different, with some displaying colocalisation and others a negative DoC value, indicating no spatial correlation. Figure 4-28 F highlights the molecular nature of the colocalisation analysis, as we can see that some clusters of ErbB2 which are classified as colocalised with CD82 do not colocalise with a *cluster* of CD82 in the other channel, but instead must be colocalised with single molecules. These colocalisations could be due to single CD82 molecules interacting with ErbB2 – although this does not preclude these single CD82 molecules being part of a

TERM with other tetraspanins – or the localisation in the 647 channel could be an artefact due to the binding of the fluorophore to the glass coverslip.

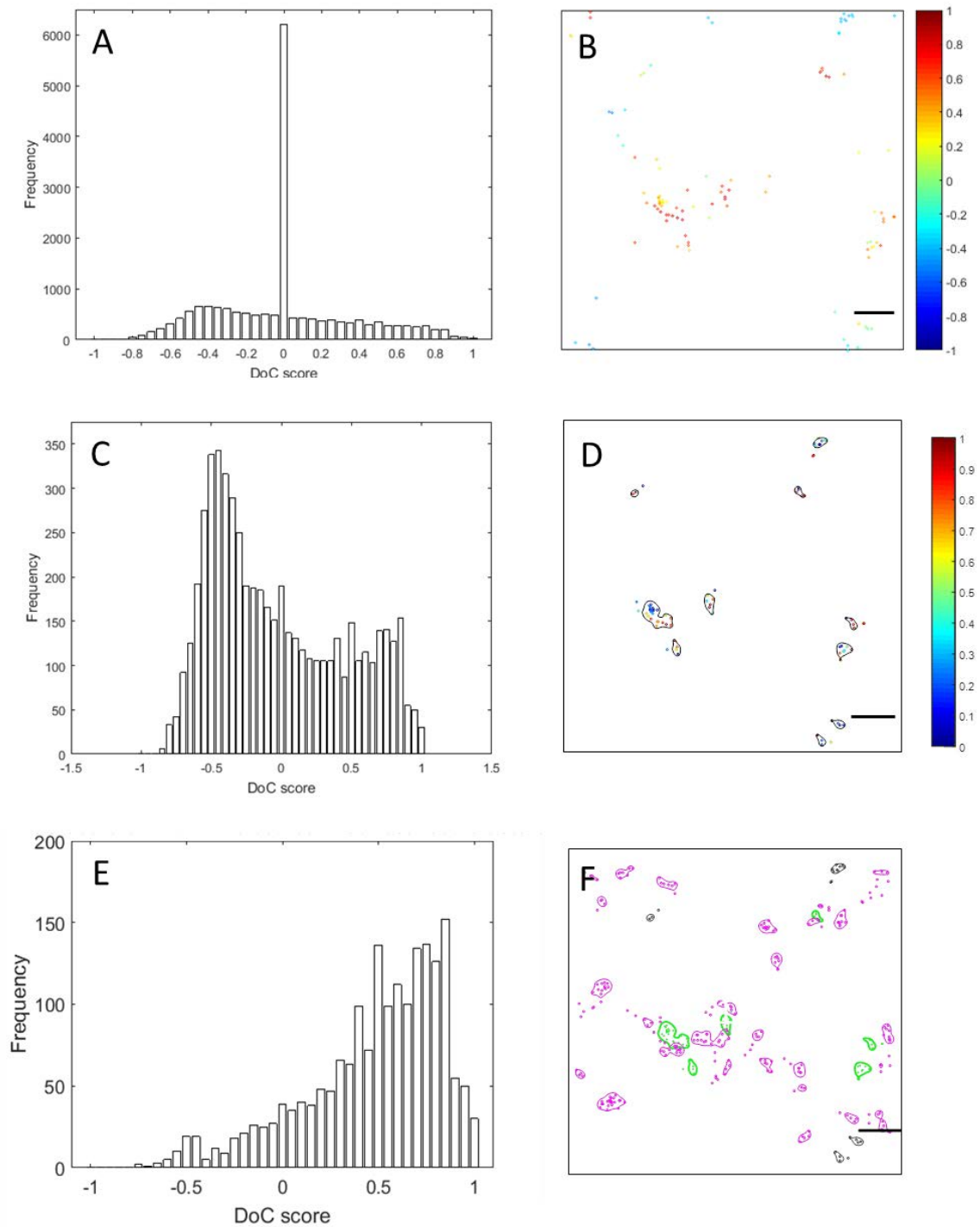

Figure 4-28: Degree of colocalisation histograms for ErbB2 with CD82 in SKBR3/CD82 with corresponding DoC maps and clusters

A) Histogram of DoC score for all localisations analysed in the ROIs selected in the Alexa 488/ErbB2 channel B) Example DoC map for a single 1500 nm^2 ROI in one of the images from which data was

extracted and pooled for A. C) Histogram of DoC score of only molecules which are classified as clustered after DBSCAN analysis. D) DoC map for the same ROI as B, with only clustered points shown, cluster contours plotted in black. E) Histogram of DoC scores of molecules in clusters classified as colocalised with CD82. Even within colocalised clusters not all molecules are colocalised, as shown by the distribution of DoC scores. F) Clustered points and cluster contours of CD82 clusters detected in the Alexa 647 channel data plotted in magenta (data not shown in A & B); co-localised clusters of ErbB2 plotted in green; non-colocalised clusters of ErbB2 plotted in grey. This ROI was chosen specifically as a good example of colocalisation where only the edges of clusters overlap, or where colocalisation is detected but does not correspond with a cluster in the CD82 channel, and is not representative of the level of clustering seen in all ROIs, which varies widely from area to area. Scale bars 200 nm. Frequency in these plots represents the contribution of each bin to the total population of molecules. N images analysed = 6, N ROIs per image = 5.

It is possible to calculate colocalisation from one channel to the other both ways, in this case the colocalisation of ErbB2 with CD82, and the colocalisation of CD82 with ErbB2, and they are not necessarily the same. We have demonstrated that due to the buffer conditions used in this study, the localisation density is always higher in the 647 channel, and consequently the colocalisation of the 488 channel with the 647 channel is always higher than vice versa. As we are mainly interested in the determining the properties of ErbB2 clusters in a variety of conditions, with relation to CD82 expression and colocalisation, this analysis approach works well for the experimental data we have acquired.

4.10 ErbB2 distribution in SKBR3 and MCF7 cell lines relative to CD82 expression

Preliminary work presented in section 4.7 was analysed using the results of the second-pass of the multi-pass DBSCAN algorithm, as detailed in section 4.8.1. In the multi-pass DBSCAN analysis, calculation of cluster area is implemented by determining the area bounded by joining the boundary points of a cluster, whereas in ClusDoc a 15 nm smoothing of the density map followed by thresholding is used to determine cluster area. Since these calculations yield slightly different values for consistency ClusDoc analysis was used to generate all the figures and results presented in this section.

4.10.1 Effect of changes in CD82 expression on ErbB2 cluster properties

Initially we sought to determine whether CD82 expression in SKBR3 and MCF7 cells affected the distribution/clustering of ErbB2 such that a difference would be visible in the distribution of cluster properties when all clusters were considered. We also investigated specifically those clusters of ErbB2 which colocalised with CD82 molecules, to see if this colocalisation had any effect on the ErbB2 cluster properties.

Generally we have chosen to present results showing the number of molecules per cluster and the density within those clusters. We expect these parameters to reveal if changes to the cluster properties are induced as a result of differing protein expression (i.e. comparison between cell lines) or in response to stimulation, as the number of molecules per cluster should give an indication of the scale of the molecular organisation and if larger complexes are being formed, and the cluster density may give an indication of interactions taking place within clusters. ErbB2 is known to form both hetero and homodimers, and while the effect of the formation of heterodimers on cluster density is not easy to predict – it could decrease apparent cluster density by increasing the space between ErbB2 molecules; increase the density by causing ErbB2 molecules to become more closely packed together; or cause little change if ErbB2 molecules leave the cluster to take part in interactions – ErbB2 homodimerisation is likely to increase the cluster density, as the distance between the interacting ErbB2 molecules will decrease. Therefore, a change in cluster density could be indicative of changes to ErbB2 interactions, and along with information on the number of molecules present in a cluster should provide an insight into the effect of CD82 expression on ErbB2 clustering.

Whilst we are interested specifically in the role of TERMs in mediating ErbB2 dynamics and distribution, based on the data we have, we chose to calculate colocalisation of ErbB2 clusters with CD82 molecules, without requiring those CD82 molecules to also be part of a cluster. This decision was made on the basis that we do not fully understand TERM formation, and while the literature suggested that multiple species of tetraspanin together formed TERMs [50], more recent work using

the super-resolution imaging technique stimulated emission depletion (STED) microscopy [49] has suggested that different species of tetraspanin segregate in the plasma membrane, and do not cluster together. Based on this ongoing open question of whether multiple tetraspanin species are involved in TERMs or if they are separate, and the fact that we cannot guarantee every single molecule of CD82 on the surface has been labelled and imaged, we concluded that we could reasonably assume that colocalisation of at least two molecules of ErbB2 in the same cluster with CD82 molecules indicated a likely interaction with some underlying structure containing CD82, be that an incompletely labelled CD82-enriched microdomain, or a TERM containing CD82 amongst other tetraspanins, and was therefore a suitable threshold with which to classify ErbB2 clusters as colocalised with CD82.

A

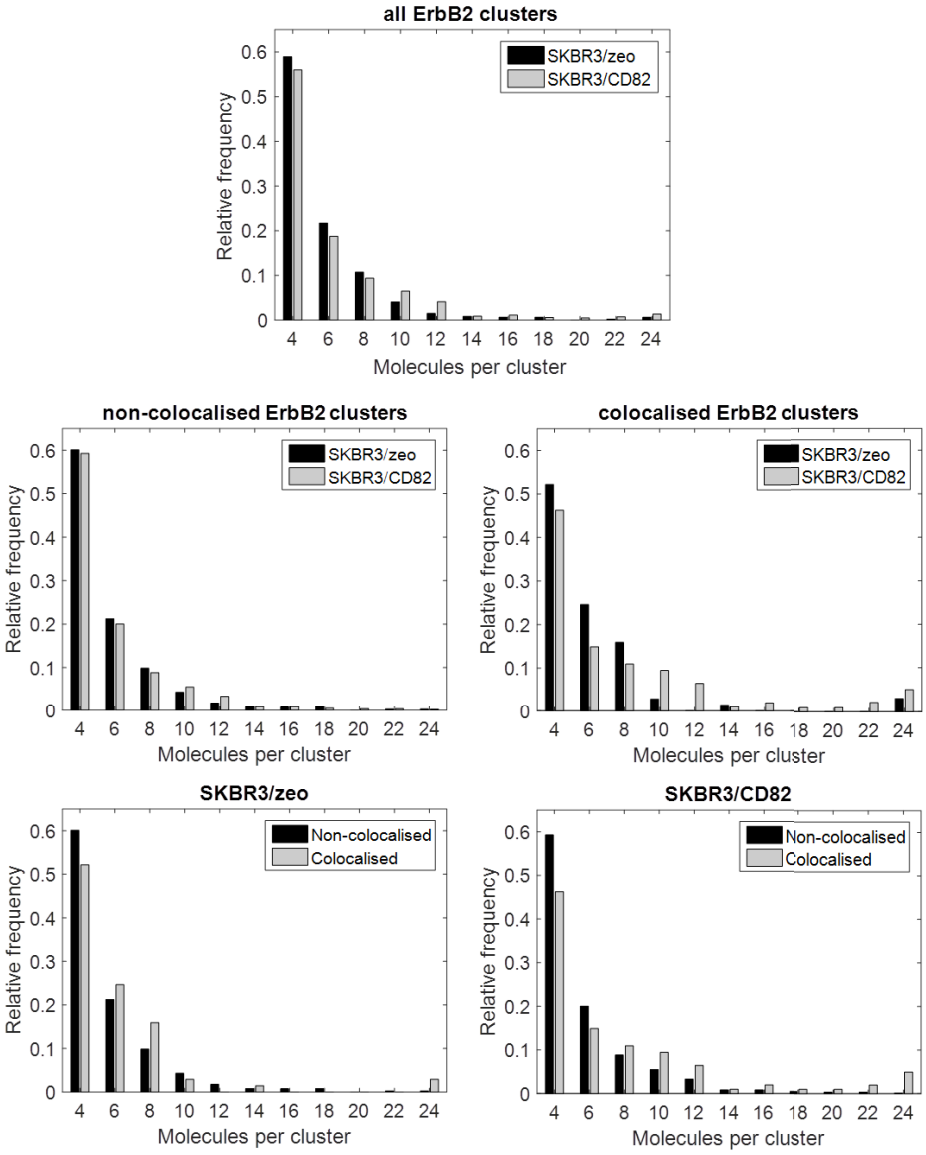
all ErbB2 clusters
SKBR3/zeo
SKBR3/CD82
Relative frequency
Molecules per cluster
non-colocalised ErbB2 clusters
colocalised ErbB2 clusters
SKBR3/zeo
Non-colocalised
Colocalised
SKBR3/CD82

B

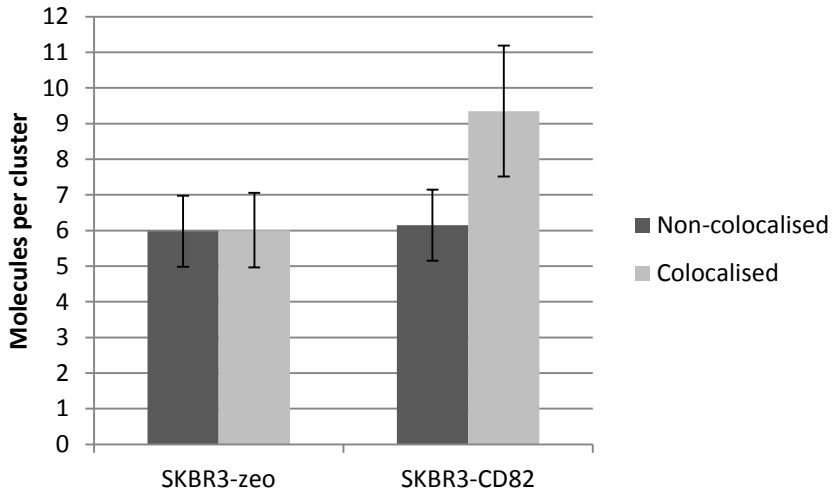
Molecules per cluster
SKBR3-zeo
SKBR3-CD82
Non-colocalised
Colocalised

Figure 4-29: Analysis of ErbB2 clusters colocalised with CD82 in SKBR3 cells – molecules per cluster
The distribution of ErbB2 and CD82 on SKBR3 and SKBR3/CD82 cells was imaged using dSTORM and used to determine ErbB2 cluster properties in relation to their colocalisation with CD82. An ErbB2 cluster was classified as colocalised with CD82 if 2 or more molecules in the cluster had a DoC score > 0.4 with the CD82 data. A) Histograms of the number of molecules per cluster are presented for all ErbB2 clusters (top row); non-colocalised clusters (middle left) and colocalised clusters (middle right) in SKBR3/zeo and SKBR3/CD82; and clusters in SKBR3/zeo (bottom left) and SKBR3/CD82 (bottom right) split into colocalised and non-colocalised clusters. The difference in the molecules per cluster distribution of colocalised and non-colocalised clusters in SKBR3/CD82 was found to be significant ($p = 0.0468$). The difference between colocalised and non-colocalised clusters in SKBR3/zeo was not found to be statistically significant. B) Mean number of molecules per cluster with error bars representing twice the standard error on the mean. Number of cells analysed, SKBR3/zeo = 6, SKBR3/CD82 = 6. Distributions of cluster properties were compared using two-sample Kolmogorov-Smirnov tests to determine the significance of difference, p-values < 0.05 were considered significant. Relative frequency normalised by N clusters in each condition.

Figure 4-29 shows how the number of molecules of ErbB2 per cluster is affected by CD82 over-expression (top histogram, Figure 4-29 A), and specifically in relation to colocalisation with CD82 molecules. CD82 overexpression does not have a significant effect on the number of molecules of ErbB2 per cluster considering the total population of clusters, consistent with the results presented in Table 4-4 and Table 4-5. Comparing the histogram distributions for the total cluster population with the Kolmogorov-Smirnov test indicates that the values are drawn from the same distribution, therefore we can say that CD82 expression does not have an effect on the cluster properties of the total population of ErbB2 clusters. However, comparing the number of molecules in colocalised and non-colocalised clusters in both SKBR3/zeo and SKBR3/CD82 (bottom row, Figure 4-29 A) we can see that there is a slight shift upwards in the distribution, towards larger clusters in the colocalised condition. This could be explained someway by the increased size of larger ErbB2 clusters increasing the probability of the molecules colocalising with any molecule on the cell surface, although this assumes a random distribution of proteins, which is not the case in the plasma membrane [4], so it is possible there is some specific colocalisation of larger ErbB2 clusters with CD82. In particular from B it can be seen that the increase in the mean number of molecules per cluster in colocalised clusters in SKBR3/CD82 is statistically significant, while in SKBR3/zeo no such increase is observed.

Comparing the histogram distributions for colocalised versus non-colocalised clusters in SKBR3/CD82 via the two-sample Kolmogorov-Smirnov test also supports this, yielding p = 0.0468 for colocalised versus non-colocalised clusters, so the distribution of molecules per cluster is different in the colocalised subpopulation. Further work may determine why this difference is only evident in CD82 over-expressing cells and not SKBR3/zeo, such as investigating the number of colocalised molecules per cluster in each cell line to see if perhaps a larger number of molecules colocalise in the CD82-overexpressing cells and are mediating larger ErbB2 cluster sizes.

The mean size of ErbB2 clusters in this study was found to be around 6 molecules per cluster for both CD82 colocalised and non-colocalised clusters in SKBR3/zeo cells, and around 6 and 9 molecules per cluster respectively for non-colocalised and colocalised clusters in SKBR3/CD82, corresponding to mean areas of 2200-3300 nm^2. Assuming circular clusters (in order to facilitate estimation of a cluster radius for comparison with the results of other studies), these areas correspond to cluster diameters of around 30 nm. This correlates well with the results of Nagy et al., who showed using number and brightness analysis on CHO cells that in the absence of stimulation, ErbB2 was present in pre-formed clusters [241]. The number and brightness analysis revealed that ErbB2 was present in 'microclusters' of 5-15 molecules, and outside these clusters 3-5 ErbB2 molecules were homoassociated, with little monomeric protein observed. Yang et al. have also revealed clustering of ErbB2 via electron microscopy with immunogold labelling, with a mean cluster size of around 9 proteins. A number of results in the literature yield different mean values for the size of ErbB2 clusters, with Kaufman et al. finding an ErbB2 cluster size of around 67 nm determined via a local density based analysis of localisation microscopy data on Cal-51 and SKBR3 (breast cancer cells over-expressing ErbB2) and AG11132 (healthy donor human mammary epithelial cells), to values of 10^3 molecules and 500 nm diameters from previous scanning near-field optical microscopy (NSOM) experiments on SKBR3 cells [247]. Kaufman suggests that this variation demonstrates the need for a better characterization of the nanoscale expression pattern of ErbB2. However, in light of

the literature it is clear that the cluster properties determined in an individual study are heavily dependent both on the precise method of imaging and analysis applied, the parameters in which results are expressed (and any assumptions made in the calculation of said parameters), and the expression pattern of a plethora of proteins in the cell.

Examining the ErbB2 cluster density distributions in our model system (Figure 4-30 A and Table 4-8) we can see that in both colocalised and non-colocalised cluster sub-populations the majority have a density between 2000-3500 molecules/μm^2, and that there is little change in the distribution between SKBR3/zeo and SKBR3/CD82, also shown in Figure 4-30 B. There is a potentially interesting feature in the histogram distributions in Figure 4-30 however, which is the hint of a bimodal distribution of cluster densities. In order to see if such a distribution can be clearly identified in that data more imaging will be required, so that more clusters can be sampled to fill out the histogram further. Initial attempts to fit a bimodal distribution to this data were not successful. If such a distribution is identified it may be possible to determine a values or threshold by which the lower and higher density clusters could be separated. From a biological perspective there is a logical explanation for the presence two populations of clusters with lower and higher densities, with the higher density clusters containing more homodimers and therefore possibly undergoing different interactions than the lower density clusters. It would be interesting to study this specific subpopulation of clusters in relation to their colocalisation with CD82, to see if colocalisation with CD82 is the same across both subpopulations.

It has previously been reported by this group that over-expression of CD82 results in a higher level of association of ErbB2 with CD82 [1]. The data presented here supports this finding, showing an almost two-fold increase in the number of ErbB2 molecules classified as colocalised with CD82 in CD82 over-expressing cells. Interestingly, despite the increased colocalisation of ErbB2 with CD82, the properties of size and molecular density in ErbB2 clusters are broadly similar between the

control and CD82 over-expressing conditions, with the exception of the significant increase in the number of molecules per ErbB2 cluster colocalised with CD82 in SKBR3/CD82 cells.

A

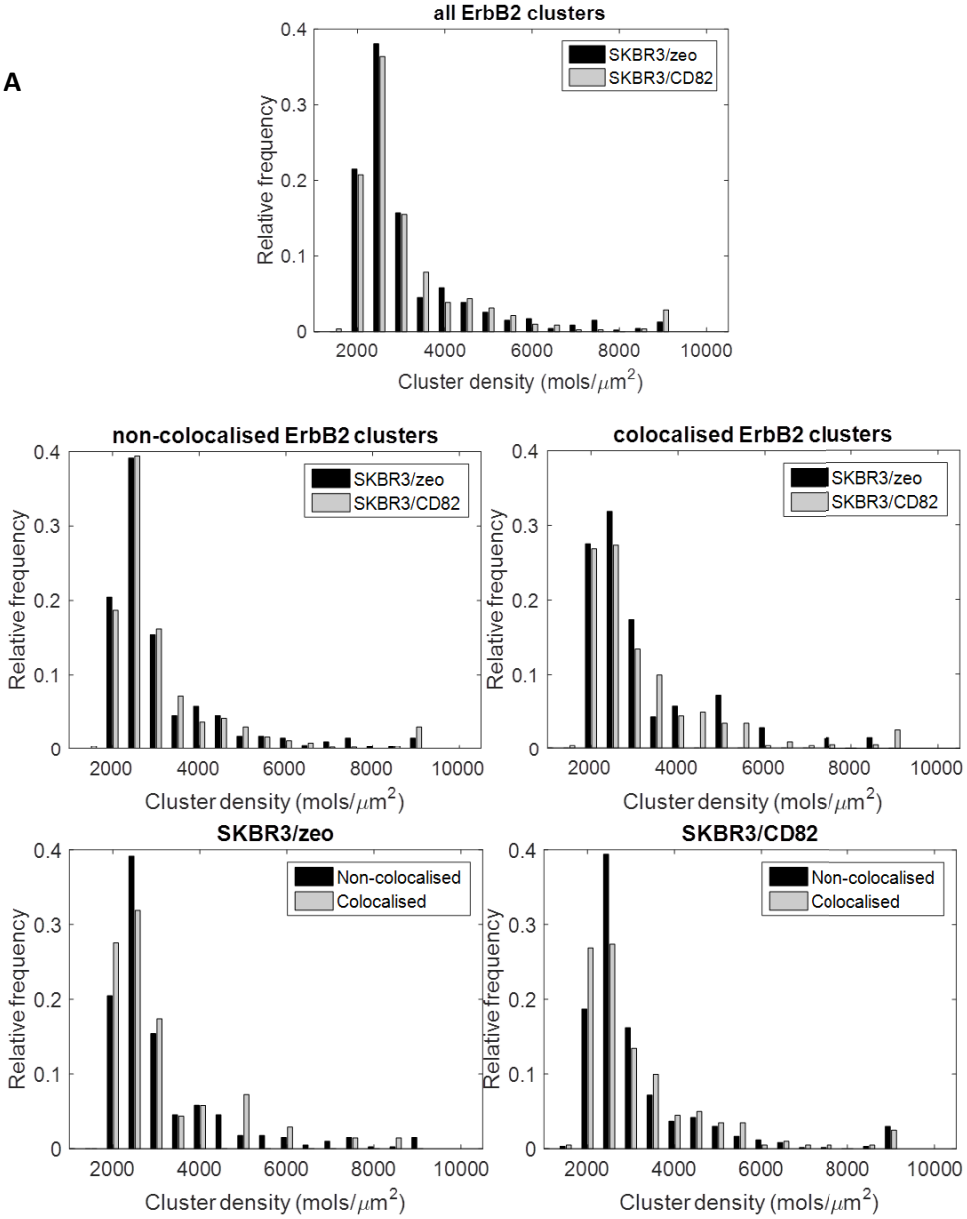
all ErbB2 clusters
SKBR3/zeo
SKBR3/CD82
Relative frequency
Cluster density (mols/μm^2)
non-colocalised ErbB2 clusters
colocalised ErbB2 clusters
SKBR3/zeo
SKBR3/CD82
Non-colocalised
Colocalised

B

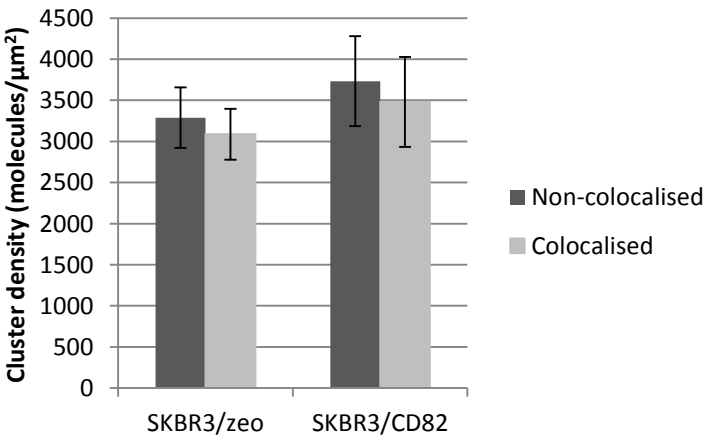
Cluster density (molecules/µm²)
SKBR3/zeo
SKBR3/CD82
Non-colocalised
Colocalised

Figure 4-30: Density of ErbB2 clusters in SKBR3 cells in relation to colocalisation with CD82
Clusters of ErbB2 on dual labelled SKBR3 cells were analysed as described in previous figure caption to determine cluster properties in relation to CD82 colocalisation. A) Histogram of molecular density in ErbB2 clusters for all clusters (top row); non-colocalised clusters in SKBR3/zeo compared with non-colocalised clusters in SKBR3/CD82 (middle left) and colocalised clusters in SKBR3/zeo compared with colocalised clusters in SKBR3/CD83 (middle right); and non-colocalised clusters compared with colocalised clusters in SKBR3/zeo (bottom left) and in SKBR3/CD82 (bottom right). No statistically significant difference between the distributions was detected. B) Mean cluster density with error bars representing twice the standard error on the mean. Number of cells analysed, SKBR3/zeo = 6, SKBR3/CD82 = 6.

Table 4-8: ErbB2 cluster properties in SKBR3 cells relative to colocalisation with CD82

	SKBR3/zeo		**SKBR3/CD82**	
	Non-colocalised	**Colocalised**	**Non-colocalised**	**Colocalised**
Mean molecules per cluster ± s.d.	5.98±2.88	6.01±4.34	6.15±3.30	9.35±13.01
Mean cluster area ± s.d. (nm^2)	2217±1401	2478±1939	2294±1607	3364±3305
Mean cluster density ± s.d. (molecules/μm^2)	3288±3656	3087±1280	3732±6687	3481±3176
Total number of clusters	396	69	599	201

Table 4-9: Proportion of all molecules with degree of colocalisation greater than the threshold value of 0.4 in each cell line

Proportion of molecules with DoC > 0.4	**SKBR3/zeo**	**SKBR3/CD82**
ErbB2→CD82 (%)	8.44	14.72
CD82→ErbB2 (%)	0.87	2.43

Table 4-9 shows the proportion of all molecules in the selected ROIs that have a DoC score greater tha the 0.4 threshold for colocalisation. We can see that a small amount of ErbB2 molecules colocalise with CD82, and that this proportion is increased in SKBR3/CD82 relative to SKBR3/zeo cells, as would be expected from a purely probabilistic perspective. The reverse data, showing colocalisation of CD82 with ErbB2 highlights a problem with the data in this study, which was that the signal from whichever protein was labelled with Alexa-647 (CD82 in this dataset) was much higher than the signal from the protein labelled with Alexa-488. That there were more localisations in the 647 channel than the 488 meant that colocalisation of the 488 channel with 647 would always

result in some colocalisation, while performing the calculation in the opposite direction resulted in virtually no correlation between localisations in the 647 channel with 488, since the 647 data was much more dense. It was therefore not possible to calculate both the colocalisation of ErbB2 with CD82 and vice versa from the same dataset.

4.10.2 Effect of changes in CD82 expression on CD82 cluster properties

In order to investigate how the properties of CD82 enriched microdomains might change with CD82 over-expression, we examined the properties of CD82 clusters in both SKBR3 and MCF7 cells engineered to over-express CD82, and also in MCF7 cells expressing palmitoylation deficient CD82.

From the reconstructed images in Figure 4-31 it is clear that in CD82 over-expressing cells the amount of CD82 detected is increased over the whole cell membrane, relative to the control. It can also be seen that the distribution of both CD82 and ErbB2 varies across the cell, being more dense in some areas than others, and in some places ErbB2 particularly seems to be densely distributed around specific shapes (such as in Figure 4-31 top right). This variation across cells and between cells can go some way to explain the large standard deviations in the cluster properties, as denser and more sparsely populated areas of the cell may exhibit different cluster populations, or result in different clusters being detected by the density based clustering algorithm. It is possible that if the more densely populated areas of the cell exhibit different cluster properties this may be resolved in the histograms of the cluster properties, possibly resulting in a bimodal distribution.

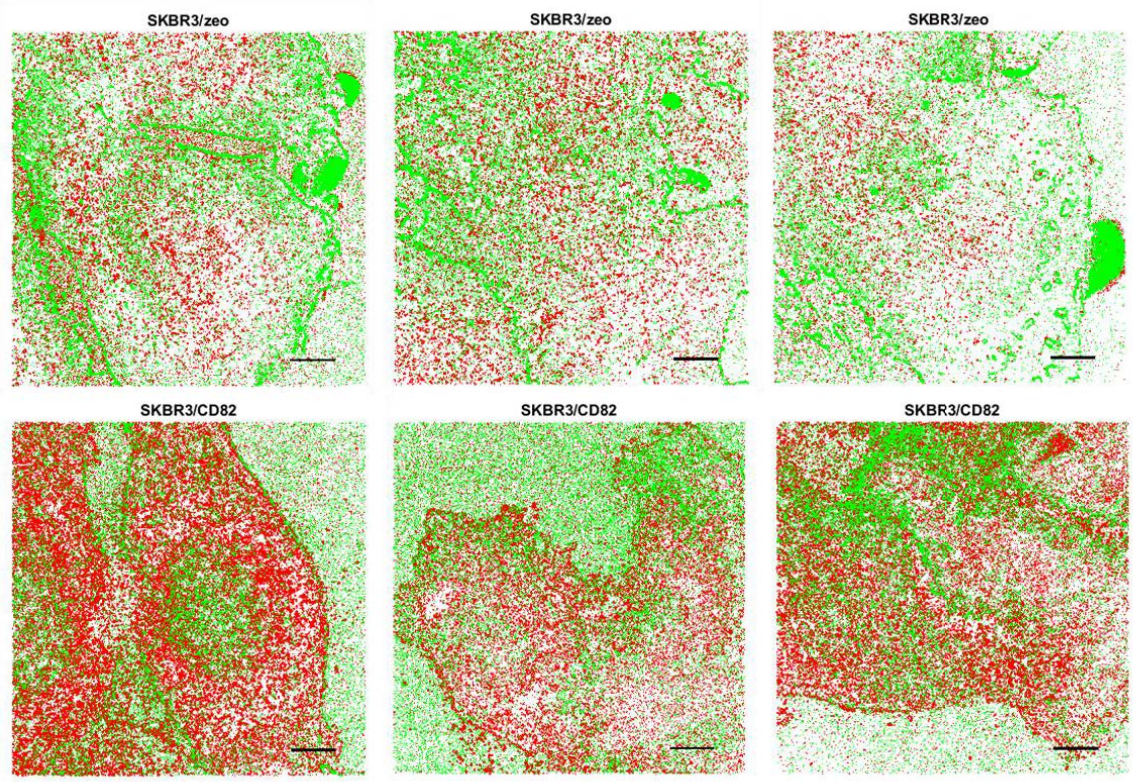

Figure 4-31: Representative dSTORM localisation images of ErbB2 and CD82 distribution in SKBR3/zeo and SKBR3/CD82 cells
ErbB2 was labelled with Alexa-488, and CD82 with Alexa-647 on SKBR3/zeo (top row) and SKBR3/CD82 (bottom row) cells and imaged using dSTORM microscopy. Reconstruction and drift correction was performed with the nSTORM software to recover the localisations of ErbB2 and CD82, which were plotted in MATLAB using the scatter plot function with arbitrary point sizes and brightness (intensity and size not scaled relative to number of photons detected). Green points represent ErbB2 localisations, red points represent CD82. Scale bar 5 μm.

Table 4-10 shows a greater than two-fold increase in the number of clusters of CD82 per μm^2, which correlates with the obvious increase in surface expression of CD82 observed in the representative images in Figure 4-31. Interestingly, the distributions in Figure 4-33 demonstrate that the properties of these clusters change little between the control and CD82 over-expressing condition, and a similar result is observed in the MCF7 cell line shown in Figure 4-34, comparing the properties of CD82 clusters in the control and CD82 over-expressing condition. This shows that over-expression of CD82 does not change the properties of the clusters themselves, but rather results in an increased number of clusters with the same distribution of properties. This supports to the argument that the plasma membrane is organised in specific microdomains and segregated into distinct areas, as

opposed to composed of randomly distributed proteins across the membrane, in which case greater numbers of CD82 on the membrane would be expected to lead to larger clusters, rather than the effect we have observed. This is illustrated in the schematic diagram in Figure 4-32..

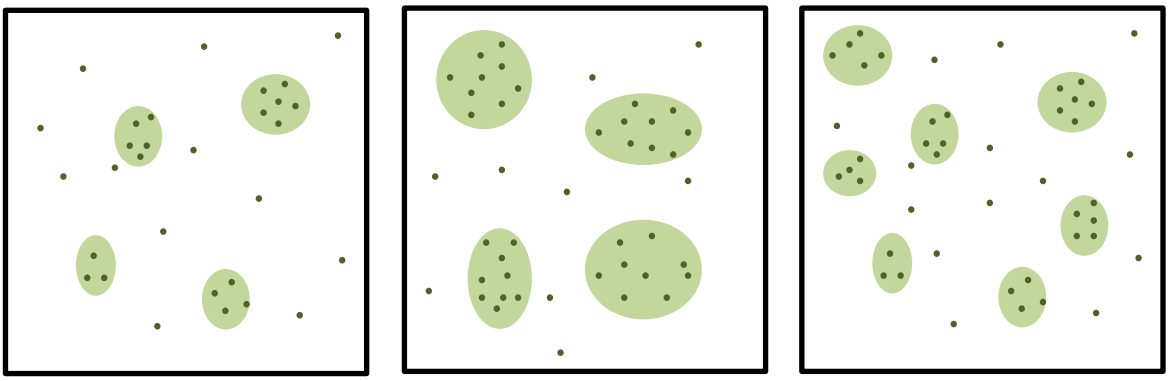

Figure 4-32: Hypothetical changes to cluster properties with increased protein expression
In wild-type conditions (left-most diagram) the protein molecules form clusters which may be of a characteristic size, or have a certain distribution of sizes. When the protein is over-expressed, in the absence of any underlying segregation of the plasma membrane we may expect to see generally larger clusters of the protein form (case A, middle diagram). In the case where there is some underlying segregation of the plasma membrane, or where the protein clusters are organised in some specific way relative to the other components of the membrane, we may expect to see a larger number of generally similarly characterised clusters form (case B, right-most image).

In SKBR3/zeo cells the contribution to the largest bin in both the molecules per cluster and cluster density distribution is higher than that from SKBR3/CD82, which contributes to the higher mean values for these parameters observed in SKBR3/zeo, however we can see from the distribution that the bulk of the clusters exhibit similar properties in both conditions. From Figure 4-34 B we see that CD82 overexpression in MCF7 cells results in an increase in the size of CD82 clusters, in contrast to the results from SKBR3 cells – however, from the distribution of cluster properties we see that the bulk of clusters are not changed in their properties, and thus this apparent change may be attributed to sampling effects or clustering artefacts.

Interestingly in Table 4-11 we see that the proportion of CD82 molecules which are clustered does not decrease relative to the control or CD82 over-expressing condition when palmitoylation deficient

CD82 is expressed, and that a similar number of clusters with similar properties are detected per μm^2. This unexpected result contrasts with the expected change to cluster properties, given a crucial mechanism for CD82 interaction has been removed. In MCF7 cells the number of CD82 molecules in clusters in the condition where palmitoylation deficient CD82 is expressed increases twofold compared to the wild-type CD82 expression, however the standard deviation in the number of molecules per cluster is also much larger in the palmitoylation deficient CD82 condition. Clusters of CD82 also appear slightly larger in the palmitoylation deficient condition, so it may be that by removing palmitoylation of CD82 the way in which the CD82 molecules associate to form clusters changes, resulting in the change in size.

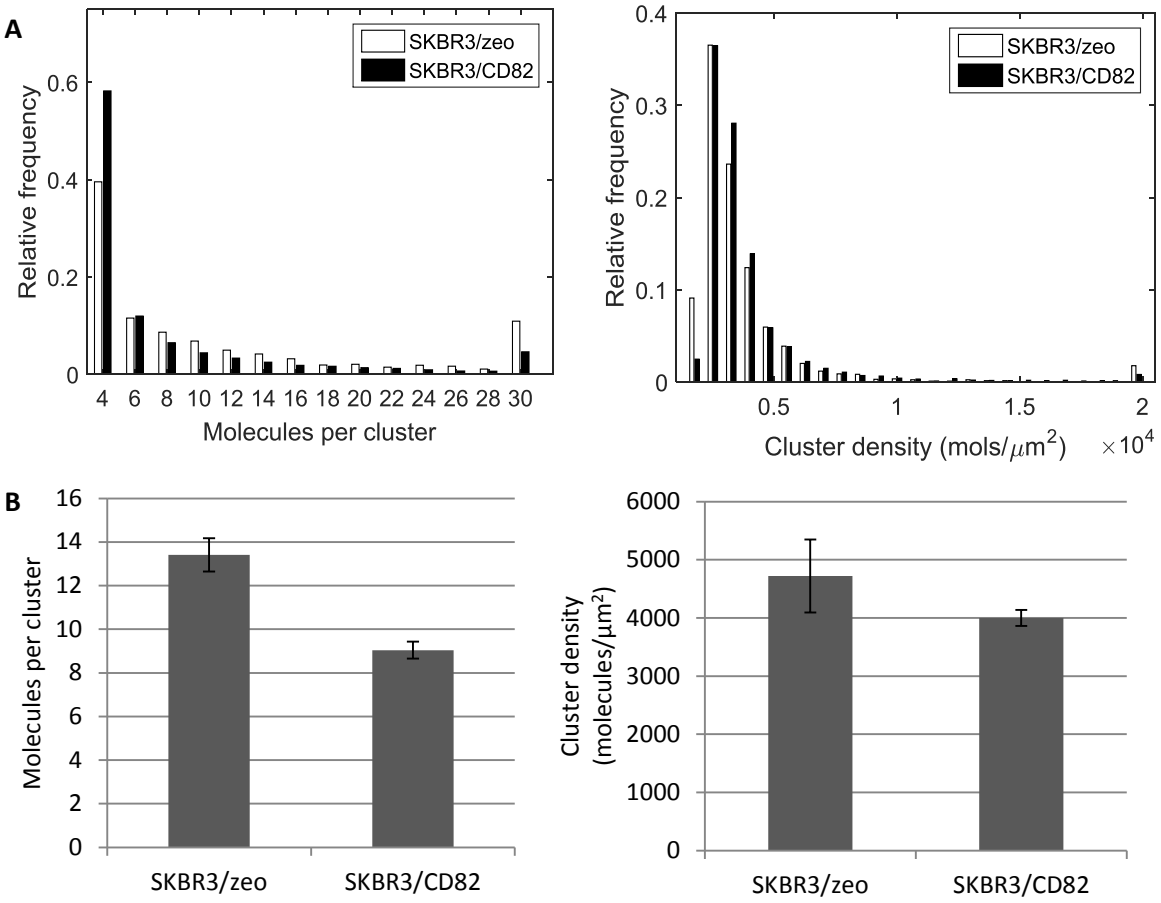

Figure 4-33: CD82 cluster properties in SKBR3 cells
The distribution of Alexa-647 labelled CD82 was imaged using dSTORM, and cluster properties determined using ClusDoc DBSCAN analysis. A) Cluster properties in SKBR3 cells over-expressing CD82 were compared with those in control cells. Two sample Kolmogorov-Smirnov tests were performed and no statistically significant difference was detected between the distributions of cluster properties (molecules per cluster, cluster area, or cluster density) in cells overexpressing CD82, and the control cells. B) Mean molecules per cluster and cluster density of CD82 in SKBR3 cells. Error bars represent twice the standard error on the mean. Number of cells analysed SKBR3/zeo = 5, SKBR3/CD82 = 5.

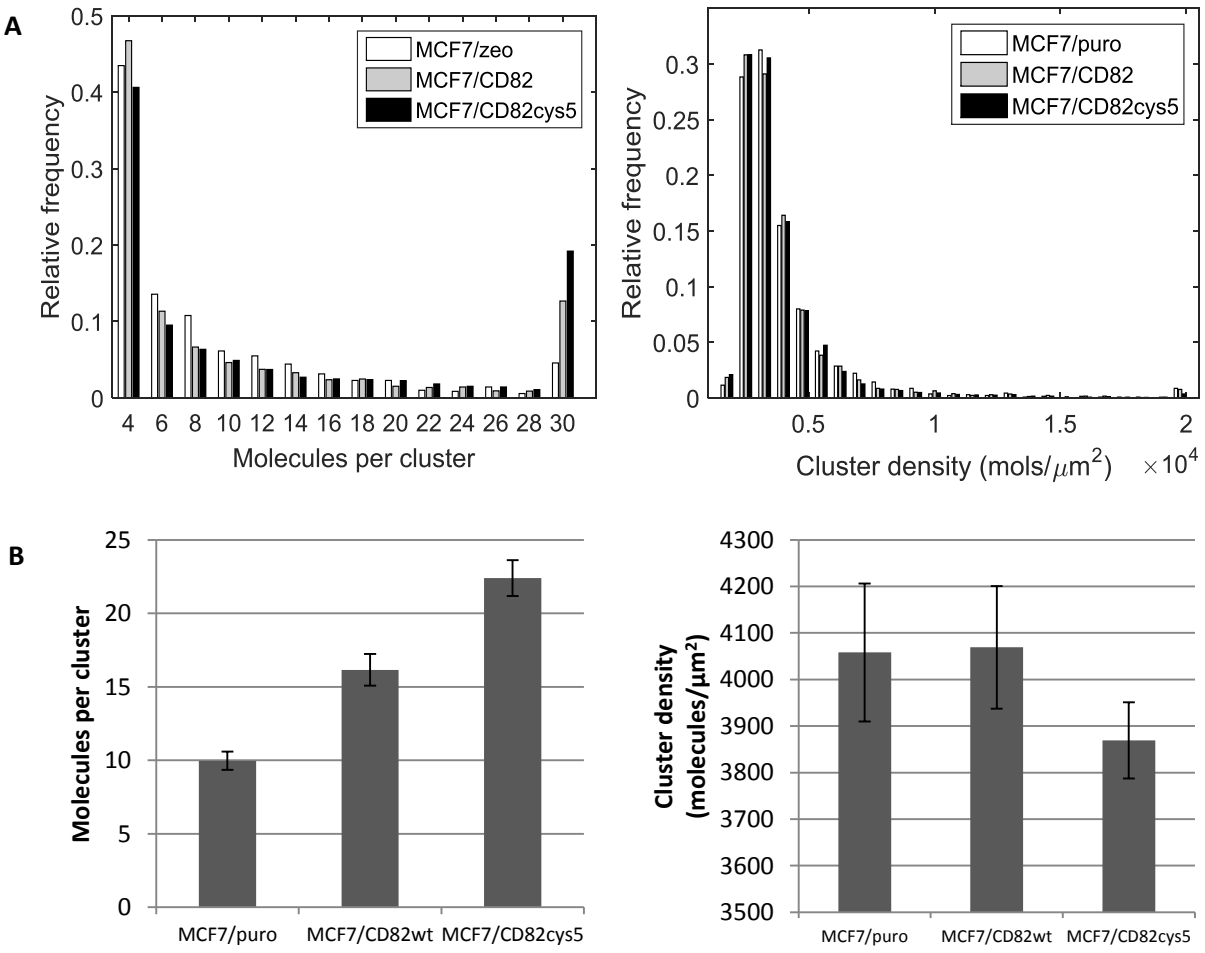

Figure 4-34: CD82 cluster properties in MCF7 cells

The distribution of Alexa-647 labelled CD82 was imaged using dSTORM, and cluster properties determined using ClusDoc DBSCAN analysis. A) Cluster properties in MCF7 cells over-expressing CD82, or expressing the palmitoylation deficient CD82 (CD82cys5) were compared with those in control cells. Two sample Kolmogorov-Smirnov tests were performed and no statistically significant difference was detected between the distributions of cluster properties (molecules per cluster, cluster area, or cluster density) in cells overexpressing CD82 or expressing the palmitoylation deficient version, and the control cells. B) Mean molecules per cluster and cluster density of CD82 in MCF7 cells. Error bars represent twice the standard error on the mean. Number of cells analysed MCF7/puro = 4, MCF7/CD82wt = 4, MCF7/CD82cys5 = 5.

Table 4-10: CD82 cluster properties in SKBR3 cells

	SKBR3/zeo	SKBR3/CD82
Molecules per Cluster ± s.d.	13.41±17.14	9.04±14.01
Cluster area (nm^2) ± s.d.	4604±5860	3134±5060
Cluster density (molecules/ μm^2) ± s.d.	4720±14113	3999±4923
Clusters/μm^2	3.25	8.39
Localisations/μm^2	54.12	128.8512
Proportion molecules clustered	80.57%	58.85%
Total number of clusters analysed	2032	5243

Table 4-11: CD82 cluster properties in MCF7

	MCF7/puro	MCF7/CD82wt	MCF7/CD82cys5
Molecules per cluster ± s.d.	9.97±11.50	16.15±30.31	22.40±40.83
Cluster area (nm^2) ± s.d.	2993±3511	4832±8306	6398±1037
Cluster density (molecules/ μm^2) ± s.d.	4058±2773	4069±3693	3869±2754
Clusters/μm^2	2.80	6.31	7.28
Localisations/μm^2	33.33	136.65	198.55
Proportion molecules clustered	83.82%	74.55%	82.04%
Total number of clusters analysed	1401	3157	4547

4.11 Effect of CD82 expression on ErbB2 clustering in response to treatment with the ErbB ligands EGF and heregulin, and the ErbB2 targeting drug Herceptin

4.11.1 Motivation

Using biochemical methods our group previously reported that CD82 modulated activity of ErbB receptors, specifically EGFR and ErbB2, as a result of cell-surface re-distribution of the receptors (REF). Here we used advanced imaging techniques to investigate further the effects of CD82 on the biological properties and activity of ErbB2. Specifically, we examined the effects of a panel of ErbB targeting treatments on ErbB2 clustering in SKBR3 and MCF7 cells in relation to CD82 expression levels. We also examined colocalisation of ErbB2 with CD82 and with an anti-phosphotyrosine antibdody, in response to the applied treatments.

To stimulate cells we used EGF, the ligand for ErbB1/EGFR; Herceptin, a humanised monoclonal antibody against Erbb2 which is a therapeutic drug used in the treatment of ErbB2 over-expressing breast cancers; and heregulin, the ligand for ErbB3. The homo and hetero-interactions of ErbB family members in cancer cell lines, and their response to various stimulants and drugs are complex, and widely reviewed in the literature [37], [66], [69], [248]. The following paragraphs focus on the action of EGF, Herceptin and heregulin, in the context of the interactions or re-distribution of the ErbB receptors that they mediate, in order to aid in the interpretation of the results of clustering.

It has been shown that upon ligand binding to EGFR extracellular domains there is an increase in the proportion of dimerized receptor, leading to activation of intracellular tyrosine kinase, auto- and cross-phosphorylation of tyrosines in the C-terminus [249], triggering downstream signalling. Activation of EGFR kinase by ligand binding also induces the internalization of the receptor complexes [249]–[251].

Herceptin targets the ErbB2 receptor by binding to the juxtamembrane portion of the extracellular domain, which in turn limits the receptor's ability to activate its tyrosine kinase, in turn limiting the activation of downstream signalling pathways [252]. Herceptin does not block the heterodimerisation of ErbB2 with ErbB3, however it does inhibit the interaction of ErbB2 with EGFR [253], [254], and also seems to inhibit ErbB2 homodimerisation [253]. Herceptin is reported in some studies to have little effect on ErbB2 activation status or to cause a change in ErbB2 phosphorylation [255], [256], while others report a decrease in phosphorylation [256]. Previous work in this group has shown increased basal phosphorylation of ErbB2 in SKBR3/CD82 cells, as a result of which we have sought to understand whether CD82 expression changes the distribution or dynamics of the receptor in steady state conditions [1]. It has also been suggested that high levels of ErbB2 homodimers may predict a positive response to Herceptin [253].

heregulin initiates ErbB2/ErbB3 heterodimerisation [257], triggering downstream pathways involved in oncogenesis [258]. Stimulation with heregulin has been shown, via immunoelectron microscopy, to cause a large increase in the size of ErbB3 clusters [230].

We chose to investigate the effect of treatment with ErbB targeting molecules for two reasons – firstly to elucidate any effect of CD82 expression on the cluster properties of ErbB2 in response to these treatments; and secondly as the literature contains conflicting reports regarding the effect of stimulation on ErbB2 clusters and we sought to understand why this might be. ErbB2 is known to be activated by each of the ErbB family members on ligand binding [254], however the effect of ligand binding on the spatial distribution/re-distribution of ErbB2 is subject to conflicting reports in the literature.

Nagy et al. found using number and brightness analysis that ErbB2 clusters in Chinese hamster ovary (CHO) cells decreased in size upon EGF stimulation, and concluded that ErbB2 clusters are dispersed upon ligand stimulation [241]; yet in a previous paper using NSOM reported an EGF-induced

increase in ErbB2 cluster size and concluded that an increase in cluster size may constitute a general phenomenon in the activation of erbB2 [259]. Yang et al also investigated the distribution of ErbB receptors in steady state conditions and in response to stimulation, using immunoelectron microscopy on SKBR3 cells, and reported no change in cluster properties after addition of EGF, or after 1 hour treatment with inhibitors to block ErbB2 phosphorylation. Treatment with EGF would be expected to initiate the formation of both EGFR homodimers and EGFR/ErbB2 heterodimers and thus might have been reflected in a change to ErbB2 distribution, however in this study no such effect was observed. Double labelling for ErbB2 and phosphorylated ErbB2 also showed little change in the properties of clusters of ErbB2 showing the label marking the presence of phosphorylated ErbB2 after the addition of EGF [230]. Using NSOM Abulrob et al also report no change in ErbB2 cluster properties after stimulation with EGF [251].

We hypothesized that treatment of cells might have two possible outcomes: increased density in ErbB2 clusters if the molecules become more closely packed or decreased density if ErbB2 molecules are recruited to form heterodimers, which would appear as a lone molecule in the dSTORM image, and thus would not be detected in the cluster analysis. The latter might result in a decrease in the number of molecules per cluster, if ErbB2 leaves clusters to take part in alternative interactions. Dual colour imaging targeting the potential dimerization partner may be an interesting avenue for future work, since then a change may be detected in terms of increased colocalisation representing increased dimerization.

Yang et al. found that pairs of ErbB receptors (ErbB1/ErbB2, ErbB2/ErbB3, ErbB1/ErbB3) showed very little coclustering even after stimulation [230]. Valley et al. suggest that this unexpected segregation of receptors suggests a possible mechanism though which membrane microdomains may regulate heterointeractions [37]. This theory is of particular interest, and motivated our investigation of ErbB2 clustering in response to stimulation, as we suspect that TERMs may be

involved in regulating ErbB2 interactions. By examining clustering of ErbB2 after treatment or stimulation in control and CD82 over-expressing cells, we aimed to compare the pattern of response observed in each cell line, since this could provide evidence to support or exclude CD82 microdomains as one of the microdomains playing a role in ErbB spatial segregation.

It is difficult to predict the possible effects of treatment with any of the panel of ErbB targeting molecules used in this study on ErbB2 cluster properties, as we can see there is controversy in the literature over the effect of many of the treatments. We will instead try to correlate the results we observe with the present theories around ErbB2 interactions and the role of CD82 in mediating these.

4.11.2 Results

The results of the panel of stimulation experiments performed are presented in Figure 4-35 and Table 4-12.

Figure 4-35 A shows the molecular density in ErbB2 clusters in SKBR3/zeo and SKBR3/CD82 cells in response to treatment with a panel of ErbB2 targeting molecules. These histograms represent the total population of ErbB2 clusters detected on these cells, and we see subtle changes in both cell lines in the density in ErbB2 clusters in response to treatment with EGF, Herceptin or heregulin.

On stimulation with EGF there is a slight shift towards less dense clusters in both SKBR3/zeo and SKBR3/CD82 cell lines. Stimulation with Herceptin seems to have little effect on cluster density in either cell line. Stimulation with heregulin however, appears to cause little change to the least dense clusters in both cell lines, but does hint at the presence of an increase in the population of clusters with around 4000-5000 molecules/μm^2. Although subtle and requiring further work to establish validity, this change could be indicative of an organisational change in ErbB2 clusters in response to heregulin stimulation of ErbB3.

From Figure 4-35 B we can see that on stimulation with EGF and heregulin there is a slight increase in the number of molecules of ErbB2 per cluster in both cell lines, however neither shift is statistically significant. We can see from Figure 4-35 A that there is a slight increase in the number of ErbB2 clusters in the lowest density bin in these same conditions, and the formation of ErbB1/ErbB2 and ErbB2/ErbB3 heterodimers will likely introduce space in between ErbB2 molecules, so this result may indicate that we are detecting larger less dense ErbB2 clusters after stimulation due to the inclusion of ErbB1 and ErbB3 molecules dimerised with ErbB2 after stimulation. The change is not statistically significant according to Kolmogorov-Smirnov tests performed on the distributions, but it may be that a longer serum starvation before stimulation is required (cells were serum starved for 1 hour in these experiments), or that the magnitude of the change is small enough to require larger sample numbers. The magnitude of the change in cluster properties and proportion of molecules clustered does not appear to be different between SKBR3/zeo and SKBR3/CD82, in the bulk population, as can be seen from the data in Table 4-12.

After treatment with Herceptin, SKBR3/zeo cells show an increase in the number of clusters with 4-6 molecules, while in SKBR3/CD82 there is a decrease in the number of these smallest clusters and a shift towards larger clusters, however the change is not significant, according to the Kolmogorov-Smirnov test performed. The change in the number of ErbB2 molecules per cluster is interesting however; further investigation could reveal how ErbB2 clusters change over time as dimerisation and activation occurs. In future work it would be interesting to examine the clustering of ErbB2 at different time points after stimulation, to see if perhaps CD82 has a role in mediating the rate of the response rather than the magnitude.

A

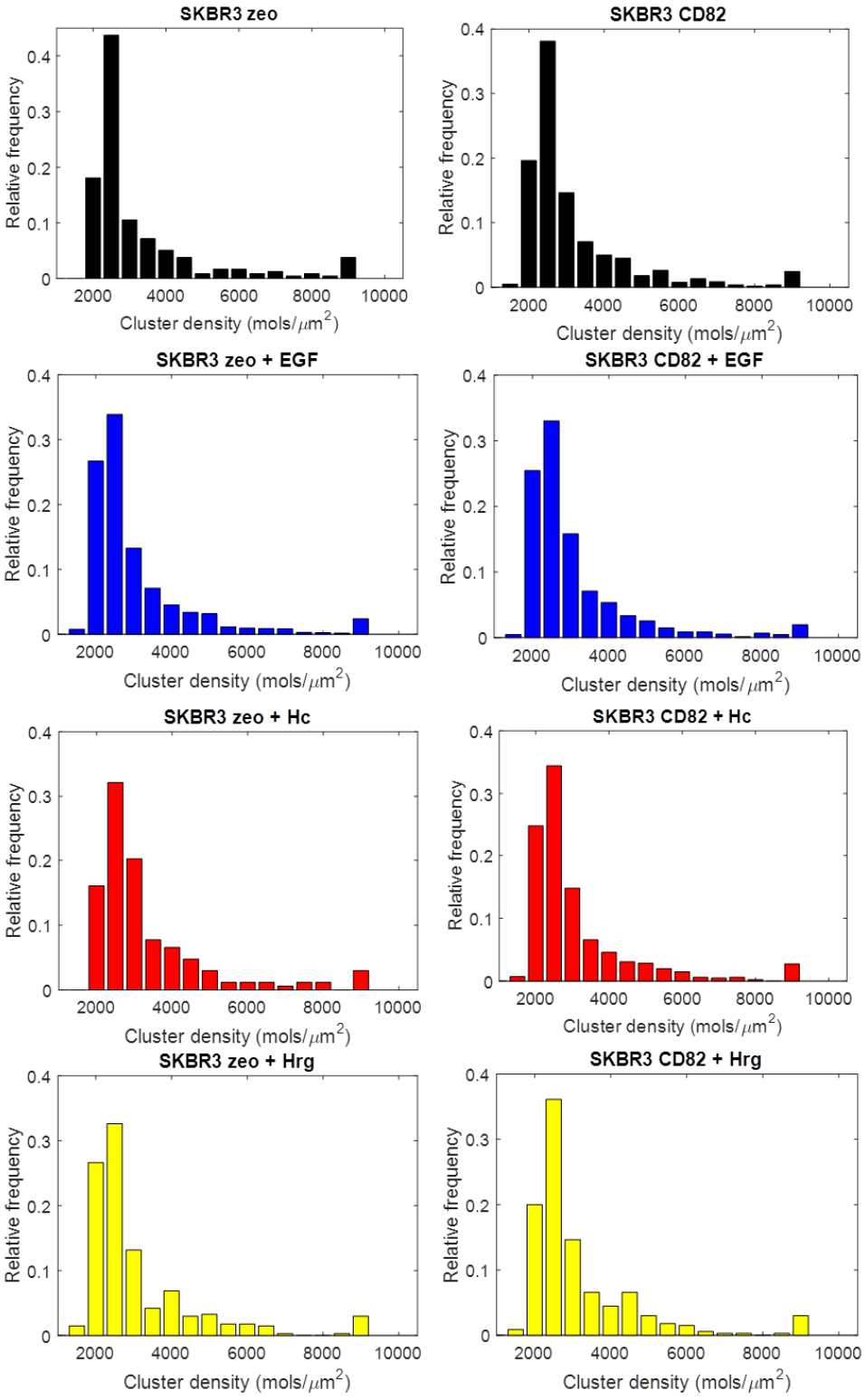
SKBR3 zeo
SKBR3 CD82
SKBR3 zeo + EGF
SKBR3 CD82 + EGF
SKBR3 zeo + Hc
SKBR3 CD82 + Hc
SKBR3 zeo + Hrg
SKBR3 CD82 + Hrg
Relative frequency
Cluster density (mols/μm^2)
0
0.1
0.2
0.3
0.4
2000
4000
6000
8000
10000

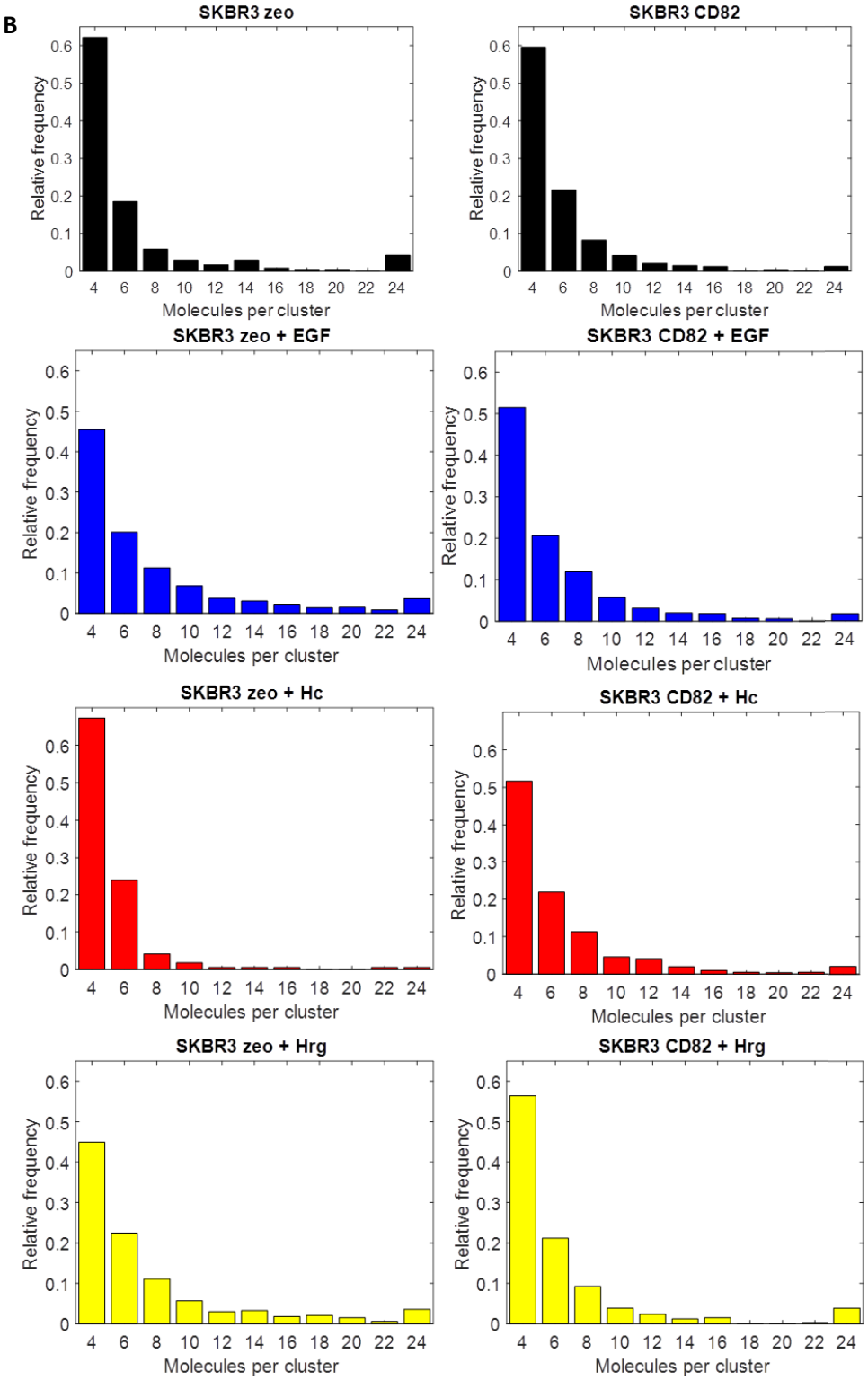

Figure 4-35: Molecules of ErbB2 per cluster in SKBR3/zeo and SKBR3/CD82 cells after ErbB2 targeting treatments

In all conditions except Herceptin treatment, SKBR3/zeo and SKBR3/CD82 cells were labelled (post-fixation) with 2µg/ml Herceptin and anti-human Alexa-488. In the Herceptin treatment condition, Herceptin was applied for 1-hour, before cells were fixed and rinsed, before blocking and applying the secondary anti-human Alexa-488 as per the normal protocol. Cluster properties for ErbB2 were determined using the ClusDoc implementation of DBSCAN. The density of ErbB2 in clusters in

SKBR3/zeo and SKBR3/CD82 is shown in the control condition, and after treatment with either 10ng/ml EGF for 5 minutes, 2μg/ml Herceptin for 1 hour, or 10ng/ml heregulin for 1 hour. Cells were serum starved for 1 hour prior to fixation or treatment. The histograms show the cluster properties for all clusters of ErbB2 (without splitting the population into colocalised and non-colocalised with CD82). Relative frequency is calculated by normalising the values of each bin to the maximum in each condition. **A)** Distributions of molecular density of ErbB2 in clusters, **B)** Distribution of the number of molecules per cluster in ErbB2 clusters. Data from at least 3 cells in each condition.

In MCF7 cells we only examined the effect of heregulin stimulation (10 ng/ml/1h) on ErbB2 clustering (Figure 4-36). Comparison of ErbB2 cluster properties (cluster area and number of molecules per cluster) in MCF7/puro, MCF7/CD82wt and MCF7/CD82cys5 before and after stimulation with heregulin revealed small but statistically non-significant differences (Kolmogorov-Smirnov test) between the stimulated and control condition.

Nagy et al. have previously shown using NSOM that in SKBR3 cells, activation with heregulin led to an increase in the mean cluster diameter from approximately 50 nm in non-activated cells to 60-90 nm after stimulation. They also observed that the average size of ErbB2 clusters on an ErbB2-transfected line of CHO cells was similar to that on activated SKBR3 cells; a finding which correlated with an observed increase in baseline tyrosine phosphorylation of ErbB2 in cells expressing only ErbB2 (no other ErbB receptors) [259]. From this they concluded that an increase in cluster size constitutes a general phenomenon in the activation of ErbB2. It is interesting therefore that in cells which express ErbB2 at a very low level, activation with heregulin appears to result in a decrease in ErbB2 cluster size.

Table 4-12: Properties of ErbB2 clusters in stimulated SKBR3 cells

Condition	Cluster density ± s.d. (mols/µm^2)	Molecules per cluster	Cluster area (nm^2) ± s.d.	% molecules clustered	Total clusters analysed
SKBR3/zeo control	$4.08x10^3 \pm 7.3x10^3$	9.82 ± 25.5	$3.23x10^3 \pm 5.96x10^3$	21.92	238
SKBR3/CD82 control	$3.64x10^3 \pm 6.54x10^3$	6.72 ± 9.14	$2.57x10^3 \pm 4.5x10^3$	29.93	1066
SKBR3/zeo + EGF	$3.42x10^3 \pm 4.36x10^3$	8.25 ± 7.31	$2.26x10^3 \pm 3.43x10^3$	44.58	1880
SKBR3/zeo + Herceptin	$3.51x10^3 \pm 2.60x10^3$	5.95 ± 8.39	$1.96x10^3 \pm 1.31x10^3$	17.00	168
SKBR3/zeo + Heregulin	$4.03 x10^3 \pm 8.38x10^3$	8.83 ± 12.39	$3.49x10^3 \pm 5.46x10^3$	36.49	334
SKBR3/CD82 + EGF	$3.31x10^3 \pm 3.76x10^3$	7.17 ± 6.33	$2.77x10^3 \pm 2.99x10^3$	39.12	1494
SKBR3/CD82 + Herceptin	$3.58 x10^3 \pm 7.16 x10^3$	7.05 ± 6.2	$2.71x10^3 \pm 2.66x10^3$	32.15	805
SKBR3/CD82 + Heregulin	$3.63x10^3 \pm 4.97x10^3$	8.57 ± 15.82	$3.46x10^3 \pm 7.80x10^3$	24.28	335

Table 4-13: ErbB2 cluster properties in MCF7 cells after treatment with 10ng/ml heregulin

	MCF7/puro		**MCF7/CD82wt**		**MCF7/CD82cys5**	
	Control	+ Hrg	Control	+ Hrg	Control	+ Hrg
Molecules per cluster ± s.d.	17.04±18.21	10.54±7.92	14.68±17.37	10.46±7.97	17.04±18.21	14.72±13.27
Cluster density ±s.d. (molecules/µm^2)	3792±3427	3519±3052	3418±5572	3457±4211	3792±3427	3728±3225
Cluster area ±s.d. (nm^2)	5302±5526	3683±2801	5478±5890	3778±2990	5302±5526	4611±3410
Clusters/µm^2	0.87	0.98	0.58	1.01	0.87	1.24
Total clusters analysed	200	369	288	505	868	619

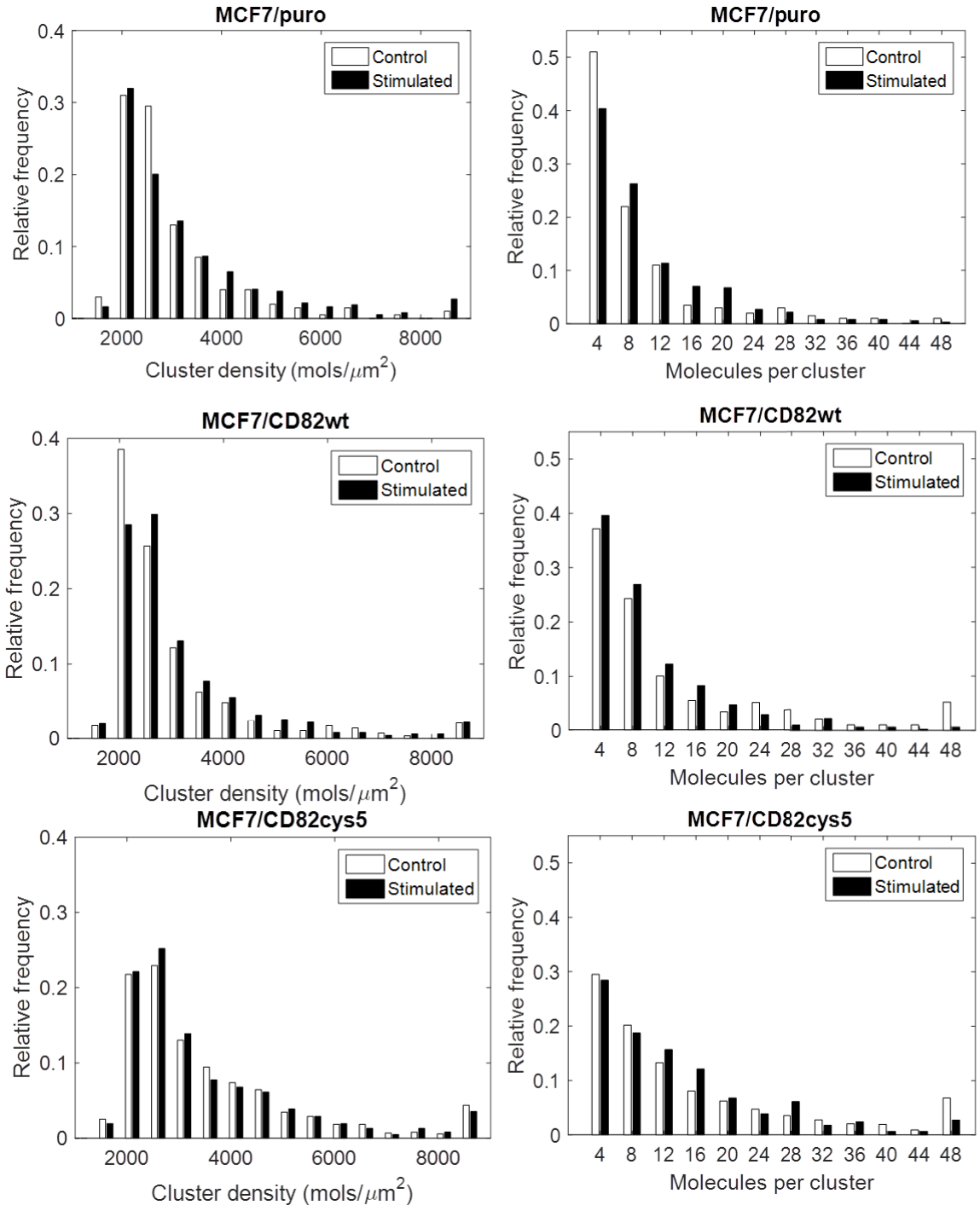

Figure 4-36: ErbB2 cluster density and molecules per cluster in MCF7 cells after stimulation with 10ng/ml heregulin

Cluster density and number of molecules of Erbb2 per cluster in MCF7/puro, MCF7/CF82wt and MCF7/CD82cys5 cells labelled in single colour with Alexa-647 were determined after stimulation with Hergulin. Cells analysed: MCF7/puro control = 4, +Hrg = 3; MCF7/CD82wt control = 4, +Hrg = 4; MCF7/CD82cys5 control = 8, +Hrg = 4.

4.11.3 Analysis of effect of stimulation on colocalisation of ErbB2 with phosphotyrosine and CD82

Following analysis of the cluster properties of ErbB2 after treatment with EGF, heregulin, or Herceptin, we then examined the data for SKBR3 cells in more depth, sub-classifying clusters according to whether they were colocalised with CD82. We also examined the colocalisation of ErbB2 with anti-phosphotyrosine mAb after treatment with EGF and Herceptin.

Figure 4-37 shows the number of molecules per ErbB2 cluster in SKBR3/zeo and SKBR3/CD82 cell lines, before and after stimulation with EGF or Herceptin, in clusters colocalised with phosphotyrosine signal and those not. From this we can see that in the control condition that of the smallest clusters of 4 molecules, there are more colocalised with phosphotyrosine than non-colocalised, which may indicate that smaller clusters are more active or accessible for interactions, or that in these cells ErbB2 exists mainly in pre-formed dimers that are active. This second interpretation of the data is supported by previous results from this group showing an increase basal level of phosphorylation in CD82 over-expressing cells. After stimulation with EGF this pattern is still the same, with the distribution of molecule numbers in clusters colocalised with phosphotyrosine signal being shifted more towards smaller values than those which are not colocalised. This result is particularly interesting as it contrasts with the pattern seen in CD82 colocalisation of ErbB2 clusters, where the colocalised clusters seem to be slightly larger. This result implies that phosphotyrosine colocalised clusters and CD82 colocalised clusters are distinct populations with different properties.

After stimulation with EGF the proportion of colocalised clusters with a large number of molecules (18+) decreases in both SKBR3/zeo and SKBR3/CD82, while the distribution of molecules per cluster in the colocalised clusters does not appear to change. This is clear evidence that stimulation with EGF initiates the dispersal of large ErbB2 clusters, which would be consistent with the findings of Nagy et al [241], although in contrast to the several other studies discussed in the preceding section.

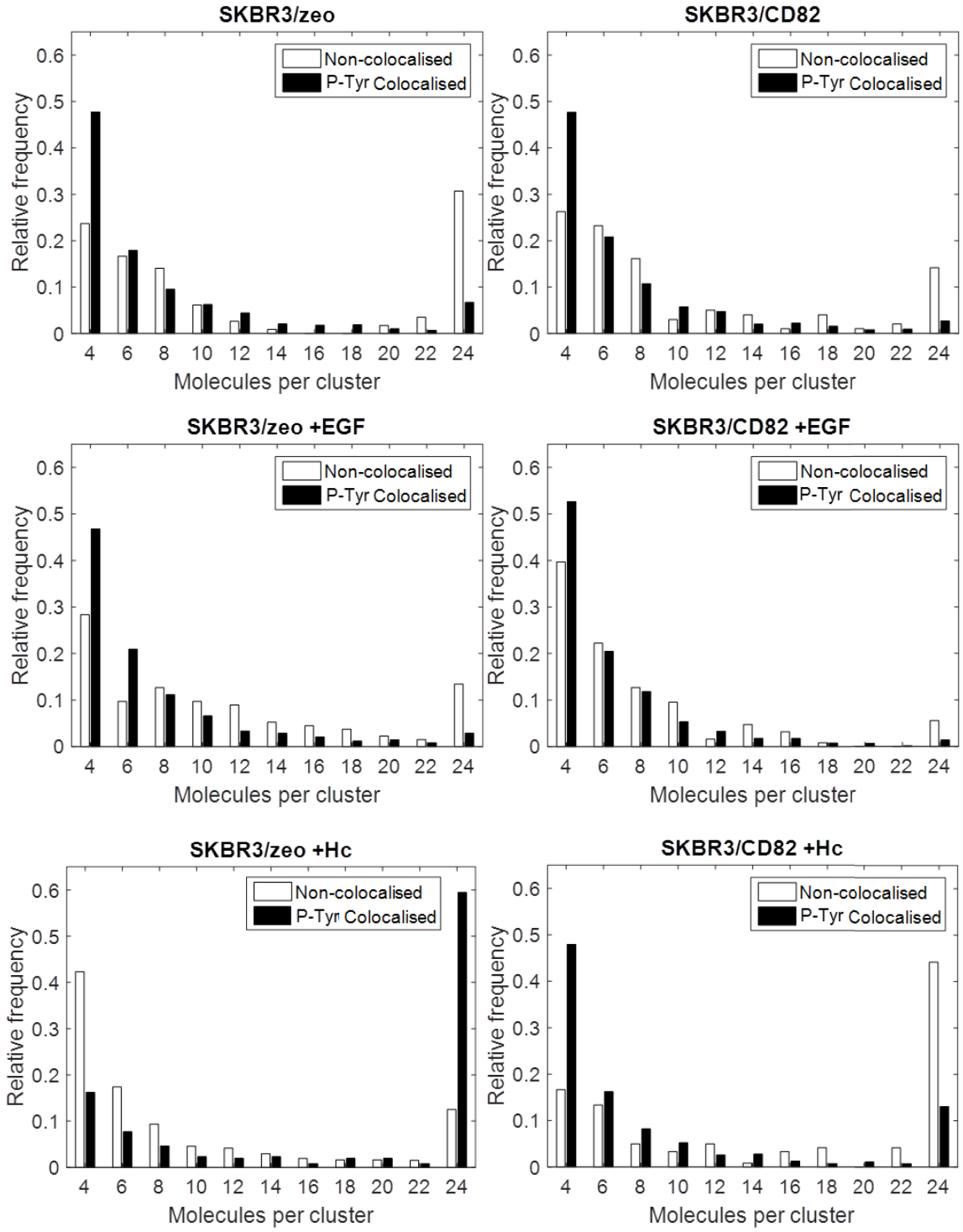

Figure 4-37: Erbb2 molecules per cluster after stimulation with EGF or Herceptin in relation to colocalisation with phospho-tyrosine specific antibody

ErbB2 was labelled with Herceptin and Alexa-488, and phosphotyrosine (P-Tyr) was labelled with Alexa-647. Clustering was performed with the ClusDoc implementation, and then clusters were sub-classified according to whether they colocalised with P-Tyr signal. P-Tyr colocalised clusters are those where at least 2 molecules are colocalised with signal from the P-Tyr channel, and therefore likely phosphorylated, or in interaction with a phosphorylated molecule. Number of cells analysed,

SKBR3/zeo control = 6, SKBR3/CD82 control = 7; SKBR3/zeo + EGF = 5, SKBR3/CD82 + EGF = 5; SKBR3/zeo +Hc = 5, SKBR3/CD82 +Hc = 4.

On stimulation with Herceptin a large increase in the number of molecules per cluster is observed in clusters containing phosphotyrosine signal in SKBR3/zeo, and in SKBR3/CD82 there is a large increase in the number of molecules per cluster in those not colocalised with phosphorylation. This result is surprising, as CD82 expression does not seem to have a large effect on cluster properties in any other condition. Further data would need to be gathered to confirm this effect.

Even disregarding the phosphotyrosine colocalisation status of the clusters of Ebrb2 after stimulation with Herceptin in the bottom row of Figure 4-37, the increase in the number of molecules per cluster (both colocalised and non-colocalised clusters combined, and in both cell lines) is surprising. To acquire the data presented in Figure 4-35 A, SKBR3/zeo and SKBR3/CD82 cells were treated with Herceptin before fixation and labelling under the same conditions as the for the data presented in Figure 4-37, except that for Figure 4-35 A labelling was only performed in single colour. However the contrast between the results in the third row of Figure 4-35, and those in the third row of Figure 4-37 is clear - the marked increase in the proportion of clusters in the largest bin in response to Herceptin treatment that is observed in Figure 4-37 is absent in the corresponding plots in Figure 4-35. The reason for this discrepancy between the datasets is unclear, and further experiments would be required to explain the difference in these observations.

In terms of the proportion of clusters which contain phosphotyrosine signal, the proportion of ErbB2 clusters which colocalise with the phosphotyrosine specific signal in the control condition is 6.84% in SKBR3/zeo and 10.06% in SKBR3/CD82, and after stimulation with EGF is 7.13% and 8.43% respectively. The change in these values between the control and stimulated conditions is very small and likely to be attributable to variation between cells, indicating that we are not able to detect an increase in phosphotyrosine signal in ErbB2 clusters after EGF stimulation using dual colour dSTORM. This is consistent with the hypothesis that EGF stimulation disperses Erbb2 clusters, in which case an

increase in phosphotyrosine signal from molecules of ErbB1/ErbB2 outside clusters is expected. We can see from the distribution presented in Figure 4-37 that the response to EGF stimulation is not markedly different in cells over-expressing CD82 compared to the control cells, indicating that CD82 expression does not have a role in altering ErbB2 clustering after EGF stimulation.

After Herceptin treatment, there is an increase in the proportion of clusters which contain molecules colocalised with the phosphotyrosine specific signal in both SKBR3/zeo and SKBR3/CD82. The proportion of clusters colocalised with phosphorylation signal after Herceptin treatment in SKBR3/zeo is 20.85% and in SKBR3/CD82 18.29%. That this is an increase compared to the control condition is a surprising result, as Herceptin treatment has been shown by this group previously [1] to cause a decrease in ErbB2 phosphorylation over a period of 4 hours, while this higher proportion of colocalised clusters indicates that in response to Herceptin treatment ErbB2 clusters with phosphorylated molecules, which could also be ErbB2, or other spatially associated molecules. The anti-phosphotyrosine antibody is not ErbB2 specific so the increase in colocalisation with phosphotyrosine signal could be due to any phosphotyrosine present in close proximity/in clusters with ErbB2. There is however, evidence in the literature that ErbB2 phosphorylation increases over shorter periods of time, in response to treatment with Herceptin [260] which may be what we have observed here.

The result in the bottom row of Figure 4-37 is surprising, clearly showing a large increase in the number of molecules per cluster colocalised with phosphorylation specific signal in SKBR3/zeo after Herceptin treatment. The reverse is seen in SKBR3/CD82, where the number of molecules in those clusters not detected as colocalised with phosphorylation increases after Herceptin treatment. These results are in contrast with that of Figure 4-38, where in both SKBR3/zeo and SKBR3/CD82 there are few clusters with greater than 10 molecules in both the control and Herceptin treated conditions. The contrast in these distributions raises questions about the reproducibility of

quantitative microscopy data. Due to the large amounts of time required for image acquisition and subsequent processing and analysis, results are often presented from small numbers of cells. However, between the two populations of cells analysed in the post-treatment condition in these experiments (9 cells for the data in Figure 4-37, 7 cells for the data in Figure 4-38) there is clearly significant variation. This highlights the importance of consistency in the experimental and analytical approach, and in sampling as large a population as possible. This is also indicative of the need for further work to optimise dual colour imaging approaches, particularly where quantitative results are required. Without further work to repeat the data collection in both the control and Herceptin treated conditions both in the presence of anti-phosphotyrosine antibody and without, the reason for the presence of much larger clusters of ErbB2 in the Figure 4-37 subset of the data than in the Figure 4-38 subset cannot be determined. Both of these experiments were performed under the same conditions, using the same batch of primary and secondary antibody against ErbB2, with all other experimental conditions constant, therefore the reason for the contrasting results is not clear. This said, imaging studies performed by Peckys et al. have demonstrated that populations of SKBR3 cells are highly heterogeneous in their expression of ErbB2 between individual cells and between different membrane regions of the same cell (membrane ruffles and flat areas) [243], which could give rise to different cluster distributions.

Previous work conducted by this group [1] showed that the phosphorylation of ErbB2 is lower in the control condition in SKBR3/zeo than in SKBR3/CD82 cells. This correlates well with the data presented in Figure 4-37, where higher colocalisation of ErbB2 with phosphotyrosine specific signal is observed in SKBR3/CD82 than in SKBR3/zeo (6.84% of clusters in SKBR3/zeo and 10.06% in SKBR3/CD82). However, this previous study also found that after a 1 hour incubation with Herceptin, the phosphorylation of ErbB2 decreased in both cell lines. In contrast, the imaging data reveals a higher colocalisation of Erbb2 with phosphotyrosine specific signal after the 1 hour Herceptin treatment (20.85% in SKBR3/zeo and 18.29% in SKBR3/CD82). This increased colocalisation does not

directly imply increased ErbB2 phosphorylation, as the antibody is not specific to ErbB2, but does imply ErbB2 resides in increasingly activated clusters after incubation with Herceptin.

From Figure 4-38 we can see that generally CD82 colocalised clusters are slightly larger than non-colocalised clusters and that this applies in both the control and stimulated conditions. Aside from the slight shift towards larger clusters the distribution of molecules per cluster is broadly similar in both SKBR3/zeo and SKBR3/CD82 and does not change significantly on after treatment with Herceptin or heregulin. Together the data indicates that over-expression of CD82 does not have a significant effect on the spatial organisation of ErbB2 on the membrane.

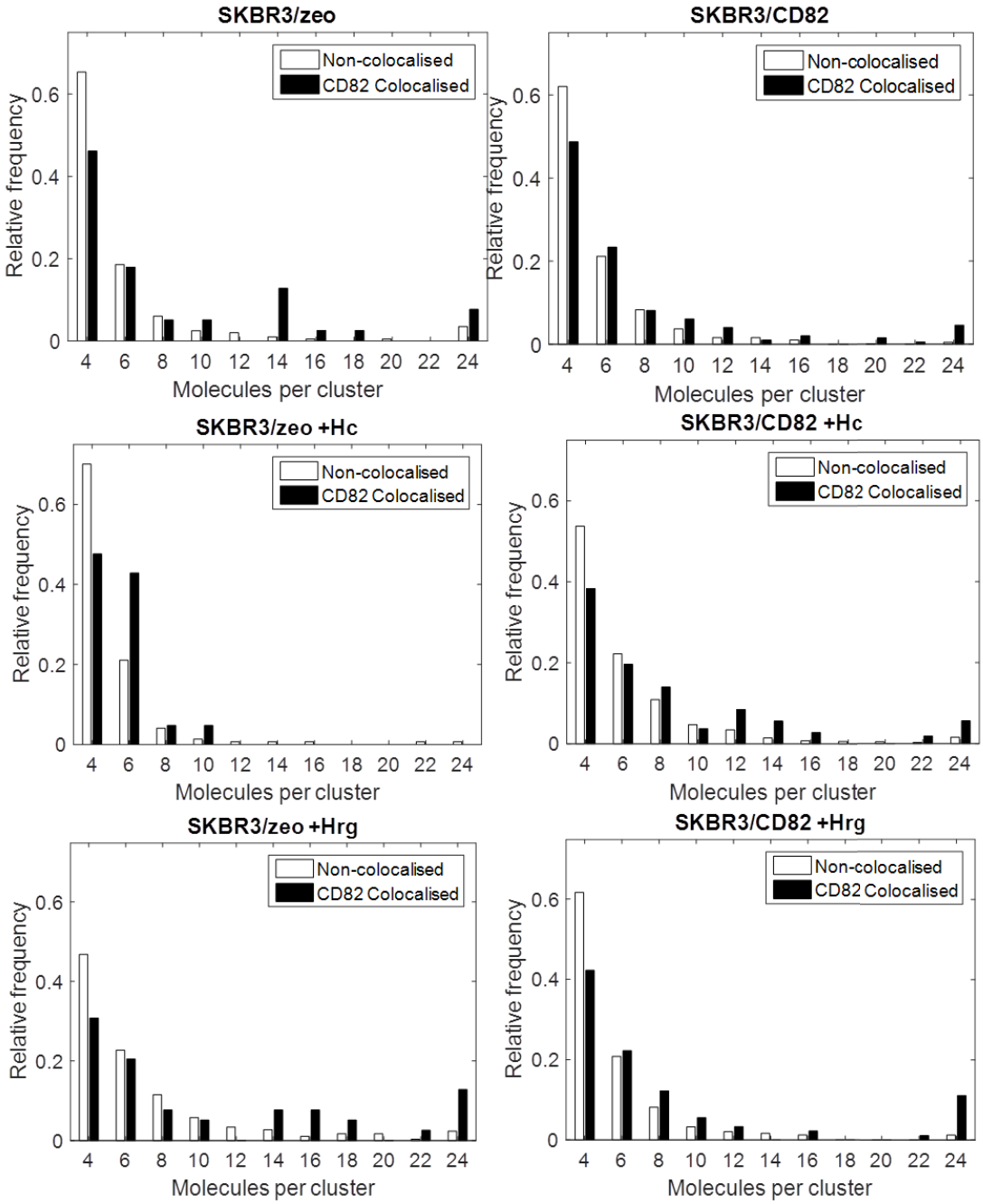

Figure 4-38: Erbb2 molecules per cluster after treatment with Herceptin or heregulin in relation to colocalisation with CD82

ErbB2 was labelled with Herceptin and Alexa-488, and CD82 was labelled with Alexa-647. Clustering was performed with the ClusDoc implementation, and then clusters were sub-classified according to whether they colocalised with CD82. ErbB2 clusters with at least 2 molecules colocalised with CD82 were classified as colocalised. The number of molecules of ErbB2 per cluster was determined in SKBR3/zeo and SKBR3/CD82 cells after stimulation with Herceptin or heregulin in relation to the colocalisation of the cluster with CD82. Number of cells analysed: SKBR3/zeo control = 5, SKBR3/CD82 control = 7; SKBR3/zeo +Hc = 3, SKBR3/CD82 +Hc = 4; SKBR3/zeo + Hrg = 2, SKBR3/CD82 +Hrg = 6.

4.12 Conclusions and future work

4.12.1 Future work on analysis

In the results presented above, the majority of ErbB2 clusters contain around 4-6 molecules, and have a diameter of roughly 30-40 nm on average (assuming circular clusters). These sizes could correspond to ErbB2 homodimers, based on the target-label distance and localisation precision described in section 4.9. Although the minimum number of points from which a cluster can be formed was set to four within 50 nm for analysis of ErbB2 localisations, it is possible that multiple localisations could result from the same molecule blinking on and off a number of times, and therefore that these clusters could actually represent single homodimers. The parameters of MinPts and ε used in the analysis are consistent with those used in other studies of ErbB2 clustering – for example Kaufman et al. employed a density based clustering approach, where the critical density for a cluster was set to 530 points/μm^2 which is equivalent to a minimum number of five neighbours around each detected molecule within a radius of 60 nm.

Despite the uncertainty regarding the contribution of repeated molecule blinking to the recovered localisations, if the clustering is performed requiring a higher minimum number of points to ensure that at least several molecules are represented, then smaller clusters would be excluded and this potential information lost. This highlights the difficulty of extracting quantitative data with confidence from a system with so many unknown variables, such as the degree of labelling, the number of antibodies bound to each site, the number of blinking events etc. These are difficulties inherent with quantitative analysis of single molecule localisation data, but with further improvements in labelling and imaging approaches, greater certainty in the precise molecular stoichiometry of detected clusters will be possible.

There is a need in future studies to develop methods which either result in higher point density through better labelling or imaging conditions, or analysis methods which are more robust to low point density. The methods employed in this study generally perform poorly where the point density is low – either finding clusters which are erroneously large due to large values of ε in DBSCAN, or failing to return clusters due to the ClusDoc script returning an error if no clusters are detected in an ROI. Such methods would also allow the extension of this study to other cell lines. In this study, imaging of ErbB2 and CD82 distribution on MCF7 cells was performed, but it was not possible to extract meaningful results from the data as the point density of both proteins was too low for successful analysis with ClusDoc, and the analysis with multi-pass DBSCAN resulted in the calculation of too large a search radius to return biologically meaningful clusters.

The choice of parameters for DBSCAN analysis effects the population of clusters detected in the data – larger values for ε and MinPts can identify clusters that would be considered background using a smaller radius, while smaller radii can identify substructures which would be obscured by the detection of larger clusters. The problems posed by the need to select certain values when the true underlying structure of the data is unkown can be overcome to some degree by using a multi-pass implementation to look at multiple spatial scales, but the ε value should be kept consistent between analyses to avoid biasing the clustering depending on the density in the specific area being analysed, and the results obtained are still dependent on selection of an appropriate value for MinPts. Other methods for clustering such as Expectation Maximisation of a Guassian Mixture (EMGM) [261] have been proposed to circumvent such issues, and it may be that further development of analysis methods for SMLM data is required. It has been suggested that the relatively recently developed SR Tesseler algorithm may be better at clustering where the difference in density between the cluster and the background is not large (i.e. for sparse data) [225]. It may be interesting to consider a performing a comparative study of results obtained via these and other approaches in future work.

For now, the imaging and analysis methods employed must be carefully considered when comparing results with those of other researchers, and researchers should be aware that both can influence the quantification of results, so care should be taken when making comparisons between studies.

Another avenue which may be interesting to pursue in future work is analysis of inter-cluster structure - examining molecular distribution inside clusters can reveal density gradients, or multiple density gradients, which can reveal whether a cluster is made of one large structure, or several smaller (connected) groups. It would be interesting to examine the inter-cluster structure of proteins known to associate with CD82 or other tetraspanins under different expression conditions, to see if the inter-cluster properties change as a result of modulation of their spatial arrangement by TERMs.

The above detailed approach could be used to investigate the response of ErbB2 to a treatment or in CD82 over-expressing conditions, and may reveal the presence or formation of homo or heterodimers, and further detail regarding the substructure of protein clusters.

1.1.1 Future experimental work

In future studies, it may be possible to remove some of the intracellular variability observed in the clustering results by classifying cells before quantitative analysis as high, medium or low-expressors of ErbB2, in advance of performing quantitative analysis, since the expression of ErbB2 has been shown to be both highly heterogeneous between populations [243] and important for the clustering of ErbB receptors in response to stimulation [230]. This may allow a more specific study of the role of ErbB2 over-expression in ErbB signalling, and development of more targeted therapeutic approaches.

The density of labelling affects the number of localisations per frame over the whole duration of image acquisition [262] – this is a particular problem in low density labelled samples, where the number of localisations per frame decreases over the course of imaging, as the supply of ‘on’ fluorophores is not replenished at the rate of bleaching. This presents a challenge for imaging

samples where high labelling density is not possible, for example in cells where expression of the target protein is low. However, this challenge may be circumvented by certain developing approaches such as PAINT, where the fluorophore is replenished over the course of image acquisition [205], [263], [264].

As discussed in the previous section, limitations on the quantitative data that can be reliably extracted from dSTORM images result from uncertainty around factors such as the degree of labelling and incidence of blinking events. Whilst data subject to such uncertainties is still valuable for comparison of relative cluster properties and molecule numbers between samples imaged and analysed subject to the same uncertainties, the results are not truly quantitative in terms of being an accurate representation of molecular numbers. In order to develop a true picture of molecular stoichiometry in clusters, and reliably compare results from different studies, a truly quantitative approach such as PC-PALM is required [265].

4.12.2 Conclusions

In this chapter we have shown a strong dependence of imaging and subsequent clustering results on the precise imaging conditions, in terms of fluorophore and buffer conditions, and highlighted the importance of careful optimisation and consideration of these in interpreting results. We have shown that CD82 over-expression, and colocalisation of ErbB2 clusters with CD82 does not significantly affect ErbB2 cluster properties in non-stimulated cells.

We have shown that CD82 over-expression results in a higher number of clusters per unit area on the membrane, but does not change the properties of the clusters themselves such as size or density. This may indicate some underlying organisation of TERMs which is not altered by over-expression.

Ligand driven dimerization of ErbB receptors is fundamental to their activation, and we have shown that CD82 over-expression does not significantly alter ErbB2 cluster properties in response to

treatment with ErbB1 or ErbB3 ligands, nor in response to the therapeutic drug Herceptin. This indicates that CD82 does not modulate ErbB activation by spatially modulating ErbB distribution. We have shown no significant change in bulk ErbB2 cluster properties in response to the treatments studied, however we hypothesise that CD82 may have a role in mediating the rate of response via clustering/dimerisation to treatments, which may be interesting to investigate in future work. Heterogeneity in the expression level of ErbB2 in the cellular population may also be masking any changes in the response to treatment as a result of differing CD82 expression, as it is possible that high and low expressors of ErbB2 exhibit different responses.

Chapter 5 – Conclusions

Using dynamic imaging techniques, in particular single molecule tracking we have shown that there is little effect of CD82 expression on the diffusion and confinement of ErbB2 molecules diffusing in the plasma membrane of cells expressing ErbB2 at both high (SKBR3) and low (MCF7) levels. By analysing single molecule trajectories to determine the diffusion coefficient of entire trajectories and within trajectories, and a technique to detect temporary lateral confinement of single molecules, we were able to parameterise the confinement of ErbB2 molecules in the different cell lines studied, and compare these between high and low CD82 expression conditions. We found that the proportion of trajectories undergoing mixed motion (i.e. exhibiting both confined and Brownian motion segments) was similar in both CD82 over-expressing and control cells, therefore it seems unlikely that interactions with CD82 TERMS themselves is responsible for ErbB2 confinement. In addition to this, we found using dual colour imaging techniques that there is limited colocalisation, in particular co-confinement, of ErbB2 and CD82 in SKBR3/CD82 cells.

We have however, demonstrated for the first time, the potential of simultaneous application of SOFI and SMT to provide the capacity for super resolution imaging of the distribution of an entire population of membrane proteins, on a conventional microscope, in combination with the specificity of single molecule tracking and the ability to probe diffusion properties of molecular motion in the context of their localisation with respect to other proteins of interest.

Using the static super-resolution imaging dSTORM we have performed a comprehensive study to determine the most appropriate conditions and methods for both data collection (imaging) and analysis. We have in particular highlighted the importance of carefully selecting pairs of fluorophores which perform optimally under similar conditions, in order not to bias the clustering results based on the density of signal collected as a result of probe performance rather than protein distribution.

Using dSTORM we showed, again, limited change to the clustering of ErbB2 with CD82 overexpression, in both MCF7 and SKBR3 cells. We investigated the role of CD82 in mediating the response of ErbB2 clustering after treatment with ErbB targeting molecules, but found that CD82 expression does not significantly change the distribution of the cluster properties in response to stimulation. However, further work refining both the imaging conditions and analysis may yet reveal minor changes which are masked by the bulk population.

References

[1] E. McGrowder, “The role of the metastasis suppressor tetraspanin CD82/KAI1 in trastuzumab-mediated cellular responses,” University of Birmingham, 2012.

[2] E. Odintsova *et al.*, “Metastasis Suppressor Tetraspanin CD82/KAI1 Regulates Ubiquitylation of Epidermal Growth Factor Receptor,” *J. Biol. Chem.* , vol. 288, no. 36, pp. 26323–26334, Sep. 2013.

[3] G. M. Cooper, “Structure of the Plasma Membrane,” in *The Cell: A Molecular Approach. 2nd edition*, 2000.

[4] G. L. Nicolson, “The Fluid—Mosaic Model of Membrane Structure: Still relevant to understanding the structure, function and dynamics of biological membranes after more than 40 years,” *Biochim. Biophys. Acta - Biomembr.*, vol. 1838, no. 6, pp. 1451–1466, Jun. 2014.

[5] S. J. Singer and G. L. Nicolson, “The Fluid Mosaic Model of the Structure of Cell Membranes,” *Science (80-.).*, vol. 175, no. 4023, pp. 720–731, 1972.

[6] M. Yáñez-Mó, O. Barreiro, M. Gordon-Alonso, M. Sala-Valdés, and F. Sánchez-Madrid, “Tetraspanin-enriched microdomains: a functional unit in cell plasma membranes.,” *Trends Cell Biol.*, vol. 19, no. 9, pp. 434–46, Sep. 2009.

[7] J. Bernardino de la Serna, G. J. Schütz, C. Eggeling, and M. Cebecauer, “There Is No Simple Model of the Plasma Membrane Organization ,” *Frontiers in Cell and Developmental Biology* , vol. 4. p. 106, 2016.

[8] A. Kusumi *et al.*, “Membrane mechanisms for signal transduction: the coupling of the meso-scale raft domains to membrane-skeleton-induced compartments and dynamic protein complexes.,” *Semin. Cell Dev. Biol.*, vol. 23, no. 2, pp. 126–144, Apr. 2012.

[9] A. Kusumi, K. G. N. Suzuki, R. S. Kasai, K. Ritchie, and T. K. Fujiwara, “Hierarchical mesoscale domain organization of the plasma membrane.,” *Trends Biochem. Sci.*, vol. 36, no. 11, pp. 604–15, Nov. 2011.

[10] F. R. Maxfield, “Plasma membrane microdomains,” *Curr. Opin. Cell Biol.*, vol. 14, no. 4, pp. 483–487, Aug. 2002.

[11] D. Lingwood and K. Simons, “Lipid Rafts As a Membrane-Organizing Principle,” *Science (80-.).*, vol. 327, no. 5961, p. 46 LP-50, Dec. 2009.

[12] A. K. Neumann, M. S. Itano, and K. Jacobson, “Understanding lipid rafts and other related membrane domains,” *F1000 Biol. Rep.*, vol. 2, p. 31, Apr. 2010.

[13] A. Badana *et al.*, “Lipid Raft Integrity Is Required for Survival of Triple Negative Breast Cancer Cells,” *J. Breast Cancer*, vol. 19, no. 4, pp. 372–384, Dec. 2016.

[14] “Paradigm Shift of the Plasma Membrane Concept from the Two-Dimensional Continuum Fluid to the Partitioned Fluid: High-Speed Single-Molecule Tracking of Membrane Molecules,” *Annu. Rev. Biophys. Biomol. Struct.*, vol. 34, no. 1, pp. 351–378, May 2005.

[15] P. G. Saffman and M. Delbrück, “Brownian motion in biological membranes,” *Proc. Natl. Acad. Sci.* , vol. 72, no. 8, pp. 3111–3113, Aug. 1975.

[16] T. Fujiwara, K. Ritchie, H. Murakoshi, K. Jacobson, and A. Kusumi, “Phospholipids undergo hop diffusion in compartmentalized cell membrane,” *J. Cell Biol.*, vol. 157, no. 6, p. 1071 LP-1082, Jun. 2002.

[17] K. Suzuki, K. Ritchie, E. Kajikawa, T. Fujiwara, and A. Kusumi, “Rapid Hop Diffusion of a G-Protein-Coupled Receptor in the Plasma Membrane as Revealed by Single-Molecule Techniques,” *Biophys. J.*, vol. 88, no. 5, pp. 3659–3680, May 2005.

[18] Y. M. Umemura, M. Vrljic, S. Y. Nishimura, T. K. Fujiwara, K. G. N. N. Suzuki, and A. Kusumi, “Both MHC Class II and its GPI-Anchored Form Undergo Hop Diffusion as Observed by Single-Molecule Tracking,” *Biophys. J.*, vol. 95, no. 1, pp. 435–450, Jul. 2008.

[19] K. Jaqaman *et al.*, “Cytoskeletal Control of CD36 Diffusion Promotes Its Receptor and Signaling Function,” *Cell*, vol. 146, no. 4, pp. 593–606, Feb. 2017.

[20] N. L. Andrews *et al.*, “Actin restricts Fc[epsiv]RI diffusion and facilitates antigen-induced receptor immobilization,” *Nat Cell Biol*, vol. 10, no. 8, pp. 955–963, Aug. 2008.

[21] B. Treanor *et al.*, “The Membrane Skeleton Controls Diffusion Dynamics and Signaling through the B Cell Receptor,” *Immunity*, vol. 32, no. 2, pp. 187–199, Feb. 2017.

[22] C. Espenel *et al.*, “Single-molecule analysis of CD9 dynamics and partitioning reveals multiple modes of interaction in the tetraspanin web.,” *J. Cell Biol.*, vol. 182, no. 4, pp. 765–76, Aug. 2008.

[23] D. V. Köster *et al.*, “Actomyosin dynamics drive local membrane component organization in an in vitro active composite layer,” *Proc. Natl. Acad. Sci.*, vol. 113, no. 12, p. E1645 LP-E1654, Mar. 2016.

[24] T. K. Fujiwara *et al.*, “Confined diffusion of transmembrane proteins and lipids induced by the same actin meshwork lining the plasma membrane,” *Mol. Biol. Cell*, vol. 27, no. 7, pp. 1101–1119, Feb. 2016.

[25] W. S. Trimble and S. Grinstein, “Barriers to the free diffusion of proteins and lipids in the plasma membrane,” *J. Cell Biol.*, vol. 208, no. 3, p. 259 LP-271, Feb. 2015.

[26] M. F. Garcia-Parajo, a. Cambi, J. a. Torreno-Pina, N. Thompson, and K. Jacobson, “Nanoclustering as a dominant feature of plasma membrane organization,” *J. Cell Sci.*, vol. 127, no. 23, pp. 4995–5005, Nov. 2014.

[27] S. A. Freeman *et al.*, “Integrins Form an Expanding Diffusional Barrier that Coordinates Phagocytosis,” *Cell*, vol. 164, no. 1, pp. 128–140, Feb. 2017.

[28] R. S. Kasai *et al.*, “Full characterization of GPCR monomer–dimer dynamic equilibrium by single molecule imaging,” *J. Cell Biol.*, vol. 192, no. 3, p. 463 LP-480, Feb. 2011.

[29] K. G. N. Suzuki, T. K. Fujiwara, M. Edidin, and A. Kusumi, “Dynamic recruitment of phospholipase Cγ at transiently immobilized GPI-anchored receptor clusters induces IP₃–Ca²⁺ signaling: single-molecule tracking study 2,” *J. Cell Biol.*, vol. 177, no. 4, p. 731 LP-742, May 2007.

[30] K. G. N. Suzuki, T. K. Fujiwara, F. Sanematsu, R. Iino, M. Edidin, and A. Kusumi, “GPI-anchored receptor clusters transiently recruit Lyn and Gα for temporary cluster immobilization and Lyn activation: single-molecule tracking study 1,” *J. Cell Biol.*, vol. 177, no. 4, p. 717 LP-730, May 2007.

[31] S. K. Saka, A. Honigmann, C. Eggeling, S. W. Hell, T. Lang, and S. O. Rizzoli, “Multi-protein assemblies underlie the mesoscale organization of the plasma membrane,” *Nat. Commun.*, vol. 5, p. 4509, Jul. 2014.

[32] A. S. Harding and J. F. Hancock, “Using plasma membrane nanoclusters to build better signaling circuits,” *Trends Cell Biol.*, vol. 18, no. 8, pp. 364–371, Feb. 2017.

[33] S. J. Plowman, C. Muncke, R. G. Parton, and J. F. Hancock, “H-ras, K-ras, and inner plasma membrane raft proteins operate in nanoclusters with differential dependence on the actin cytoskeleton,” *Proc. Natl. Acad. Sci.* , vol. 102, no. 43, pp. 15500–15505, Oct. 2005.

[34] I. A. Prior and J. F. Hancock, “Ras trafficking, localization and compartmentalized signalling,” *Semin. Cell Dev. Biol.*, vol. 23, no. 2, pp. 145–153, Apr. 2012.

[35] D. Goswami *et al.*, “Nanoclusters of GPI-Anchored Proteins Are Formed by Cortical Actin-Driven Activity,” *Cell*, vol. 135, no. 6, pp. 1085–1097, Feb. 2017.

[36] P. Winckler *et al.*, “Identification and super-resolution imaging of ligand-activated receptor dimers in live cells,” *Sci. Rep.*, vol. 3, p. 2387, Aug. 2013.

[37] C. C. Valley, K. A. Lidke, and D. S. Lidke, “The Spatiotemporal Organization of ErbB Receptors: Insights from Microscopy,” *Cold Spring Harb. Perspect. Biol.*, vol. 6, no. 2, p. a020735, Feb. 2014.

[38] R. G. W. Anderson and K. Jacobson, “A Role for Lipid Shells in Targeting Proteins to Caveolae, Rafts, and Other Lipid Domains,” *Science (80-.).*, vol. 296, no. 5574, p. 1821 LP-1825, Jun. 2002.

[39] G. P. Otto and B. J. Nichols, “The roles of flotillin microdomains – endocytosis and beyond,” *J. Cell Sci.*, vol. 124, no. 23, p. 3933 LP-3940, Dec. 2011.

[40] P. Lajoie, J. G. Goetz, J. W. Dennis, and I. R. Nabi, “Lattices, rafts, and scaffolds: domain regulation of receptor signaling at the plasma membrane,” *J. Cell Biol.*, vol. 185, no. 3, p. 381 LP-385, May 2009.

[41] A. Delaguillaumie *et al.*, “Tetraspanin CD82 controls the association of cholesterol-dependent microdomains with the actin cytoskeleton in T lymphocytes: relevance to co-stimulation,” *J. Cell Sci.*, vol. 117, no. 22, p. 5269 LP-5282, Oct. 2004.

[42] E. Rubinstein, F. Le Naour, C. Lagaudrière-Gesbert, M. Billard, H. Conjeaud, and C. Boucheix, “CD9, CD63, CD81, and CD82 are components of a surface tetraspan network connected to HLA-DR and VLA integrins,” *Eur. J. Immunol.*, vol. 26, no. 11, pp. 2657–2665, Nov. 1996.

[43] P. Angelisová, I. Hilgert, and Á. Ho<rej<sí, “Association of four antigens of the tetraspans family (CD37, CD53, TAPA-1, and R2/C33) with MHC class II glycoproteins,” *Immunogenetics*, vol. 39, no. 4, pp. 249–256, 1994.

[44] F. Berditchevski, M. M. Zutter, and M. E. Hemler, “Characterization of novel complexes on the

cell surface between integrins and proteins with 4 transmembrane domains (TM4 proteins).," *Mol. Biol. Cell* , vol. 7, no. 2, pp. 193–207, Feb. 1996.

[45] F. Berditchevski and E. Odintsova, "Characterization of Integrin–Tetraspanin Adhesion Complexes: Role of Tetraspanins in Integrin Signaling," *J. Cell Biol.*, vol. 146, no. 2, pp. 477–492, Jul. 1999.

[46] F. Berditchevski, K. F. Tolias, K. Wong, C. L. Carpenter, and M. E. Hemler, "A Novel Link between Integrins, Transmembrane-4 Superfamily Proteins (CD63 and CD81), and Phosphatidylinositol 4-Kinase," *J. Biol. Chem.* , vol. 272, no. 5, pp. 2595–2598, Jan. 1997.

[47] O. Barreiro *et al.*, "Endothelial adhesion receptors are recruited to adherent leukocytes by inclusion in preformed tetraspanin nanoplatforms," *J. Cell Biol.*, vol. 183, no. 3, pp. 527–542, Nov. 2008.

[48] E. Odintsova, J. Voortman, E. Gilbert, and F. Berditchevski, "Tetraspanin CD82 regulates compartmentalisation and ligand-induced dimerization of EGFR.," *J. Cell Sci.*, vol. 116, no. Pt 22, pp. 4557–66, Nov. 2003.

[49] M. Zuidscherwoude, F. Göttfert, V. M. E. Dunlock, C. G. Figdor, G. van den Bogaart, and A. B. van Spriel, "The tetraspanin web revisited by super-resolution microscopy," *Sci. Rep.*, vol. 5, p. 12201, Jul. 2015.

[50] S. Nydegger, S. Khurana, D. N. Krementsov, M. Foti, and M. Thali, "Mapping of tetraspanin-enriched microdomains that can function as gateways for HIV-1.," *J. Cell Biol.*, vol. 173, no. 5, pp. 795–807, Jun. 2006.

[51] C. M. Termini, K. A. Lidke, and J. M. Gillette, "Tetraspanin CD82 Regulates the Spatiotemporal Dynamics of PKCα in Acute Myeloid Leukemia," *Sci. Rep.*, vol. 6, p. 29859, Jul. 2016.

[52] S. Charrin, F. le Naour, O. Silvie, P.-E. Milhiet, C. Boucheix, and E. Rubinstein, "Lateral organization of membrane proteins: tetraspanins spin their web," *Biochem. J.*, vol. 420, no. 2, p. 133 LP-154, May 2009.

[53] D. Hanahan, R. A. Weinberg, and S. Francisco, "The Hallmarks of Cancer Review University of California at San Francisco," vol. 100, pp. 57–70, 2000.

[54] D. Hanahan and R. A. Weinberg, "Hallmarks of cancer: The next generation," *Cell*, vol. 144, no. 5, pp. 646–674, 2011.

[55] "Cancer registration statistics, England: first release, 2015." Office for National Statistics, 2017.

[56] C. M. Perou *et al.*, "Molecular portraits of human breast tumours.," *Nature*, vol. 406, no. 6797, pp. 747–752, Aug. 2000.

[57] D. J. Slamon *et al.*, "Studies of the HER-2/neu proto-oncogene in human breast and ovarian cancer," *Science (80-.).*, vol. 244, no. 4905, p. 707 LP-712, May 1989.

[58] N. R. Lemoine *et al.*, "Amplification and overexpression of the EGF receptor and c-erbB-2 proto-oncogenes in human stomach cancer.," *Br. J. Cancer*, vol. 64, no. 1, pp. 79–83, Jul. 1991.

[59] G. Sauter *et al.*, “Heterogeneity of erbB-2 Gene Amplification in Bladder Cancer,” *Cancer Res.*, vol. 53, no. 10, p. 2199 LP-2203, May 1993.

[60] G. Stenman, J. Sandros, A. Nordkvist, J. Mark, and P. Sahlin, “Expression of the ERBB2 protein in benign and malignant salivary gland tumors,” *Genes, Chromosom. Cancer*, vol. 3, no. 2, pp. 128–135, Mar. 1991.

[61] M. Tateishi, T. Ishida, T. Mitsudomi, S. Kaneko, and K. Sugimachi, “Prognostic value of c-erbB-2 protein expression in human lung adenocarcinoma and squamous cell carcinoma,” *Eur. J. Cancer Clin. Oncol.*, vol. 27, no. 11, pp. 1372–1375, 1991.

[62] L. A. Carey, “Through a Glass Darkly: Advances in Understanding Breast Cancer Biology, 2000-2010,” *Clin. Breast Cancer*, vol. 10, no. 3, pp. 188–195, 2010.

[63] M. Tan, J. Yao, and D. Yu, “Overexpression of the c-erbB-2 Gene Enhanced Intrinsic Metastasis Potential in Human Breast Cancer Cells without Increasing Their Transformation Abilities,” *Cancer Res.*, vol. 57, no. 6, p. 1199 LP-1205, Mar. 1997.

[64] S. E. Moody *et al.*, “Conditional activation of Neu in the mammary epithelium of transgenic mice results in reversible pulmonary metastasis,” *Cancer Cell*, vol. 2, no. 6, pp. 451–461, Mar. 2017.

[65] T. Holbro, G. Civenni, and N. E. Hynes, “The ErbB receptors and their role in cancer progression,” *Exp. Cell Res.*, vol. 284, no. 1, pp. 99–110, Mar. 2003.

[66] N. E. Hynes and H. a Lane, “ERBB receptors and cancer: the complexity of targeted inhibitors.,” *Nat. Rev. Cancer*, vol. 5, no. 5, pp. 341–354, May 2005.

[67] D. Slamon, G. Clark, S. Wong, W. Levin, a Ullrich, and W. McGuire, “Human breast cancer: correlation of relapse and survival with amplification of the HER-2/neu oncogene,” *Science (80-.).*, vol. 235, no. 4785, pp. 177–182, Jan. 1987.

[68] A. L. a Wong and S.-C. Lee, “Mechanisms of Resistance to Trastuzumab and Novel Therapeutic Strategies in HER2-Positive Breast Cancer.,” *Int. J. Breast Cancer*, vol. 2012, Jan. 2012.

[69] C. L. Arteaga and J. A. Engelman, “ERBB Receptors: From Oncogene Discovery to Basic Science to Mechanism-Based Cancer Therapeutics,” *Cancer Cell*, vol. 25, no. 3, pp. 282–303, Mar. 2014.

[70] H. Zhang *et al.*, “ErbB receptors: from oncogenes to targeted cancer therapies,” *J. Clin. Invest.*, vol. 117, no. 8, pp. 2051–2058, Aug. 2007.

[71] J. G. Paez *et al.*, “EGFR mutations in lung, cancer: Correlation with clinical response to gefitinib therapy,” *Science (80-.).*, vol. 304, no. 5676, pp. 1497–1500, 2004.

[72] W. Pao *et al.*, “EGF receptor gene mutations are common in lung cancers from ‘never smokers’ and are associated with sensitivity of tumors to gefitinib and erlotinib,” *Proc. Natl. Acad. Sci. U. S. A.*, vol. 101, no. 36, pp. 13306–13311, 2004.

[73] T. J. Lynch *et al.*, “Activating Mutations in the Epidermal Growth Factor Receptor Underlying Responsiveness of Non-Small-Cell Lung Cancer to Gefitinib,” *N. Engl. J. Med.*, vol. 350, no. 21, pp. 2129–2139, 2004.

[74] Y. Yarden and G. Pines, “The ERBB network: At last, cancer therapy meets systems biology,” *Nat. Rev. Cancer*, vol. 12, no. 8, pp. 553–563, 2012.

[75] “Comprehensive molecular portraits of human breast tumours,” *Nature*, vol. 490, no. 7418, pp. 61–70, Oct. 2012.

[76] B. Jaiswal *et al.*, “Oncogenic ERBB3 Mutations in Human Cancers,” *Cancer Cell*, vol. 23, no. 5, pp. 603–617, 2013.

[77] T. D. Prickett *et al.*, “Analysis of the tyrosine kinome in melanoma reveals recurrent mutations in ERBB4,” *Nat. Genet.*, vol. 41, no. 10, pp. 1127–1132, 2009.

[78] R. Gilbertson *et al.*, “Novel ERBB4 juxtamembrane splice variants are frequently expressed in childhood medulloblastoma,” *Genes Chromosom. Cancer*, vol. 31, no. 3, pp. 288–294, 2001.

[79] Y. Yarden and M. X. Sliwkowski, “Untangling the ErbB signalling network,” *Nat. Rev. Mol. Cell Biol.*, vol. 2, no. 2, pp. 127–137, 2001.

[80] J. R. Grandis *et al.*, “Levels of TGF-α and EGFR Protein in Head and Neck Squamous Cell Carcinoma and Patient Survival,” *JNCI J. Natl. Cancer Inst.*, vol. 90, no. 11, pp. 824–832, Jun. 1998.

[81] K. Yonesaka *et al.*, “Activation of ERBB2 signaling causes resistance to the EGFR-directed therapeutic antibody cetuximab,” *Sci. Transl. Med.*, vol. 3, no. 99, p. 99ra86-99ra86, Sep. 2011.

[82] T. Wilson, D. Lee, L. Berry, D. Shames, and J. Settleman, “Neuregulin-1-Mediated Autocrine Signaling Underlies Sensitivity to HER2 Kinase Inhibitors in a Subset of Human Cancers,” *Cancer Cell*, vol. 20, no. 2, pp. 158–172, 2011.

[83] N. E. Hynes, “ErbB2: From an EGFR Relative to a Central Target for Cancer Therapy,” *Cancer Res.*, vol. 76, no. 13, p. 3659 LP-3662, Jun. 2016.

[84] D. J. Leahy, “Structure and Function of the Epidermal Growth Factor (EGF⁄ErbB) Family of Receptors,” in *Cell Surface Receptors*, vol. Volume 68, B. T.-A. in P. Chemistry, Ed. Academic Press, 2004, pp. 1–27.

[85] T. P. J. Garrett *et al.*, “The Crystal Structure of a Truncated ErbB2 Ectodomain Reveals an Active Conformation, Poised to Interact with Other ErbB Receptors,” *Mol. Cell*, vol. 11, no. 2, pp. 495–505, Mar. 2017.

[86] S. A. Crone *et al.*, “ErbB2 is essential in the prevention of dilated cardiomyopathy,” *Nat. Med.*, vol. 8, p. 459, May 2002.

[87] van G. H. Melenhorst WB, Mulder GM, Xi Q, Hoenderop JG, Kimura K, Eguchi S, “Epidermal growth factor receptor signaling in the kidney,” *Hypertension*, vol. 52, no. 6, pp. 987–93, 2008.

[88] G. V. Røsland and A. S. T. Engelsen, “Novel Points of Attack for Targeted Cancer Therapy,” *Basic Clin. Pharmacol. Toxicol.*, vol. 116, no. 1, pp. 9–18, Jan. 2015.

[89] D. J. Slamon *et al.*, “Use of Chemotherapy plus a Monoclonal Antibody against HER2 for Metastatic Breast Cancer That Overexpresses HER2,” *N. Engl. J. Med.*, vol. 344, no. 11, pp.

783–792, Mar. 2001.

[90] T. Vu and F. X. Claret, “Trastuzumab: Updated Mechanisms of Action and Resistance in Breast Cancer,” *Front. Oncol.*, vol. 2, p. 62, Jun. 2012.

[91] A. Chung, X. Cui, W. Audeh, and A. Giuliano, “Current status of anti-her2 therapies: predicting and overcoming herceptin resistance,” *Clin. Breast Cancer*, vol. 13, no. 4, pp. 223–232, Aug. 2013.

[92] D. Gajria and S. Chandarlapaty, “HER2-amplified breast cancer: mechanisms of trastuzumab resistance and novel targeted therapies,” *Expert Rev. Anticancer Ther.*, vol. 11, no. 2, pp. 263–275, Feb. 2011.

[93] C. L. Vogel *et al.*, “Efficacy and Safety of Trastuzumab as a Single Agent in First-Line Treatment of HER2-Overexpressing Metastatic Breast Cancer,” *J. Clin. Oncol.*, vol. 20, no. 3, pp. 719–726, Feb. 2002.

[94] C. A. Hudis, “Trastuzumab — Mechanism of Action and Use in Clinical Practice,” *N. Engl. J. Med.*, vol. 357, no. 1, pp. 39–51, Jul. 2007.

[95] S. Levy and T. Shoham, “Protein-protein interactions in the tetraspanin web.,” *Physiology (Bethesda).*, vol. 20, no. 45, pp. 218–224, Aug. 2005.

[96] E. Todres, J. B. Nardi, and H. M. Robertson, “The tetraspanin superfamily in insects,” *Insect Mol. Biol.*, vol. 9, no. 6, pp. 581–590, 2000.

[97] S. Huang *et al.*, “The phylogenetic analysis of tetraspanins projects the evolution of cell–cell interactions from unicellular to multicellular organisms,” *Genomics*, vol. 86, no. 6, pp. 674–684, Dec. 2005.

[98] S. Charrin, S. Jouannet, C. Boucheix, and E. Rubinstein, “Tetraspanins at a glance.,” *J. Cell Sci.*, vol. 127, no. Pt 17, pp. 3641–8, Sep. 2014.

[99] H. Maecker, S. Todd, and S. Levy, “The tetraspanin superfamily: molecular facilitators.,” *FASEB J.*, 1997.

[100] M. E. Hemler, “Tetraspanin functions and associated microdomains.,” *Nat. Rev. Mol. Cell Biol.*, vol. 6, no. 10, pp. 801–811, Oct. 2005.

[101] B. Zimmerman, B. J. McMillan, T. C. M. Seegar, A. C. Kruse, and S. C. Blacklow, “Crystal structure of human tetraspanin CD81 reveals a conserved cholesterol binding cavity,” *J. Immunol.*, vol. 196, no. 1 Supplement, p. 132.6 LP-132.6, May 2016.

[102] B. Zimmerman *et al.*, “Crystal Structure of a Full-Length Human Tetraspanin Reveals a Cholesterol-Binding Pocket,” *Cell*, vol. 167, no. 4, p. 1041–1051.e11, Mar. 2017.

[103] C. Boucheix and E. Rubinstein, “Tetraspanins,” *Cell. Mol. Life Sci. C.*, vol. 58, no. 2001, pp. 1189–1205, 2001.

[104] L. E. Bradbury, G. S. Kansas, S. Levy, R. L. Evans, and T. F. Tedder, “The CD19/CD21 signal transducing complex of human B lymphocytes includes the target of antiproliferative antibody-1 and Leu-13 molecules.,” *J. Immunol.*, vol. 149, no. 9, p. 2841 LP-2850, Nov. 1992.

[105] S. C. Todd, S. G. Lipps, L. Crisa, D. R. Salomon, and C. D. Tsoukas, “CD81 expressed on human thymocytes mediates integrin activation and interleukin 2-dependent proliferation.,” *J. Exp. Med.*, vol. 184, no. 5, p. 2055 LP-2060, Nov. 1996.

[106] M. E. Hemler, “Tetraspanin Proteins Mediate Cellular Penetration, Invasion, and Fusion Events and Define a Novel Type of Membrane Microdomain,” *Annu. Rev. Cell Dev. Biol.*, vol. 19, no. 1, pp. 397–422, Nov. 2003.

[107] M. Zöller, “Tetraspanins: push and pull in suppressing and promoting metastasis.,” *Nat. Rev. Cancer*, vol. 9, no. 1, pp. 40–55, Jan. 2009.

[108] F. Berditchevski, E. Odintsova, S. Sawada, and E. Gilbert, “Expression of the Palmitoylation-deficient CD151 Weakens the Association of α3β1 Integrin with the Tetraspanin-enriched Microdomains and Affects Integrin-dependent Signaling ,” *J. Biol. Chem.* , vol. 277, no. 40, pp. 36991–37000, Oct. 2002.

[109] M. E. Hemler, “Tetraspanin proteins promote multiple cancer stages,” *Nat. Rev. Cancer*, vol. 14, no. 1, pp. 49–60, Dec. 2014.

[110] K. Phillips and A. White, “Correlation between reduction of metastasis in the MDA-MB-435 model system and increased expression of the Kai-1 protein,” *Mol. …*, vol. 120, no. January, pp. 111–120, 1998.

[111] T. Takeda, N. Hattori, T. Tokuhara, Y. Nishimura, M. Yokoyama, and M. Miyake, “Adenoviral transduction of MRP-1/CD9 and KAI1/CD82 inhibits lymph node metastasis in orthotopic lung cancer model.,” *Cancer Res.*, vol. 67, no. 4, pp. 1744–9, Feb. 2007.

[112] F.-S. Liu *et al.*, “KAI1 Metastasis Suppressor Protein Is Down-Regulated during the Progression of Human Endometrial Cancer,” *Clin. Cancer Res.*, vol. 9, no. 4, p. 1393 LP-1398, Apr. 2003.

[113] C. Xu *et al.*, “CD82 endocytosis and cholesterol-dependent reorganization of tetraspanin webs and lipid rafts,” *FASEB J.* , vol. 23, no. 10, pp. 3273–3288, Oct. 2009.

[114] S. CHIGITA *et al.*, “CD82 inhibits canonical Wnt signalling by controlling the cellular distribution of β-catenin in carcinoma cells,” *Int. J. Oncol.*, vol. 41, no. 6, pp. 2021–2028, Dec. 2012.

[115] M. Abe, T. Sugiura, M. Takahashi, K. Ishii, M. Shimoda, and K. Shirasuna, “A novel function of CD82/KAI-1 on E-cadherin-mediated homophilic cellular adhesion of cancer cells,” *Cancer Lett.*, vol. 266, no. 2, pp. 163–170, Aug. 2008.

[116] B. A. Millis, “Evanescent-Wave Field Imaging: An Introduction to Total Internal Reflection Fluorescence Microscopy,” in *Molecular Profiling: Methods and Protocols*, V. Espina and L. A. Liotta, Eds. Totowa, NJ: Humana Press, 2012, pp. 295–309.

[117] A. L. Mattheyses, S. M. Simon, and J. Z. Rappoport, “Imaging with total internal reflection fluorescence microscopy for the cell biologist,” *J. Cell Sci.*, vol. 123, no. 21, p. 3621 LP-3628, Oct. 2010.

[118] R. H. Webb, “Confocal optical microscopy,” *Reports Prog. Phys.*, vol. 59, no. 3, p. 427, 1996.

[119] A. Fine, “Confocal Microscopy: Principles and Practice,” *Cold Spring Harb. Protoc.* , vol. 2007, no. 10, p. pdb.top22, Oct. 2005.

[120] C. Manzo and M. F. Garcia-Parajo, “A review of progress in single particle tracking: from methods to biophysical insights.,” *Rep. Prog. Phys.*, vol. 78, no. 12, p. 124601, Dec. 2015.

[121] D. Alcor, G. Gouzer, and A. Triller, “Single-particle tracking methods for the study of membrane receptors dynamics.,” *Eur. J. Neurosci.*, vol. 30, no. 6, pp. 987–997, Sep. 2009.

[122] A. Kusumi, T. A. Tsunoyama, K. M. Hirosawa, R. S. Kasai, and T. K. Fujiwara, “Tracking single molecules at work in living cells,” *Nat Chem Biol*, vol. 10, no. 7, pp. 524–532, Jul. 2014.

[123] J. Elf, G.-W. Li, and X. S. Xie, “Probing Transcription Factor Dynamics at the Single-Molecule Level in a Living Cell,” *Science (80-.).*, vol. 316, no. 5828, p. 1191 LP-1194, May 2007.

[124] J. C. M. Gebhardt *et al.*, “Single-molecule imaging of transcription factor binding to DNA in live mammalian cells,” *Nat Meth*, vol. 10, no. 5, pp. 421–426, May 2013.

[125] S. Courty, C. Luccardini, Y. Bellaiche, G. Cappello, and M. Dahan, “Tracking Individual Kinesin Motors in Living Cells Using Single Quantum-Dot Imaging,” *Nano Lett.*, vol. 6, no. 7, pp. 1491–1495, Jul. 2006.

[126] U. Kubitscheck, R. Veith, J. Ritter, and J.-P. Siebrasse, “Messenger RNA Trafficking in Living Cells,” in *Single Particle Tracking and Single Molecule Energy Transfer*, Wiley-VCH Verlag GmbH & Co. KGaA, 2009, pp. 43–65.

[127] F. Pinaud, S. Clarke, A. Sittner, and M. Dahan, “Probing cellular events, one quantum dot at a time,” *Nat. Methods*, vol. 7, no. 4, pp. 275–285, Apr. 2010.

[128] G. Giannone, E. Hosy, J.-B. Sibarita, D. Choquet, and L. Cognet, “High-content super-resolution imaging of live cell by uPAINT.,” *Methods Mol. Biol.*, vol. 950, pp. 95–110, Jan. 2013.

[129] L. Lanzanò and E. Gratton, “Orbital single particle tracking on a commercial confocal microscope using piezoelectric stage feedback,” *Methods Appl. Fluoresc.*, vol. 2, no. 2, p. 24010, May 2014.

[130] J. J. Han, C. Kiss, A. R. M. Bradbury, and J. H. Werner, “Time-Resolved, Confocal Single-Molecule Tracking of Individual Organic Dyes and Fluorescent Proteins in Three Dimensions,” *ACS Nano*, vol. 6, no. 10, pp. 8922–8932, Oct. 2012.

[131] R. Heintzmann and G. Ficz, “Breaking the resolution limit in light microscopy,” *Brief. Funct. Genomics*, vol. 5, no. 4, pp. 289–301, Dec. 2006.

[132] T. Dertinger, R. Colyer, G. Iyer, S. Weiss, and J. Enderlein, “Fast, background-free, 3D super-resolution optical fluctuation imaging (SOFI),” *Proc. Natl. Acad. Sci. *, vol. 106, no. 52, pp. 22287–22292, Dec. 2009.

[133] H. Bannai, S. Lévi, C. Schweizer, M. Dahan, and A. Triller, “Imaging the lateral diffusion of membrane molecules with quantum dots.,” *Nat. Protoc.*, vol. 1, no. 6, pp. 2628–34, Jan. 2006.

[134] W. Pitkeathly, “Four Dimensional Analysis of Vesicle Dynamics During Cell Migration,” University of Birmingham, 2016.

[135] P. Dedecker, S. Duwé, R. K. Neely, and J. Zhang, “Localizer: fast, accurate, open-source, and modular software package for superresolution microscopy,” *J. Biomed. Opt.*, vol. 17, no. 12,

p. 126008, Dec. 2012.

[136] D. Axelrod, D. E. Koppel, J. Schlessinger, E. Elson, and W. W. Webb, “Mobility measurement by analysis of fluorescence photobleaching recovery kinetics.,” *Biophys. J.*, vol. 16, no. 9, pp. 1055–69, Sep. 1976.

[137] E. a Reits and J. J. Neefjes, “From fixed to FRAP: measuring protein mobility and activity in living cells.,” *Nat. Cell Biol.*, vol. 3, no. 6, pp. E145-7, Jun. 2001.

[138] M. J. Dayel, E. F. Hom, and A. S. Verkman, “Diffusion of green fluorescent protein in the aqueous-phase lumen of endoplasmic reticulum.,” *Biophys. J.*, vol. 76, no. 5, pp. 2843–2851, May 1999.

[139] V. Levi and E. Gratton, “Exploring dynamics in living cells by tracking single particles,” *Cell Biochem. Biophys.*, vol. 48, no. 1, pp. 1–15, May 2007.

[140] Z. Xiao *et al.*, “Single-Molecule Study of Lateral Mobility of Epidermal Growth Factor Receptor 2/HER2 on Activation,” *J. Phys. Chem. B*, vol. 112, no. 13, pp. 4140–4145, Apr. 2008.

[141] J. Chao, S. Ram, E. S. Ward, and R. J. Ober, “Ultrahigh accuracy imaging modality for super-localization microscopy.,” *Nat. Methods*, vol. 10, no. 4, pp. 335–338, Apr. 2013.

[142] M. P. Steinkamp, S. T. Low-Nam, S. Yang, K. A. Lidke, D. S. Lidke, and B. S. Wilson, “erbB3 Is an Active Tyrosine Kinase Capable of Homo- and Heterointeractions,” *Mol. Cell. Biol.* , vol. 34, no. 6, pp. 965–977, Mar. 2014.

[143] G. Orr, D. Hu, S. Ozçelik, L. K. Opresko, H. S. Wiley, and S. D. Colson, “Cholesterol dictates the freedom of EGF receptors and HER2 in the plane of the membrane.,” *Biophys. J.*, vol. 89, no. 2, pp. 1362–1373, Aug. 2005.

[144] J. Potel *et al.*, “EWI-2wint promotes CD81 clustering that abrogates Hepatitis C Virus entry,” *Cell. Microbiol.*, vol. 15, no. 7, pp. 1234–1252, 2013.

[145] P. Rassam, E. Margeat, P. Dosset, E. Rubinstein, and P.-E. Milhiet, “Analyzing Differential Dynamics of CD9 and CD81 with Single Molecule Tracking,” *Biophys. J.*, vol. 102, no. 3, p. 653a, Jul. 2017.

[146] B. E. Snaar-Jagalska, A. Cambi, T. Schmidt, and S. de Keijzer, “Single-Molecule Imaging Technique to Study the Dynamic Regulation of GPCR Function at the Plasma Membrane,” *Methods Enzymol.*, vol. 521, pp. 47–67, 2013.

[147] K. G. N. Suzuki, R. S. Kasai, T. K. Fujiwara, and A. Kusumi, “Single-Molecule Imaging of Receptor–Receptor Interactions,” *Methods Cell Biol.*, vol. 117, pp. 373–390, 2013.

[148] F. Pinaud, X. Michalet, G. Iyer, E. Margeat, H.-P. Moore, and S. Weiss, “Dynamic Partitioning of a GPI-Anchored Protein in Glycosphingolipid-Rich Microdomains Imaged by Single-Quantum Dot Tracking,” *Traffic*, vol. 10, no. 6, pp. 691–712, Jun. 2009.

[149] Y. Chen, W. R. Thelin, B. Yang, S. L. Milgram, and K. Jacobson, “Transient anchorage of cross-linked glycosyl-phosphatidylinositol–anchored proteins depends on cholesterol, Src family kinases, caveolin, and phosphoinositides,” *J. Cell Biol.*, vol. 175, no. 1, pp. 169–178, Oct. 2006.

[150] M. De Brabander, R. Nuydens, H. Geerts, and C. R. Hopkins, “Dynamic behavior of the

transferrin receptor followed in living epidermoid carcinoma (A431) cells with nanovid microscopy," *Cell Motil. Cytoskeleton*, vol. 9, no. 1, pp. 30–47, 1988.

[151] H. Geerts *et al.*, "Nanovid tracking: a new automatic method for the study of mobility in living cells based on colloidal gold and video microscopy," *Biophys. J.*, vol. 52, no. 5, pp. 775–782, 1987.

[152] M. J. Saxton and K. Jacobson, "Single-particle tracking: applications to membrane dynamics.," *Annu. Rev. Biophys. Biomol. Struct.*, vol. 26, pp. 373–399, Jan. 1997.

[153] E. Betzig and R. J. Chichester, "Single Molecules Observed by Near-Field Scanning Optical Microscopy," *Science (80-.).*, vol. 262, no. 5138, p. 1422 LP-1425, Nov. 1993.

[154] Y. Sako, S. Minoghchi, and T. Yanagida, "Single-molecule imaging of EGFR signalling on the surface of living cells.," *Nat. Cell Biol.*, vol. 2, no. 3, pp. 168–172, Mar. 2000.

[155] R. Iino, I. Koyama, and A. Kusumi, "Single molecule imaging of green fluorescent proteins in living cells: E-cadherin forms oligomers on the free cell surface.," *Biophys. J.*, vol. 80, no. 6, pp. 2667–2677, Jun. 2001.

[156] G. S. Harms *et al.*, "Single-molecule imaging of l-type Ca(2+) channels in live cells.," *Biophys. J.*, vol. 81, no. 5, pp. 2639–2646, Nov. 2001.

[157] M. Dahan, S. Lévi, C. Luccardini, P. Rostaing, B. Riveau, and A. Triller, "Diffusion Dynamics of Glycine Receptors Revealed by Single-Quantum Dot Tracking," *Science (80-.).*, vol. 302, no. 5644, p. 442 LP-445, Oct. 2003.

[158] S. Ram, P. Prabhat, J. Chao, E. S. Ward, and R. J. Ober, "High accuracy 3D quantum dot tracking with multifocal plane microscopy for the study of fast intracellular dynamics in live cells.," *Biophys. J.*, vol. 95, no. 12, pp. 6025–43, Dec. 2008.

[159] K. Gonda, T. M. Watanabe, N. Ohuchi, and H. Higuchi, "In vivo nano-imaging of membrane dynamics in metastatic tumor cells using quantum dots.," *J. Biol. Chem.*, vol. 285, no. 4, pp. 2750–2757, Jan. 2010.

[160] P. M. Haggie, J. K. Kim, G. L. Lukacs, and A. S. Verkman, "Tracking of Quantum Dot-labeled CFTR Shows Near Immobilization by C-Terminal PDZ Interactions," *Mol. Biol. Cell* , vol. 17, no. 12, pp. 4937–4945, Dec. 2006.

[161] D. S. Lidke, P. Nagy, T. M. Jovin, and D. J. Arndt-Jovin, "Biotin-ligand complexes with streptavidin quantum dots for in vivo cell labeling of membrane receptors.," *Methods Mol. Biol.*, vol. 374, pp. 69–79, Jan. 2007.

[162] A. M. SMITH and S. NIE, "Semiconductor Nanocrystals: Structure, Properties, and Band Gap Engineering," *Acc. Chem. Res.*, vol. 43, no. 2, pp. 190–200, Feb. 2010.

[163] H. Ng, A. Lu, G. Lin, L. Qin, and Z. Yang, *The Potential of Liposomes with Carbonic Anhydrase IX to Deliver Anticancer Ingredients to Cancer Cells in Vivo*, vol. 16. 2014.

[164] N. Chenouard *et al.*, "Objective comparison of particle tracking methods.," *Nat. Methods*, vol. 11, no. 3, pp. 281–289, Mar. 2014.

[165] H. Deschout *et al.*, "Precisely and accurately localizing single emitters in fluorescence

microscopy.," *Nat. Methods*, vol. 11, no. 3, pp. 253–66, Mar. 2014.

[166] J. B. Pawley, "Fundamental Limits in Confocal Microscopy," in *Handbook Of Biological Confocal Microscopy*, J. B. Pawley, Ed. Boston, MA: Springer US, 2006, pp. 20–42.

[167] J. C. Waters, "Accuracy and precision in quantitative fluorescence microscopy," *J. Cell Biol.*, vol. 185, no. 7, p. 1135 LP-1148, Jun. 2009.

[168] S. A. Haider *et al.*, "Fluorescence microscopy image noise reduction using a stochastically-connected random field model," *Sci. Rep.*, vol. 6, p. 20640, Feb. 2016.

[169] H. Qian, M. P. Sheetz, and E. L. Elson, "Single particle tracking. Analysis of diffusion and flow in two-dimensional systems.," *Biophys. J.*, vol. 60, no. 4, pp. 910–921, Oct. 1991.

[170] I. F. Sbalzarini and P. Koumoutsakos, "Feature point tracking and trajectory analysis for video imaging in cell biology.," *J. Struct. Biol.*, vol. 151, no. 2, pp. 182–95, Aug. 2005.

[171] H. Ewers, A. E. Smith, I. F. Sbalzarini, H. Lilie, P. Koumoutsakos, and A. Helenius, "Single-particle tracking of murine polyoma virus-like particles on live cells and artificial membranes," *Proc. Natl. Acad. Sci. United States Am.* , vol. 102, no. 42, pp. 15110–15115, Oct. 2005.

[172] M. Kinder and W. Brauer, "Classification of trajectories—extracting invariants with a neural network," *Neural Networks*, pp. 1–10, 1993.

[173] J. Owens and A. Hunter, "Application of the self-organising map to trajectory classification," *Visual Surveillance, 2000. Proceedings. Third IEEE International Workshop on*. pp. 77–83, 2000.

[174] R. Das, C. W. Cairo, and D. Coombs, "A hidden Markov model for single particle tracks quantifies dynamic interactions between LFA-1 and the actin cytoskeleton.," *PLoS Comput. Biol.*, vol. 5, no. 11, p. e1000556, Nov. 2009.

[175] J. a Helmuth, C. J. Burckhardt, P. Koumoutsakos, U. F. Greber, and I. F. Sbalzarini, "A novel supervised trajectory segmentation algorithm identifies distinct types of human adenovirus motion in host cells.," *J. Struct. Biol.*, vol. 159, no. 3, pp. 347–358, Sep. 2007.

[176] R. Simson, E. D. Sheets, and K. Jacobson, "Detection of temporary lateral confinement of membrane proteins using single-particle tracking analysis.," *Biophys. J.*, vol. 69, no. 3, pp. 989–993, Sep. 1995.

[177] M. J. Saxton, "Lateral diffusion in an archipelago. Effects of impermeable patches on diffusion in a cell membrane.," *Biophys. J.*, vol. 39, no. 2, pp. 165–73, Aug. 1982.

[178] N. Meilhac, L. Le Guyader, L. Salomé, and N. Destainville, "Detection of confinement and jumps in single-molecule membrane trajectories," *Phys. Rev. E*, vol. 73, no. 1, p. 11915, Jan. 2006.

[179] S. a Menchón, M. G. Martín, and C. G. Dotti, "APM_GUI: analyzing particle movement on the cell membrane and determining confinement.," *BMC Biophys.*, vol. 5, no. 1, p. 4, Jan. 2012.

[180] A. Serge, N. Bertaux, H. Rigneault, and D. Marguet, "Dynamic multiple-target tracing to probe spatiotemporal cartography of cell membranes," *Nat Meth*, vol. 5, no. 8, pp. 687–694, Aug. 2008.

[181] N. Ruthardt, D. C. Lamb, and C. Bräuchle, “Single-particle tracking as a quantitative microscopy-based approach to unravel cell entry mechanisms of viruses and pharmaceutical nanoparticles.,” *Mol. Ther.*, vol. 19, no. 7, pp. 1199–1211, Jul. 2011.

[182] L. C. C. Elliott, M. Barhoum, J. M. Harris, and P. W. Bohn, “Trajectory analysis of single molecules exhibiting non-brownian motion.,” *Phys. Chem. Chem. Phys.*, vol. 13, no. 10, pp. 4326–34, Mar. 2011.

[183] M. A. Thompson, J. M. Casolari, M. Badieirostami, P. O. Brown, and W. E. Moerner, “Three-dimensional tracking of single mRNA particles in Saccharomyces cerevisiae using a double-helix point spread function,” *Proc. Natl. Acad. Sci.* , vol. 107, no. 42, pp. 17864–17871, Oct. 2010.

[184] D. Thomas, H. Mike, V. Robert, S. Markus, and W. Shimon, “Superresolution Optical Fluctuation Imaging with Organic Dyes,” *Angew. Chemie Int. Ed.*, vol. 49, no. 49, pp. 9441–9443, 2010.

[185] T. Dertinger, R. Colyer, R. Vogel, J. Enderlein, and S. Weiss, “Achieving increased resolution and more pixels with Superresolution Optical Fluctuation Imaging (SOFI),” *Opt. Express*, vol. 18, no. 18, pp. 18875–18885, Aug. 2010.

[186] X. Zhang *et al.*, “Development of a Reversibly Switchable Fluorescent Protein for Super-Resolution Optical Fluctuation Imaging (SOFI),” *ACS Nano*, vol. 9, no. 3, pp. 2659–2667, Mar. 2015.

[187] N. Otsu, “A Threshold Selection Method from Gray-Level Histograms,” *IEEE Trans. Syst. Man. Cybern.*, vol. 9, no. 1, pp. 62–66, 1979.

[188] T. Lukeš *et al.*, “Quantifying protein densities on cell membranes using super-resolution optical fluctuation imaging,” *Nat. Commun.*, vol. 8, no. 1, p. 1731, 2017.

[189] W. Vandenberg and P. Dedecker, “Effect of probe diffusion on the SOFI imaging accuracy,” *Sci. Rep.*, vol. 7, p. 44665, Mar. 2017.

[190] P. A. Tipler and G. Mosca, *Physics for Scientists and Engineers*, 6th ed. W. H. Freeman and Company, 2008.

[191] “The Rayleigh Criterion.” [Online]. Available: http://hyperphysics.phy-astr.gsu.edu/hbase/phyopt/Raylei.html.

[192] S. Ram, E. S. Ward, and R. J. Ober, “Beyond Rayleigh’s criterion: A resolution measure with application to single-molecule microscopy,” *Proc. Natl. Acad. Sci. United States Am.* , vol. 103, no. 12, pp. 4457–4462, Mar. 2006.

[193] S. W. H. and S. J. S. and M. B. and X. Z. and R. H. and M. J. B. and J. B. and G. S. and H. H. and P. T. and A. H. and S. J. and I. T. and L. C. Cordes, “The 2015 super-resolution microscopy roadmap,” *J. Phys. D. Appl. Phys.*, vol. 48, no. 44, p. 443001, 2015.

[194] B. Huang, M. Bates, and X. Zhuang, “Super resolution fluorescence microscopy,” *Annu. Rev. Biochem.*, vol. 78, pp. 993–1016, 2009.

[195] H. Deschout, A. Shivanandan, P. Annibale, M. Scarselli, and A. Radenovic, “Progress in quantitative single-molecule localization microscopy,” *Histochem. Cell Biol.*, vol. 142, no. 1,

pp. 5–17, 2014.

[196] F. Fricke, J. Beaudouin, R. Eils, and M. Heilemann, “One, two or three? Probing the stoichiometry of membrane proteins by single-molecule localization microscopy,” *Sci. Rep.*, vol. 5, p. 14072, Sep. 2015.

[197] M. Linde, V. D., Löschberger, A., Klein, T., Heidbreder, M., Wolter, S., Heilemann, M., & Sauer *et al.*, “Direct stochastic optical reconstruction microscopy with standard fluorescent probes,” *Nat. Protoc.*, vol. 6, no. 7, pp. 991–1009, Jun. 2011.

[198] R. Thompson, D. Larson, and W. Webb, “Precise nanometer localization analysis for individual fluorescent probes,” *Biophys. J.*, vol. 82, pp. 2775–2783, 2002.

[199] M. J. Rust, M. Bates, and X. Zhuang, “Sub-diffraction-limit imaging by stochastic optical reconstruction microscopy (STORM),” *Nat Meth*, vol. 3, no. 10, pp. 793–796, Oct. 2006.

[200] M. Heilemann *et al.*, “Subdiffraction-Resolution Fluorescence Imaging with Conventional Fluorescent Probes,” *Angew. Chemie Int. Ed.*, vol. 47, no. 33, pp. 6172–6176, Aug. 2008.

[201] R. R. E. R. Thompson, D. D. R. Larson, and W. W. W. Webb, “Precise Nanometer Localization Analysis for Individual Fluorescent Probes,” *Biophys. J.*, vol. 82, no. 5, pp. 2775–2783, May 2002.

[202] M. Fernandez-Suarez and A. Y. Ting, “Fluorescent probes for super-resolution imaging in living cells,” *Nat Rev Mol Cell Biol*, vol. 9, no. 12, pp. 929–943, Dec. 2008.

[203] G. Patterson, M. Davidson, S. Manley, and J. Lippincott-Schwartz, “Superresolution Imaging using Single-Molecule Localization,” *Annu. Rev. Phys. Chem.*, vol. 61, pp. 345–367, 2010.

[204] S. A. McKinney, C. S. Murphy, K. L. Hazelwood, M. W. Davidson, and L. L. Looger, “A bright and photostable photoconvertible fluorescent protein for fusion tags,” *Nat. Methods*, vol. 6, no. 2, pp. 131–133, Feb. 2009.

[205] E. Betzig *et al.*, “Imaging Intracellular Fluorescent Proteins at Nanometer Resolution,” *Science (80-.).*, vol. 313, no. 5793, p. 1642 LP-1645, Sep. 2006.

[206] J. R. A. and S. T. R. and M. W. Davidson, “Single molecule localization microscopy for superresolution,” *J. Opt.*, vol. 15, no. 9, p. 94001, 2013.

[207] G. T. Dempsey, J. C. Vaughan, K. H. Chen, M. Bates, and X. Zhuang, “Evaluation of fluorophores for optimal performance in localization-based super-resolution imaging,” *Nat Meth*, vol. 8, no. 12, pp. 1027–1036, Dec. 2011.

[208] L. Nahidiazar, A. V Agronskaia, J. Broertjes, B. van den Broek, and K. Jalink, “Optimizing Imaging Conditions for Demanding Multi-Color Super Resolution Localization Microscopy,” *PLoS One*, vol. 11, no. 7, p. e0158884, Jul. 2016.

[209] N. Olivier, D. Keller, P. Gönczy, and S. Manley, “Resolution Doubling in 3D-STORM Imaging through Improved Buffers,” *PLoS One*, vol. 8, no. 7, p. e69004, Jul. 2013.

[210] Q. Zheng, S. Jockusch, Z. Zhou, and S. C. Blanchard, “The Contribution of Reactive Oxygen Species to the Photobleaching of Organic Fluorophores,” *Photochem. Photobiol.*, vol. 90, no. 2, pp. 448–454, Mar. 2014.

[211] C. E. Aitken, R. A. Marshall, and J. D. Puglisi, “An Oxygen Scavenging System for Improvement of Dye Stability in Single-Molecule Fluorescence Experiments(),” *Biophys. J.*, vol. 94, no. 5, pp. 1826–1835, Mar. 2008.

[212] J. Vogelsang *et al.*, “A Reducing and Oxidizing System Minimizes Photobleaching and Blinking of Fluorescent Dyes,” *Angew. Chemie Int. Ed.*, vol. 47, no. 29, pp. 5465–5469, 2008.

[213] J. C. Vaughan, G. T. Dempsey, E. Sun, and X. Zhuang, “Phosphine Quenching of Cyanine Dyes as a Versatile Tool for Fluorescence Microscopy,” *J. Am. Chem. Soc.*, vol. 135, no. 4, pp. 1197–1200, Jan. 2013.

[214] J. Schnitzbauer, M. T. Strauss, T. Schlichthaerle, F. Schueder, and R. Jungmann, “Super-resolution microscopy with DNA-PAINT,” *Nat. Protoc.*, vol. 12, no. 6, pp. 1198–1228, Jun. 2017.

[215] S. Wolter *et al.*, “rapidSTORM: accurate, fast open-source software for localization microscopy,” *Nat Meth*, vol. 9, no. 11, pp. 1040–1041, Nov. 2012.

[216] H. Babcock, Y. M. Sigal, and X. Zhuang, “A high-density 3D localization algorithm for stochastic optical reconstruction microscopy,” *Opt. Nanoscopy*, vol. 1, no. 1, p. 6, 2012.

[217] P. B. Stetson, “DAOPHOT: A Computer Program for Crowded-Field Stellar Photometry,” *Publ. Astron. Soc. Pacific*, vol. 99, no. 613, p. 191, 1987.

[218] S. J. Holden, S. Uphoff, and A. N. Kapanidis, “DAOSTORM: an algorithm for high- density super-resolution microscopy,” *Nat Meth*, vol. 8, no. 4, pp. 279–280, Apr. 2011.

[219] F. A. Espinoza, J. M. Oliver, B. S. Wilson, and S. L. Steinberg, “Using Hierarchical Clustering and Dendrograms to Quantify the Clustering of Membrane Proteins,” *Bull. Math. Biol.*, vol. 74, no. 1, pp. 190–211, Jan. 2012.

[220] P. Sengupta, T. Jovanovic-Talisman, D. Skoko, M. Renz, S. L. Veatch, and J. Lippincott-Schwartz, “Probing protein heterogeneity in the plasma membrane using PALM and pair correlation analysis,” *Nat Meth*, vol. 8, no. 11, pp. 969–975, Nov. 2011.

[221] J. Zhang, K. Leiderman, J. R. Pfeiffer, B. S. Wilson, J. M. Oliver, and S. L. Steinberg, “Characterizing the topography of membrane receptors and signaling molecules from spatial patterns obtained using nanometer-scale electron-dense probes and electron microscopy,” *Micron*, vol. 37, no. 1, pp. 14–34, Jan. 2006.

[222] M. A. Kiskowski, J. F. Hancock, and A. K. Kenworthy, “On the Use of Ripley’s K-Function and Its Derivatives to Analyze Domain Size,” *Biophys. J.*, vol. 97, no. 4, pp. 1095–1103, Aug. 2009.

[223] U. Endesfelder, K. Finan, S. J. Holden, P. R. Cook, A. N. Kapanidis, and M. Heilemann, “Multiscale Spatial Organization of RNA Polymerase in Escherichia coli,” *Biophys. J.*, vol. 105, no. 1, pp. 172–181, Jul. 2013.

[224] M. Ester, H.-P. Kriegel, J. Sander, and X. Xu, “A Density-based Algorithm for Discovering Clusters a Density-based Algorithm for Discovering Clusters in Large Spatial Databases with Noise,” in *Proceedings of the Second International Conference on Knowledge Discovery and Data Mining*, 1996, pp. 226–231.

[225] F. Levet *et al.*, “SR-Tesseler: a method to segment and quantify localization-based super-

resolution microscopy data," *Nat Meth*, vol. 12, no. 11, pp. 1065–1071, Nov. 2015.

[226] L. Andronov, I. Orlov, Y. Lutz, J.-L. Vonesch, and B. P. Klaholz, "ClusterViSu, a method for clustering of protein complexes by Voronoi tessellation in super-resolution microscopy," *Sci. Rep.*, vol. 6, p. 24084, Apr. 2016.

[227] L. Andronov, Y. Lutz, J.-L. Vonesch, and B. P. Klaholz, "SharpViSu: integrated analysis and segmentation of super-resolution microscopy data," *Bioinformatics*, vol. 32, no. 14, pp. 2239–2241, Jul. 2016.

[228] A. Mazouchi and J. N. Milstein, "Fast Optimized Cluster Algorithm for Localizations (FOCAL): a spatial cluster analysis for super-resolved microscopy," *Bioinformatics*, vol. 32, no. 5, pp. 747–754, Mar. 2016.

[229] M. Daszykowski, B. Walczak, and D. L. Massart, "Looking for Natural Patterns in Analytical Data. 2. Tracing Local Density with OPTICS," *J. Chem. Inf. Comput. Sci.*, vol. 42, no. 3, pp. 500–507, May 2002.

[230] S. Yang *et al.*, "Mapping ErbB receptors on breast cancer cell membranes during signal transduction," *J. Cell Sci.*, vol. 120, no. 16, p. 2763 LP-2773, Aug. 2007.

[231] B. D. Ripley, "Modelling Spatial Patterns," *J. R. Stat. Soc. Ser. B*, vol. 39, no. 2, pp. 172–212, 1977.

[232] S. V Pageon, P. R. Nicovich, M. Mollazade, T. Tabarin, and K. Gaus, "Clus-DoC: a combined cluster detection and colocalization analysis for single-molecule localization microscopy data," *Mol. Biol. Cell* , vol. 27, no. 22, pp. 3627–3636, Nov. 2016.

[233] A. Pertsinidis *et al.*, "Ultrahigh-resolution imaging reveals formation of neuronal SNARE/Munc18 complexes in situ," *Proc. Natl. Acad. Sci. U. S. A.*, vol. 110, no. 30, pp. E2812–E2820, Jul. 2013.

[234] D. Bar-On *et al.*, "Super-resolution Imaging Reveals the Internal Architecture of Nano-sized Syntaxin Clusters," *J. Biol. Chem.*, vol. 287, no. 32, pp. 27158–27167, Aug. 2012.

[235] M. Ankerst, M. M. Breunig, H.-P. Kriegel, and J. Sander, "OPTICS: Ordering Points to Identify the Clustering Structure," in *Proceedings of the 1999 ACM SIGMOD International Conference on Management of Data*, 1999, pp. 49–60.

[236] M. Daszykowski, B. Walczak, and D. L. Massart, "Looking for natural patterns in data: Part 1. Density-based approach," *Chemom. Intell. Lab. Syst.*, vol. 56, no. 2, pp. 83–92, 2001.

[237] M. Daszykowski, B. Walczak, and D. L. Massart, "Looking for natural patterns in data," *Chemom. Intell. Lab. Syst.*, vol. 56, no. 2, pp. 83–92, 2001.

[238] M. R. and F. F. and H. B. and O. Ö. and B. H. and H. Brismar, "Measuring true localization accuracy in super resolution microscopy with DNA-origami nanostructures," *New J. Phys.*, vol. 19, no. 2, p. 25013, 2017.

[239] S. Malkusch, U. Endesfelder, J. Mondry, M. Gelléri, P. J. Verveer, and M. Heilemann, "Coordinate-based colocalization analysis of single-molecule localization microscopy data," *Histochem. Cell Biol.*, vol. 137, no. 1, pp. 1–10, Jan. 2012.

[240] D. R. Whelan and T. D. M. Bell, “Image artifacts in Single Molecule Localization Microscopy: why optimization of sample preparation protocols matters,” *Sci. Rep.*, vol. 5, p. 7924, Jan. 2015.

[241] P. Nagy, J. Claus, T. M. Jovin, and D. J. Arndt-Jovin, “Distribution of resting and ligand-bound ErbB1 and ErbB2 receptor tyrosine kinases in living cells using number and brightness analysis.,” *Proc. Natl. Acad. Sci. U. S. A.*, vol. 107, no. 38, pp. 16524–16529, Sep. 2010.

[242] J. Wang, X. Yu, S. V Boriskina, and B. M. Reinhard, “Quantification of Differential ErbB1 and ErbB2 Cell Surface Expression and Spatial Nanoclustering through Plasmon Coupling,” *Nano Lett.*, vol. 12, no. 6, pp. 3231–3237, Jun. 2012.

[243] D. B. Peckys, U. Korf, and N. de Jonge, “Local variations of HER2 dimerization in breast cancer cells discovered by correlative fluorescence and liquid electron microscopy,” *Sci. Adv.*, vol. 1, no. 6, Jul. 2015.

[244] C. M. Termini, M. L. Cotter, K. D. Marjon, T. Buranda, K. a Lidke, and J. M. Gillette, “The membrane scaffold CD82 regulates cell adhesion by altering α4 integrin stability and molecular density.,” *Mol. Biol. Cell*, vol. 25, no. 10, pp. 1560–73, May 2014.

[245] B. Zhou, L. Liu, M. Reddivari, and X. A. Zhang, “The Palmitoylation of Metastasis Suppressor KAI1/CD82 Is Important for Its Motility- and Invasiveness-Inhibitory Activity,” *Cancer Res.*, vol. 64, no. 20, p. 7455 LP-7463, Oct. 2004.

[246] P. Bagossi, G. Horváth, G. Vereb, J. Szöllösi, and J. Tözsér, “Molecular Modeling of Nearly Full-Length ErbB2 Receptor,” *Biophys. J.*, vol. 88, no. 2, pp. 1354–1363, Jul. 2017.

[247] R. KAUFMANN, P. MÜLLER, G. HILDENBRAND, M. HAUSMANN, and C. CREMER, “Analysis of Her2/neu membrane protein clusters in different types of breast cancer cells using localization microscopy,” *J. Microsc.*, vol. 242, no. 1, pp. 46–54, 2011.

[248] R. B. Jones, A. Gordus, J. A. Krall, and G. MacBeath, “A quantitative protein interaction network for the ErbB receptors using protein microarrays.,” *Nature*, vol. 439, no. 7073, pp. 168–74, Jan. 2006.

[249] R. N. Jorissen, F. Walker, N. Pouliot, T. P. J. Garrett, C. W. Ward, and A. W. Burgess, “Epidermal growth factor receptor: mechanisms of activation and signalling,” *Exp. Cell Res.*, vol. 284, no. 1, pp. 31–53, 2003.

[250] C. Mineo, G. N. Gill, and R. G. W. Anderson, “Regulated Migration of Epidermal Growth Factor Receptor from Caveolae,” *J. Biol. Chem.* , vol. 274, no. 43, pp. 30636–30643, Oct. 1999.

[251] A. Abulrob *et al.*, “Nanoscale Imaging of Epidermal Growth Factor Receptor Clustering: EFFECTS OF INHIBITORS ,” *J. Biol. Chem.* , vol. 285, no. 5, pp. 3145–3156, Jan. 2010.

[252] P. V, M. H, and D. L, “Trastuzumab (Herceptin) Therapy and ERBB2 (HER2) Genotype,” in *Medical Genetics Summaries [Internet]*, 2012.

[253] R. Ghosh *et al.*, “Trastuzumab has preferential activity against breast cancers driven by HER2 homodimers,” *Cancer Res.*, vol. 71, no. 5, pp. 1871–1882, Mar. 2011.

[254] T. S. Wehrman, W. J. Raab, C. L. Casipit, R. Doyonnas, J. H. Pomerantz, and H. M. Blau, “A system for quantifying dynamic protein interactions defines a role for Herceptin in

modulating ErbB2 interactions," *Proc. Natl. Acad. Sci. U. S. A.*, vol. 103, no. 50, pp. 19063–19068, Dec. 2006.

[255] Y. Nagata *et al.*, "PTEN activation contributes to tumor inhibition by trastuzumab, and loss of PTEN predicts trastuzumab resistance in patients.," *Cancer Cell*, vol. 6, no. 2, pp. 117–127, Aug. 2004.

[256] H. A. Lane, I. Beuvink, A. B. Motoyama, J. M. Daly, R. M. Neve, and N. E. Hynes, "ErbB2 Potentiates Breast Tumor Proliferation through Modulation of p27(Kip1)-Cdk2 Complex Formation: Receptor Overexpression Does Not Determine Growth Dependency," *Mol. Cell. Biol.*, vol. 20, no. 9, pp. 3210–3223, May 2000.

[257] N. Dey, C. Williams, B. Leyland-Jones, and P. De, "A critical role for HER3 in HER2-amplified and non-amplified breast cancers: function of a kinase-dead RTK," *Am. J. Transl. Res.*, vol. 7, no. 4, pp. 733–750, Apr. 2015.

[258] T. Holbro, R. R. Beerli, F. Maurer, M. Koziczak, C. F. Barbas, and N. E. Hynes, "The ErbB2/ErbB3 heterodimer functions as an oncogenic unit: ErbB2 requires ErbB3 to drive breast tumor cell proliferation," *Proc. Natl. Acad. Sci.* , vol. 100, no. 15, pp. 8933–8938, Jul. 2003.

[259] P. Nagy, A. Jenei, A. K. Kirsch, J. Szollosi, S. Damjanovich, and T. M. Jovin, "Activation-dependent clustering of the erbB2 receptor tyrosine kinase detected by scanning near-field optical microscopy," *J. Cell Sci.*, vol. 112, no. 11, p. 1733 LP-1741, Jun. 1999.

[260] M. Dokmanovic and W. J. Wu, "Trastuzumab-induced HER2 phosphorylation: exploring the mechanisms and implications," *Recept. Clin. Investig.*, vol. 1, no. 4, pp. 2–6, 2014.

[261] A. R. Hendrik Deschout, Ilia Platzman, Daniel Sage, Lely Feletti, Joachim P. Spatz, "Investigating the inner structure of focal adhesions with single-molecule localization microscopy," 2017.

[262] J. Sanders, "Direct stochastic optical reconstruction microscopy (dSTORM) imaging of cellular structures," University of Manchester, 2015.

[263] W. R. Legant *et al.*, "High-density three-dimensional localization microscopy across large volumes," *Nat Meth*, vol. 13, no. 4, pp. 359–365, Apr. 2016.

[264] R. P. J. Nieuwenhuizen, M. Bates, A. Szymborska, K. A. Lidke, B. Rieger, and S. Stallinga, "Quantitative Localization Microscopy: Effects of Photophysics and Labeling Stoichiometry," *PLoS One*, vol. 10, no. 5, p. e0127989, May 2015.

[265] P. Sengupta, S. Van Engelenburg, and J. Lippincott-Schwartz, "Visualizing cell structure and function with point-localization superresolution imaging," *Dev. Cell*, vol. 23, no. 6, pp. 1092–1102, Dec. 2012.